Report
R-20-06
November 2022

Project NukPrio – Identification of elements with greatest sorption data needs for the KBS-3 repository

James Crawford

SVENSK KÄRNBRÄNSLEHANTERING AB

SWEDISH NUCLEAR FUEL
AND WASTE MANAGEMENT CO

Box 3091, SE-169 03 Solna
Phone +46 8 459 84 00
skb.se

SVENSK KÄRNBRÄNSLEHANTERING

ISSN 1402-3091
SKB R-20-06
ID 1922457

November 2022

Project NukPrio – Identification of elements with greatest sorption data needs for the KBS-3 repository

James Crawford, Kemakta Konsult AB

Keywords: Sorption, Geosphere, Retardation, Transport.

Abstract

In the safety assessment SR-Site (SKB 2011) and its more recent iteration PSAR (SKB 2022a), the migration of 44 different radionuclides through the geosphere was evaluated using transport modelling to establish the radiological dose consequences of engineered barrier failure over extended periods of time (up to 1 My). In the safety assessment calculations, the main process that hinders the migration of radionuclides is matrix diffusion coupled with sorption on internal micro-surfaces of the porous rock matrix. Of central importance to this transport modelling is the assignment of partitioning coefficients (K_d values) for the presumed linear sorption of radionuclides on site specific rock types in contact with different groundwater compositions. Since many of the radionuclides have K_d values associated with order of magnitude, or greater uncertainty this is a significant source of uncertainty in the estimation of far-field radiotoxicity fluxes to the biosphere.

Given that large multifactorial studies of sorption are time consuming and resource intensive, the need has arisen to establish a prioritised list of elements for focused studies in the continued site investigations at Forsmark. This report documents screening calculations that have been made to identify a small subset of elements whose K_d uncertainty might have the greatest impact on total radiological risk estimates. For this we have used SKB supplied near-field boundary conditions for a range of canister failure times and the central corrosion scenario of SR-Site and PSAR as a reference case. Consideration has been given both to first-order effects of K_d variation as well as mutual interactions between different radionuclides. Mutual interactions can arise due to dynamics of progeny ingrowth in decay chains as well as other less-intuitive ensemble effects relating to breakthrough peak timing and duration of otherwise unrelated radionuclides.

The resulting short-list of 15 elements has been divided into three tiers of importance to safety assessment. First tier elements whose K_d uncertainty contributes most to the overall uncertainty are identified as Ni, Se, Nb, Ra, and Pb. C might also be considered part of this group, although only for early engineered barrier failure times. Second tier elements which have a significantly less, although non-negligible, impact are Np, Pu, and Tc. In variant case calculations made using alternative dose conversion factors taken from SR-PSU (SKB 2014), Zr and Cs are found to be elevated in importance relative to Se and Nb, which are reduced in importance. For this reason, Zr and Cs are included as second tier elements even though they are of only minor importance in the SR-Site/PSAR reference case. Third tier elements are not directly important, although include useful geochemical analogues (Am, Eu, Th). U is included as a third-tier element to account for the possibility of altered relative importance if different near-field solubility assumptions are made, although it is not found to be important in the SR-Site/PSAR reference case. Other elements are shown to make sufficiently small contributions that even very large changes in K_d have inconsequential impacts on the total radiotoxicity flux for the release scenarios considered.

Sammanfattning

I säkerhetsanalysen SR-Site (SKB 2011) och dess uppdatering PSAR (SKB 2022a) utvärderades migrationen av 44 olika radionuklider genom geosfären med hjälp av transportmodellering för att fastställa de radiologiska doskonsekvenserna av en simulerad fallerande ingenjörsbarriär varvid längre tidsperioder (upp till 1 miljon år) studeras. I beräkningarna inom säkerhetsanalysen ansågs den huvudsakliga transportfördröjningsprocessen som hindrar migrationen av radionuklider vara matrisdiffusion i kombination med sorption på inre mikroytor i den porösa bergmatrisen. Av central betydelse för denna transportmodellering är tilldelningen av fördelningskoefficienter (K_d-värden) för den antagna linjära sorptionen av radionuklider på platsspecifika bergarter i kontakt med olika grundvattenkompositioner. Eftersom många av radionukliderna har K_d-värden som bara är kända till sin storleksordning, eller av än större osäkerhet, är detta en signifikant källa till osäkerhet vid uppskattningen av flödet av radiotoxicitet till biosfären.

Med tanke på att stora multifaktoriella studier av sorption är tids- och resurskrävande har behovet uppkommit att upprätta en prioriterad lista över grundämnen för fokuserade studier i de fortsatta platsundersökningarna vid Forsmark. Denna rapport dokumenterar beräkningar som har gjorts för att identifiera en mindre delmängd av grundämnen vars osäkerhet i K_d kan ha störst inverkan på de totala radiologiska riskuppskattningarna. För detta har vi använt de av SKB tillhandahållna randvillkoren gällande närområdet för en rad kapselbrottstider och det centrala korrosionsscenariot inom SR-Site samt PSAR som referensfall. Hänsyn har tagits till både första ordningens effekter i variationen av K_d och ömsesidiga interaktioner mellan olika radionuklider. Ömsesidiga interaktioner kan uppstå på grund av dynamiken för inväxt av radionuklider i sönderfallskedjorna såväl som andra mindre intuitiva effekter relaterade till samtidiga genombrottstider och varaktigheter för annars orelaterade radionuklider.

Den resulterande kortlistan med 15 grundämnen har delats in i tre nivåer med avseende på hur viktiga de är inom säkerhetsanalysen. Den första nivån innehåller de grundämnen vars osäkerhet i K_d bidrar mest till den totala osäkerheten. Dessa grundämnen identifieras som Ni, Se, Nb, Ra och Pb. C kan också betraktas som en del av denna grupp, men endast för en tidigt fallerande ingenjörsbarriär. Den andra nivån innehåller de grundämnen som har en signifikant mindre, men inte försumbar inverkan. Dessa grundämnen är Np, Pu, och Tc. I variantanalyser gjorda med alternativa dos konverteringsantaganden tagna från SR-PSU (SKB 2014) har Zr och Cs identifierats som mer viktiga till bekostnad av Se och Nb som nedgraderas i betydelse. Därför har Zr och Cs inkluderats till nivå två även om dessa är av begränsad betydelse i SR-Site/PSAR referensfallet.

Den tredje nivån innehåller mestadels grundämnen som utgör praktiska geokemiska analogier (Am, Eu, Th) för andra ämnen men spelar en liten roll för säkerheten. U inkluderas i den tredje nivån för att gardera mot eventuell ökning i betydelse ifall av alternativa antaganden gällande löslighet i närzonen. Andra element har visat sig ge så små bidrag, även vid mycket stora förändringar i K_d, att de har en obetydlig inverkan på det totala radiotoxicitetsflödet för de övervägda scenarierna.

Contents

1 Introduction

In the radionuclide transport report (SKB 2010b), calculations of radionuclide release, transport, and dose consequences were made for different scenarios and cases from the SR-Site Safety Assessment (SKB 2011). Since spent nuclear fuel contains many different radionuclides and because calculations are computationally demanding, a "short-list" of radionuclides, judged to contribute most to overall risk, were selected for the transport calculations. In the radionuclide transport calculations, source terms corresponding to containment failures at different canister positions simulated using the COMP23 code (Vahlund and Hermansson 2006) were combined with a simplified retardation model for geosphere transport. The retardation model was based on linear sorption (conditionally constant K_d values) and matrix diffusion in a rock matrix of limited extent where radionuclide migration was assumed to occur in flow-bearing fractures intersecting the tunnels and deposition holes comprising the repository. These previous calculations have been updated as part of the PSAR Safety Assessment for the KBS-3 repository (SKB 2022b).

The radionuclide screening calculations allowed the initial set of radionuclides specified with inventories in the spent fuel report (SKB 2010a) to be reduced from 56 (excluding short-lived decay chain members), to a more manageable set of 37 for quantitative calculations using FARF31 (Norman and Kjellbert 1991) in deterministic calculations and MARFA (Painter and Mancillas 2013) for probabilistic scenarios. The K_d values recommended for use in transport calculations were given in Crawford (2010) for geosphere sorption.

Unlike the ranking procedure that was used to short-list the most important radionuclides, the selection and recommendation of K_d data for the calculations did not take into consideration which elements and redox states were most important for the outcome of the safety assessment calculations. In general, the K_d data report (Crawford 2010) treated all elements and redox states as equally important from a data standpoint even though only a very small subset was actually supported by measurements on representative site-specific materials and groundwater compositions. Recommendations were given for 41 different elements and redox states (Table 1-1), although only 8 were based on actual site-specific data (indicated as "SDM Data") with an additional 7 assumed to be approximate geochemical analogues of the site-specific data sets. Of the remaining recommended values, 8 were directly based on literature data values of varying quality, 9 were assigned by assumed geochemical analogy with the literature data values, and a further 9 were assumed to be conservatively non-sorbing.

Table 1-1. Provenance of recommended K_d data given in Crawford (2010) for use in SR-Site radionuclide transport calculations. In the last column, a judgement by the author is given as to the perceived adequacy of the data recommendation for safety assessment application conditions. This judgement should be considered to be only qualitative and should be considered in the context of individual radionuclide contributions to far-field dose rates.

Element (redox State)	Data Attribution in Crawford (2010)	Comment by author
Ac(III)	geochemical analogy with Am(III)/Eu(III)	acceptably accurate for application
Ag(I)	geochemical analogy with Cs(I)	poor geochemical analogy
Am(III)	SDM Data (uncertain pH)	good site-specific data support
C, HCO_3^-	conservative assumption (non-sorbing)	underestimates sorptivity
C, CH_4	conservative assumption (non-sorbing)	acceptably accurate for application
C, $-CO_2H$	conservative assumption (non-sorbing)	may underestimate sorptivity
Cd(II)	geochemical analogy with Ni(II)	acceptably accurate for application
Cl(-I)	conservative assumption (non-sorbing)	acceptably accurate for application
Cm(III)	geochemical analogy with Am(III)/Eu(III)	acceptably accurate for application
Cs(I)	SDM Data	good site-specific data support
Eu(III)	SDM Data (uncertain pH)	good site-specific data support
H(I)	conservative assumption (non-sorbing)	acceptably accurate for application
Ho(III)	geochemical analogy with Am(III)/Eu(III)	acceptably accurate for application
I(-I)	conservative assumption (non-sorbing)	acceptably accurate for application
Mo(VI)	conservative assumption (non-sorbing)	underestimates sorptivity
Nb(V)	literature data	inaccurate literature data estimate
Ni(II)	SDM Data (uncertain pH)	adequate site-specific data support (requires improvement)
Np(IV)	literature data/assumed same as Pu(IV)	likely to be inaccurate
Np(V)	SDM Data (uncertain Eh/pH)	uncertain (requires improvement)
Pa(IV)	assumed same as Pa(V)	inaccurate estimate
Pa(V)	literature data	inaccurate estimate
Pb(II)	literature data (bounding estimate only)	highly inaccurate estimate
Pd(II)	literature data	inaccurate estimate
Pu(III)	geochemical analogy with Am(III)/Eu(III)	acceptably accurate for application
Pu(IV)	literature data	possibly inaccurate estimate (uncertain redox state)
Pu(V)	literature data	possibly inaccurate estimate (uncertain redox state)
Pu(VI)	literature data	possibly inaccurate estimate (uncertain redox state)
Ra(II)	SDM Data	adequate site-specific data support (requires improvement)
S(-II)	conservative assumption (non-sorbing)	underestimates sorptivity
Se(-II)	assumed same as Se(IV)	significantly overestimates sorptivity
Se(IV)	literature data	inaccurate estimate
Se(VI)	assumed same as Se(IV)	overestimates sorptivity
Sm(III)	geochemical analogy with Am(III)/Eu(III)	acceptably accurate for application
Sn(IV)	literature data	possibly inaccurate estimate
Sr(II)	SDM Data	good site-specific data support
Tc(IV)	literature data/assumed same as Pu(IV)	likely to be inaccurate
Tc(VII)	conservative assumption (non-sorbing)	acceptably accurate for application
Th(IV)	literature data/assumed same as Pu(IV)	likely to be inaccurate
U(IV)	literature data/assumed same as Pu(IV)	likely to be inaccurate
U(VI)	SDM Data (uncertain Eh/pH)	uncertain (requires improvement)
Zr(IV)	literature data	possibly inaccurate estimate

Since a large multifactorial experimental campaign to quantify sorption of all relevant elements and redox states is impractical to carry out (i.e., including all feasible combinations of rock type, water type, particle size, contact time, etc), in this report an effort is made to identify which elements might have the greatest impact on the outcome of Safety Assessment calculations if more accurate site-specific sorption data were available. This helps inform resource planning of how much effort should be committed to individual elements versus other aspects of Safety Assessment which may be more important. The identification of important elements is approached by revisiting the central corrosion case from SR-Site/PSAR and performing a screening sensitivity analysis on the radiotoxicity fluxes calculated for individual radionuclides. In this way elements whose contribution to the total transported radiotoxicity is particularly sensitive to K_d can be assessed systematically.

In this report, elements and geochemical analogues identified as important are discussed for possible inclusion in a future laboratory campaign for detailed site descriptive modelling at the Forsmark site. Although some of these were previously investigated in the site investigation, SDM-Site (Byegård et al. 2008, Selnert et al. 2009), issues of representativity and applicability to in situ conditions suggest that additional measurements may need to be made in some cases. The list of prioritised elements must also be considered in the context of which are feasible to study in a laboratory setting and whether there are suitable geochemical analogues for elements and redox states that are more difficult to work with. We also briefly consider which elements are most likely to provide useful information for calibration of linear free energy relations used in extrapolation of sorption data to different groundwater composition and to predict data for elements not directly studied in laboratory experiments.

As can be readily appreciated from Table 1-1, there was considerable data uncertainty for many of the radionuclides included in the geosphere transport calculations. Some of the underlying assumptions of geochemical analogies might also be considered questionable as was already discussed in Crawford (2010). Furthermore, as has been noted in Randall (2012) and Bertetti (2014), the assumptions used in the derivation of recommended K_d values from site specific measurement data might have resulted in overly cautious values which underestimate sorption in the rock matrix.

2 Overview of geosphere transport calculations

To prioritise the relative importance of radionuclides in transport calculations, it is necessary to have well-defined release scenarios since this has an understandably significant influence on the outcome. By release scenario, here we mean both the near-field source term and accompanying flux boundary condition as well as the hydrodynamic characteristics of migration paths in the geosphere leading from the repository to the surface. Although it is possible to conceptualise many hypothetical scenarios for radionuclide release and transport to the biosphere, there are enough commonalities between the different scenarios considered for the KBS-3 repository in the transport modelling report (SKB 2010b) that we regard it sufficient to focus on a small number of representative cases.

In this report, the "central corrosion variant" of the "canister failure due to corrosion scenario" in SR-Site (SKB 2010b) and PSAR (SKB 2022b) is used as a prototype example for our analysis. Here, this variant is referred to simply as the central corrosion case. This case is a relatively pessimistic scenario since it assumes that the engineered barrier of the bentonite buffer surrounding the canister is completely eroded allowing free advective flow within the deposition hole. Furthermore, it is assumed that the copper canister and iron insert are completely corroded and provide no transport resistance to the dissolution and migration of radionuclides from the deposition hole. As noted in Crawford and Löfgren (2019), the central corrosion case gave the highest radiological risk estimates in SR-Site out of the scenarios that were deemed feasible to occur.

The central corrosion case together with the case of canister failure due to shear load were identified as the two most risk significant cases considered in both SR-Site (SKB 2010b) and PSAR (SKB 2022b). The shear load case, however, was deemed a relatively unlikely scenario with an average canister failure rate estimated at 0.078 canisters per million years under pessimistic assumptions (SKB 2011). The main difference between the two cases is the imposition of solubility limits for the near field and no credit is taken for geosphere retardation in the shear load case. In the central corrosion case, solubility limits are only imposed on U and Th. There is an additional variant of the shear load case where erosion of buffer is considered. In this case, the flow rate at the canister is assumed sufficiently high that solubility limits can be neglected. Since neither variant of the shear load case considers geosphere retardation, they are not considered relevant for the present analysis.

It can be noted that many of the variant cases and "residual" scenarios studied in SR-Site differ mostly in terms of the time of canister failure and the overall resistance to mass transfer from canister positions to transport paths in the surrounding rock. This variability mostly affects the peak height and duration of the instant and corrosion release fractions and to a lesser extent the maximum fluxes associated with dissolution release. To address this variability in the present work we consider multiple failure times of 1 ky, 10 ky, and 100 ky. Although the early canister failure times might be considered unrealistic in the context of SR-Site for the central corrosion case, the aim is to attempt to cover a broad range of possibilities that might affect the outcome.

To further simplify the analysis, we consider only the Q1 path where radionuclides migrate directly into a transmissive fracture intersecting a hypothetical canister position. The relation between the Q1 (intersecting fracture), Q2 (transport via the excavation damaged zone) and Q3 (transport via the deposition tunnel) transport routes is shown schematically in Figure 2-1. For the central corrosion case studied in this work, the Q1 transport path is considered dominant and neglecting the subsidiary transport paths should not change the analysis in any substantive way.

For our present purposes, we are interested in identifying which radionuclides impart greatest sensitivity to the summed far-field radiotoxicity flux because of altered geosphere retardation. The set of radionuclides that fulfils this criterion is not necessarily the same as the set of most important dose-determining radionuclides since some radionuclides experience greater retardation related attenuation than others. While it is relatively clear, for example, that I-129 is one of the most important dose-determining radionuclides, altered retardation in the geosphere is expected to have only a negligible impact on far field dose rates since its half-life is at least 5–6 orders of magnitude greater than its retarded travel time largely irrespective of K_d value used in transport modelling.

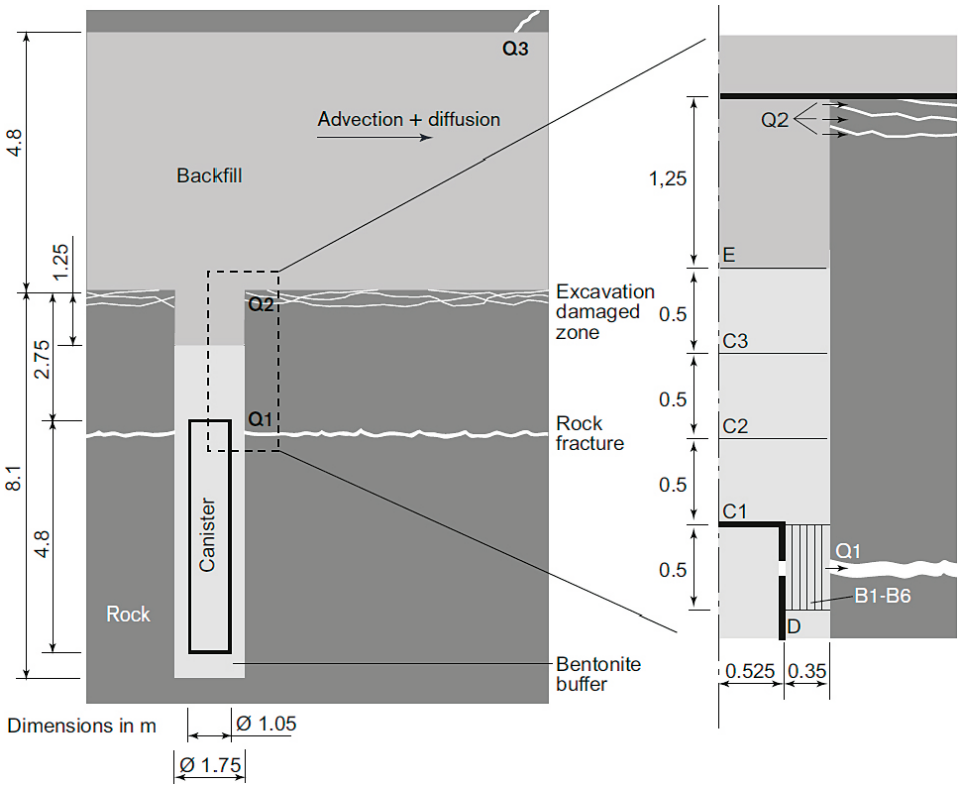

Figure 2-1. *Schematic picture of the compartments (including modelled sub-compartments) for the case with growing pinhole failure taken from the SR-Site Transport Modelling Report (SKB 2010b). The transport paths Q1, Q2 and Q3 to a fracture intersecting the deposition hole, to the excavation damaged zone, and to a fracture intersecting the deposition tunnel, respectively, are also shown.*

In this report, the FARF31 transport code (Norman and Kjellbert 1990, Lindgren et al. 2002, Elert et al. 2004) is used for the simulation of radionuclide transport and estimation of far-field release. The calculation chain for the calculations used previously in SR-Site (SKB 2010b) is summarised in Figure 2-2. Information concerning the global hydrodynamic properties of transport pathways is based on hydrogeological simulations with ConnectFlow (Joyce et al. 2010). This information is passed to the COMP23 program by way of a summary output (.ptb) file. The information consists of the so-called flow "triplets" consisting of the F-factor, advective travel time, and equivalent flow rate, Q_{eq} at each canister position. The near-field boundary condition is calculated by the COMP23 program based on the hydrodynamic data input as well as independently calculated radionuclide inventory and near-field transport parameters (for details, see SKB 2010b). Output from COMP23 is stored in several intermediate output files in the Matlab (.mat) proprietary format. Since the output from COMP23 cannot be directly used by the FARF31 program, a wrapper code is necessary to generate input files for the far-field transport calculations. For the calculations in this report, we have achieved this coupling using a script-based interface coded in Matlab. This is described in more detail in Section 3.

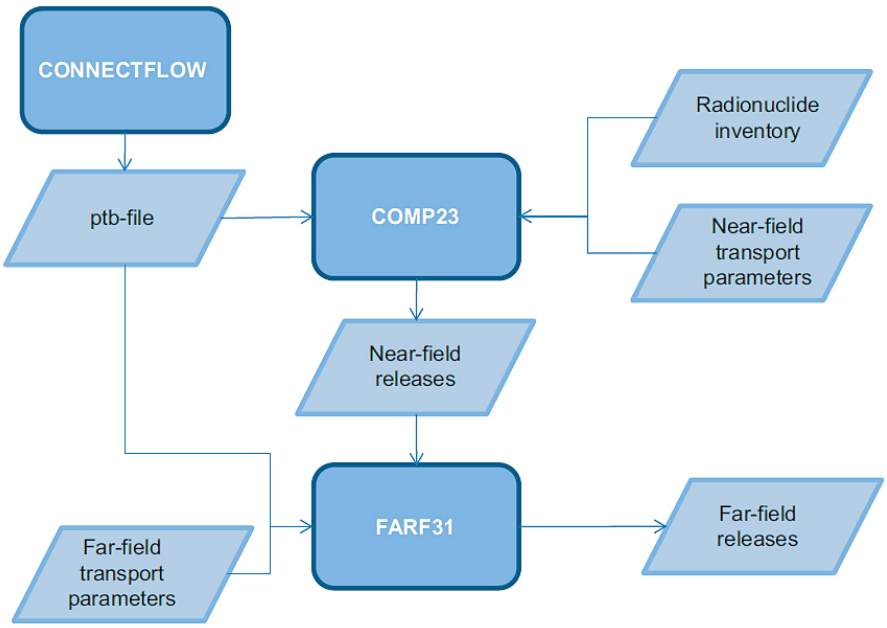

Figure 2-2. *Overview of model linkages and data flows for radionuclide transport simulations using FARF31 (taken from SKB 2010b).*

In SR-Site, landscape dose factors (LDF) were also calculated for the conversion of far-field activity fluxes (Bq/y) to equivalent Dose values (Sv/y) for the most exposed individual using a detailed compartment model of the biosphere (Avila et al. 2010). The landscape dose factors vary significantly over time depending on the dominant climate regime, presence of lakes and submerged zones, and anthropogenic land use in the immediate vicinity of the radionuclide release footprint. In both SR-Site and PSAR, however, the compartment model used for biosphere dose calculations is decoupled from the geosphere transport calculations and it is not possible to a priori assign accurate LDF values on account of the stochastic nature of canister failure time which is coupled to individual realisations of the geosphere hydrogeological model. To simplify dose calculations in both SR-Site and PSAR, LDF values corresponding to the worst-case scenario of land use and climate were assumed for the entire safety assessment period of 1 My thereby adding another layer of conservatism to the calculations.

In SR-Site, the first canister was predicted to fail at 114 ky after repository closure in a deposition location associated with a relatively low repository to surface advective travel time of 6.4 y and a low-range hydrodynamic transport resistance (F-Factor) of roughly 5.4×10^4 y/m. The matrix diffusion and sorptive retardation effect associated with such a flowpath is relatively weak, although not completely absent for many of the dose determining radionuclides in the Safety Assessment. The boundary condition for transport calculations is strongly influenced by the canister failure time, however, and the inventory of radionuclides remaining 114 ky after deposition is very different to that at earlier times when greater quantities of faster decaying radionuclides may be still present in the waste. As mentioned previously, we attempt to bound some uncertainty relating to canister failure time by considering three case studies with different failure times (1 ky, 10 ky, and 100 ky) in the present study. Although very early failure times of 1 ky and 10 ky are considered highly unlikely (see Section 10.4.9 in the main report of SR-Site; SKB 2011), the calculations are used to provide indications of which radionuclides dominate in the different release scenarios and whether there are significant differences. In the remainder of this report the scenario with canister failure time at 100 ky is referred to as the “reference scenario” for canister failure.

2.1 Input data for calculations

In this chapter a brief overview of the input data for the calculations is given to facilitate transparency and reproducibility. Parts of this text are reproduced from Crawford and Löfgren (2019) where the same data have been used.

2.1.1 Reference case radionuclides

The list of radionuclides modelled in SR-Site and PSAR is simplified relative to the initial inventory to avoid simulating radionuclides with very short half-lives and converging decay chains. The details of these simplifications are given in SKB (2010b) and Crawford and Löfgren (2019). The radionuclides modelled, half-lives, and decay chain simplifications are given in Table 2-1. Neither Mo-93 nor Nb-93m was included in the central corrosion case for SR-Site nor PSAR owing to their short half-lives and relatively low inventory at deposition (radiotoxicity basis), although they were retained for residual "what if" case studies for early canister failure. Since we explicitly consider the possibility of early canister failure in the calculations in this report they have been included here for screening purposes through the entire calculation chain.

Nb-93m is interesting in that it is a progeny radionuclide of both Mo-93 and Zr-93 and is thus an example of a converging decay chain in the present context. The decay chain involving Mo-93, Zr-93, and Nb-93m is the only non-actinide chain that is modelled explicitly in this work. Although the far-field modelling code FARF31 cannot simulate converging decay chains, with appropriate scripting of input/output then such processes can be modelled without restriction. Since Mo-93 and Nb-93m were not modelled as part of the near-field boundary condition, only the instant release fraction is considered in this work, although ingrowth from decay of Zr-93 along migration paths is calculated. More details on the handling of this special decay chain is given in Section 2.1.5.

There are some other minor differences relative to the previous work relating to half-lives used in the calculations. The present set of half-lives approved for use in PSAR (except for Rn-222 and Se-79) is taken from the SCALE program v6.1 (Rearden and Jessee 2016) and values are rounded to three significant figures. The updated half-lives for Rn-222 and Se-79 are the same as used in PSAR and are taken from Singh et al. (2011) and Singh (2016), respectively. The reason for using this particular data set is so that the same numerical values are used across the different tools used for calculation of the source term inventory (SCALE), near-field flux boundary condition (COMP23), and far-field radionuclide migration calculations (FARF31).

Table 2-1. Decay chain simplifications, half-lives, and inventory assumptions (SKB 2022b) for radionuclides considered as a calculation basis in this report. The column labelled "Inventory assumptions" indicates which radionuclides were added together (molar basis) to obtain the inventory for the source term to avoid calculating converging decay chain branches. Zr-93, Mo-93, and Nb-93m form a short decay chain sequence (sc) as indicated in the second column.

Radionuclide	Decay chain	Half-life (y)	Descendant	Inventory assumptions (inventories summed on a molar basis)
Pu-240	4*n*	6 560	U-236	Pu-240, Cm-244
U-236	4*n*	2.34×10^{7}	Th-232	U-236
Th-232	4*n*	1.41×10^{10}	-	Th-232
Cm-245	4*n* + 1	8 520	Am-241	Cm-245
Am-241	4*n* + 1	433	Np-237	Am-241
Np-237	4*n* + 1	2.15×10^{6}	U-233	Np-237, U-237
U-233	4*n* + 1	1.59×10^{5}	Th-229	U-233, Pa-233
Th-229	4*n* + 1	7 350	-	Th-229
Cm-246	4*n* + 2	4 770	Pu-242	Cm-246
Pu-242	4*n* + 2	3.74×10^{5}	U-238	Pu-242
U-238	4*n* + 2	4.47×10^{9}	U-234	U-238
U-234	4*n* + 2	2.46×10^{5}	Th-230	U-234, Am-242m, Pu-238, Am-242, Cm-242, Np-238, Th-234, Pa-234m
Th-230	4*n* + 2	7.55×10^{4}	Ra-226	Th-230
Ra-226	4*n* + 2	1 600	Rn-222	Ra-226
Rn-222	4*n* + 2	0.0105	Pb-210	neglected (flowpath ingrowth only)
Pb-210	4*n* + 2	22.2	-	Pb-210

Radionuclide	Decay chain	Half-life (y)	Descendant	Inventory assumptions (inventories summed on a molar basis)
Am-243	4*n* + 3	7370	Pu-239	Am-243
Pu-239	4*n* + 3	2.41×10^4	U-235	Pu-239, Cm-243, Np-239
U-235	4*n* + 3	7.04×10^8	Pa-231	U-235
Pa-231	4*n* + 3	3.28×10^4	Ac-227	Pa-231
Ac-227	4*n* + 3	21.8	-	Ac-227
Ag-108m	-	439	-	Ag-108m
C-14	-	5710	-	C-14
Cd-113m	-	14.1	-	Cd-113m
Cl-36	-	3.01×10^5	-	Cl-36
Cs-135	-	2.3×10^6	-	Cs-135
Cs-137	-	30.1	-	Cs-137
Eu-152	-	13.6	-	Eu-152
H-3	-	12.3	-	H-3
Ho-166m	-	1200	-	Ho-166m
I-129	-	1.57×10^7	-	I-129
Nb-94	-	2.03×10^4	-	Nb-94
Ni-59	-	7.6×10^4	-	Ni-59
Ni-63	-	101	-	Ni-63
Pd-107	-	6.5×10^6	-	Pd-107
Se-79	-	3.27×10^5	-	Se-79
Sm-151	-	90.1	-	Sm-151
Sn-121m	-	43.9	-	Sn-121
Sn-126	-	2.6×10^5	-	Sn-126
Sr-90	-	28.8	-	Sr-90
Tc-99	-	2.11×10^5	-	Tc-99
Zr-93	sc	1.53×10^6	Nb-93m	Zr-93
Mo-93	sc	4000	Nb-93m	only instant release fraction modelled
Nb-93m	sc	16.2	-	neglected (flowpath ingrowth only)

2.1.2 Elemental solubilities in the near field and instant release fractions

In the calculations of near field boundary conditions made using COMP23, solubility limited release of radionuclides is generally considered for cases where transport from a canister is sufficiently slow that solubility limits can be potentially exceeded when calculating corrosion and dissolution release. In SR-Site and PSAR, solubility limitations were considered mostly relevant for the cases where there was no significant buffer erosion (SKB 2010b, 2022b) and radionuclide transport from a canister deposition hole would then be largely diffusion dominated. For the central corrosion case and its variants, solubility limitations were neglected except for U and Th. In the case of U, the solubility limitation was imposed due to the large mole fraction of U-238 in the spent fuel which might be expected to exceed solubility limits relatively easily if allowed to dissolve irreversibly. This is deemed to be the case even at the relatively high deposition hole flowrates associated with the central corrosion case.

In SR-Site it was demonstrated that neglecting solubility limitations of other radioelements would tend to overpredict radiological consequences and therefore could be defended as being a conservative assumption given uncertainties associated with the simplified solubility calculations. In the case of Th, on the other hand, assuming a vanishingly low solubility (10^{-27} mol/L) of Th would maximise the in situ production of Ra-226 in the canister which was also a conservative assumption given the clear importance of Ra-226 as a dose dominant nuclide at long times. The solubility limitations assumed in the central corrosion case and the more general solubility limitations for other cases are summarised in Table 2-2.

Table 2-2. Solubility assumptions for the central corrosion case as well as median solubilities for the generalised case based on the data delivery supplied by SKB for this work, (SKB 2022b[1]). The value of 1.0×10^{17} mol/L is arbitrary although implies effectively infinite solubility in numerical calculations.

Radioelement	solubility, (mol/L) central corrosion case*	solubility, (mol/L) generalised case
Ac	1.0×10^{17}	1.0×10^{17}
Ag	1.0×10^{17}	2.44×10^{-6}
Am	1.0×10^{17}	1.21×10^{-6}
C	1.0×10^{17}	1.0×10^{17}
Cd	1.0×10^{17}	1.0×10^{17}
Cl	1.0×10^{17}	1.0×10^{17}
Cm	1.0×10^{17}	1.32×10^{-6}
Cs	1.0×10^{17}	1.0×10^{17}
Eu	1.0×10^{17}	1.0×10^{17}
H	1.0×10^{17}	1.0×10^{17}
Ho	1.0×10^{17}	2.25×10^{-6}
I	1.0×10^{17}	1.0×10^{17}
Nb	1.0×10^{17}	5.69×10^{-5}
Ni	1.0×10^{17}	1.82×10^{-4}
Np	1.0×10^{17}	1.29×10^{-9}
Pa	1.0×10^{17}	3.22×10^{-7}
Pb	1.0×10^{17}	7.64×10^{-7}
Pd	1.0×10^{17}	3.95×10^{-6}
Pu	1.0×10^{17}	1.35×10^{-6}
Ra	1.0×10^{17}	2.54×10^{-6}
Rn	1.0×10^{17}	1.0×10^{17}
Se	1.0×10^{17}	6.19×10^{-9}
Sm	1.0×10^{17}	6.31×10^{-8}
Sn	1.0×10^{17}	1.01×10^{-7}
Sr	1.0×10^{17}	1.19×10^{-3}
Tc	1.0×10^{17}	4.43×10^{-9}
Th	1.0×10^{-30}	5.70×10^{-9}
U	9.86×10^{-10}	3.87×10^{-10}
Zr	1.0×10^{17}	1.80×10^{-8}
Mo	1.0×10^{17}	1.0×10^{17}

*) These values are for the probabilistic cases only. For the deterministic calculations median values of the probabilistic data is used, see Table 21-21, Appendix L, in SKB (2022b).

In the present work, the same solubility limitations have been applied to the instant release fraction as assumed in the COMP23 near-field boundary condition which was supplied by SKB[1] (SKB 2022b). The solubility limitations in the transport calculations considered in the far-field transport calculations therefore correspond to the first numerical column of Table 2-2. This was done so that the combined source term would be internally consistent. As can be readily appreciated from Table 2-2, only Th and U have assigned solubility limits that are not effectively infinite. In scoping calculations, however, the impact of including solubility limitations has been considered for some fission and activation products. These additional scoping calculations are documented in Appendix A for Se-79, Tc-99, and Zr-93. Essentially, the assumption of a solubility limitation truncates the upper concentration limit for the pulse associated with the instant release fraction (Se-79) and corrosion release fraction (Tc-99 and Zr-93) and allows the release associated with these fractions to persist for a longer time until the inventory of precipitated radionuclide is depleted by flow and transport through the deposition hole. The absence of solubility limitation might be considered a conservative assumption owing to a higher peak transported activity for these radionuclides during the pulse release. This, however, should also be weighed against the use of a pulse LDF rather than an LDF for more uniformly delayed release given that the latter is typically two or more orders of magnitude larger for a given activity flux. This is not expected to significantly alter the relative importance ranking in the present report, although might be of relevance for dose calculations.

[1] Additional information may be found in SKBdoc 1929341 ver 1.0 – Radionuclide transport calculations for the PSAR.

The instant and corrosion release fractions as well as total molar inventories of those radionuclides (including dissolution release fraction) are listed in Table 2-3. These data are used to calculate the near-field boundary condition for instant release using the analytical model described in Appendix A and are part of the data supplied by SKB for this work[2] (SKB 2022b).

Table 2-3. Instant (IRF), and corrosion (CRF) release fractions as well as initial inventory (mol/canister) at time of deposition, t_0 (2045 CE (Common Era)) for specific radionuclides based on the data delivery supplied by SKB for this work[2] (SKB 2022b).

Radioelement	Instant release fraction	Corrosion release fraction	inventory at t_0 (2045 CE), mol/canister
Ag-108m	3.0×10^{-4}	0.9997	1.6×10^{-1}
C-14	9.2×10^{-2}	0.49	4.99×10^{-2}
Cd-113m	1.0	0.0	3.40×10^{-4}
Cl-36	8.79×10^{-2}	0.02	8.64×10^{-3}
Cs-135	2.93×10^{-2}	0.0	6.45
Cs-137	2.93×10^{-2}	0.0	10.1
H-3	1.0	0.0	7.25×10^{-3}
I-129	2.93×10^{-2}	0.0	3.08
Mo-93	4.8×10^{-3}	0.97	8.81×10^{-4}
Nb-93m	4.66×10^{-4}	0.99953	7.75×10^{-2}
Nb-94	5.44×10^{-4}	0.99946	3.25×10^{-1}
Ni-59	5.4×10^{-3}	0.99	2.25
Ni-63	5.6×10^{-3}	0.99	3.18×10^{-1}
Pd-107	2.0×10^{-3}	0.0	5.74
Se-79	4.39×10^{-3}	3.9×10^{-4}	1.67×10^{-1}
Sn-121m	4.8×10^{-4}	2.9×10^{-2}	2.77×10^{-3}
Sn-126	3.0×10^{-4}	0.0	8.97×10^{-1}
Sr-90	2.5×10^{-3}	0.0	6.21
Tc-99	2.0×10^{-3}	3.6×10^{-4}	19.9
Zr-93	1.7×10^{-5}	0.11	21.3
U-233	0.0	0.44	1.17×10^{-4}

2.1.3 Dose Conversion Factors

In SR-Site and PSAR, the approach was to calculate far-field activity fluxes in the transport modelling and then apply dose conversions factors separately to convert activity flux (Bq/y) to radiotoxicity flux (Sv/y). For this purpose, Landscape Dose Factors (LDF's) were calculated using a compartmentalised model of the biosphere where different biosphere objects and coupling paths are represented explicitly. A detailed overview of this modelling work can be found in the SR-Site report by (Avila et al. 2010) which was the basis for the values used in SR-Site. Although landscape dose factors for each radionuclide typically vary over time during different climate domains, it is difficult to apply dynamic values transparently in transport calculations where canister failure times and the time varying far-field radionuclide fluxes are calculated using modelling tools in an independent calculation chain.

To simplify this process in SR-Site and PSAR, conservative average values are taken from the compartmentalised biosphere model that are then assumed for the entire safety assessment period without explicitly accounting for uncertain timing and duration of different climate domains as well as unpredictable periods of anthropogenic land use at the surface. For SR-Site, LDF's were calculated for several different climate domains corresponding to temperate, periglacial, glacial, and global warming conditions (SKB 2010c). Typically, the LDF's used in the safety assessment calculations correspond to interglacial temperate climate conditions where human settlement is presumed to exist at the surface and local farming, fishing, and drinking water extraction is assumed. This overpredicts dose conversion factors for periods during which human settlement at the surface is significantly curtailed or not possible, although is justified in the context of the regulatory aspect of performance assessment.

[2] Additional information may be found in SKBdoc 1929341 ver 1.0 – Radionuclide transport calculations for the PSAR.

More discussion concerning this can be found in the transport modelling report for SR-Site (SKB 2010b). For this report, however, we are only interested in identifying which radionuclides have the greatest impact on the summed radiotoxicity flux for a given change in sorptive retardation and the simplifications related to the assumption of a constant LDF are of lesser importance to the outcome of the work.

A key difference between the present work and simulations carried out in SR-Site and PSAR is that we have elected to model a larger set of radionuclides with instant release fraction than were considered in the previous work. This has been done with the aim of including them in the screening analysis where earlier canister failure times could potentially lead to non-negligible far-field radiotoxicity fluxes. While so-called "basic" landscape dose factors were calculated for most radionuclides that were modelled in the corrosion and dissolution release fractions in SR-Site, not all radionuclides had "pulse" dose factors calculated for fast, time-limited release. The reason why this is problematic is because LDF's calculated for sustained lifetime (~70 y) intake of a low level of radionuclides are typically 2–4 orders of magnitude higher than for pulse intake sustained over very short time periods on the order of 1 y.

Some of the radionuclides not modelled in SR-Site as part of the corrosion and dissolution release fraction (i.e., Cd-113m, Eu-152, H-3, Sn-121m, and Mo-93) were given basic LDF values in PSAR that were numerically identical to that calculated for Se-79. Since Se-79 has the highest LDF value, this can be justified by appealing to arguments of conservatism, at least for the purposes of screening calculations involving these very short-lived radionuclides. This was found to be problematic in the present work for Nb-93m which was not explicitly modelled as part of a decay chain in SR-Site or PSAR. Since a non-negligible production of Nb-93m occurs via ingrowth from decay of corrosion released Zr-93, this was found to give unrealistic far-field radiotoxicity fluxes for this nuclide which elevates its status from minor importance to being the dose dominant nuclide in all modelled scenarios.

Selenium, however, being an important micronutrient and subject to bioconcentration effects in trophic webs is an unusual element. Assuming the same LDF for Nb-93m as for Se-79 is questionable as it is likely to significantly overestimate the importance of Nb-93m. Instead, in the present work the basic LDF for Nb-93m was assumed to be in parity with Ni-59. This is also likely to overestimate the importance of Nb-93m given that the LDF for Ni-59 is ingestion dominated while Nb-93m should be dominated by external exposure. It is assumed here, however, as a conservative ceiling for the dose calculation. It is noted that a maximum LDF of 10^{-15} (Sv y^{-1}/Bq y^{-1}) is given in SR-PSU (SKB 2014) for Nb-93m is roughly two orders of magnitude less than that assumed in the present work. This discrepancy has negligible impact on the relative ranking of important sorbing elements in the present work though, owing to the relatively greater importance of Nb-94.

For the expanded set of radionuclides considered in the present work not including Nb-93m, the use of basic LDF values commensurate with Se-79 is not an issue owing to their short half-lives and relatively low release rate which makes them trivial contributors to total radiotoxicity flux. For the instant release fraction, however, it is not possible to directly exclude them in scenarios of early canister failure. An alternative means of estimating pulse LDF values was therefore required for the screening calculations.

To include the additional 13 instant release radionuclides (see Table 2-4) in the present screening calculations, three simplified, although complementary approaches were taken. The first approach was to establish correlations between basic and pulse LDF's for related sets of radionuclides that were included in SR-Site and use this to make a "guesstimate" of what a reasonable value should be for radionuclides that were not previously considered as part of the instant release fraction. The correlation between pulse and basic LDF's for fission and activation products is shown in Figure 2-3. This is obviously inaccurate since it combines radionuclides that are dependent on different, or at least mixed radiotoxicity exposure mechanisms and may be associated with uncertainties of two or more orders of magnitude. The approach was deemed sufficient for present purposes, however, since the dose dominant radionuclides were already reasonably well quantified, and extrapolated values mostly concern radionuclides with relatively low instant release fractions.

The second approach was to dispense with landscape dose factors and instead use raw dose conversion factors for ingestion (DCF-I) for both instant release as well as for the corrosion and dissolution release fraction. Ingestion dose factors were taken from the ICRP compendium of dose coefficients (ICRP 2012). The reason for assuming the same DCF-I values for both instant- and corrosion/dissolution-

release fractions was to remove bias that would arise from using dose conversion factors calculated with very different underlying assumptions. Although ingestion dose factors are used as input to the compartmentalised modelling used to calculate LDF's they are weighted by mode of ingestion whereby different intake routes are associated with different fluxes that reflect transfer processes in the biosphere. The use of dose conversion factors for ingestion is equivalent to the situation where all radionuclides appearing at the end of a migration path are directly consumed by the most exposed individual without dilution. It is more conservative than the case of direct exposure via well water consumption which is additionally weighted by the amount of water an individual will consume in a year and the volumetric flow of the well.

The third approach was to simply assume the same LDF values for the instant release fraction as that which was used for corrosion/dissolution release fraction. Although calculations were made based on this assumption, this is not as transparent as using raw DCF-I values since basic LDF's still need to be estimated for Mo-93 and Nb-93m which were not considered in SR-Site or PSAR.

Since the assumption of a specific set of dose conversion factors has a relatively large impact on the results, we additionally consider a variant case based on LDF values reported in SKB (2014) and used for transport calculations in the SR-PSU safety assessment (SKB 2015). In the SR-PSU safety assessment, however, pulse LDF's were not used. For the calculations made in this report using LDF values from SFR, we therefore assume the same LDF's for the instant release fraction as for the corrosion and dissolution release fractions (i.e., the same assumption as for approach 3 discussed previously). In summary, the following case studies are considered:

1) SR-Site/PSAR modelling approach. Use of separate Pulse LDF and Basic LDF values for the instant release (IRF) and corrosion/dissolution release fractions (CDRF), respectively. Pulse LDF values for radionuclides that were not explicitly modelled in SR-Site/PSAR are taken from the correlation in Figure 2-3;
2) Use of raw dose conversion factors for direct ingestion (DCF-I);
3) Use of Basic LDF values taken from SR-Site/PSAR without differentiating between IRF and CDRF fractions (henceforth referred to as the VC-LDF case);
4) Use of LDF values taken from SR-PSU (SKB 2014, Table 10-1, p 161) without differentiating between IRF and CDRF fractions (henceforth referred to as the SFR-LDF case).

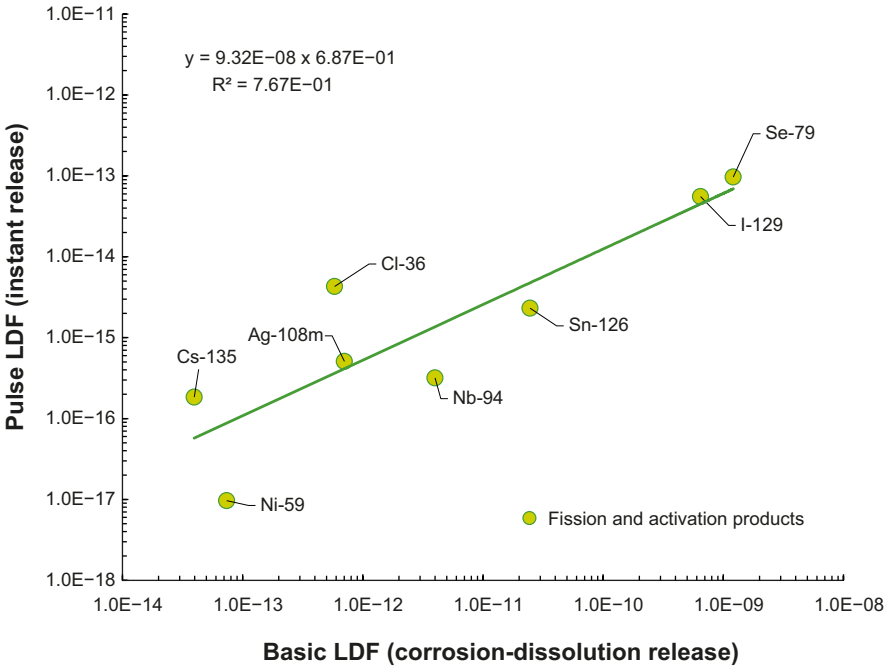

Figure 2-3. *Correlation between Basic LDF's for corrosion and dissolution release used in SR-Site/PSAR and Pulse LDF's for the instant release fraction. The fitted power law expression is used in the present work to provide rough estimates of Pulse LDF's for radionuclides not covered in the previous work.*

Table 2-4. Landscape dose factors (LDF) for radionuclides considered in the SR-Site (SKB 2010b) and PSAR (SKB 2022b) modelling work. Basic (corrosion and dissolution fraction) and pulse (instant release) LDF values are given (n/a = not applicable) as well as dose conversion factors (ICRP 2012) for ingestion (DCF-I) used as an alternative calculation basis in this report. Pulse LDF values are taken from SR-Site/PSAR where available and estimated from the correlation in Figure 2-3 in other cases. LDF-SFR values are also given for the variant case based on SFR-PSU (SKB 2014). Neither Mo-93, nor Nb-93m were explicitly modelled in SR-Site or PSAR although they have been included in this work.

Radionuclide	Basic LDF (Sv/y per Bq/y)	Pulse LDF (Sv/y per Bq/y)	DCF-I (Sv/y per Bq/y)	LDF-SFR (Sv/y per Bq/y)
Pu-240	1.88×10^{-12}	n/a	2.50×10^{-7}	2.40×10^{-12}
U-236	1.85×10^{-12}	n/a	4.70×10^{-8}	5.50×10^{-12}
Th-232	1.72×10^{-12}	n/a	2.30×10^{-7}	2.60×10^{-12}
Cm-245	1.58×10^{-12}	n/a	2.10×10^{-7}	2.20×10^{-12}
Am-241	1.46×10^{-12}	n/a	2.00×10^{-7}	1.70×10^{-12}
Np-237	4.83×10^{-11}	n/a	1.10×10^{-7}	1.30×10^{-12}
U-233	2.50×10^{-12}	n/a	5.10×10^{-8}	5.90×10^{-12}
Th-229	3.61×10^{-12}	n/a	4.90×10^{-7}	5.90×10^{-12}
Cm-246	1.55×10^{-12}	n/a	2.10×10^{-7}	2.00×10^{-12}
Pu-242	1.89×10^{-12}	n/a	2.40×10^{-7}	2.80×10^{-12}
U-238	1.85×10^{-12}	n/a	4.50×10^{-8}	5.40×10^{-12}
U-234	3.62×10^{-12}	n/a	4.90×10^{-8}	5.7×10^{-12}
Th-230	1.31×10^{-11}	n/a	2.10×10^{-7}	2.40×10^{-12}
Ra-226	3.75×10^{-12}	n/a	2.80×10^{-7}	4.30×10^{-12}
Rn-222	5.20×10^{-14}	n/a	5.20×10^{-14}	(4) 5.20×10^{-12}
Pb-210	1.39×10^{-11}	n/a	6.90×10^{-7}	6.10×10^{-12}
Am-243	1.53×10^{-12}	n/a	2.00×10^{-7}	2.00×10^{-12}
Pu-239	1.94×10^{-12}	n/a	2.50×10^{-7}	2.70×10^{-12}
U-235	2.76×10^{-12}	n/a	4.70×10^{-8}	5.70×10^{-12}
Pa-231	8.10×10^{-12}	n/a	7.10×10^{-7}	8.40×10^{-12}
Ac-227	8.00×10^{-12}	n/a	1.10×10^{-6}	1.00×10^{-11}
Ag-108m	7.05×10^{-13}	(3) 5.08×10^{-16}	2.30×10^{-9}	5.40×10^{-14}
C-14	5.44×10^{-12}	1.69×10^{-15}	5.80×10^{-10}	7.90×10^{-15}
Cd-113m	(1) 1.21×10^{-9}	6.92×10^{-14}	2.30×10^{-8}	2.20×10^{-13}
Cl-36	5.84×10^{-13}	(3) 4.29×10^{-15}	9.30×10^{-10}	7.50×10^{-13}
Cs-135	3.96×10^{-14}	(3) 1.84×10^{-16}	2.00×10^{-9}	2.00×10^{-13}
Cs-137	1.20×10^{-13}	1.23×10^{-16}	1.30×10^{-8}	1.30×10^{-13}
Eu-152	(1) 1.21×10^{-9}	6.92×10^{-14}	1.40×10^{-9}	1.20×10^{-14}
H-3	(1) 1.21×10^{-9}	6.92×10^{-14}	4.20×10^{-11}	1.20×10^{-15}
Ho-166m	5.90×10^{-14}	7.53×10^{-17}	2.00×10^{-9}	2.10×10^{-14}
I-129	6.46×10^{-10}	(3) 5.56×10^{-14}	1.10×10^{-7}	8.00×10^{-12}
Nb-94	4.00×10^{-12}	(3) 3.18×10^{-16}	1.70×10^{-9}	3.80×10^{-14}
Ni-59	7.39×10^{-14}	(3) 9.67×10^{-18}	6.30×10^{-11}	2.90×10^{-14}
Ni-63	1.21×10^{-15}	5.20×10^{-18}	1.50×10^{-10}	1.70×10^{-15}
Pd-107	6.73×10^{-15}	1.69×10^{-17}	3.70×10^{-11}	1.90×10^{-14}
Se-79	1.21×10^{-9}	(3) 9.70×10^{-14}	2.90×10^{-9}	3.00×10^{-13}
Sm-151	7.16×10^{-16}	3.63×10^{-18}	9.80×10^{-11}	8.50×10^{-16}
Sn-121m	(1) 1.21×10^{-9}	6.92×10^{-14}	3.80×10^{-10}	(1) 3.00×10^{-13}
Sn-126	2.47×10^{-11}	(3) 2.31×10^{-15}	4.70×10^{-9}	2.00×10^{-13}
Sr-90	2.19×10^{-13}	(3) 1.85×10^{-16}	2.80×10^{-8}	2.80×10^{-13}
Tc-99	8.98×10^{-13}	8.98×10^{-13}	6.40×10^{-10}	1.70×10^{-13}
Zr-93	2.77×10^{-14}	4.48×10^{-17}	1.10×10^{-9}	1.80×10^{-13}
Mo-93	(1) 1.21×10^{-9}	6.92×10^{-14}	3.10×10^{-9}	5.50×10^{-12}
Nb-93m	(2) 7.39×10^{-14}	8.79×10^{-17}	1.20×10^{-10}	1.00×10^{-15}

Notes:

(1) LDF assumed to be same as for Se-79.

(2) LDF for Nb-93m assumed same as for Ni-59.

(3) SR-Site Pulse LDF value.

(4) assumed same as SR-Site Basic LDF value.

In the present work, we have focused mostly on the first (SR-Site LDF's) and second approach (DCF-I) since the third approach significantly overinflates the relative importance of the pulse release fraction and does not add a great deal of additional information. The fourth case study is intended to give additional insight into sensitivity of modelling results to the choice of dose conversion factors, although is also expected to inflate the relative importance of the pulse release fraction. Comparison of results obtained using LDF values taken from SR-Site and SR-PSU, however, is best done for the VC-LDF (case 3) and SFR-LDF (case 4) since they make the same assumption that the instant release fraction is assigned the same LDF as for the corrosion/dissolution release fraction.

A comparison of the Basic LDF values used in SR-Site/PSAR with those used in SR-PSU is shown in Figure 2-4. There are a number of significant differences here that are worth mentioning. Among the more important fission and activation products (cf Figure 3-1), the LDF's for Zr-93 and Cs-135 are roughly a factor of five greater in SR-PSU, while those for I-129 and Nb-94 are reduced by about two orders of magnitude. The LDF for C-14 in SR-PSU also stands out being reduced by a factor of 700 relative to the basic LDF in SR-Site/PSAR while that for Se-79 is decreased by a factor of over 4 000. In general, most of the fission and activation products have reduced LDF's relative to SR-Site/PSAR, while those for actinide chain members are modestly increased. Notable exceptions are Pb-210 whose LDF is reduced by a factor of 2, and Np-237 whose LDF is reduced by a factor of nearly 40. As shown later in Section 5, these changes may have some significance for which elements are identified as being of particular importance in the sensitivity analyses. A detailed comparison of breakthrough curves for the base case K_d parameterisation using the four different approaches for radiotoxicity conversion can be found in Appendix B.

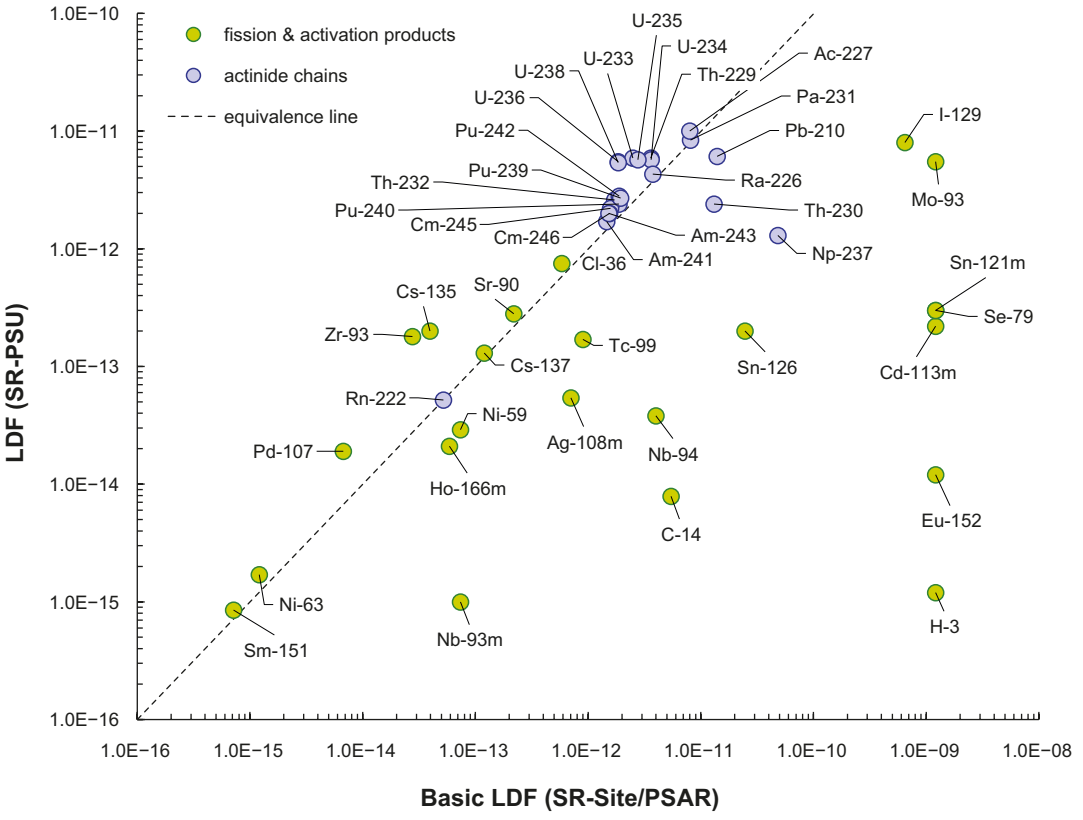

Figure 2-4. *Comparison of Basic LDF's for corrosion and dissolution release used in SR-Site/PSAR and LDF values reported in SKB (2014) for use in transport calculation made within SR-PSU (SKB 2015).*

2.1.4 Base case material properties assumed in SR-Site

In SR-Site, the rock surrounding all flow paths was assumed to be homogenous. The assigned K_d values for sorption were taken directly from Crawford (2010). The effective diffusivity was based on formation factor estimates derived from in situ resistivity measurements performed in the site investigation boreholes KFM01D, KFM06A, and KFM08C. From the deliberations in the SR-Site data report (SKB 2010c), a generic effective diffusivity for cations and non-charged solutes was specified as 6.3×10^{-7} m^2/y while the rock porosity was set to 0.18 % for all species. For anionic solutes, an anion exclusion factor of 0.32 was assumed for effective diffusivity based on comparison of laboratory measurements of iodide and tritium diffusion described in Vilks et al. (2005) giving an effective diffusivity of 2.0×10^{-7} m^2/y. Element specific transport properties of the site-specific rock are compiled in Table 2-5. The maximum penetration depth, although effectively infinite in the calculations, was set to 12.5 m to reflect half the spacing between hydraulically conducting fractures at repository depth and thus to ensure that the retention capacity of the rock would not be double counted.

Table 2-5. Material properties of the undisturbed rock used in the different corrosion scenarios (i.e., canister failure at 100 ky, 10 ky, and 1 ky) based on numerical values from SKB (2010a, Table 3-3). The K_d values given in this table are referred to as the base case parameterisation in this report and are identical with those used in SR-Site and PSAR transport calculations.

Radioelement	Anion exclusion factor, f_{AE}	Effective diffusivity, D_e (m^2/y)	Sorption coefficient, K_d (m^3/kg)
Ac	1	6.3×10^{-7}	1.5×10^{-2}
Ag	1	6.3×10^{-7}	3.5×10^{-4}
Am	1	6.3×10^{-7}	1.5×10^{-2}
C	1	6.3×10^{-7}	0
Cl	0.32	2.0×10^{-7}	0
Cm	1	6.3×10^{-7}	1.5×10^{-2}
Cs	1	6.3×10^{-7}	3.5×10^{-4}
Ho	1	6.3×10^{-7}	1.5×10^{-2}
I	0.32	2.0×10^{-7}	0
Mo	0.32	2.0×10^{-7}	0
Nb	1	6.3×10^{-7}	2.0×10^{-2}
Ni	1	6.3×10^{-7}	1.1×10^{-3}
Np	1	6.3×10^{-7}	5.3×10^{-2}
Pa	1	6.3×10^{-7}	5.9×10^{-2}
Pb	1	6.3×10^{-7}	2.5×10^{-2}
Pd	1	6.3×10^{-7}	5.2×10^{-2}
Po	0.32	2.0×10^{-7}	0
Pu	1	6.3×10^{-7}	1.5×10^{-2}
Ra	1	6.3×10^{-7}	2.4×10^{-4}
Se	0.32	2.0×10^{-7}	3×10^{-4}
Sm	1	6.3×10^{-7}	1.5×10^{-2}
Sn	1	6.3×10^{-7}	1.6×10^{-1}
Sr	1	6.3×10^{-7}	3.4×10^{-6}
Tc	1	6.3×10^{-7}	5.3×10^{-2}
Th	1	6.3×10^{-7}	5.3×10^{-2}
U	1	6.3×10^{-7}	5.3×10^{-2}
Zr	1	6.3×10^{-7}	2.1×10^{-2}

2.1.5 Near-field boundary condition

The calculations made in this report use a modified boundary condition for transport calculations which includes the instant release fraction of quickly leaching radionuclides. The instant release fraction comprises radionuclides segregated to the gap between the fuel and cladding as well as grain boundary porosity of fuel elements. The instant release fraction is also conceptualised to include the inventory of so-called "crud" deposits on the outer surface of the cladding. In SR-Site and PSAR, the different release fractions are treated separately on the basis that the appropriate landscape dose factors for the instant release fraction (IRF) differ numerically from that for the corrosion- and dissolution release fraction (CDRF). In SR-Site and PSAR, the dose is calculated separately assuming that the inventory of instant release radionuclides is mobilised immediately within the first year after canister failure. The results of this separate calculation were presented in the form of an abbreviated table in the SR-Site transport modelling report (SKB 2010b). In the present work, the far-field radiotoxicity flux associated with instant release is calculated independently and added to that of the corrosion and dissolution breakthrough flux in postprocessing using consistent LDF values for each fraction. This is a similar approach to what was done in Crawford and Löfgren (2019) in response to a request by the Swedish Radiation Safety Authority (SSM) for the instant release fraction to be included in a deterministic calculation to illustrate the impact of instant release on the combined dose estimates.

In the previous report, the instant release fraction was modelled by assuming the IRF inventory was released as a square pulse of one-year duration in accordance with the original assumption in SKB (2010b). Since the LDF values for pulse-mobilised radionuclides are typically 100–10 000 times lower than the LDF values defined for the slow-release corrosion and dissolution release fractions (termed "basic" LDF values in SR-Site), a fast pulse release is not necessarily more conservative from a dose perspective than a slower release over a longer time. This, however, also depends on the dilution and attenuation characteristics of the individual radionuclide in the geosphere so this needs to be considered on a case-by-case basis. Owing to the relatively strong transport retardation of Tc-99, for example, the basic LDF was considered appropriate even for the pulse release fraction in SR-Site. Other more weakly-retarded radionuclides were assigned "pulse" LDF values owing to their short residence time in the geosphere.

In the present work, the procedure from the previous work documented in Crawford and Löfgren (2019) is extended to consider a more accurate account of the pulse release by modelling the source term for the instant release fraction as a continuously stirred tank reactor (CSTR) where mixing dilution occurs in the deposition hole with a constant flowrate of water and matrix diffusive retardation on the rock interface to the deposition hole. The flowrate for the calculation is assumed to be the same as that in SR-Site/PSAR for the deposition hole being considered (0.733 m^3/y). The flowrate associated with canister failures varies from 0.024 – 0.733 m^3/y in the different realisations of the semi-correlated hydrogeological model in SR-Site and PSAR, so the value modelled in the present work may be considered to be at the high-end of simulated values. For a minimally sorbing and long-lived radionuclide, the rate of concentration decrease in the canister hole deriving from the instant release fraction is inversely proportional to the water residence time in the canister hole thereby giving an exponential decay of concentration. Depending on the volume of residual buffer and canister corrosion products remaining the deposition hole, the water residence time can be as great as 26 y. In the simplified calculations made for SR-Site, on the other hand, the entire instant release fraction is assumed to be mobilised in the space of a year at constant concentration. This implies a roughly 26 times greater initial concentration of radionuclide that is assumed to cease after exactly 1 y of flushing at constant concentration.

If the pulse release associated with the instant release fraction were to be significantly extended in time, a reasonable argument could be made to use the basic LDF values instead of pulse LDF values on the basis that the release can no longer be considered an instantaneous exposure. In that case, the more gradual release associated with the stirred tank concept could potentially give higher equivalent dose rates even if the activity flux is less simply due to the different LDF factors used in the calculations. While this is something that might be considered in greater detail in future safety assessment studies, the impact of this is judged to be limited in the present context since it mostly affects non-sorbing or very weakly sorbing radionuclides and is not expected to strongly alter the relative ranking of sorbing radionuclides.

The near-field boundary condition for the corrosion and dissolution release fractions was calculated as part of a special data delivery by the PSAR modelling team[3] using the COMP23 code for the three assumed canister failure times (t_{Adv}, time for onset of advective flow) of 1 ky, 10 ky, and 100 ky. Since the purpose of this work is for relative importance screening of sorbing elements, the canister failure times are arbitrary and should only be considered as indicative of potential near field fluxes if failure were to occur at these times, however unlikely such scenarios might be. A purpose written code was created in MATLAB to calculate a separate near-field boundary condition associated with the instant release fraction since the COMP23 calculations only include corrosion and dissolution release fractions. A more detailed account of the calculation of the instant release fraction is given in Appendix A. The near-field boundary condition for the instant release and corrosion/dissolution release fractions are used in separate far-field transport calculations, although are combined in post-processing for presentation purposes. The near field boundary condition including all contributions from pulse-, corrosion-, and dissolution release fractions are plotted in Figure 2-5 to Figure 2-8.

The radionuclides associated with the instant release fraction can mostly be considered separately and decay chains do not need to be explicitly modelled (except for Nb-93m) which simplifies the mathematical description of the problem considerably. For Nb-93m, which is a descendant radionuclide of both Zr-93 and Mo-93, the half-life is sufficiently short relative to its retarded transport time that the chain decay can be neglected for the instant release source term. Most of the far-field flux of this nuclide is formed by ingrowth along geosphere migration paths from decay of Zr-93 (and to a lesser extent Mo-93) so the presence or absence of Nb-93m in the source term has limited impact on far-field calculation results.

The combined near-field boundary condition is plotted in Figure 2-5 for the new CSTR-modelled instant release fraction for an assumed canister failure at 100 ky. The data are calculated as activity fluxes (Bq/y) and then converted to equivalent radiotoxicity fluxes for plotting purposes using the LDF conversion factors ($Sv \times y^{-1}/Bq \times y^{-1}$). The radiotoxicity fluxes are calculated separately for the instant release and corrosion-dissolution release fractions and then summed in the plot to give a complete view of radiotoxicity contributions from each contributing fraction. Radionuclides with a significant instant release fraction start at an initially high flux which decreases over time due to the elution of the initial concentration of dissolved solute in the deposition hole. Radionuclides with an insignificant instant release fraction exhibit an initially increasing flux trend due to the corrosion release fraction dissolving into the initially zero-concentration water in the deposition hole. The concentration in the deposition hole appears to take about 3–5 years for the dissolution and elution fluxes to reach a steady state after which the eluted radionuclide flux is constant in the COMP23 results up until the corrosion release period concludes 1 ky after canister failure.

For comparison, the combined near-field boundary condition is plotted in Figure 2-6 for the square pulse modelled instant release fraction for an assumed canister failure at 100 ky. The main difference is for Tc-99 where the 1 y square pulse instant release exhibits a roughly 25 times greater peak flux than the CSTR-modelled release which remains at a lower, although still high level for a significantly longer period. Similar behaviour can be seen for Cs-135, although the time constant for the instant release is different to Tc-99 owing to slightly lower matrix diffusive retardation at the interface of the deposition hole with the surrounding rock. The differences are less clear for other solutes, although a similar trend can be made out for I-129 with a more modest change in peak concentration. Apparent discontinuities in the trends for Se-79, Sn-126, Cl-36, and Cs-135 in the 1 y square pulse release are simply due to the large difference in the LDF factors for instant release vs. corrosion and dissolution release rather than physical transport mechanisms. Also, Cl-36 also falls out of the top 15 dose contributors to be replaced by Pa-231 when the instant release is modelled as a CSTR.

[3] SKBdoc 1929341 ver 1.0 – Radionuclide transport calculations for the PSAR.

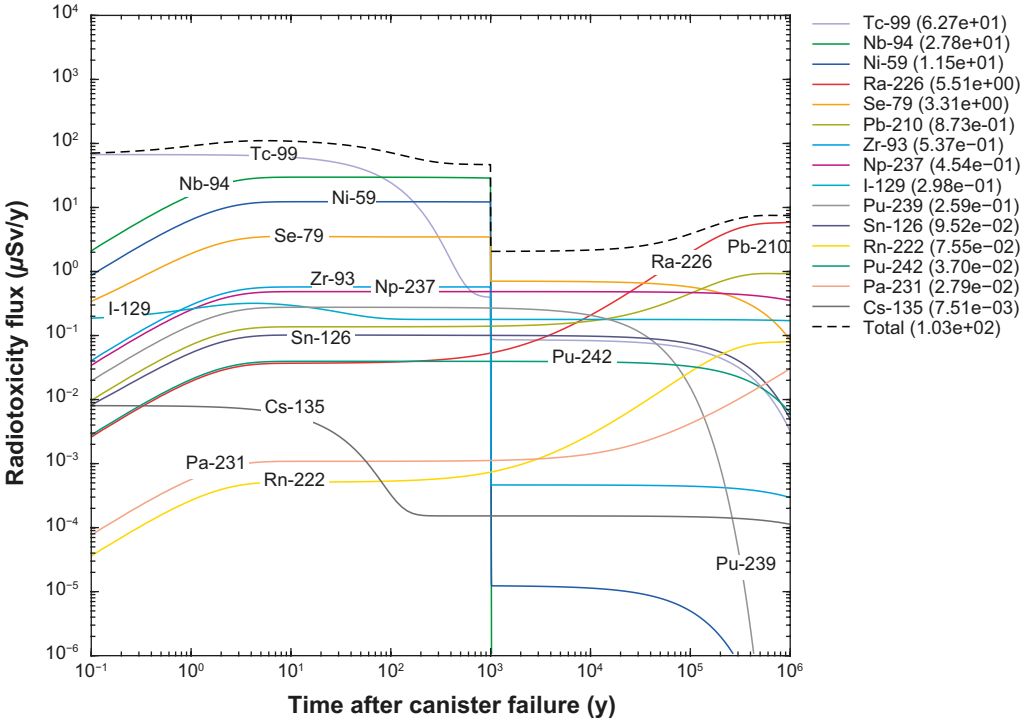

Figure 2-5. *Combined near-field boundary condition for the instant release fraction (IRF) modelled as a CSTR system as well as corrosion and dissolution release fractions (CDRF) calculated by COMP23 for canister failure at 100 ky. Data are presented as equivalent radiotoxicity fluxes (µSv/y) based on the LDF factors defined separately for IRF and CDRF release fractions. The time on the x-axis is in relation to canister failure. Only the top 15 radiotoxicity contributing radionuclides are plotted.*

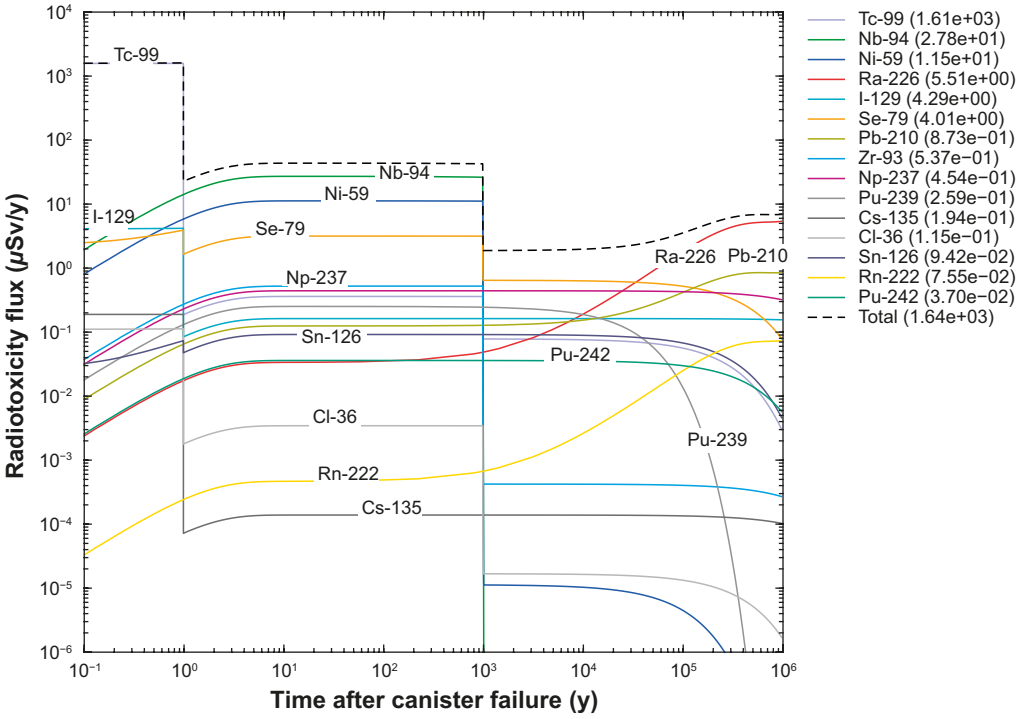

Figure 2-6. *Combined near-field boundary condition for the instant release fraction (IRF) modelled as a square pulse of 1 y duration as well as corrosion and dissolution release fractions (CDRF) calculated by COMP23 for canister failure at 100 ky. Data are presented as equivalent radiotoxicity fluxes (µSv/y) based on the LDF factors defined separately for IRF and CDRF release fractions. The time on the x-axis is in relation to canister failure. Only the top 15 radiotoxicity contributing radionuclides are plotted.*

The near-field boundary condition for very early canister failure with CSTR-modelled instant release is plotted in Figure 2-7 for canister failure at 1 ky and in Figure 2-8 for failure at 10 ky. The corresponding plots for 1 y duration square pulse modelled instant release can be found in Appendix A. The main difference for the early failure cases relative to failure at 100 ky is a much more prominent role for Nb-94 and C-14, which having relatively short half-lives exhibit considerably higher fluxes at short failure times relative to that at 100 ky. Although Nb-94 is still the second ranked radionuclide behind Tc-99 in terms of its peak radiotoxicity flux at 100 ky, C-14 decays sufficiently that it falls to 18th place.

The sensitivity analyses presented in later chapters for transport retardation are dependent on the assumed near-field boundary condition and case studies with earlier canister failure times typically giving different results for the ranking of dose dominant radionuclides. Although the central corrosion case is a deterministic calculation, the first canister failure time (114 ky in SR-Site) is based on stochastic buffer erosion and canister corrosion calculations assuming a range of pessimistic assumptions for hydrogeology and groundwater chemistry. These are more fully detailed in the SR-Site Corrosion Report (SKB 2010d) and in Chapter 10 of the SR-Site Main Report (SKB 2011) and corresponding references for PSAR (SKB 2022a). Although interesting for the purposes of the present report, earlier canister failure times than that predicted for the SR-Site or PSAR central corrosion cases can therefore be considered less likely.

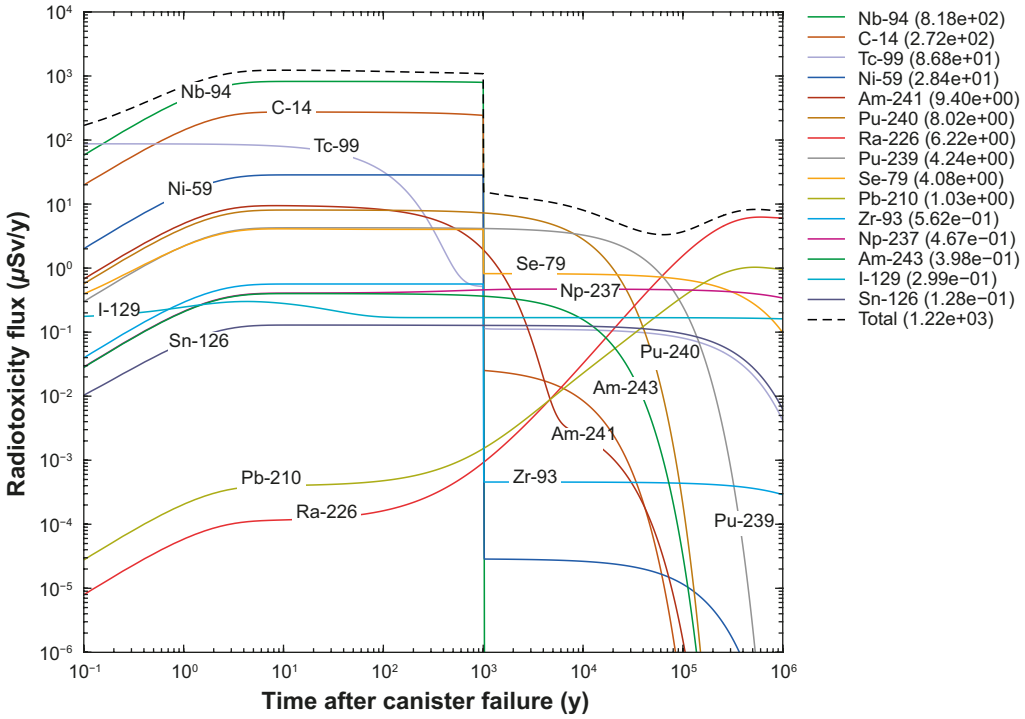

Figure 2-7. *Combined near-field boundary condition for the instant release fraction (IRF) modelled as a CSTR system as well as corrosion and dissolution release fractions (CDRF) calculated by COMP23 for canister failure at 1 ky. Data are presented as equivalent radiotoxicity fluxes (μSv/y) based on the LDF factors defined separately for IRF and CDRF release fractions. The time on the x-axis is in relation to canister failure. Only the top 15 radiotoxicity contributing radionuclides are plotted.*

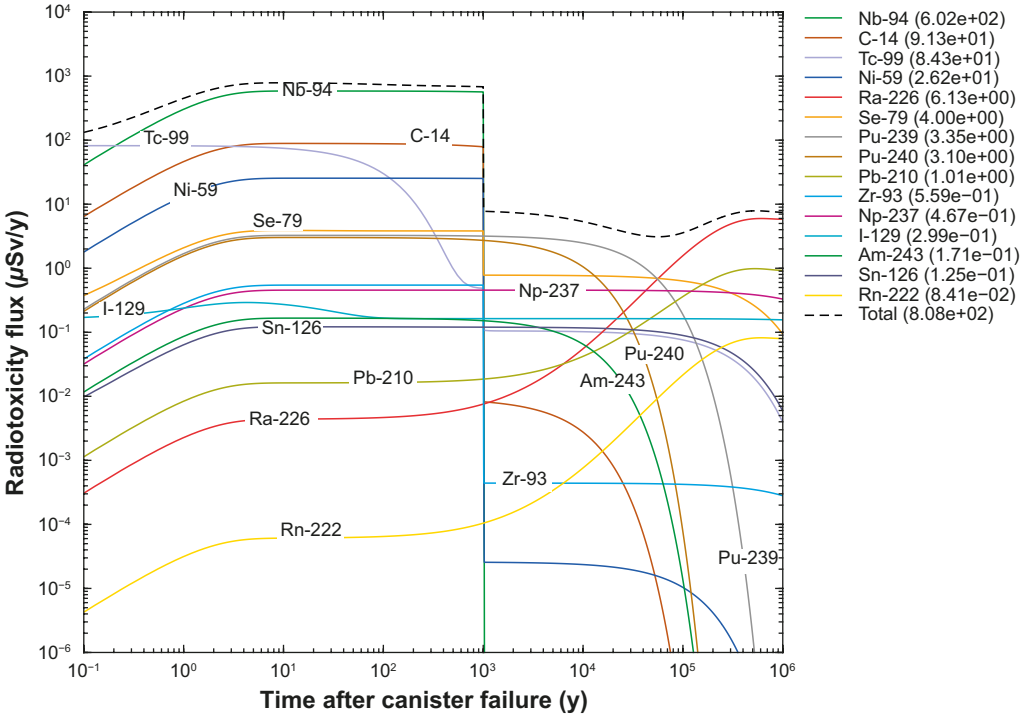

Figure 2-8. *Combined near-field boundary condition for the instant release fraction (IRF) modelled as a CSTR system as well as corrosion and dissolution release fractions (CDRF) calculated by COMP23 for canister failure at 10 ky. Data are presented as equivalent radiotoxicity fluxes (μSv/y) based on the LDF factors defined separately for IRF and CDRF release fractions. The time on the x-axis is in relation to canister failure. Only the top 15 radiotoxicity contributing radionuclides are plotted.*

There are, however, other canister failure modes (shear load, isostatic load, pinhole case, etc) and exposure scenarios (e.g., direct intrusion) that may be relevant for early times after repository failure. Many of these are discussed in the SR-Site Transport Modelling Report (SKB 2010b) and are not explicitly dealt with in the present analysis. It is clear from the reported dose calculations in SKB (2010b), however, that the same radionuclides that are considered dose dominant in the central corrosion case are probably also dose-dominant in the cases considering other failure modes, although not necessarily in the exact same order of importance. Here, we note that an identification of dose dominant radionuclides is not the primary purpose of the present analysis. The purpose of this work is more general and seeks to categorise the ability of individual elements to exert an influence on the total instantaneous radiotoxicity (dose) regardless of whether it is directly associated with the peak dose achieved in the safety assessment, or not. We could frame this alternatively in terms of the question: *is the total radiotoxicity flux at any point of the breakthrough curve altered in any significant fashion by an uncertain K_d for the specified element?*

Calculations incorporating different boundary conditions for alternative deterministic cases were beyond the scope of the current work so have not been considered. Notwithstanding this, additional scoping calculations have been made for hypothetical early canister failure times. These are addressed as hypothetical, “what if” calculations as an addendum to the main sensitivity analysis for the central corrosion case with canister failure at 100 ky.

3 Far-field radiotoxicity fluxes for modelled scenarios under reference conditions

In this section we make far-field transport calculations for the main scenario of canister failure at 100 ky as well as the scenarios deemed less likely with canister failure at 1 ky and 10 ky. In these calculations, we use the base case material properties as recommended for use in SR-Site and PSAR to establish a frame of reference for the sensitivity calculations in Section 4. The SR-Site and PSAR central corrosion case considers a flowpath F-factor of 5.4×10^4 y/m and an advective travel time of 6.4 y. This represents a flowpath featuring relatively poor transport retardation properties which is relevant since such flowpaths are much more likely to dominate far-field radiotoxicity fluxes than flowpaths featuring high F-factors. The Péclet number was set to 10 which corresponds to a typical amount of dispersion customarily assumed in transport calculations and is the same as used in SR-Site and PSAR transport calculations.

In the present work we have used the same FARF31 safety assessment code, as was used for the deterministic calculation cases in the SR-Site transport modelling report (SKB 2010b) and now in PSAR (SKB 2022b). It is a simple model based on a Laplace space solution of the one-dimensional advection-dispersion equation in a hypothetical stream tube with one-dimensional diffusion into a homogeneous secondary porosity in a direction orthogonal to the fluid flow. Chain decay and in-growth are included in the model and it is formulated in terms of the advective travel time in the longitudinal direction as the independent variable. The Laplace space solution for a unit response transfer function is numerically inverted to the time domain and the breakthrough curve for transported radionuclides is then obtained by convolution of the response function with the input source term.

The code is input file based and for this work we used the most recent version of the NuDec-Farf31 interface as described in Crawford and Löfgren (2019). NuDec-Farf31 is a Matlab-based code that calls FARF31 as an external program with automatic input and output management via shell commands in scratch directory. The far-field radiotoxicity flux calculated using FARF31 for the near-field boundary condition for a canister failure time of 100 ky is shown in Figure 3-1. The conversion of activity flux to equivalent radiotoxicity is made assuming basic LDF values for the corrosion and dissolution fractions and pulse LDF values for the instant release calculated in separate simulations and then added in post-processing. The result of this calculation using the SR-Site (and PSAR) recommended K_d values as specified in Table 2-5 is referred to as the base case in following chapters and corresponds to the central corrosion case of SR-Site and PSAR. Apart from a slightly differing canister failure time (i.e., 100 ky instead of 114 ky), the main difference between the present calculations and those made in SR-Site and PSAR is that we consider only the Q1 migration path (cf Figure 2-1) and include the instant release fraction explicitly.

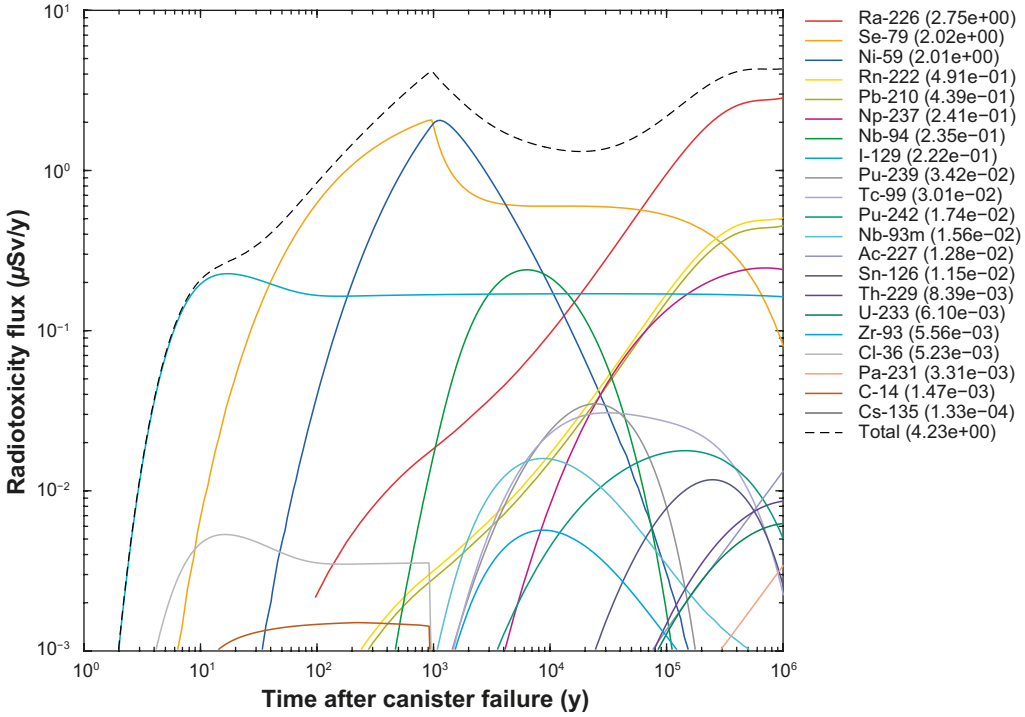

Figure 3-1. *Equivalent far-field radiotoxicity flux (μSv/y) calculated using NuDec-Farf31, for the base case, including both the instant release fraction (IRF) modelled as a CSTR and corrosion/dissolution release fraction (CDRF). The legend is sorted by peak flux within the time frame of the safety assessment. The time on the x-axis is relative to canister failure at 100 ky post-closure. Only radionuclides contributing more than 0.1 % of the total radiotoxicity are plotted.*

The corresponding result obtained using the near-field boundary condition with a 1 y square pulse instant release is shown in Figure 3-2. The only observable difference between the CSTR modelled IRF and the square pulse case is a slightly shallower breakthrough peak for I-129 and Cl-36 when modelled as a CSTR. Interestingly, the opposite behaviour is discernible for Tc-99 and Cs-135, where the peak fluxes are slightly higher although the difference is relatively minor. For Tc-99, this is the result of delayed release of the IRF augmenting the subsequent pulse associated with the corrosion release fraction which dominates the subsequent breakthrough. For Cs-135 (although not visible in the figures due to the scaling of the y-axis), the effect is due to a very slight augmentation of the peak associated with the dissolution release fraction. The differences in peak radiotoxicity breakthrough for the different representations of the near field boundary condition for the IRF, however, are extremely sensitive to the choice of LDF used to model the IRF pulse release. As shown in Appendix B, the LDF variant case assuming uniform LDF values (as might be motivated for the case of an IFR modelled as a CSTR release) gives much higher peak breakthrough radiotoxicity than the peak breakthrough calculated for a square pulse IRF release of 1 y duration.

The result for the case with early canister failure at 1 ky assuming the IRF modelled as a CSTR is shown in Figure 3-3 and shows a much more important role for C-14 and Nb-94 corrosion release than in the base case as might be expected from the higher inventory of these radionuclides being present at early times due to their relatively short half-lives. The breakthrough for the case with canister failure at 10 ky is shown in Figure 3-4 and is similar to that for the case with 1 ky canister failure. The only substantive difference between these two cases is a lower peak flux of C-14 and Nb-94 in the 10 ky failure case relative to the 1 ky failure case. Many of the other radionuclides also have slightly reduced peak fluxes for the early release at 10 ky relative to 1 ky reflecting larger inventories at shorter timescales.

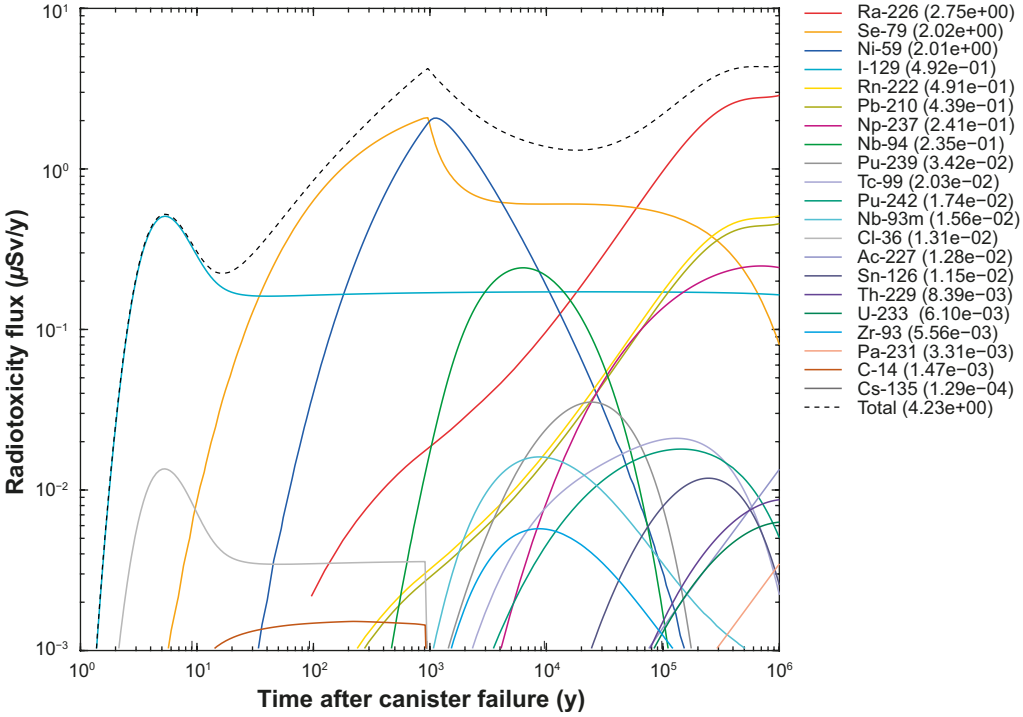

Figure 3-2. *Equivalent far-field radiotoxicity flux (μSv/y) calculated using NuDec-Farf31, for the base case, including both the instant release fraction (IRF) modelled as a square pulse of 1 y duration, and corrosion/dissolution release fraction (CDRF). The legend is sorted by peak flux within the time frame of the safety assessment. The time on the x-axis is relative to canister failure at 100 ky post-closure. Only radionuclides contributing more than 0.1 % of the total radiotoxicity are plotted.*

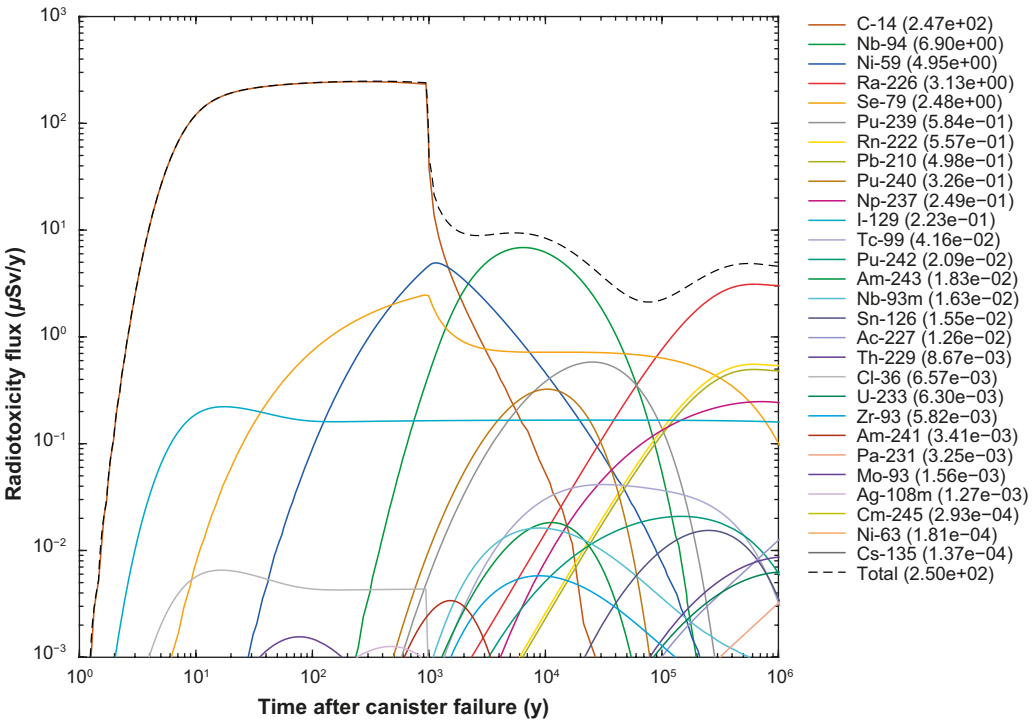

Figure 3-3. *Equivalent far-field radiotoxicity flux (μSv/y) calculated using NuDec-Farf31, for the case with early canister failure at 1 ky, including both the instant release fraction (IRF) and corrosion/dissolution release fraction (CDRF). The legend is sorted by peak flux within the time frame of the safety assessment. The time on the x-axis is relative to canister failure at 1 ky post-closure. Only radionuclides contributing more than 0.1 % of the total radiotoxicity are plotted.*

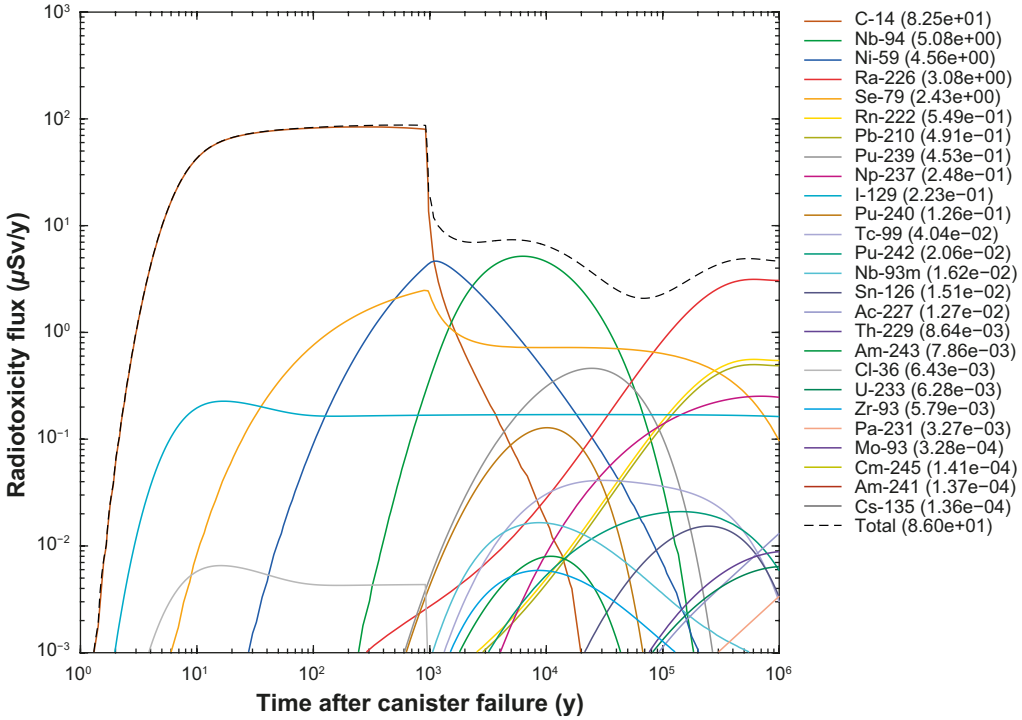

Figure 3-4. *Equivalent far-field radiotoxicity flux (μSv/y) calculated using NuDec-Farf31, for the case with early canister failure at 10 ky, including both the instant release fraction (IRF) and corrosion/dissolution release fraction (CDRF). The legend is sorted by peak flux within the time frame of the safety assessment. The time on the x-axis is relative to canister failure at 10 ky post-closure. Only radionuclides contributing more than 0.1 % of the total radiotoxicity are plotted.*

4 K_d sensitivity analysis for radiotoxicity flux calculations

When attempting to establish a priority list of different radionuclides that are critical to safety assessment of a repository for radioactive substances, there are several different performance metrics that can be used. One obvious metric is the contribution to total transported radiotoxicity either as an instantaneous peak flux, or time-integrated flux. For regulatory authorities, the peak total transported radiotoxicity (peak dose) is usually the performance measure of most interest since it has greatest relevance for assessing the radiological risk to the most exposed individual in a population living near a waste repository.

Since total transported radiotoxicity is equal to the sum of contributions from different radionuclides, however, some radionuclides may have a very large impact, while others may be insignificant and could reasonably be neglected altogether. Furthermore, the contribution of a given radionuclide to the peak total dose summed over the contributions of many radionuclides does not necessarily correspond to the peak dose of the radionuclide itself. In the base case simulations described in the previous chapter (Figure 3-1), the total dose during the first 10^4 years after onset of advective flow in the canister deposition hole is dominated by I-129, Se-79, Ni-59, and Nb-94. Significant transported radiotoxicity derived from actinide chains only starts to become important at times significantly greater than 10^4 years.

Similar behaviour is also seen for the early release case studies, although C-14 and Nb-94 are significantly elevated in importance in the early canister failure cases. As can be seen from Figure 3-1 there are also three local maxima for total transported radiotoxicity corresponding roughly to the instant, corrosion, and dissolution release fractions in the spent fuel canisters. The peaks of subordinate radionuclides (e.g., Nb-94, Pu-239, Tc-99, Zr-93, etc), however, do not coincide with the total dose maxima.

In this report, we are interested in identifying which radionuclides would have the greatest impact on safety assessment outcomes if more accurate sorption data were available. A radionuclide that currently has very poor K_d data support, for example, may have very little additional impact even if exhaustive investigations are carried out to improve the K_d recommendation. Seen through the lens of a cost-benefit analysis, it would be better to focus on radionuclides that have the greatest potential for altering safety assessment performance measures. Ideally, one would also seek to choose radionuclides that have the best chance of increasing mechanistic understanding of sorption processes. Some elements and redox states that could be of much benefit for mechanistic understanding, however, may be identified in the present analysis as being of subordinate importance and might be missed by a pure focus on dose rates achieved in safety assessment. The ambition of increasing mechanistic understanding therefore may be partly in conflict with selection driven purely by safety assessment considerations and a more holistic perspective should therefore be considered before a final choice is made.

There are two principal modes by which an altered K_d value can attenuate transported radiotoxicity. These are decay and dilution. For decay-related attenuation, an altered retarded transport time relative to the half-life of the radionuclide has a direct impact on the amount of remaining radionuclide contributing to the far-field dose rate at the end of a flowpath. An increased travel time due to enhanced retardation, for example, allows more time for an individual radionuclide to decay during migration thereby giving a lower transported radiotoxicity. Conversely, a decreased retardation gives a higher transported radiotoxicity. While this is always true for a single, non-chain radionuclide decaying to a stable product (i.e., most fission and activation products), the situation is more complex for actinides since an altered retardation also impacts the ingrowth of descendant radionuclides along a migration path. For actinide chains it is not always correct to assume that a high retardation factor is conservative, and in some cases, it is feasible for reduced mobility of parent radionuclides to result in higher dose rates of descendant radionuclides.

The impact of decay related attenuation on individual radionuclides can be quantified by calculating the relative activity that reaches the biosphere relative to the amount that is released in the near field. This is relatively easy to calculate using a simplified transport model such as that described by Tang et al. (1981). The effect of decay related attenuation can also be quantified in terms of the travel time for an instantaneous pulse release relative to the half-life of a migrating radionuclide. From the analytical solution for a pulse release neglecting hydrodynamic dispersion (e.g., Neretnieks 1980), the travel time corresponding to peak breakthrough, t_{peak} can be shown to be:

$$t_{\text{peak}} = t_w + \frac{1}{6} D_e \varepsilon_p R_p F^2 \tag{4-1}$$

This result is obtained by taking the time derivative of the cumulative residence time distribution and solving to identify the stationary point of zero slope. This corresponds to the maximum of the breakthrough curve for a Dirac pulse and is a reasonably representative measure of relative retardation for solutes featuring different sorptivity. Although this is a very simplified account of transport, the ratio of peak travel time to half-life, $t_{peak}/t_{½}$ is a useful measure since it can be very easily used to screen radionuclides for the impact of decay related attenuation. As an example, Figure 4-1 shows the fraction of released activity that reaches the biosphere calculated using the Tang et al. (1981) model plotted against the ratio, $t_{peak}/t_{½}$.

In Figure 4-1, one can see that radionuclides with very short travel times relative to half-life ($t_{peak}/t_{½} < 0.001$) are ineffectively retarded for the F-factor considered in the calculation. Even with very high F-factors, radionuclides such as I-129 and Cl-36 are unlikely to benefit from improved quantification of K_d. Ratios in the range $0.001 < t_{peak}/t_{½} < 1$, on the other hand, are modestly affected by decay attenuation and are reasonably likely to benefit from improved quantification of sorption, although more so for flowpaths featuring higher F-factors.

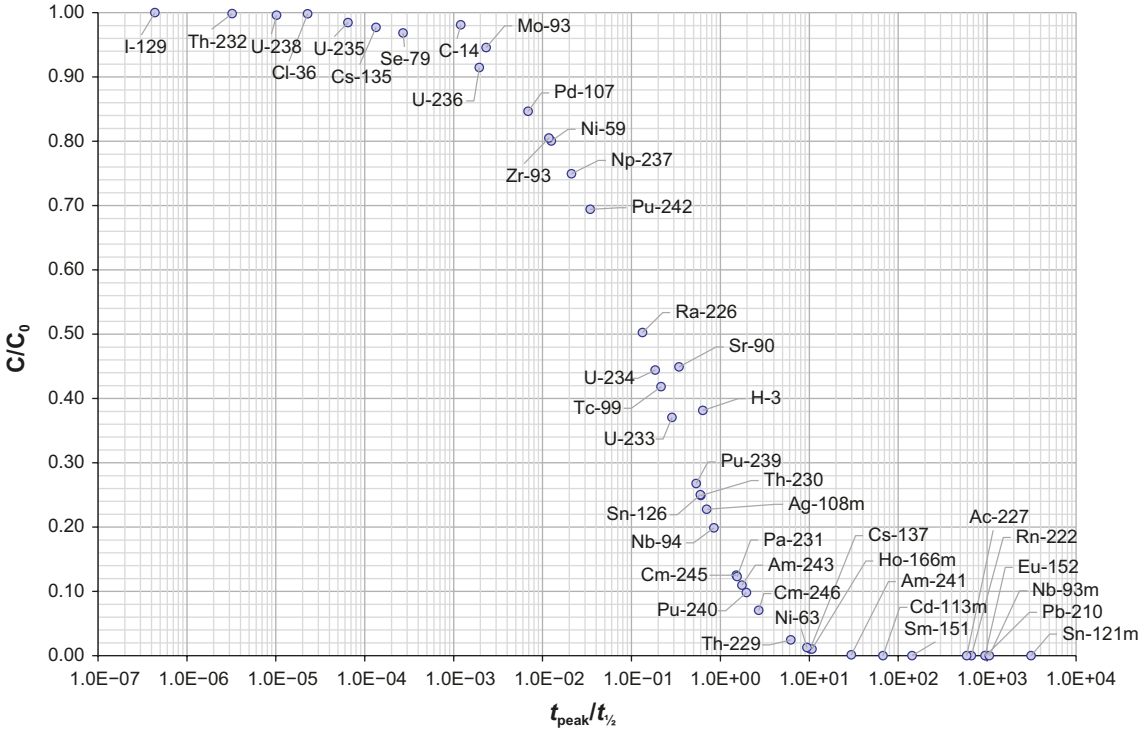

Figure 4-1. *Fraction of released activity that reaches the biosphere (C/C_0) plotted as a function of peak transport time relative to half-life. Here, the same F-factor of 5.4×10^4 y/m is assumed as for the central corrosion case.*

A $t_{peak}/t_{½}$ ratio much greater than unity, on the other hand, implies relatively strong decay-related attenuation. Radionuclides in this group are also unlikely to directly contribute to far-field radiotoxicity fluxes even with significant changes in K_d. This is because they are already strongly attenuated and moderate changes in retardation are unlikely to change this. Some radionuclides such as Pb-210, Ac-227, and Pa-231 have $t_{peak}/t_{½}$ ratios that imply strong attenuation for transport from a canister position, although are still important to consider since they are produced by ingrowth along transport paths in the far-field.

Although a useful screening tool, this first-order analysis does not say much about the context of total transported radiotoxicity which is important for deciding which of the potentially retardation-sensitive radionuclides actually contribute to far-field fluxes. To study individual radionuclides in the context of total radiotoxicity flux dose and determine the most important dose contributors requires more detailed transport simulations. Such simulations are carried out in the following sections.

For dilution-related attenuation, altered retardation has an influence on the spreading of a radionuclide pulse of limited duration. In this case, enhanced retardation spreads the arrival of the same amount of solute out over a longer time so that far-field radiotoxicity fluxes are less than what would be the case with reduced retardation. This is the case at least for radionuclides with long half-lives relative to their retarded transport time. Dilution-related attenuation therefore is mostly only applicable to instant release and, to a lesser extent, the corrosion release fraction. Here, the same caveat applies as for attenuation by decay and increased retardation of a parent radionuclide does not automatically mean reduced radiotoxicity flux when summed over all contributors in a decay chain. In the context of dilution, it is also important to differentiate between radiotoxicity integrated over time (i.e., dose, Sv) and the radiotoxicity flux (dose rate, Sv/y). While decay reduces both total radiotoxicity and radiotoxicity flux proportionally, dilution reduces the radiotoxicity flux to greater degree than total transported radiotoxicity. This is particularly the case for very long-lived radionuclides that are released quickly in the form of a so-called instant release fraction.

In the following sections, we examine the impact of altered retardation on different radionuclides and how changes to the sorption database might impact the predicted radiological consequences in transport calculations. Since non-actinide radionuclides in most cases decay directly to stable products or have relatively trivial decay chains (i.e., where the radiotoxicity of descendant radionuclides are implicitly included in the dose factors assigned to the parent), these are handled separately to actinides. As the progeny in actinide chains have mutually inseparable, non-linear effects arising due to decay and ingrowth these require a more complex sensitivity analysis. We therefore study each of the different actinide chains separately using a response surface approach and the results are exemplified by a small number of parameter variation case studies for each decay chain.

4.1 Methodology for sensitivity analysis

Although consideration of peak transport time relative to half-life is a useful screening tool to gauge sensitivity of individual radionuclides to decay-related transport attenuation (e.g., Figure 4-1), in this work we are more interested in identifying which radionuclides have the greatest impact in the context of total radiotoxicity flux. Here, it is important to distinguish between the sum of instantaneous radiotoxicity flux of many contributing radionuclides at a specific point in time and the time-integrated sum of transported radiotoxicity. Although the latter might be an appropriate benchmark in some contexts, we focus on the total instantaneous radiotoxicity flux as this is closest to the performance measure of interest in safety assessment (i.e., the peak radiotoxicity flux relative to the regulatory limit).

It should be noted that in this work we are not necessarily interested in identifying the most important radionuclides for the safety assessment even if a de facto list of such radionuclides is obtained as a by-product. Here, we are specifically trying to ascertain what overall impact the sorption status of individual elements might have on the shape and appearance of the instantaneous total radiotoxicity curve and how much this changes due to an alteration in K_d for individual elements in question.

In the present analysis, the impact of altering retardation of individual radionuclides is quantified by comparing the instantaneous far-field peak radiotoxicity flux of the specified radionuclide to the summed instantaneous radiotoxicity flux at the same point in time. This allows us to distinguish between radionuclides that exhibit sensitivity to altered sorptivity, although are of only minor importance and those radionuclides that are both sensitive to altered K_d and have a significant impact on the

total radiotoxicity flux. Since alteration of the K_d value for an individual radionuclide changes both the timing and peak height in the breakthrough curve, the relevant total flux used as a basis for the calculation is different at different peak breakthrough times for the radionuclide in consideration as illustrated in Figure 4-2. The fraction, f_k of the total instantaneous breakthrough for radionuclide, k is calculated as:

$$\phi_k = N_{k,tk}/N_{tot,tk} \quad (4\text{-}2)$$

Where,

$N_{k,tk}$ = radiotoxicity flux of radionuclide k at breakthrough time t_k.

$N_{tot,tk}$ = total instantaneous radiotoxicity flux at time t_k.

t_k = breakthrough time corresponding to the peak breakthrough of radionuclide, k.

For most fission and activation products that either decay directly to stable elements or have progeny with trivially short half-lives, the relative importance can be determined directly from the relative dose ranking calculated in transport calculations. Given that the fluxes of these radionuclides sum to give the total radiotoxicity flux, the first-order impact of altered retardation can be estimated by varying the K_d values for each of the radionuclides independently. Since the breakthrough of each (non-chain) radionuclide is modelled independently, there are no joint chemical interactions or ingrowth effects arising between radionuclides.

Despite this, the summed instantaneous radiotoxicity flux is still dependent on the breakthrough characteristics of each contributing radionuclide. A change in the peak flux and timing of one radionuclide, for example, may have consequences for the relative importance of remaining radionuclides when ranked according to fractional contribution to the total breakthrough. In this work we refer to such interactions as indirect effects of the model parametrisation. We consider this as categorically separate to correlation between K_d values of radionuclides arising due to geochemical similarities. It is also considered to be categorically separate to interactions between radionuclides related to ingrowth in decay chains (e.g., altered retardation of a parent radionuclide intensifying, or limiting the breakthrough of one or more progeny).

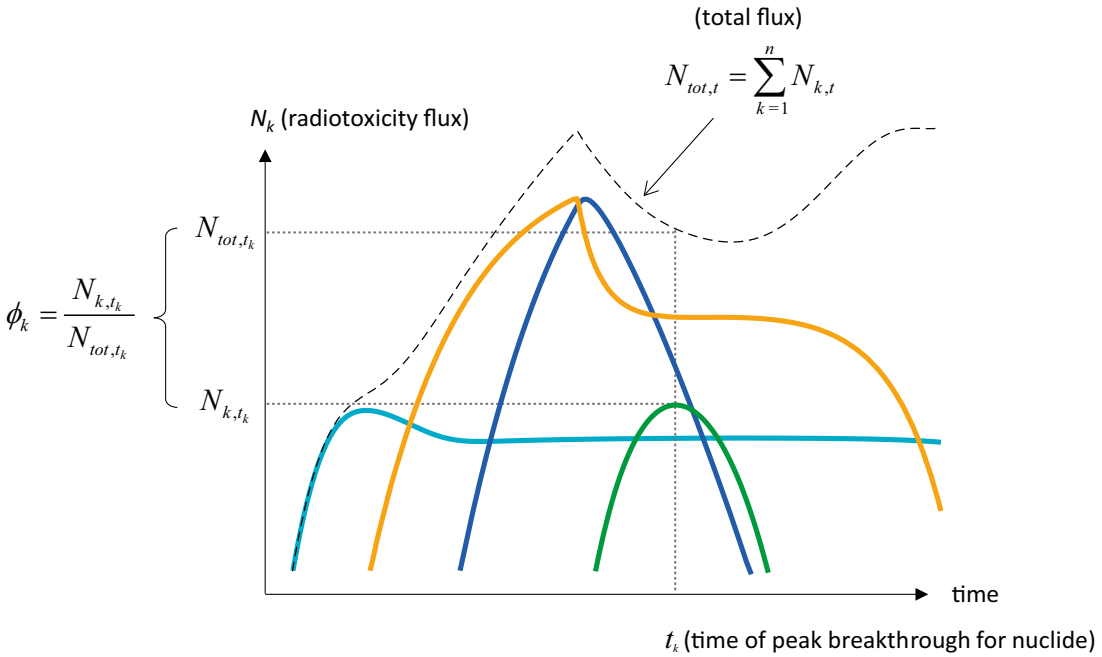

Figure 4-2. *Illustration of the key performance measure quantified in this work. The peak radiotoxicity flux, N_k of a single radionuclide is compared to the total radiotoxicity flux, N_{tot} evaluated at the same time to give an estimate of the fraction of transported radiotoxicity for which the radionuclide is responsible, ϕ_k.*

An example of a situation where indirect effects of model parameterisation might arise is illustrated by the green breakthrough curve in Figure 4-2. If the parameterisation of the model is changed in such a way that the timing of the green peak breakthrough is reduced relative to the orange and blue breakthrough curves, then the value of ϕ_k might be significantly reduced relative to the base case (i.e., if the green peak becomes overshadowed by the blue and orange curves). This might be achieved by reducing the K_d value for the nuclide represented by the green curve, although then the peak height may be increased due to the lower degree of transport retardation and geosphere attenuation implied by the K_d change.

In the case illustrated in Figure 4-2, for example, the increase in the total flux, N_{tot,t_k} at the point of reduced peak breakthrough time, t_k may outweigh the corresponding increase in N_{k,t_k} for the nuclide of interest (due to reduced retardation), thereby giving a decreased ϕ_k overall for this radionuclide. While a decrease in ϕ_k is counterintuitive relative to what one would normally expect for a scenario of reduced retardation, it is perfectly reconcilable against the ensemble breakthrough of other radionuclides. In general, the response of ϕ_k for a specific radionuclide to a change in K_d can occasionally be highly non-linear since it depends on the breakthrough timing and attenuation of other radionuclides contributing to the instantaneous radiotoxicity flux at the point of peak breakthrough.

While it is usually preferable to use a factorial experimental design of some kind to investigate sensitivity of a system to uncertain parameterisation where interactions between variables can arise, the primary aim of this work is as a screening study to ascertain a priority list of radionuclides for focused investigations. In this context, first-order effects of K_d uncertainty for non-chain radionuclides are arguably of central interest for identifying radionuclides that should be prioritised. Indirect interactions of the kind discussed above may not be strictly relevant to this process, although must be considered in the result interpretation anyway. Put another way, it may not be useful to put a lot of effort into improving the K_d value of a clearly less important radioelement if its relative importance is also conditional on the possibility that another nuclide is given a K_d value that changes in a very specific way relative to the base case parameterisation (i.e., decreased, or increased over a given threshold).

For the non-actinide radioelements, a simplified 2-level variation screening analysis was performed where the impact of K_d variation of each radionuclide was modelled separately for each radioelement without consideration of joint interactions. Given that the first order effects of K_d uncertainty are deemed to be the most important for selecting radioelements for focused study, this is presumed to be sufficiently accurate for the present purposes even though more sophisticated sensitivity analyses are certainly possible.

In the screening analysis, the K_d value of each element is varied up and down by a factor of 10 relative to the base case value while K_d values for all other elements remain fixed at their base-case values (the total range of K_d variation therefore being a factor of 100). The magnitude of K_d variation is arbitrary although deemed reasonable given that improvement to the quality of the K_d database is most likely to have impacts in this range. The range of modelled K_d variation is also roughly the same order of magnitude as the minimum–maximum uncertainty range for most sorbing radionuclides in SR-Site and PSAR and is thus consistent with the previous judgement of data uncertainty elaborated in Crawford (2010). The non-sorbing radionuclides (C-14, Cl-36, and I-129) are included here for comparative purposes only, although the base case K_d is set to 10^{-6} m^3/kg rather than non-sorbing as was the case in SR-Site and PSAR. The rationale for assigning a non-zero K_d for these calculations is discussed in the following section.

In this work, the sensitivity of total instantaneous radiotoxicity flux to altered K_d is quantified by a standardised performance measure, Ω_k defined as:

$$\Omega_k = \left| \frac{d\phi_k}{d\left(\log_{10} K_d\right)} \right| \tag{4-3}$$

For a range of varied K_d values ranging from 0.1 to 10 times the base case K_d value, we would then have:

$$\Omega_k \approx \frac{\left|\phi_{k(10\cdot K_d)} - \phi_{k(0.1\cdot K_d)}\right|}{\left(\log_{10}\left(10\cdot K_d\right) - \log_{10}\left(0.1\cdot K_d\right)\right)} = \frac{\left|\Delta\phi_k\right|}{2} \tag{4-4}$$

Although Ω_k is a relatively crude gauge of sensitivity, we deem it as being sufficient for the purpose of ranking relative importance of radionuclides in the present screening analysis. The calculation is based on absolute values since it is more straight-forward to illustrate graphically on logarithmic axes and also because we are mostly interested in whether there is a relevant impact on the contribution to total dose regardless of the sign of the change. Using the parameters ϕ_k and Ω_k as performance measures allows us to quantify in an approximate fashion, the potential for individual radionuclides to alter the shape of the radiotoxicity flux breakthrough curve.

4.1.1 Handling of non-sorbing elements

The radionuclides C-14, Cl-36, and I-129 were assigned non-sorbing status (i.e., zero K_d) in SR-Site and PSAR. Although these elements are not expected to sorb more than very weakly, they are of special interest given that I-129 and Cl-36 dominate early breakthrough of the instant release fraction. For the scenarios featuring very early canister failure times, C-14 is the most important dose-determining radionuclide by at least an order of magnitude. Anions typically sorb poorly in geomedia at normal groundwater pH levels since they only interact with positively charged surface reactive groups and most minerals have net negative charge under such conditions.

Ferric oxides, magnetite, and ferrol surface groups associated with biotite (annite) may retain some positive surface charge and be able to sorb at circumneutral to mildly basic groundwater pH levels. Ferrol binding sites are the name given to > FeOH surface functional groups associated with Fe(II) or Fe(III) containing minerals. They are analogous although have different reactivity to silanol (> SiOH) and aluminol (> AlOH) functional surface groups associated with aluminosilicates.

Fuhrmann et al. (1998) measured sorption of iodide (I^-) and iodate (IO_3^-) on pyrite, magnetite, and biotite in deionised and bicarbonate buffered water. The authors found, however, indications that only IO_3^- and not I^- would sorb in association with biotite. Although oxidation of I^- to IO_3^- is expected for trace concentrations under ambient oxidising conditions, the relevance of the associated sorption mechanism for reducing groundwater environments at repository depth is unknown (the effect of radiolysis on IO_3^- formation in the near field is not well studied). ClO_3^- can also form under ambient oxidising conditions and may sorb by an analogous sorption mechanism to IO_3^- although to the best knowledge of the author this is presently unquantified. It is mechanistically reasonable to expect weak sorption of IO_3^- due to its tetrahedral dipole structure with a positive charge in association with the central iodine atom.

There are some indications in the in-house sorption data described in the Posiva K_d data compilation for the TURVA-2012 safety case (Hakanen et al. 2014) that iodine, most likely in the form of IO_3^-, sorbs weakly on the biotite of Finnish site-specific rock types, although it is not clear whether the data are transferrable to Forsmark specific rock types which have significantly lower biotite content. The sorption data in the Posiva compilation are based largely on the work by Kulmala et al. (1998). These experiments were also performed under ambient conditions at roughly atmospheric oxidising intensity, so may not be relevant for in situ reducing conditions if the measurements are representative of IO_3^- sorption.

Carbonate, CO_3^{2-} might sorb on positively charged surface ferrol sites in a similar fashion to other oxy-anions (as inner or outer-sphere surface complexes), or as ternary inner-sphere carbonate complexes with other solution cations on otherwise negatively charged binding sites associated with silanol or aluminol surface groups. Sorption of carbonate by surface complexation has not been quantified for granitic rock, although it is likely to be relatively weak. Another possible mode of sorption for carbonate is isotope exchange on calcite surfaces. Although this may be a significant sorption mechanism for calcite rich fracture coatings, the calcite content of the rock matrix itself is typically very low at Forsmark and frequently reported as below the detection limit (~0.2 vol%, see e.g., Sandström and Stephens 2009). Owing to the low calcite content of the rock, carbonate isotope exchange is deemed unlikely to constitute a significant storage capacity for C-14 retention even if present.

For non-sorbing radionuclides, a threshold K_d value corresponding to a minimally relevant retardation effect, R_{pmin} can nonetheless be estimated:

$$K_d = \left(R_{pmin} - 1\right) \cdot \frac{\varepsilon_p}{\rho_b} \qquad (4\text{-}5)$$

For the present analysis, an R_{pmin} value of 2.5 is assumed for screening purposes. This is equal to roughly 2.5 times the retardation potential arising due to free pore storage alone. For the Forsmark site-specific rock type (metagranite) this corresponds to a base case K_d value of $\sim 10^{-6}$ m^3/kg. In the sensitivity analysis for non-decay chain radionuclides presented in the following section, the K_d value is varied by a factor of 10 (increased or reduced) relative to the base case K_d value. In the calculations presented in the next section this implies a range of K_d values from 10^{-7} m^3/kg (effectively non-sorbing) to 10^{-5} m^3/kg (weakly sorbing). In the following sensitivity analyses, the use of a non-zero threshold K_d value is only considered relevant for C-14, Cl-36, and I-129. For the cases of early canister failure, there is a non-negligible contribution from Mo-93. Although conservatively deemed non-sorbing for the purposes of SR-Site, Mo is assigned a K_d of 3×10^{-4} m^3/kg in the present work (same as for Se). In all calculations Rn-222 is assigned a K_d of zero since it is a noble gas.

4.2 Results for fission and activation products

The results of the analysis quantified in terms of the performance parameter Ω_k are shown as a bubble plot in Figure 4-3 for the fission and activation products modelled using the NuDec-Farf31 program. The horizontal axis is the ϕ_k value for the base case K_d setting corresponding to the fraction of total instantaneous radiotoxicity flux (dose) at peak breakthrough for each radionuclide, k. The relative variation of ϕ_k for each radionuclide is also visualised by mapping the marker size and colour to the coefficient of variation of peak radiotoxicity flux for each radionuclide (i.e., standard deviation of peak flux divided by mean peak flux). This is useful for showing the impact of altered K_d on the peak radiotoxicity flux for individual radionuclides since the Ω_k variable emphasises fractional changes in the context of the total instantaneous radiotoxicity flux. Cs-135, for example, has only a very small impact (i.e., effectively zero) on total radiotoxicity flux with ϕ_k varying between 3×10^{-5} and 2×10^{-3} even though the impact on the peak flux of the actual radionuclide is roughly a factor of seven.

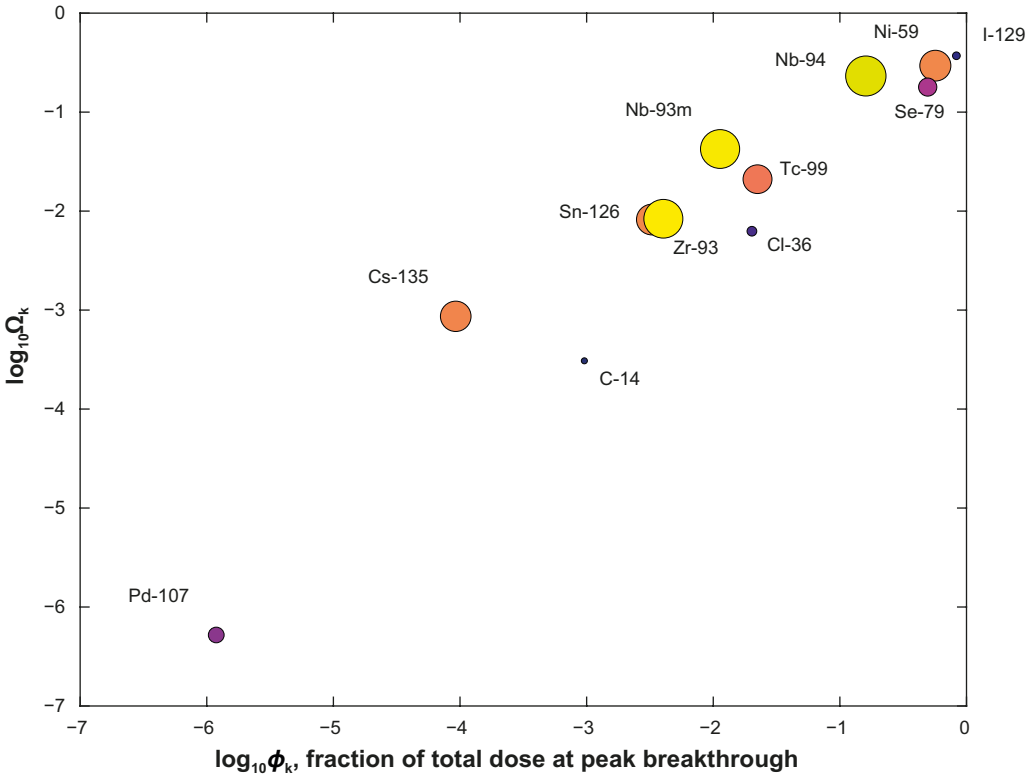

Figure 4-3. *Impact of K_d variation as quantified by the performance variable, Ω_k plotted against base case ϕ_k (reference K_d values) in the 100 ky release scenario where K_d is varied up and down by a factor of 10. Only those radionuclides that contribute non-negligible amounts to the total transported radiotoxicity ($\phi_k > 10^{-7}$) are included in the analysis. The marker size and colour are scaled by the coefficient of variation of peak flux for each radionuclide to indicate the corresponding impact of altered K_d for each radionuclide individually.*

Figure 4-3 is a useful construct for determining a priority order for which radioelements should be subject to focused investigations. In this screening process, we propose the following criteria to prioritise radionuclides:

1) The radionuclide *k* should contribute non-negligibly to total radiotoxicity flux (quantified by the variable ϕ_k).
2) The radionuclide should have significant potential to alter the total radiotoxicity flux for an altered K_d of specified magnitude (quantified by the variable Ω_k).

Since the absolute fraction, ϕ_k of the total flux at peak breakthrough and the W_k value for a given change in K_d are both relevant for the ranking, a weighted score that considers both these variables might be considered a suitable quantitative measure. It is clear from the analysis that radionuclides plotted in the upper right corner of Figure 4-3 play a significantly more important role than those in the bottom left-hand corner with the size of the marker (and its colour) indicating relative changes in peak breakthrough. Both Ni-59 and Se-79, for example, are associated with relatively smaller changes in peak radiotoxicity flux for the modelled K_d variation (as indicated by size and colour of the circular markers), although they are still more important contributors to peak total radiotoxicity than Nb-94 whose breakthrough is more strongly modulated by changing the K_d value.

I-129 is the dominant radionuclide at the time of its peak breakthrough (19.4 y) in the base case ($K_d = 10^{-6}$ m^3/kg) for canister failure at 100 ky. This is roughly three times the advective transport time indicating insignificant geosphere retardation. The instant release fraction dominates the source term, however, and at later times when the dissolution release fraction mostly governs the source flux of I-129 it is less important as a radionuclide. Overall, it is only the eighth most important radionuclide (cf Figure 3-1) in terms of the peak flux of each radionuclide. Although decreasing the K_d value for I-129 by a factor of 10 relative to the base case has no discernible impact on the radiotoxicity fraction at peak breakthrough, increasing the K_d value by a factor 10 has a much larger impact and decreases the fractional contribution to breakthrough to less than 10 % at the time of peak breakthrough.

This is a good example of an indirect effect related to peak dilution and illustrates the non-linear nature of ϕ_k as a performance measure. When the instant release fraction is modelled using the CSTR elution approach, the already dilute instant release peak is spread and diluted to such an extent that the dissolution release fraction becomes dominant with peak breakthrough then occurring at 83 ky instead of at the peak time of instant release breakthrough (ca 19 y). At this later time Ra-226 and Se-79 are the dose dominant radionuclides and I-129 is of subordinate importance. The large change in ϕ_k for I-129 at the higher K_d level is therefore mostly due to a shift of peak breakthrough timing relative to other radionuclides that are more important flux contributors at that time.

It is interesting to compare this result with what is obtained when the IRF is modelled as a square pulse of 1 y duration (cf Figure 3-2). In that case, the initial IRF peak is diluted, although not to the extent that the peak flux associated with the dissolution fraction becomes dominant. The result indicates that the attenuation of the IRF peak associated with the breakthrough of I-129 is strongly dependent on the assumed form of the near field boundary condition for the IRF and that an effect threshold is reached where any additional increase in K_d would have no substantial impact since the breakthrough then becomes dominated by the dissolution release fraction which is not appreciably affected by increased retardation owing to low decay-related attenuation for this radionuclide.

The breakthrough timing of Se-79 indicates a dominant influence of the corrosion release fraction. The main impact of increased K_d is a dilution of the corrosion release peak, while the contribution of the dissolution release fraction is not strongly altered by increased retardation. Decay-related attenuation is relatively minor due to the long half-life of the radionuclide relative to the time schedule of release. Despite the weak overall impact of K_d variation (the peak breakthrough flux varies by a factor of 4.3 relative to the base case), if one also considers the ranking of Se-79 in the top three dose determining radionuclides for the 100 ky canister failure scenario, it is clearly an interesting target for focused laboratory investigations.

The breakthrough radiotoxicity flux of both Ni-59 and Nb-94 are relatively strongly influenced by the modelled K_d variation. The peak flux of Ni-59 varies by a factor of 32 relative to the base case, while the peak flux of Nb-94 varies by a factor of about 370. Both the Ni-59 and Nb-94 peaks are clearly associated with the corrosion release fraction and are impacted by both peak dilution and decay effects due to having relatively short half-lives relative to their transport times.

Bubble plot visualisations of the results for the transport calculations with failure times at 1 ky and 10 ky are shown in Figure 4-4 and Figure 4-5, respectively. The main difference here is the much greater prominence of C-14 and Nb-94 relative to Ni-59, Se-79, and I-129. An interesting feature of the plots for early failure time is a trend reversal observed for I-129 relative to the scenario of canister failure at 100 ky for increased K_d relative to the base case. This is largely due to a shift in the timing of the peak breakthrough for I-129 relative to the breakthrough of C-14 which is still rising steeply at the time of peak breakthrough of I-129 for the base case K_d settings. Since C-14 has decayed to insignificant levels by the time of canister failure at 100 ky, the relative contribution of I-129 to the total radiotoxicity breakthrough is very different for the later canister failure time and is not comparable to the impact of altered K_d observed for canister failure at 1 ky and 10 ky.

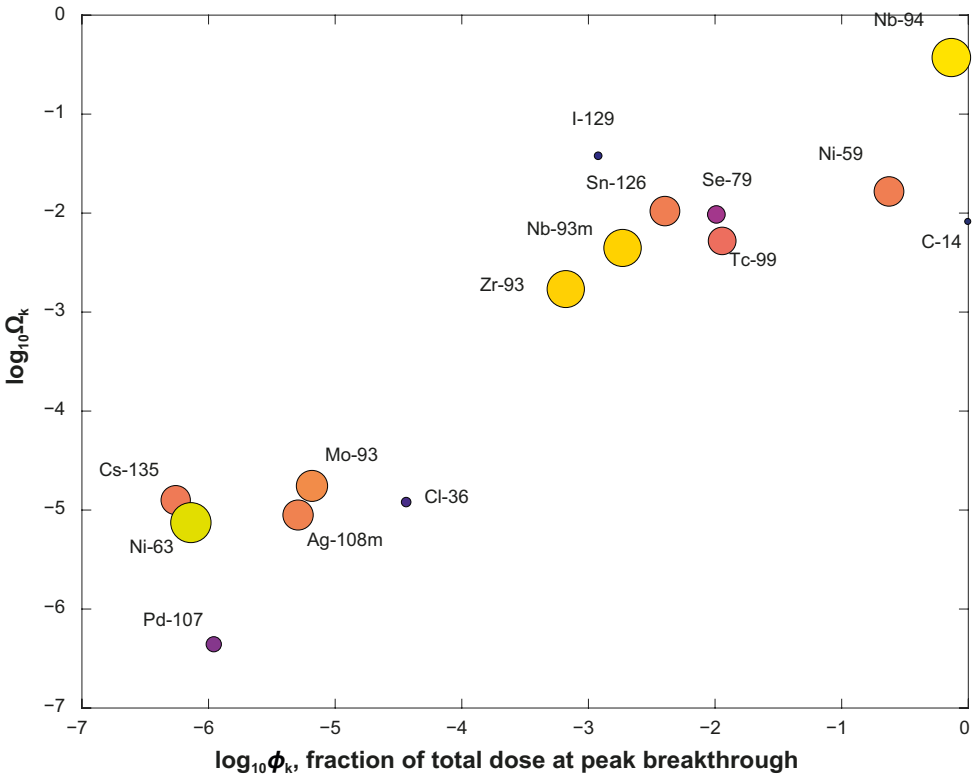

Figure 4-4. *Impact of K_d variation as quantified by the performance variable, W_k plotted against base case ϕ_k (reference K_d values) in the 1 ky release scenario where K_d is varied up and down by a factor of 10. Only those radionuclides that contribute non-negligible amounts to the total transported radiotoxicity ($\phi_k > 10^{-7}$) are included in the analysis. The marker size and colour are scaled by the coefficient of variation of peak flux for each radionuclide to indicate the corresponding impact of altered K_d for each radionuclide individually.*

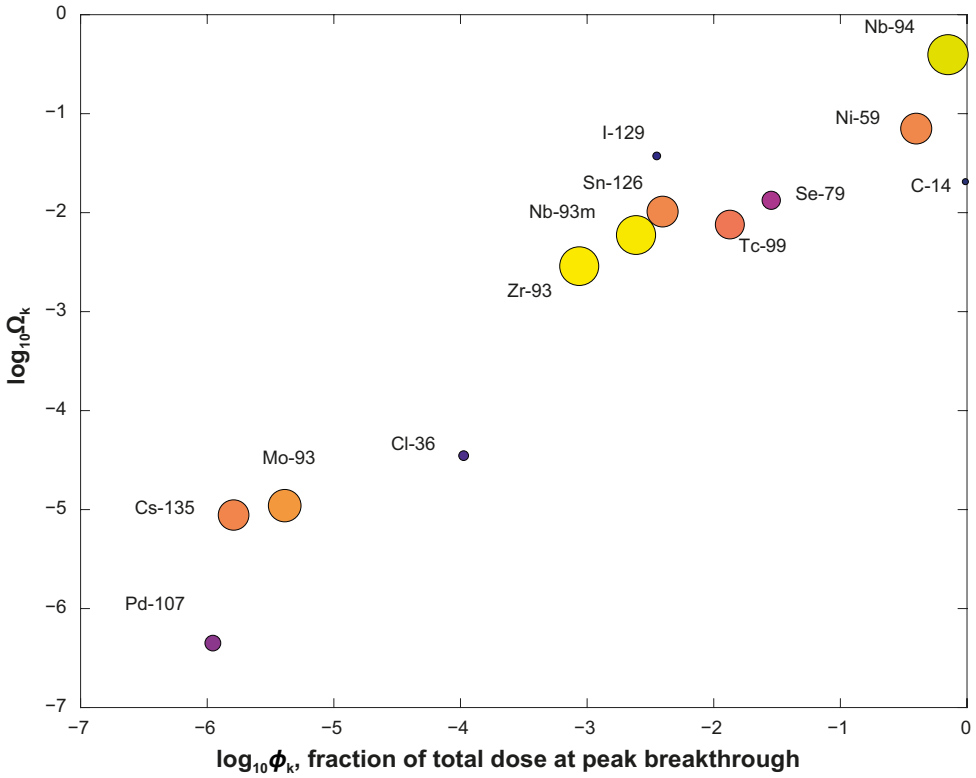

Figure 4-5. *Impact of K_d variation as quantified by the performance variable, Ω_k plotted against base case ϕ_k (reference K_d values) in the 10 ky release scenario where K_d is varied up and down by a factor of 10. Only those radionuclides that contribute non-negligible amounts to the total transported radiotoxicity ($\phi_k > 10^{-7}$) are included in the analysis. The marker size and colour are scaled by the coefficient of variation of peak flux for each radionuclide to indicate the corresponding impact of altered K_d for each radionuclide individually.*

If equal weighting of ϕ_k and Ω_k as measures of relative "importance" is assumed in the screening calculation, the linear distance of each radionuclide from the origin in the bubble plot figures (Figure 4-3 to Figure 4-5) might be considered a suitable measure for a relative importance ranking. The linear distance of each plotted point from the origin can be defined as:

$$r_k = \sqrt{(1-\omega)\cdot\phi_k^2 + \omega\cdot\Omega_k^2} \qquad (4\text{-}6)$$

Here, the parameter ω represents the relative weight given to the Ω_k variable and $1-\omega$ is the weight given to the ϕ_k variable. A value of ω equal to 0.5 therefore implies equal weighting of both performance measures. Using Equation 4-6, the relative importance of each element was calculated based on the breakthrough curves generated in the sensitivity analysis. The results of this calculation are given in Table 4-1 for the assumed LDF values given previously in Table 2-4. An alternative ranking is also given where the radiotoxicity fluxes are calculated using dose conversion factors for direct ingestion (DCF-I) rather than LDF values. As discussed previously in Section 2.1.1, this might be more appropriate for scenarios of, for example, well water contamination. The use of ingestion dose factors gives a slightly different weighting to different radionuclides and thus a different relative importance ranking than LDF's. The ingestion dose factors, however, are more well-defined and less uncertain than the LDF's extrapolated for radionuclides that weren't part of the original analysis by Avila et al. (2010).

Table 4-1. Relative importance ranking of different radionuclides as determined by an equal weighted measure of ϕ_k and Ω_k performance measures as defined in Equation 4-6. Rankings are given assuming landscape dose factors (LDF) as specified in Table 2-4 as well as the alternative case study of dose conversion factors for direct ingestion (DCF-I). The latter may be more appropriate for a contaminated well scenario. Only radionuclides featuring $\phi_k \geq 10^{-4}$ are included in the ranking.

Ranking	100 ky		10 ky		1 ky	
	LDF	DCF-I	LDF	DCF-I	LDF	DCF-I
1	I-129	I-129	C-14	I-129	C-14	I-129
2	Ni-59	Ni-59	Nb-94	Ni-59	Nb-94	Ni-59
3	Se-79	Cs-135	Ni-59	Nb-94	Ni-59	C-14
4	Nb-94	Zr-93	I-129	C-14	I-129	Nb-94
5	Tc-99	Nb-94	Se-79	Zr-93	Tc-99	Zr-93
6	Nb-93m	Nb-93m	Tc-99	Cs-135	Se-79	Cs-135
7	Cl-36	Tc-99	Sn-126	Se-79	Sn-126	Ag-108m
8	Zr-93		Nb-93m	Tc-99	Nb-93m	Ni-63
9	Sn-126		Zr-93	Nb-93m	Zr-93	Se-79
10						Tc-99
11						Nb-93m

Although I-129 is ranked first for the scenario of canister failure at 100 ky in both LDF and DCF-I cases, the utility of a laboratory programme to investigate iodide sorption is likely to be limited. This is because any sorptivity attributed to iodide will be very weak and the impact will depend to a great extent on assumptions made concerning the modelling of the instant release fraction. It is clear in the sensitivity case studies that the impact of altered K_d appears to be due to dilution of initial peak breakthrough associated with the instant release fraction and sorption has effectively no impact on the transported radiotoxicity of the dissolution release fraction owing to the very long half-life of I-129 (1.57×10^7 y).

Of the remaining ranked radionuclides, Ni-59, Se-79, and Nb-94 would appear to have the greatest potential to influence the outcome of Safety Assessment dose calculations. The effect of K_d on Se-79 breakthrough is dominated by peak dilution, however, while the effect is predominantly decay-related attenuation for Nb-94. Tc-99 and Zr-93 also appear as important radionuclides in the ranking as well as Nb-93m which is a descendant of Zr-93 decay. Owing to the short half-life of Nb-93m, much of the far-field flux of this radionuclide is likely to derive from ingrowth along migration paths rather than the near field source term. Both Tc and Zr are interesting as they are both examples of elements speciated in a tetravalent redox state whose sorptivity is poorly quantified in the K_d data recommendation from SR-Site. The same radionuclides also appear in the rankings for canister failure at 1 ky and 10 ky, although the breakthrough of C-14 overwhelmingly dominates the transported radiotoxicity for at least the first 1 ky after canister failure.

The high C-14 flux in the short failure time case studies is entirely attributable to the corrosion release fraction. Although C-14 (5.71×10^3 y) has a much shorter half-life than I-129, an altered K_d value has a limited impact on C-14 breakthrough owing to the relatively low F-factor of the transport flowpath coupled with the low expected sorptivity of C-14 as dissolved carbonate (C-14 speciated as CH_4 is not expected to sorb). Changing the K_d value by a factor of 10 around the base case value of 10^{-6} m^3/kg results in a maximum change in peak flux of about 14 % relative to the base case for C-14 assuming the F-factor of the reference scenario (5.4×10^4 y/m) as being representative. Greater attenuation by both decay and dilution attenuation mechanisms is achievable for flowpaths featuring higher F-factors. This, however, has not been quantified in the present work as it was out of scope.

Comparing the LDF variant case (VC-LDF) with the case using LDF values taken from SR-PSU (SFR-LDF) shows that Cs-135 and Zr-93 have elevated importance in the SFR-LDF case at the expense of Se-79 and Nb-94 whose importance is clearly reduced. C-14 is also significantly downgraded in importance in the SFR-LDF case relative to the VC-LDF case. Each of these changes are expected based on the relatively large changes in dose factor assigned to these radionuclides as already discussed in Section 2.1.3. It should be remembered that the dose factors values used in calculations represent maximum values over all time domains and biosphere objects modelled. While

the LDF values taken from SR-PSU represent a more developed understanding of surface geology, hydrology, and ecosystem processes than those used previously in SR-Site, they also reflect assumptions and features that might be specific to the SFR repository system (e.g., release locations relative to specific biosphere objects, absence of pulse release, etc), and are not automatically better. In this context, we consider the results obtained using different landscape dose factor assumptions as well as raw dose conversion factors for ingestion (DCF-I) as part of an overall envelope of uncertainty that should be considered before settling on a final list of prioritised elements.

Table 4-2. Relative importance ranking of different radionuclides as determined by an equal weighted measure of ϕ_k and Ω_k performance measures as defined in Equation 4-6. Rankings are given assuming variant case landscape dose factors (VC-LDF) as specified in Table 2-4 as well as the alternative case study using landscape dose factors from SR-PSU (SFR-LDF). The latter may be more appropriate for a contaminated well scenario. Only radionuclides featuring $\phi_k \geq 10^{-4}$ are included in the ranking.

Ranking	1 ky		10 ky		100 ky	
	VC-LDF	SFR-LDF	VC-LDF	SFR-LDF	VC-LDF	SFR-LDF
1	C-14	Ni-59	C-14	Ni-59	I-129	I-129
2	Nb-94	I-129	Nb-94	I-129	Se-79	Ni-59
3	Ni-59	Cs-135	Ni-59	Cs-135	Ni-59	Cs-135
4	I-129	Nb-94	I-129	Nb-94	Nb-94	Zr-93
5	Se-79	C-14	Se-79	Zr-93	Nb-93m	Cl-36
6	Tc-99	Zr-93	Tc-99	C-14	Tc-99	Nb-94
7	Sn-126	Mo-93	Sn-126	Cl-36	Sn-126	Tc-99
8	Nb-93m	Cl-36	Nb-93m	Mo-93	Zr-93	Se-79
9	Zr-93	Tc-99	Zr-93	Tc-99	Cs-135	Nb-93m
10		Ag-108m	Cl-36	Se-79	Cl-36	
11		Se-79		Nb-93m		

4.3 Results for Actinides

Since the members of actinide chains feature interactions arising due to decay and ingrowth, these are studied using a slightly different approach to that adopted for fission and activation products. In the screening calculations each decay chain is treated as a separate entity and analysed in the context of summed breakthrough radiotoxicity attributable to the specific chain rather than contribution to the total transported radiotoxicity. The reasoning for this is that, with the possible exception of the uranium ($4n + 2$) decay chain where Ra-226, Pb-210, and Rn-222 strongly dominate late time behaviour, the actinides tend to not contribute as much to the total radiotoxicity and the effects of varied K_d would be difficult to discern relative to the much more dominant fission and activation products at short to medium timescales.

To ascertain the sensitivity of simulated summed chain radiotoxicity flux in the far-field to variations in the retardation of the decay chain members, a circumscribed central composite response surface experimental design was adopted (for an overview see, e.g., Hanrahan and Lu 2006). For this purpose, the *ccdesign.m* function from the MATLAB Statistics and Machine Learning Toolbox was used. Using the *ccdesign* tool, a list of factorial combinations was defined for each decay chain where the number of factors is equal to the number of unique elements in each chain.

Here, for the central hypercube spanning the parameter space of the design we assumed the same one order of magnitude variation of the K_d values around the base case settings as adopted previously for the fission and activation products. The observed response variable in these calculations was the peak total radiotoxicity flux summed over all chain members. Since the peak radiotoxicity can vary over several orders of magnitude, the fitted response variable was the $\log_{10}$ of the peak radiotoxicity flux and the fitting terms are $\log_{10} K_d$ values for each unique radioelement. As previously, the NuDec-Farf31 program is used for the transport calculations.

After the breakthrough curves were calculated for each of the factorial K_d combinations, a response surface was then calculated using MATLAB's inbuilt linear regression fitting function. Here, only the linear and interaction terms were considered, and quadratic terms were disregarded. Although a better fit to the data may be achievable by invoking quadratic terms, they were neglected since they are confusing for the purpose of importance screening of individual flux contributors. From the fitted linear model, the relative importance of each radioelement in the model could then be inferred from the *p*-values for the fitted regression coefficients.

Since we are more interested in whether a predictor variable is important (or, not important) rather than building an actual regression model we do not report the intercept of the regression in the regression calculations. In this context, the *p*-value corresponds to the *t*-statistic of the hypothesis test that a regression coefficient is equal to zero or not. Although low *p*-values below a specified threshold (typically $p = 0.01$) value are typically taken to imply that the coefficient is statistically significant (i.e., non-zero), simply ordering the *p*-values from smallest to largest gives a good ranking of which radionuclides that dominate the analysis (at least for those with *p*-values below the specified noise threshold).

4.3.1 Thorium series (4*n*) decay chain

In SR-Site and PSAR, the thorium series (4*n*) decay chain was shortened to the three principal radionuclides Pu-240, U-236, and Th-232 as indicated in Figure 4-6. Owing to its very short half-life, the fast-decaying Cm-244 fraction was neglected, and its molar inventory was added directly to that of Pu-240 so is implicitly included in the transport calculations. The decay chain radionuclides highlighted in blue are explicitly modelled; black text signifies radionuclides that are part of the initial inventory, but where transport is neglected, and the inventory is simply added to the subsequent descendant; red signifies radionuclides implicitly modelled assuming secular equilibrium with the parent; green signifies a stable isotope decay chain terminator.

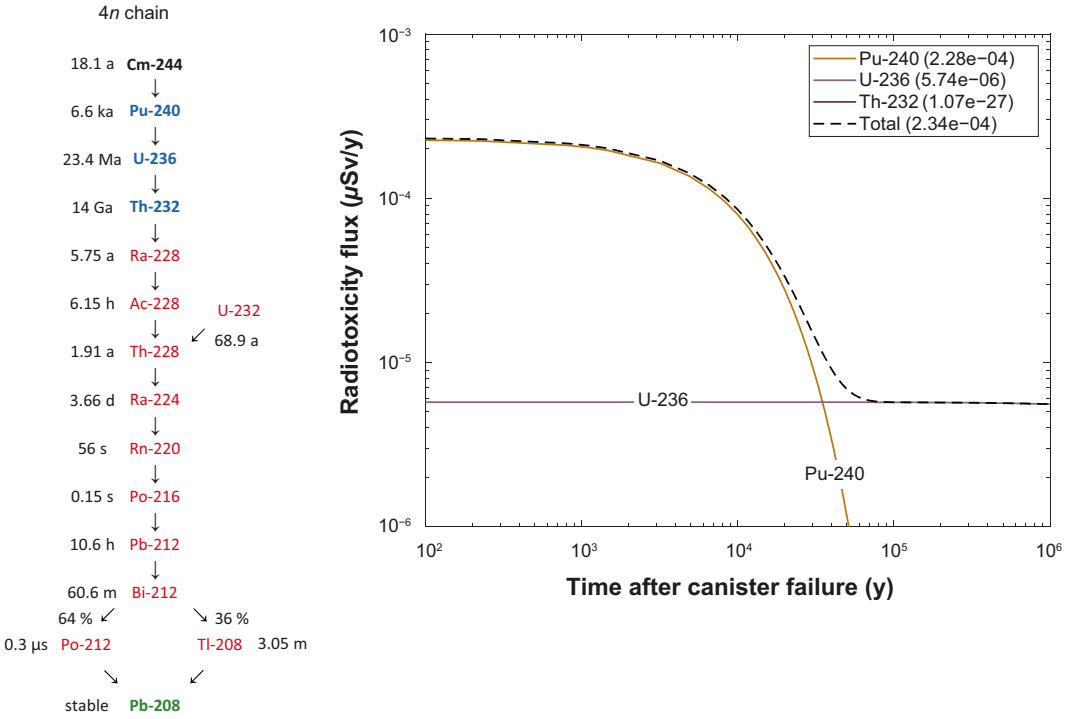

Figure 4-6. *Simplifications to the thorium (4n) decay chain (left – see text for details) and the near-field boundary condition (calculated by COMP23) for canister failure at 100 ky (right). The legend is sorted sequentially in decay order with peak near-field radiotoxicity flux (µSv/y) noted for the time frame of the safety assessment assuming basic LDF factors taken from Table 2-4.*

For this decay chain, the predictor variables were the individual K_d values for Pu, U, and Th. From the regression analysis results shown in Table 4-3 it was found that the K_d value associated with Pu-240 overwhelmingly dominated the variation of peak summed far-field radiotoxicity flux for the decay chain with a somewhat weaker contribution from U-236. Owing to the exceptionally long half-life of Th-232 and its very low near-field source flux, a change in K_d has a negligible impact on the contribution of this radionuclide and is therefore relatively unimportant for the total dose attributable to the 4*n* decay chain. This should also be considered in the context of the assumed solubility of Th in the source term which is set to an exceptionally low level (10^{-27} mol/l) in both SR-Site and PSAR. The Th-232 appearing in the far-field breakthrough is therefore mostly generated by ingrowth from U-236 decay along the migration path.

Table 4-3. Results of regression analysis based on results from the response surface factorial design (15 simulated parameter combinations for 3 predictor variables). The relative importance of individual radioelements for the peak total radiotoxicity flux can be inferred from the *p*-values in increasing order (smaller p-values imply stronger effects; *p*-values > 0.05 are presumed indistinguishable from noise and thus labelled as not applicable, "n/a"). Table headings are: estimate (regression coefficient), *p*-value (associated *p*-value for the estimate), relative ranking (importance of predictor variable or interaction effect).

	Estimate	*p*-value	Relative ranking
LK_d(Pu)	−0.71	9.2×10^{-11}	1 (main effect)
LK_d(U)	−0.31	0.042	2 (main effect)
LK_d(Th)	-1.7×10^{-5}	1.00	n/a
LK_d(Pu:U)	−0.12	0.038	1 (interaction)
LK_d(Pu:Th)	-4.7×10^{-6}	1.00	n/a
LK_d(U:Th)	-4.3×10^{-6}	1.00	n/a

The response surface calculated using the regression coefficients given in Table 4-3 is visualised in Figure 4-7 and shows the impact of varied K_d for Pu and U on the peak total flux (main effects). The response is plotted in terms of total flux deviation relative to the base case K_d parameterisation (central node of the plot). The interaction term for simultaneous K_d variation of Pu and U can be understood as flexure (twisting) of the otherwise flat response surface. It can be seen from the 3D plot that variation of K_d for U has a much-reduced impact on the peak flux when the K_d for Pu is low. This is because the peak flux is dominated by the Pu-240 breakthrough peak when K_d for Pu is low and U-236 only contributes in a minor way to the total flux. When the K_d for Pu is high, however, the total flux is dominated by the U-236 peak breakthrough and K_d for U is then relatively more important. In this context it can be understood that the interaction between the K_d for Pu and U in the regression relates to which radionuclide dominates the peak flux and the relative contribution of each radionuclide rather than a mechanistic interaction relating to ingrowth.

The total fluxes estimated in the NuDec-Farf31 simulations are shown as circular markers with stems indicating deviation from the calculated response surface estimated by linear regression. The locations of the circular markers correspond to the discrete K_d levels used in the experimental design (i.e., a 2D slice through the multidimensional parameter space of predictor variables). In some regions of the plot, the simplified response surface significantly overpredicts the impact of altered K_d on the total peak flux as calculated by NuDec-Farf31. The simplified representation of the data as a linear response surface should be interpreted as an approximate qualitative means to aid understanding rather than a proper mechanistic account of parameter dependencies.

The deviation of the response surface from the simulated data at high K_d values for Pu seems to be related to the low first order impact of K_d on U-236 breakthrough (cf Figure 4-1) due to the long half-life of U-236 relative to the retarded transport time. The half-life of Pu-240, on the other hand, is roughly in parity with the retarded travel time for the base case K_d which implies a greater sensitivity for Pu K_d. This explains why the K_d for Pu is clearly a much stronger predictor variable than the K_d for U as might be interpreted from the p-value obtained in the regression.

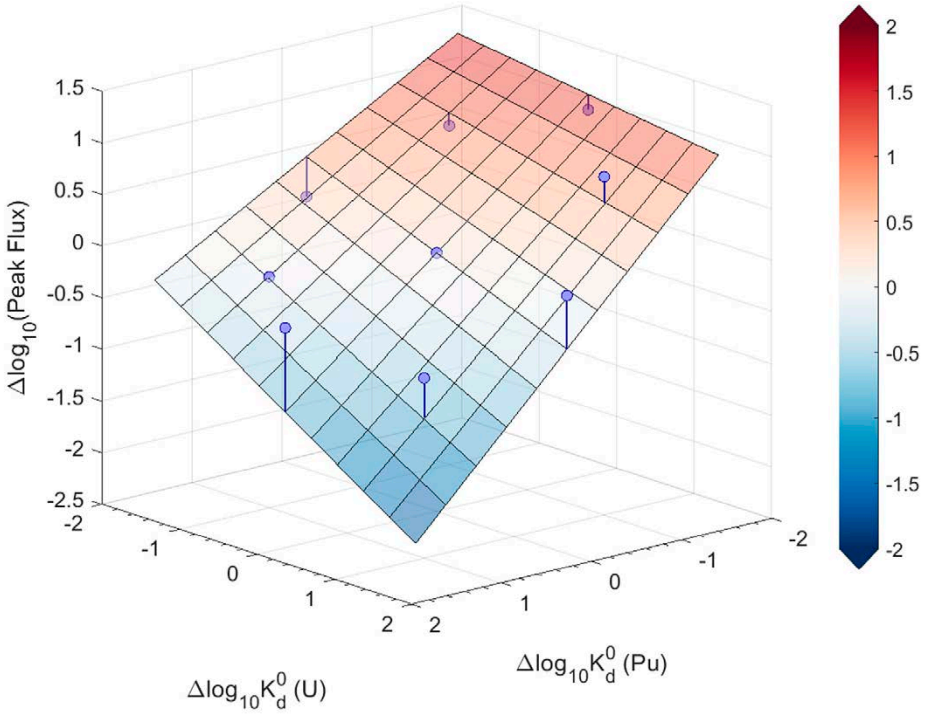

Figure 4-7. *Regression model response surface for peak far-field radiotoxicity flux (μSv/y) calculated for the 4n decay chain and a canister failure time of 100 ky (log_{10}-transformed data). Plotted circular markers with stems indicate deviations of the response surface from transport calculations. The activity flux to radiotoxicity conversion assumes the basic LDF factors taken from Table 2-4.*

Although the simplified response surface calculated using linear regression is useful for identifying the most important main effects and interactions amongst the different elements represented amongst the chain radionuclides, there are sufficient deviations from the simulated data that it is difficult to make definitive statements concerning interactions. Although more empirical in nature, it is possible to calculate an approximate response surface based on low order spline interpolation of the simulated data without specifying an underlying functional relationship. Such a surface is plotted in Figure 4-10 calculated using the *gridfit.m* function in Matlab (D'Errico 2006). The interpolated response surface is similar to that previously shown in Figure 4-7, although more precisely represents the simulation data within the circumscribed parameter space defined by the plotted data points (circular markers). Trends outside the circumscribed parameter space are not well constrained by the data so should not be considered to give an accurate account of the interaction between the two main predictor variables when considering extreme variations from the base case.

The far-field radiotoxicity flux associated with the 4*n* decay chain calculated with NuDec-Farf31 is shown in Figure 4-9 for the base case K_d parameterisation. Figure 4-10 and Figure 4-11, respectively show the impact of modifying the K_d value for Pu by decreasing or increasing it by a factor of 10. Of the 15 simulations comprising the experimental design, the cases with decreased K_d for Pu gave the highest total radiotoxicity flux from this decay chain dominated by the breakthrough of the Pu-240 peak. There was an interaction effect for simultaneous variation in K_d for Pu and U, although the impact is much smaller than the first order impact of reduced K_d for Pu. The K_d for Th has essentially no impact on the transported radiotoxicity for this decay chain. The lowest total radiotoxicity flux is associated with an increased K_d for Pu with the K_d for U either unaltered or decreased.

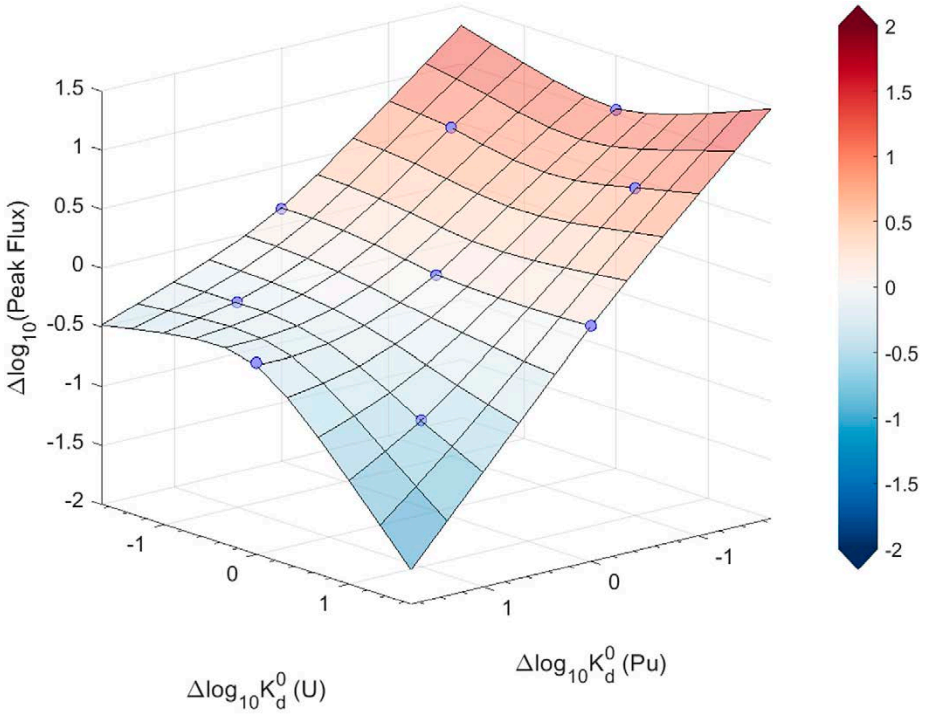

Figure 4-8. *Interpolated response surface for peak far-field radiotoxicity flux (µSv/y) calculated for the 4n decay chain and a canister failure time of 100 ky (log_{10}-transformed data). Plotted circular markers with stems indicate deviations of the response surface from transport calculations. The activity flux to radiotoxicity conversion assumes the basic LDF factors taken from Table 2-4.*

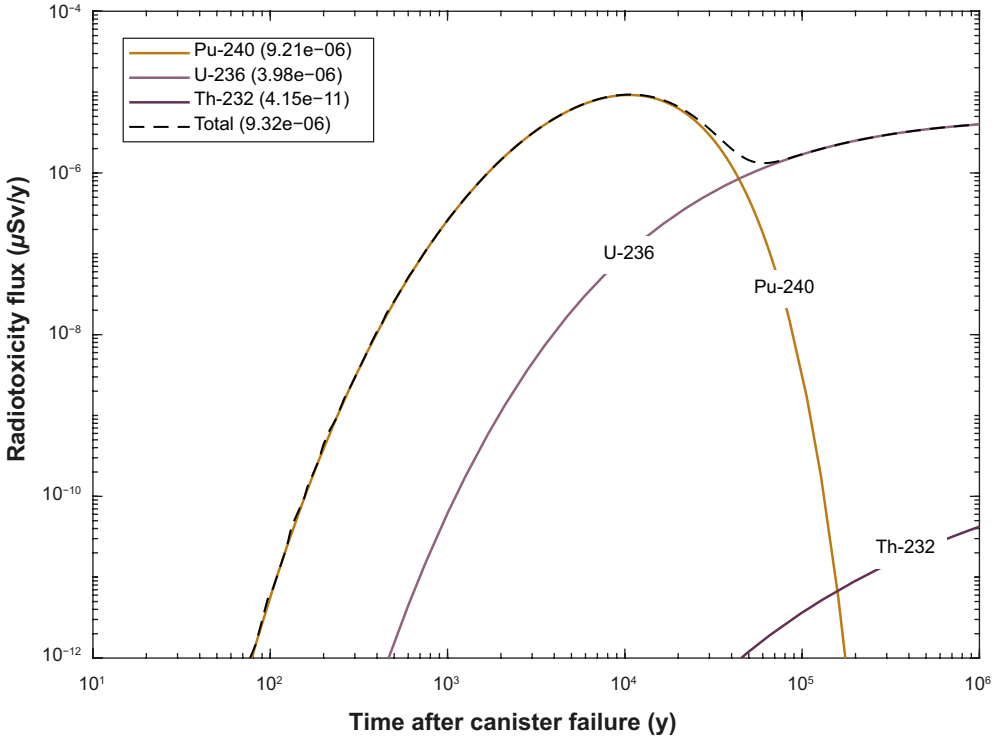

Figure 4-9. *Far-field radiotoxicity flux (µSv/y) calculated for the 4n decay chain assuming base case K_d values and a canister failure time of 100 ky. The legend is sorted sequentially in decay order with peak near-field radiotoxicity flux (µSv/y) noted for the time frame of the safety assessment. The activity flux to radiotoxicity conversion assumes the basic LDF factors taken from Table 2-4.*

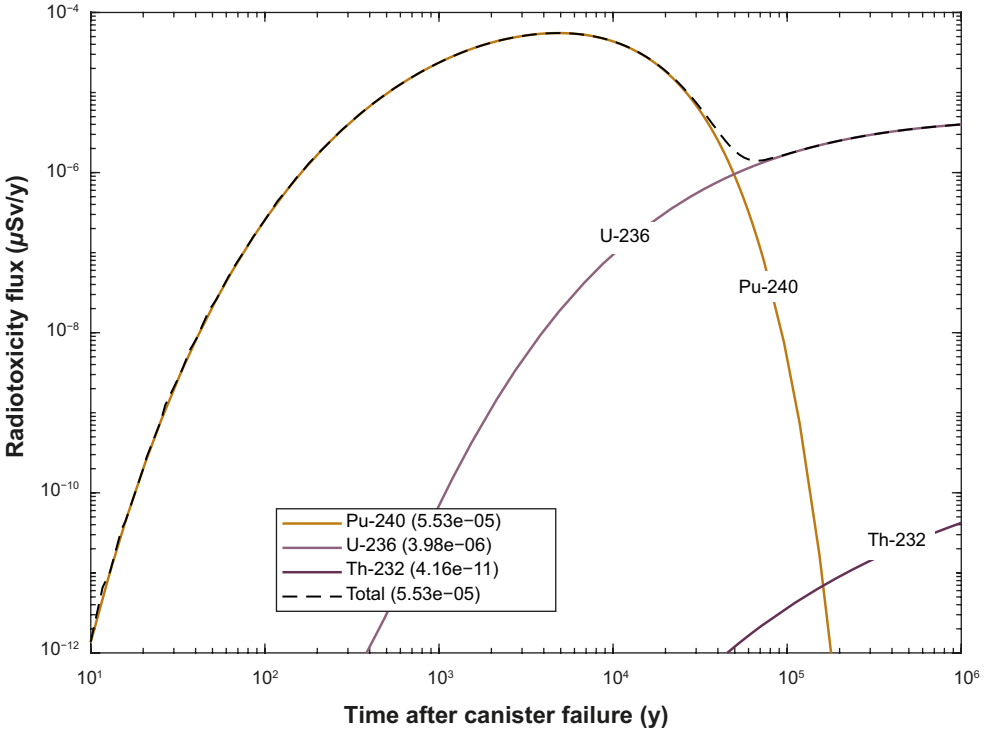

Figure 4-10. *Far-field radiotoxicity flux (μSv/y) calculated for the 4n decay chain where the K_d for Pu has been reduced by a factor of 10 (all other K_d values held constant at their base case values) and a canister failure time of 100 ky. The legend is sorted sequentially in decay order with peak near-field radiotoxicity flux (μSv/y) noted for the time frame of the safety assessment. The activity flux to radiotoxicity conversion assumes the basic LDF factors taken from Table 2-4.*

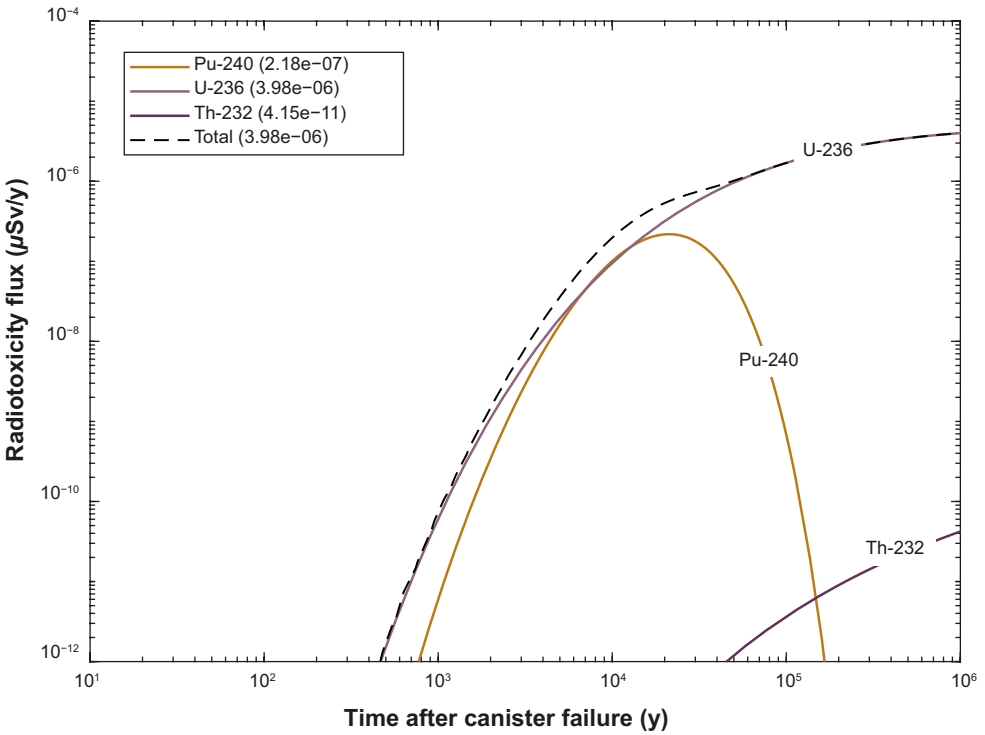

Figure 4-11. *Far-field radiotoxicity flux (μSv/y) calculated for the 4n decay chain where the K_d for Pu has been increased by a factor of 10 (all other K_d values held constant at their base case values) and a canister failure time of 100 ky. The legend is sorted sequentially in decay order with peak near-field radiotoxicity flux (μSv/y) noted for the time frame of the safety assessment. The activity flux to radiotoxicity conversion assumes the basic LDF factors taken from Table 2-4.*

The sorption strength of Pu-240 has a small but relatively insignificant impact on U-236 breakthrough by ingrowth which seems largely due to the fact that Pu-240 has a strongly decaying boundary condition flux due to its relatively short half-life, whereas that of the longer-lived U-236 is relatively constant with time. The contribution of the Pu-240 decay to the flux of U-236 therefore diminishes strongly with increasing time. The apparent interaction between K_d for Pu-240 and U-236 appears to be related to the relative peak height of the two radionuclides and consequently, which nuclide achieves the status as dominant contributor to total flux rather than a function of ingrowth.

Since the U-236 breakthrough has not yet reached steady-state after 1 My, a change in K_d has a slightly larger impact on the peak flux than it would if the breakthrough had reached a steady-state condition. This effect is largely due to the delay of the onset of U-236 steady state. The half-life of U-236, however, is sufficiently long that varying the K_d value by a factor of 10 up and down from the base case value results in only a small net change in the steady-state breakthrough flux relative to the base case.

Clearly, the peak flux due to this decay chain for a canister failure time of 100 ky is sufficiently low that it could, in principle, be neglected for the purposes of safety assessment on account of its negligible contribution towards far-field transported radiotoxicity flux. For the earlier canister failure times, however, this decay chain could potentially contribute significant amounts of far-field radiotoxicity on account of the short half-life of Pu-240 (6.56 ky). For canister failure at 10 ky, for example, the peak flux of Pu-240 is nearly 14 000 times higher than at 100 ky as shown in Figure 4-12.

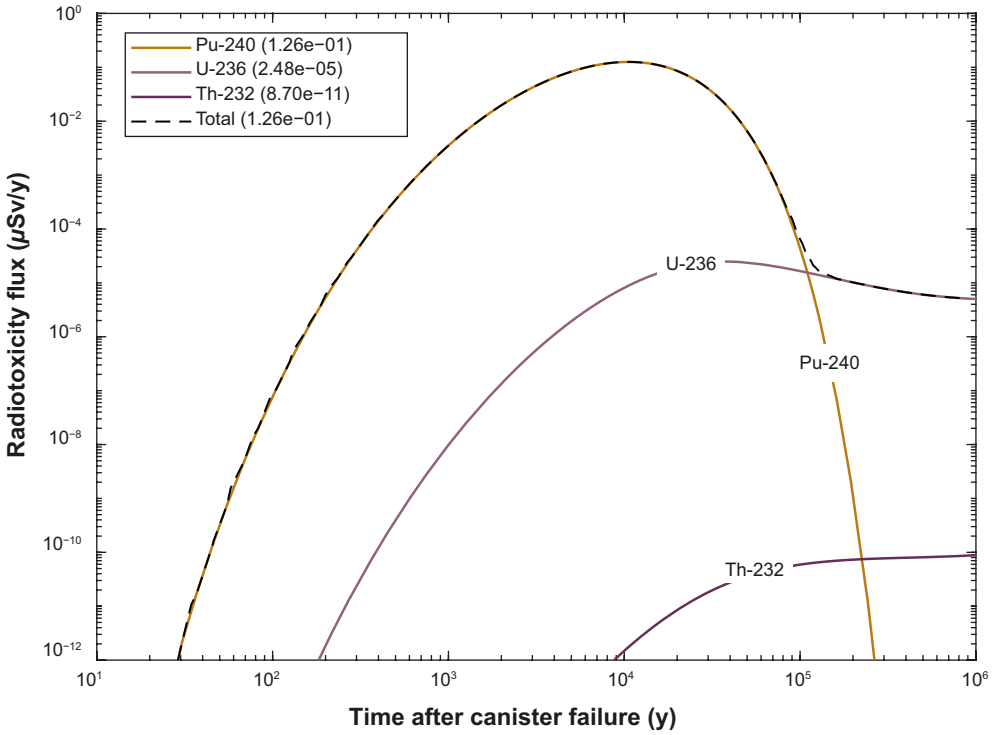

Figure 4-12. *Far-field radiotoxicity flux (μSv/y) calculated for the 4n decay chain assuming base case K_d values and a canister failure time of 10 ky. The legend is sorted sequentially in decay order with peak near-field radiotoxicity flux (μSv/y) noted for the time frame of the safety assessment. The activity flux to radiotoxicity conversion assumes the basic LDF factors taken from Table 2-4.*

4.3.2 Neptunium series (4*n* + 1) decay chain

In SR-Site and PSAR, the neptunium series (4*n* + 1) decay chain was simplified to the 5 radionuclides indicated in blue text in Figure 4-13. As previously, radionuclides highlighted in red are modelled implicitly assuming secular equilibrium with the parent, while green signifies a stable isotope decay chain terminator.

The regression analysis shown in Table 4-4 indicates an overwhelming dominance of Np on total radiotoxicity breakthrough both as a first-order effect and total effect. This is clearly related to the boundary condition which is also dominated by Np-237, the short-lived chain members Cm-245 and Am-245 having decayed to relative insignificance by the time of canister failure at 100 ky. The far-field radiotoxicity flux associated with the 4*n* + 1 decay chain is shown in Figure 4-16 for the base case parameterisation. Figure 4-17 and Figure 4-18, respectively show the impact of modifying the K_d value for Np by decreasing or increasing it by a factor of 10.

This chain is also an interesting example of an increased K_d for a progenitor radionuclide leading to increased flux of associated descendant radionuclides; in this case U-233 and Th-229. While increasing the K_d for Np increases the radiotoxicity flux attributable to descendant radionuclides, it is not enough (for the range of K_d variation studied) to outweigh the direct effect of reducing the total radiotoxicity flux which is dominated by Np-237. In all plots, the breakthrough of Cm-245 is obscured behind that of Am-241 since they are in approximate secular equilibrium. Simultaneously reduced K_d for Np and Th and increased K_d for U is a common feature for the top 6 ranked simulations (out of 27 case studies) regarding total radiotoxicity flux. Conversely, the lowest radiotoxicity flux was associated with increased K_d for Np with K_d values for other chain members held constant or decreased.

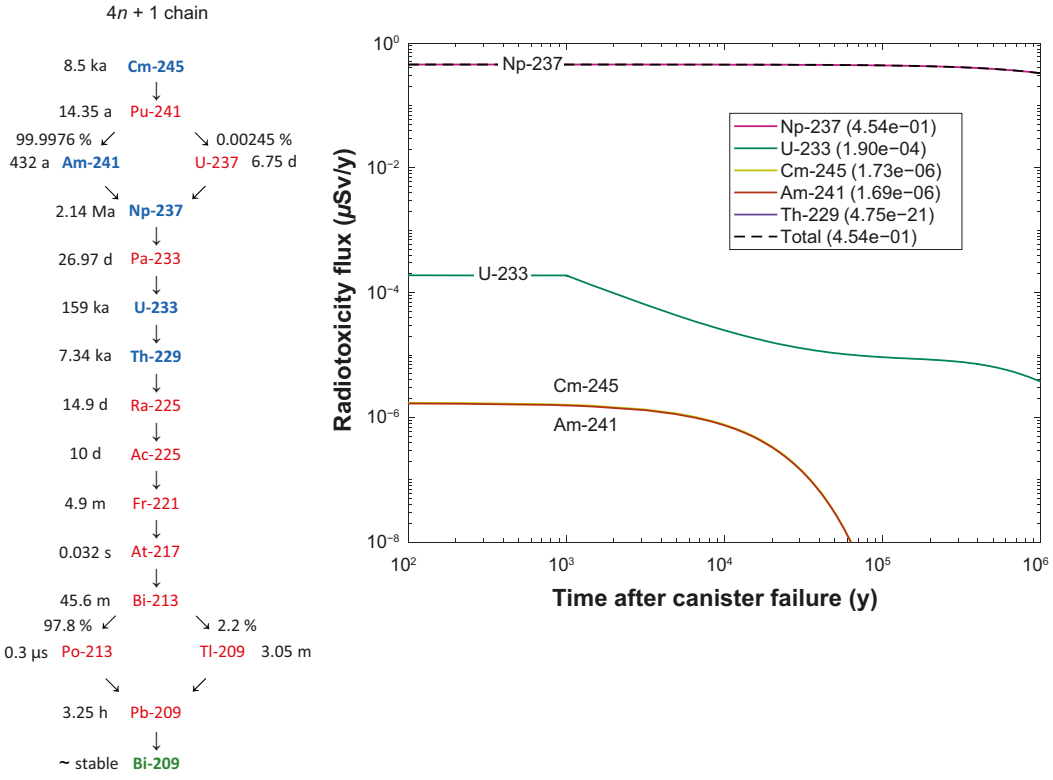

Figure 4-13. *Simplifications to the neptunium (4n + 1) decay chain (left – see text for details) and the near-field boundary condition (calculated by COMP23) for canister failure at 100 ky (right). The legend is sorted sequentially in decay order with peak near-field radiotoxicity flux (µSv/y) noted for the time frame of the safety assessment assuming basic LDF factors taken from Table 2-4.*

Table 4-4. Results of regression analysis based on results from the response surface factorial design (27 simulated parameter combinations for 5 predictor variables). The relative importance of individual radioelements for the peak total radiotoxicity flux can be inferred from the *p*-values in increasing order (smaller p-values imply stronger effects; *p*-values > 0.05 are presumed indistinguishable from noise and thus labelled as not applicable, "n/a"). Table headings are: estimate (regression coefficient), *p*-value (associated *p*-value for the estimate), relative ranking (importance of predictor variable or interaction effect).

	Estimate	*p*-value	Relative ranking
LK_d(Cm)	−0.11	0.99	n/a
LK_d(Am)	−0.11	0.99	n/a
LK_d(Np)	−0.23	5.4×10^{-9}	1 (main effect)
LK_d(U)	−0.017	0.21	n/a
LK_d(Th)	−0.28	4.0×10^{-5}	2 (main effect)
LK_d(Cm:Am)	−0.061	7.7×10^{-3}	3 (interaction)
LK_d(Cm:Np)	-3.6×10^{-4}	0.99	n/a
LK_d(Cm:U)	1.3×10^{-4}	0.99	n/a
LK_d(Cm:Th)	-2.6×10^{-4}	0.99	n/a
LK_d(Am:Np)	-3.8×10^{-4}	0.99	n/a
LK_d(Am:U)	-2.8×10^{-4}	1.00	n/a
LK_d(Am:Th)	1.2×10^{-4}	1.00	n/a
LK_d(Np:U)	0.033	0.12	n/a
LK_d(Np:Th)	−0.087	3.5×10^{-4}	1 (interaction)
LK_d(U:Th)	−0.063	5.7×10^{-3}	2 (interaction)

The response surface calculated using the regression coefficients given in Table 4-4 is visualised in Figure 4-14 and shows the impact of varied K_d for Np and Th on the total flux (main effects). The response is plotted in terms of total flux deviation relative to the base case K_d parameterisation (central node of the plot). The interaction term for K_d variation of Np and Th can be understood as flexure (twisting) of the otherwise flat response surface. As previously, the total fluxes estimated in the NuDec-Farf31 simulations are shown as circular markers with stems indicating deviation from the calculated response surface estimated by linear regression. The locations of the circular markers correspond to the discrete K_d levels used in the experimental design (i.e., a 2D slice through the multidimensional parameter space of predictor variables).

The response surface is more complicated to interpret in this case if one additionally considers deviation from the NuDec-Farf31 simulated data (circular markers). This seems to be at least partly related to the overwhelmingly dominant Np-237 breakthrough peak that is only weakly augmented by ingrowth of Th-229 while the K_d for U appears to have an impact that indistinguishable against the high breakthrough of Np-237. The interaction between Np and Th K_d appears to be ingrowth related, although the overall effect is weak. This decay chain is very strongly dominated by the near-field boundary condition where Np-237 release is at least three orders of magnitude higher than that for U-233. If the solubility limit for U in the near field was to be relaxed it is possible that U would have a prominent role to play, although this was beyond the scope of the present work. In the current simulations, the peak associated with Np-237 breakthrough is the dominant contributor for most parameter combinations, although there are a small number of cases with simultaneously high K_d for Np and low K_d for Th where Th-229 is a slightly larger dose contributor.

As previously, there are sufficient deviations from the simulated data that it is difficult to make definitive statements concerning interactions based on the simplified response surface calculated using the regression model. An empirical, low order spline interpolation of the simulated data is plotted in Figure 4-15 calculated using the *gridfit.m* function in Matlab (D'Errico 2006). The interpolated response surface is similar to that previously shown in Figure 4-14, although more precisely represents the simulation data within the circumscribed parameter space defined by the plotted data points (circular markers). Trends outside the circumscribed parameter space are not well constrained by the data so should not be considered to give an accurate account of the interaction between the two main predictor variables when considering extreme variations from the base case.

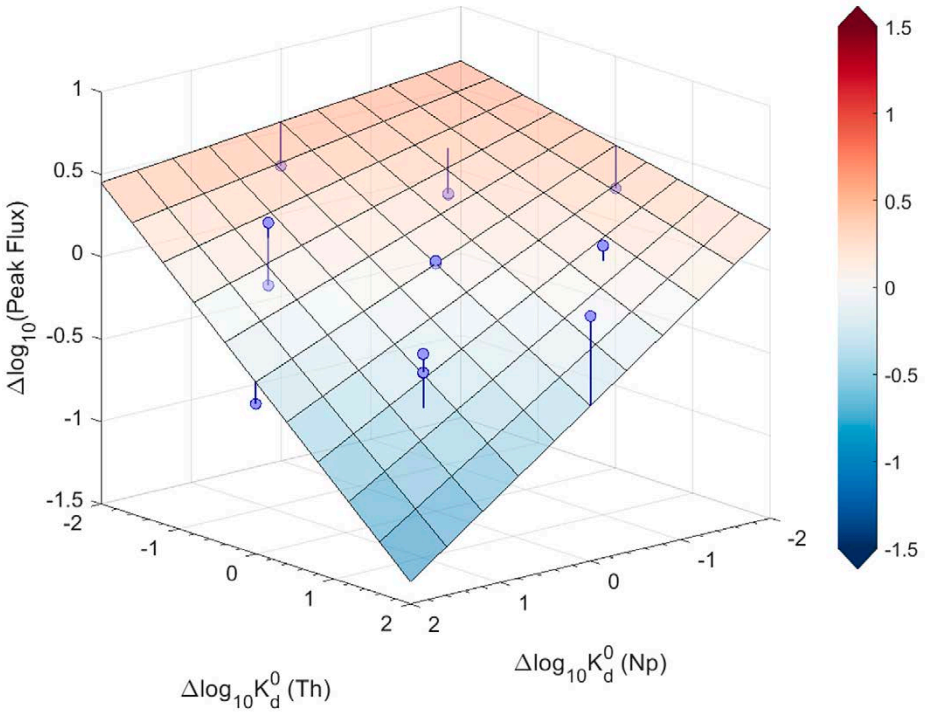

Figure 4-14. *Regression model response surface for peak far-field radiotoxicity flux (µSv/y) calculated for the 4n + 1 decay chain and a canister failure time of 100 ky (log_{10}-transformed data). Plotted circular markers with stems indicate deviations of the response surface from transport calculations. The activity flux to radiotoxicity conversion assumes the basic LDF factors taken from Table 2-4.*

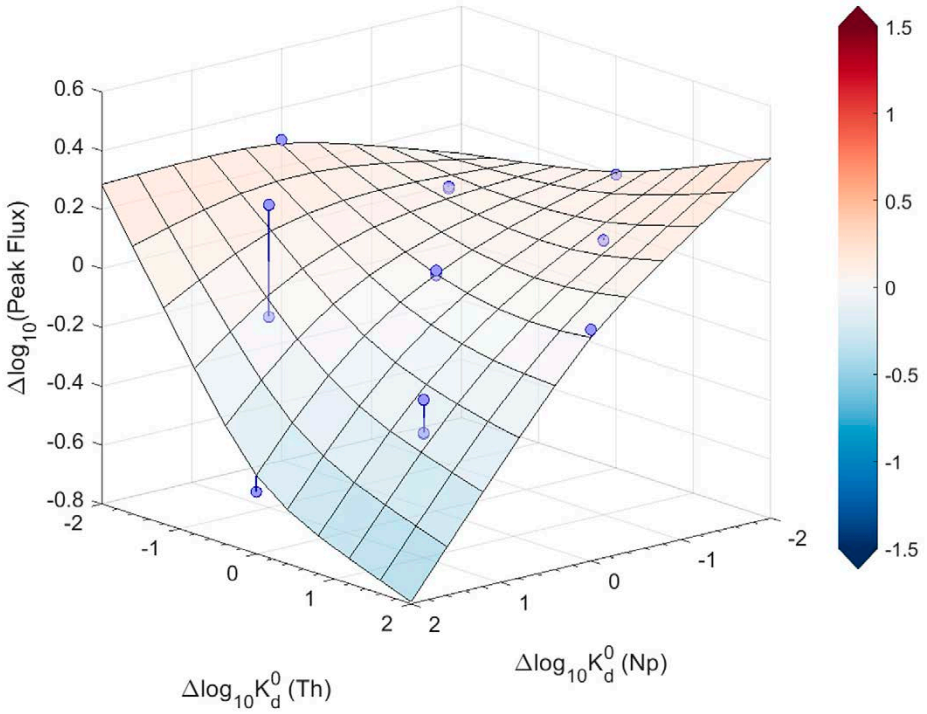

Figure 4-15. *Interpolated response surface for peak far-field radiotoxicity flux (µSv/y) calculated for the 4n + 1 decay chain and a canister failure time of 100 ky (log_{10}-transformed data). Plotted circular markers with stems indicate deviations of the response surface from transport calculations. The activity flux to radiotoxicity conversion assumes the basic LDF factors taken from Table 2-4.*

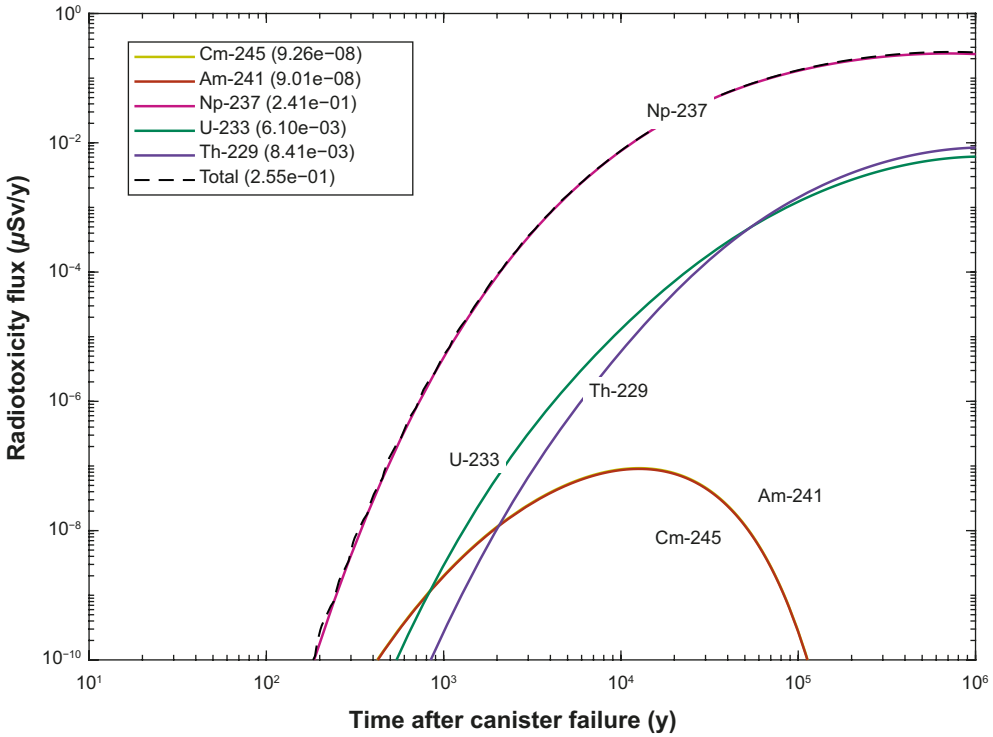

Figure 4-16. *Far-field radiotoxicity flux (μSv/y) calculated for the neptunium series (4n + 1) decay chain assuming base case K_d values and a canister failure time of 100 ky. The legend is sorted sequentially in decay order with peak near-field radiotoxicity flux (μSv/y) noted for the time frame of the safety assessment. The activity flux to radiotoxicity conversion assumes the basic LDF factors taken from Table 2-4.*

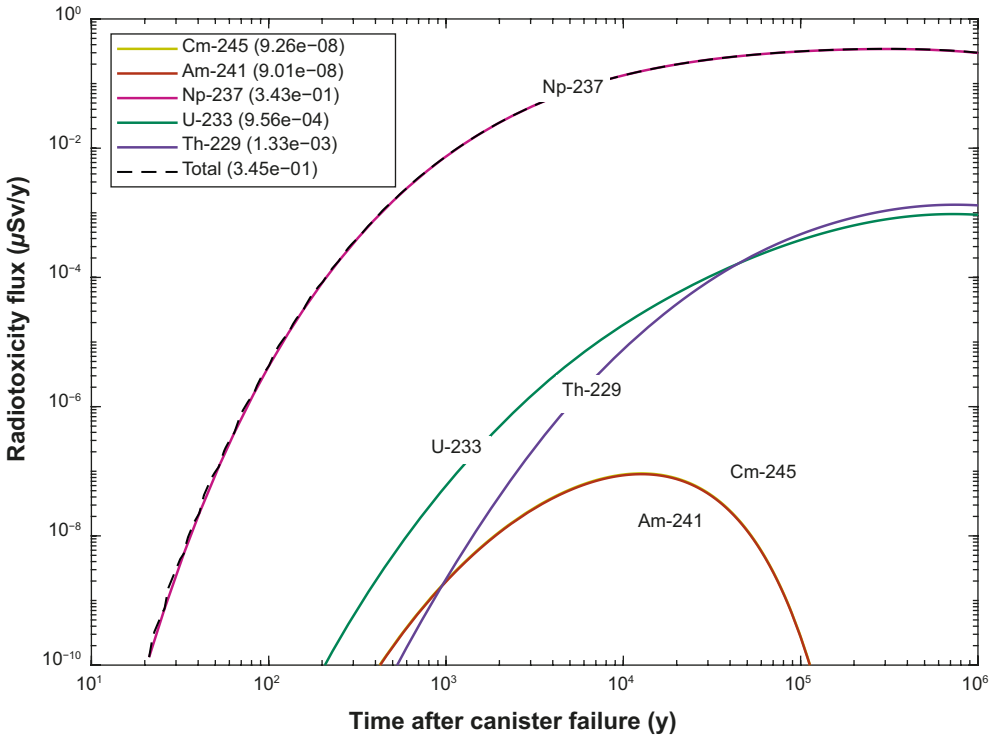

Figure 4-17. *Far-field radiotoxicity flux (μSv/y) calculated for the 4n + 1 decay chain where the K_d for Np has been reduced by a factor of 10 (all other K_d values held constant at their base case values) and a canister failure time of 100 ky. The legend is sorted sequentially in decay order with peak near-field radiotoxicity flux (μSv/y) noted for the time frame of the safety assessment. The activity flux to radiotoxicity conversion assumes the basic LDF factors taken from Table 2-4.*

The deviation of the interpolated surface for the combination of high K_d for Np and low K_d for Th in Figure 4-15 might be related to the increased relative flux contribution of U-233 (see also Figure 4-18) in this situation as well as its subsequent impact on Th-229 ingrowth. Here, a higher K_d for U gives a lower contribution of U-233 although higher Th-229 flux directly related to ingrowth. This seems to give some variability in the peak flux dependent on the K_d for U although only locally. It is interesting to note that the p-value of the regression coefficient for the U and Th interaction implies a statistically significant interaction in the regression model although seemingly subordinate to the Np and Th interaction.

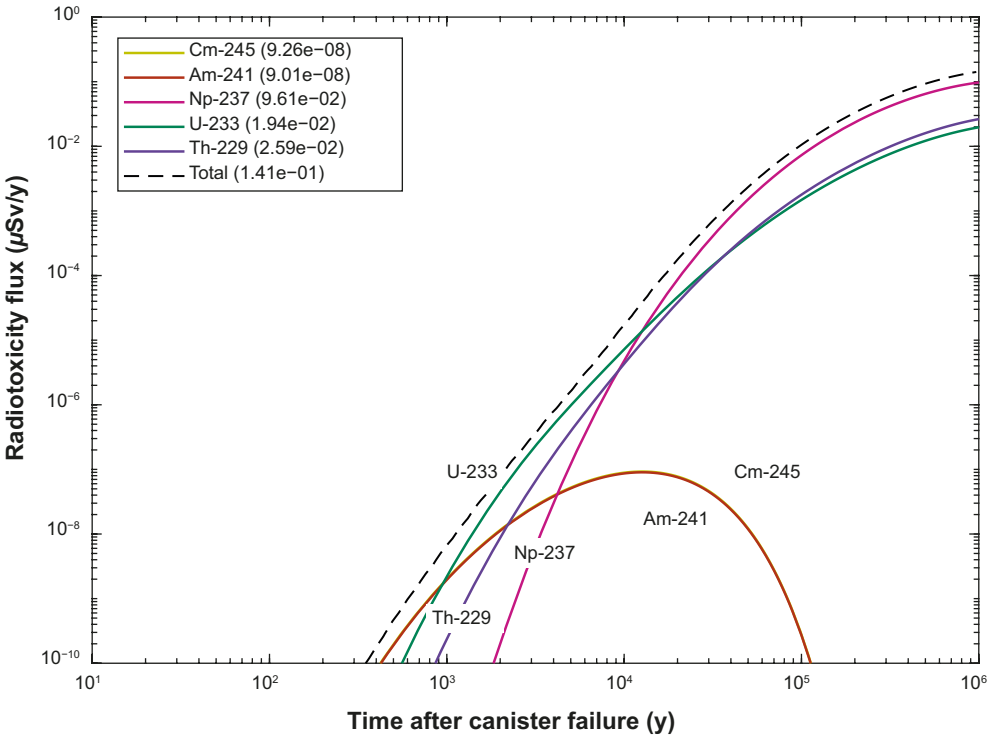

Figure 4-18. *Far-field radiotoxicity flux (μSv/y) calculated for the 4n + 1 decay chain where the K_d for Np has been increased by a factor of 10 (all other K_d values held constant at their base case values). The legend is sorted sequentially in decay order with peak near-field radiotoxicity flux (μSv/y) noted for the time frame of the safety assessment. The activity flux to radiotoxicity conversion assumes the basic LDF factors taken from Table 2-4.*

For very short canister failure times, the total radiotoxicity flux is slightly higher, although since the long-lived Np-237 nuclide (2.15 My) is such an overwhelmingly dominant contributor, the difference for 10 ky canister failure time is marginal. At shorter canister failure times, however, Cm-245 and Am-241 become more prominent contributors to the total particularly for early breakthrough.

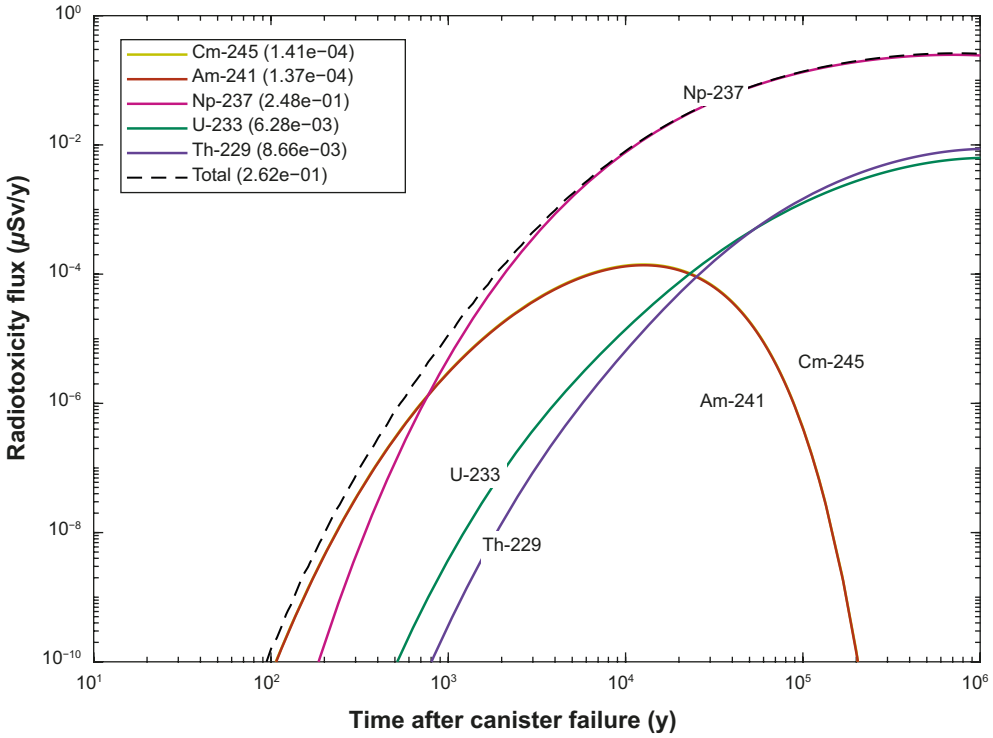

Figure 4-19. *Far-field radiotoxicity flux (μSv/y) calculated for the 4n + 1 decay chain assuming base case K_d values and a canister failure time of 10 ky. The legend is sorted sequentially in decay order with peak near-field radiotoxicity flux (μSv/y) noted for the time frame of the safety assessment. The activity flux to radiotoxicity conversion assumes the basic LDF factors taken from Table 2-4.*

4.3.3 Radium series (4*n* + 2) decay chain

The simplified 4*n* + 2 decay chain in SR-Site and PSAR was comprised of the 8 radionuclides indicated by blue text in Figure 4-20. Since the FARF31 code could not handle converging decay chains, the molar inventories of Am-242m, Pu-238, Am-242, Cm-242, Np-238, and Pa-234m were added directly to that of U-234. As previously, the decay chain radionuclides highlighted in blue are explicitly modelled in transport calculations; black text signifies radionuclides that are part of the initial inventory, but where transport is neglected, and the molar inventory is simply added to the subsequent descendant; red signifies radionuclides implicitly modelled assuming secular equilibrium with the parent; green signifies a stable isotope decay chain terminator.

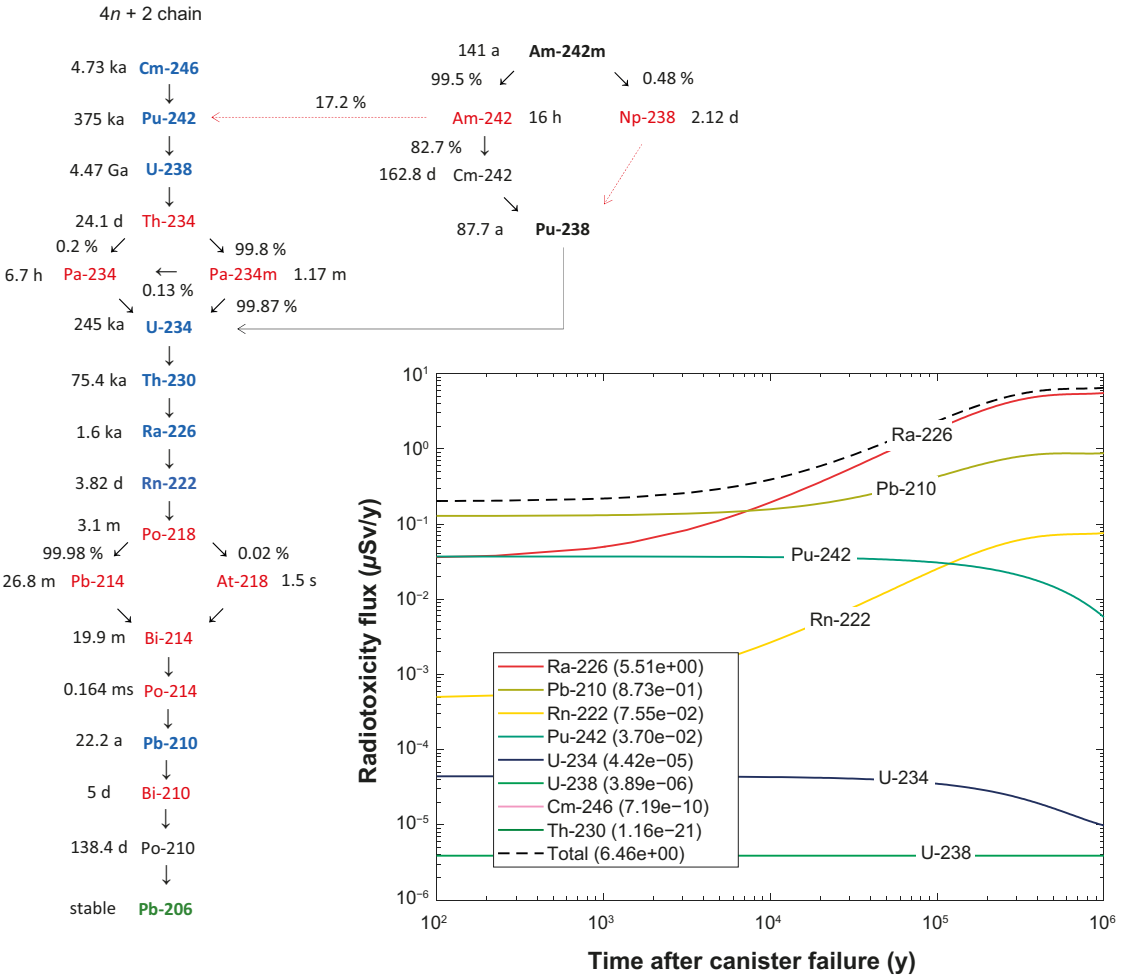

Figure 4-20. *Simplifications to the radium (4n + 2) decay chain (left – see text for details) and the near-field boundary condition (calculated by COMP23) for canister failure at 100 ky (right). The legend is sorted sequentially in decay order with peak near-field radiotoxicity flux (μSv/y) noted for the time frame of the safety assessment assuming basic LDF factors taken from Table 2-4.*

The results of the regression analysis are shown in Table 4-5. Radon (Rn-222) being a noble gas was omitted from the variation analysis and assumed to have a K_d of zero, although its contribution to total radiotoxicity flux was included in the calculations. Not unexpectedly, Pb-210 and Ra-226 are overwhelmingly dominant for this decay chain and the sorption status of chain members preceding Ra-226 has minimal effect on the transported radiotoxicity. The regression coefficients for Pb-210 and Ra-226 are both negative implying a reduction in peak radiotoxicity flux if the K_d for either radionuclide is increased.

Table 4-5. Results of regression analysis based on results from the response surface factorial design (45 simulated parameter combinations for 6 predictor variables). The relative importance of individual radioelements for the peak total radiotoxicity flux can be inferred from the *p*-values in increasing order (smaller p-values imply stronger effects; *p*-values > 0.05 are presumed indistinguishable from noise and thus labelled as not applicable, "n/a"). Table headings are: estimate (regression coefficient), *p*-value (associated *p*-value for the estimate), relative ranking (importance of predictor variable or interaction effect).

	Estimate	*p*-value	Relative ranking
LK_d(Cm)	3.10×10^{-4}	1.00	n/a
LK_d(Pu)	-7.39×10^{-4}	1.00	n/a
LK_d(U)	6.28×10^{-5}	1.00	n/a
LK_d(Th)	-2.41×10^{-5}	1.00	n/a
LK_d(Ra)	-2.66×10^{-1}	9.9×10^{-4}	2 (main effect)
LK_d(Pb)	-5.23×10^{-1}	6.7×10^{-6}	1 (main effect)
LK_d(Cm:Pu)	-5.24×10^{-5}	1.00	n/a
LK_d(Cm:U)	8.83×10^{-5}	1.00	n/a
LK_d(Cm:Th)	7.56×10^{-5}	1.00	n/a
LK_d(Cm:Ra)	3.23×10^{-6}	1.00	n/a
LK_d(Cm:Pb)	1.99×10^{-5}	1.00	n/a
LK_d(Pu:U)	-1.80×10^{-4}	1.00	n/a
LK_d(Pu:Th)	-1.54×10^{-4}	1.00	n/a
LK_d(Pu:Ra)	-3.15×10^{-5}	1.00	n/a
LK_d(Pu:Pb)	-5.38×10^{-5}	1.00	n/a
LK_d(U:Th)	4.65×10^{-5}	1.00	n/a
LK_d(U:Ra)	-5.92×10^{-6}	1.00	n/a
LK_d(U:Pb)	3.17×10^{-5}	1.00	n/a
LK_d(Th:Ra)	9.38×10^{-6}	1.00	n/a
LK_d(Th:Pb)	4.86×10^{-6}	1.00	n/a
LK_d(Ra:Pb)	-1.06×10^{-1}	1.8×10^{-3}	1 (interaction)

The response surface calculated using the regression coefficients given in Table 4-5 is visualised in Figure 4-21 and shows the impact of varied K_d for Ra and Pb on the total flux (main effects). The response is plotted in terms of total flux deviation relative to the base case K_d parameterisation (central node of the plot). The interaction term for K_d variation of Ra and Pb can be understood as flexure (twisting) of the otherwise flat response surface. As previously, the total fluxes estimated in the NuDec-Farf31 simulations are shown as circular markers with stems indicating deviation from the calculated response surface estimated by linear regression. The locations of the circular markers correspond to the discrete K_d levels used in the experimental design (i.e., a 2D slice through the multidimensional parameter space of predictor variables).

Although the regression response surface plotted in Figure 4-21 imperfectly matches the simulation data (note the deviations represented by the circular marker stems), it appears that the regression model nevertheless identifies the most important variables and interactions since there is virtually no spread of simulation data corresponding to the impact of the hidden variables (i.e., K_d values for Cm, Pu, U, Th). An empirical, low order spline interpolation of the simulated data is plotted in Figure 4-22 calculated using the *gridfit.m* function in Matlab (D'Errico 2006). The interpolated response surface is similar to that previously shown in Figure 4-21, although more precisely represents the simulation data within the circumscribed parameter space defined by the plotted data points (circular markers). Trends outside the circumscribed parameter space are not well constrained by the data so should not be considered to give an accurate account of the interaction between the two main predictor variables when considering extreme variations from the base case.

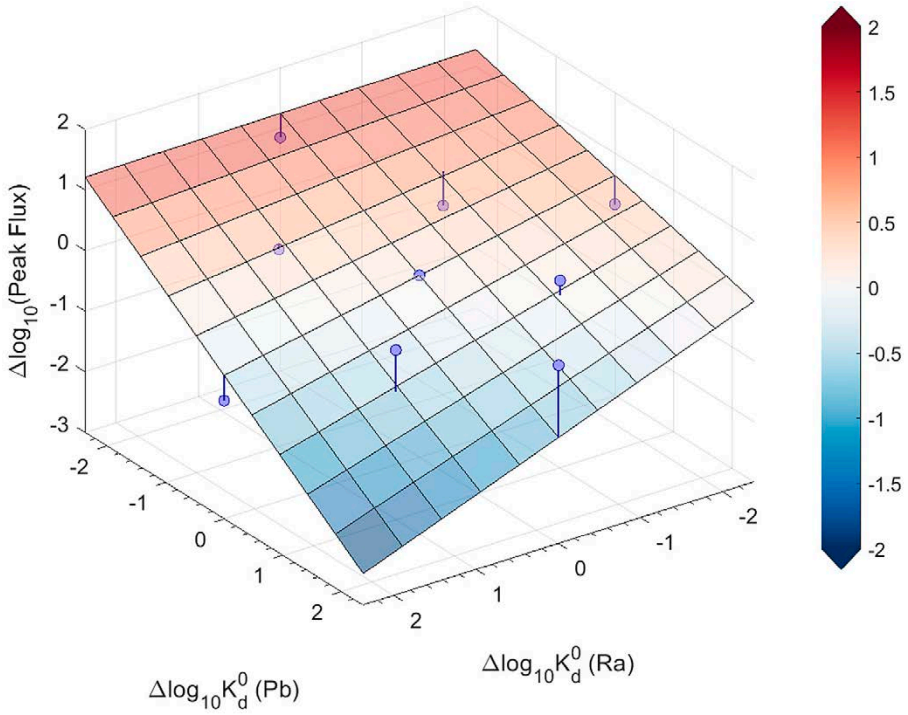

Figure 4-21. *Regression model response surface for peak far-field radiotoxicity flux (μSv/y) calculated for the 4n + 2 decay chain and a canister failure time of 100 ky (log_{10}-transformed data). Plotted circular markers with stems indicate deviations of the response surface from transport calculations. The activity flux to radiotoxicity conversion assumes the basic LDF factors taken from Table 2-4.*

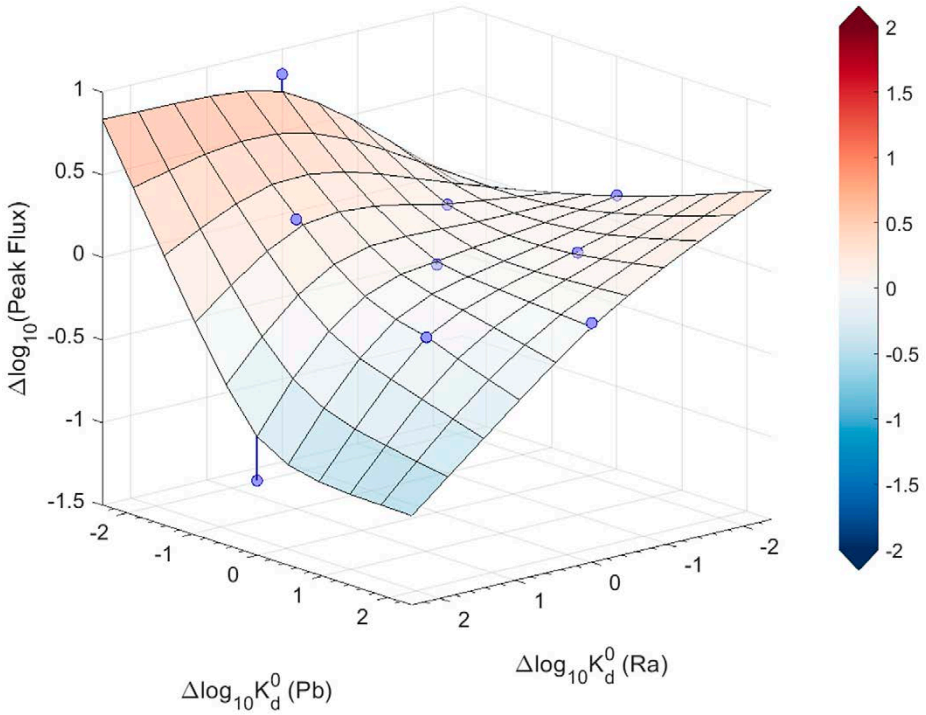

Figure 4-22. *Interpolated response surface for peak far-field radiotoxicity flux (μSv/y) calculated for the 4n + 2 decay chain and a canister failure time of 100 ky (log_{10}-transformed data). Plotted circular markers with stems indicate deviations of the response surface from transport calculations. The activity flux to radiotoxicity conversion assumes the basic LDF factors taken from Table 2-4.*

As can be seen from Figure 4-23, the high source term flux of Ra-226 clearly dominates the far-field radiotoxicity flux and ingrowth of Ra-226 from the decay of parent radionuclides along migration path seems to have little impact on either the flux of Ra-226 or the total radiotoxicity flux. The K_d assigned to Pb-210 has a very strong impact on its breakthrough owing to the very short half-life (22.2 y) of this radionuclide. It is also relevant to note that the bulk of the Pb-210 flux exiting the far-field is primarily derived from decay of the Ra-226 parent which is why the shape of the Ra-226, Rn-222, and Pb-210 breakthrough curves track each other closely.

Since the flux of Ra-226 is almost entirely source term derived, there appears to be very little contribution of radionuclides prior to Ra-226 in the decay chain to the total radiotoxicity flux. The impact of decreasing or increasing the K_d of Pu-242 by a factor of 10 is shown in Figure 4-24 and Figure 4-25, respectively. Although decreasing the K_d of Pu-242 gives a minor increase in its contribution to the far-field radiotoxicity in the short to medium term after canister failure, it has very little impact on the peak radiotoxicity at long times which is still dominated by Ra-226 and ingrowth of Rn-222 and Pb-210. A common feature of the top 6 ranked simulations (out of 45 case studies) regarding total radiotoxicity flux is an increased K_d for Ra and reduced K_d for Pb with the other chain members having only a minor impact. Interestingly, the lowest radiotoxicity flux is also associated with an increased K_d for Ra, although with unaltered or increased K_d for Pb.

It can be noted that there are small differences of about ~1 % in the estimated peak fluxes for Ra-226, Rn-222, and Pb-210 in Figure 4-23 relative to Figure 3-1. In the previous calculation using base case K_d values shown in Figure 3-1, the maximum radiotoxicity fluxes annotated in the legend were taken directly from the time series calculated for each radionuclide. Since the breakthrough for Ra-226, Rn-222, and Pb-210 are still increasing at the end of the 1 My timeframe of the safety assessment, the flux at the closest time point immediately prior to 1 My is taken to be approximately equal to the maximum value. For each of these radionuclides, the final timepoint varies in the interval 0.94 – 0.96 My so the values are slightly less than what they would be if interpolated to exactly 1 My. In Figure 4-23, however, the maximum value annotated in the legend is calculated at 1 My by interpolation within a common timeseries since this enables a more accurate estimate of the total radiotoxicity flux attributable to this decay chain.

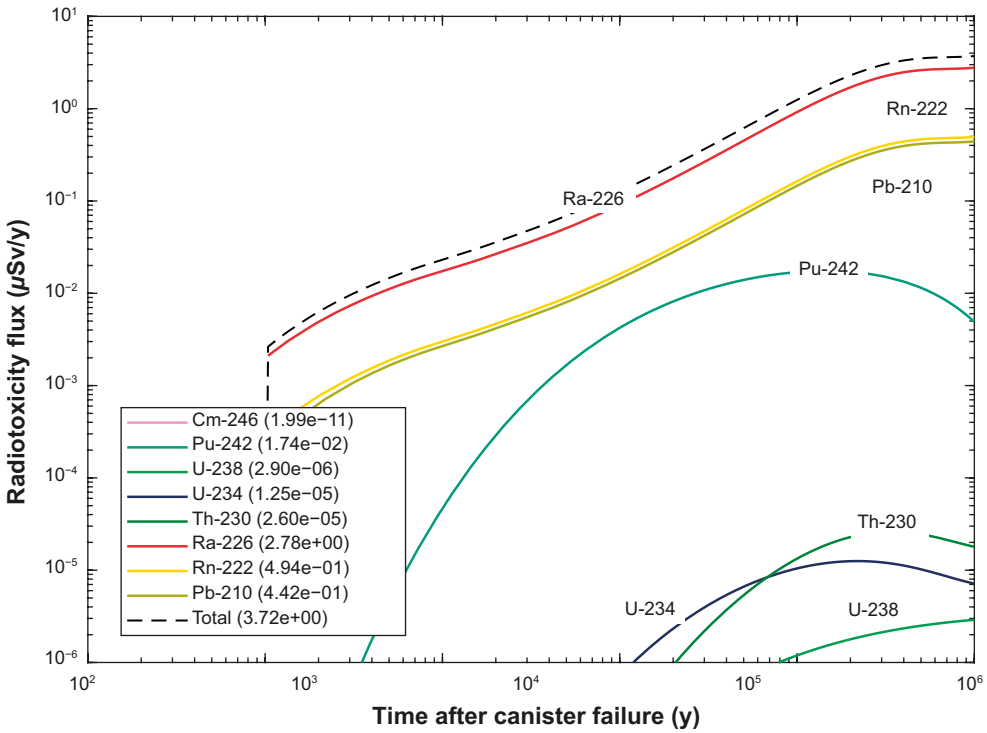

Figure 4-23. *Far-field radiotoxicity flux (μSv/y) calculated for the radium series (4n + 2) decay chain assuming base case K_d values and a canister failure time of 100 ky. The legend is sorted sequentially in decay order with peak near-field radiotoxicity flux (μSv/y) noted for the time frame of the safety assessment. The activity flux to radiotoxicity conversion assumes the basic LDF factors taken from Table 2-4.*

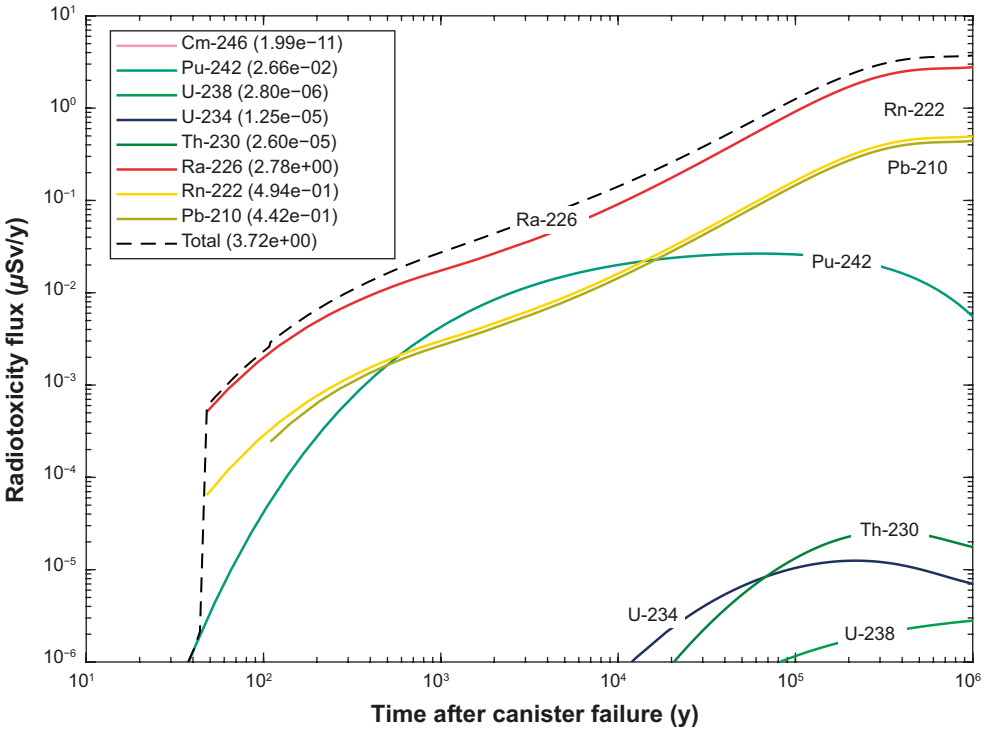

Figure 4-24. *Far-field radiotoxicity flux (μSv/y) calculated for the 4n + 2 decay chain where the K_d for Pu has been reduced by a factor of 10 (all other K_d values held constant at their base case values) and a canister failure time of 100 ky. The legend is sorted sequentially in decay order with peak near-field radiotoxicity flux (μSv/y) noted for the time frame of the safety assessment. The activity flux to radiotoxicity conversion assumes the basic LDF factors taken from Table 2-4.*

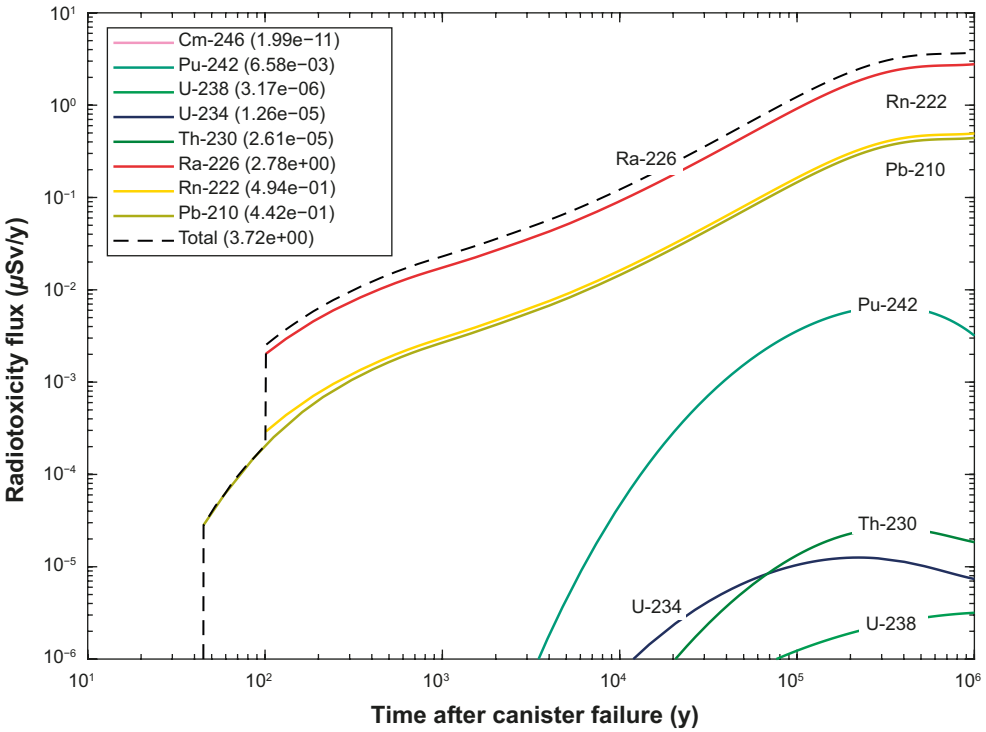

Figure 4-25. *Far-field radiotoxicity flux (μSv/y) calculated for the 4n + 2 decay chain where the K_d for Pu has been increased by a factor of 10 (all other K_d values held constant at their base case values) and a canister failure time of 100 ky. The legend is sorted sequentially in decay order with peak near-field radiotoxicity flux (μSv/y) noted for the time frame of the safety assessment. The activity flux to radiotoxicity conversion assumes the basic LDF factors taken from Table 2-4.*

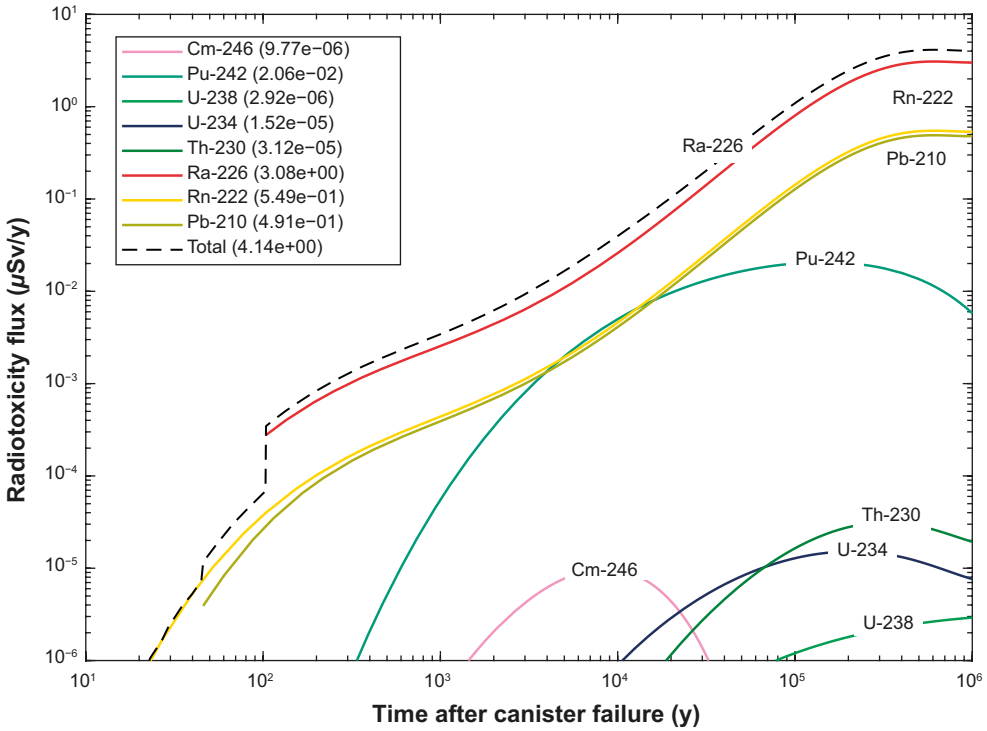

Figure 4-26. *Far-field radiotoxicity flux (μSv/y) calculated for the 4n + 2 decay chain assuming base case K_d values and a canister failure time of 10 ky. The legend is sorted sequentially in decay order with peak near-field radiotoxicity flux (μSv/y) noted for the time frame of the safety assessment. The activity flux to radiotoxicity conversion assumes the basic LDF factors taken from Table 2-4.*

For very short canister failure times, the total radiotoxicity flux is slightly higher than the 100 ky reference case, although still dominated by the Ra-226 source term and ingrowth of Rn-222 and Pb-210 along the migration path. The flux of Pu-242 and Cm-246 is noticeably higher in this case, although this does not make a very large contribution to the total radiotoxicity flux.

4.3.4 Actinium series (4*n* + 3) decay chain

In SR-Site and PSAR, the actinium series (4*n* + 3) decay chain was simplified to the 5 radionuclides indicated in blue text in Figure 4-27. As previously, radionuclides highlighted in red are modelled implicitly assuming secular equilibrium with the parent, while green signifies a stable isotope decay chain terminator.

The results of the regression analysis for this chain is shown in Table 4-6 and indicates a primary role for Pu-239 and Ac-227 as main contributors to the far-field radiotoxicity flux. For the reference scenario with canister failure at 100 ky, the peak radiotoxicity flux occurs roughly 25 ky after canister failure. Pu-239 has a relatively short half-life (24.1 ky) however, and its influence declines at long times at which point Ac-227 dominates the far-field radiotoxicity flux. The far-field radiotoxicity flux is shown in Figure 4-30 for the base case K_d settings.

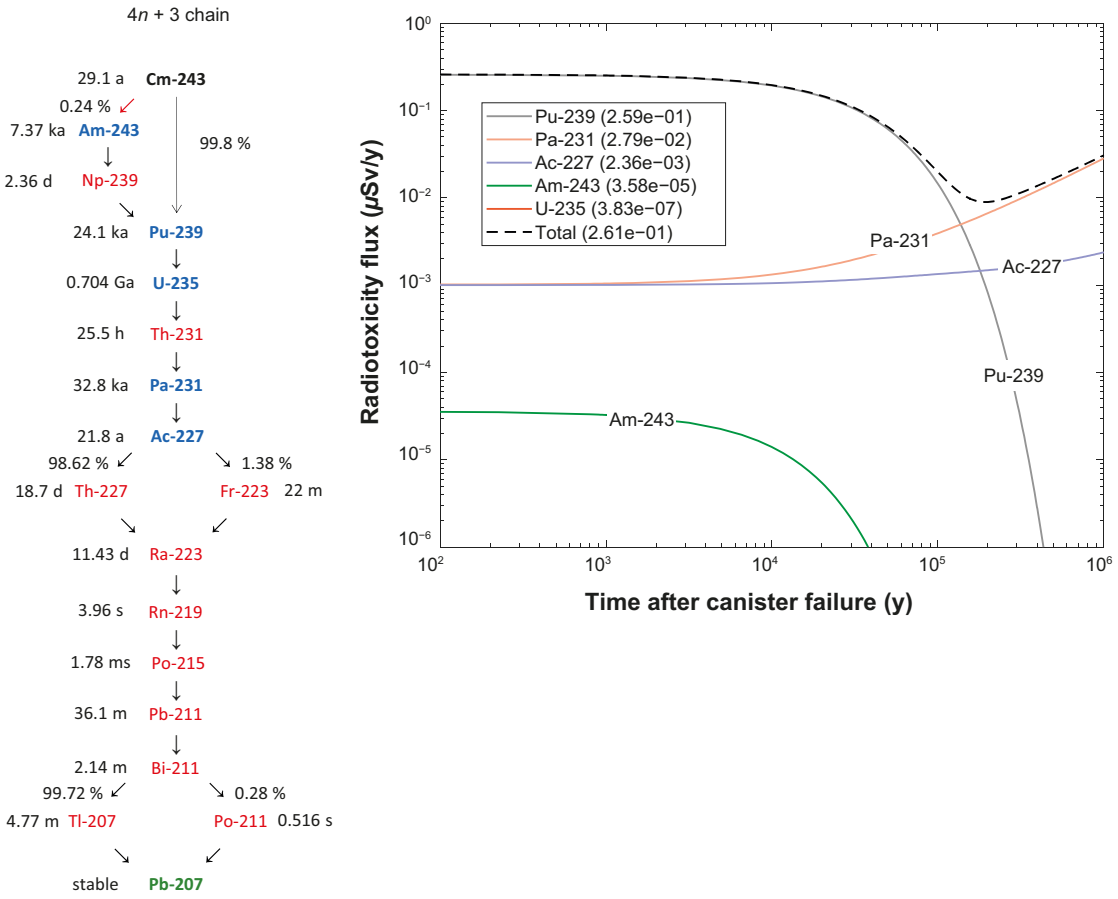

Figure 4-27. *Simplifications to the actinium (4n + 3) decay chain (left – see text for details) and the near-field boundary condition (calculated by COMP23) for canister failure at 100 ky (right). The legend is sorted sequentially in decay order with peak near-field radiotoxicity flux (μSv/y) noted for the time frame of the safety assessment assuming basic LDF factors taken from Table 2-4.*

Table 4-6. Results of regression analysis based on results from the response surface factorial design (27 simulated parameter combinations for 5 predictor variables). The relative importance of individual radioelements for the peak total radiotoxicity flux can be inferred from the *p*-values in increasing order (smaller p-values imply stronger effects; *p*-values > 0.05 are presumed indistinguishable from noise and thus labelled as not applicable, "n/a"). Table headings are: estimate (regression coefficient), *p*-value (associated *p*-value for the estimate), relative ranking (importance of predictor variable or interaction effect).

	Estimate	*p*-value	Relative ranking
LK_d(Am)	−0.12	1.00	n/a
LK_d(Pu)	−0.89	2.3×10^{-6}	1 (main effect)
LK_d(U)	−0.16	0.97	n/a
LK_d(Pa)	−0.37	0.29	n/a
LK_d(Ac)	−0.88	8.1×10^{-6}	2 (main effect)
LK_d(Am:Pu)	3.9×10^{-4}	1.00	n/a
LK_d(Am:U)	−0.088	0.18	n/a
LK_d(Am:Pa)	6.0×10^{-4}	0.99	n/a
LK_d(Am:Ac)	-3.5×10^{-3}	0.96	n/a
LK_d(Pu:U)	2.5×10^{-3}	0.97	n/a
LK_d(Pu:Pa)	−0.081	0.22	n/a
LK_d(Pu:Ac)	−0.25	6.1×10^{-4}	1 (interaction)
LK_d(U:Pa)	-3.5×10^{-3}	0.96	n/a
LK_d(U:Ac)	5.9×10^{-4}	0.99	n/a
LK_d(Pa:Ac)	−0.087	0.18	n/a

The response surface calculated using the regression coefficients given in Table 4-6 is visualised in Figure 4-28 and shows the impact of varied K_d for Pu and Ac on the total flux (main effects). The response is plotted in terms of total flux deviation relative to the base case K_d parameterisation (central node of the plot). The interaction term for K_d variation of Pu and Ac can be understood as flexure (twisting) of the otherwise flat response surface. As previously, the total fluxes estimated in the NuDec-Farf31 simulations are shown as circular markers with stems indicating deviation from the calculated response surface estimated by linear regression. The locations of the circular markers correspond to the discrete K_d levels used in the experimental design (i.e., a 2D slice through the multidimensional parameter space of predictor variables).

Although the regression response surface plotted in Figure 4-28 imperfectly matches the simulation data (note the deviations represented by the circular marker stems), it appears that the regression model nevertheless identifies the most important variables and interactions since there is very little spread of results corresponding to the impact of the hidden variables (i.e., K_d values for Am, U, Pa). An empirical, low order spline interpolation of the simulated data is plotted in Figure 4-29 calculated using the *gridfit.m* function in Matlab (D'Errico 2006). The interpolated response surface is similar to that previously shown in Figure 4-28, although more precisely represents the simulation data within the circumscribed parameter space defined by the plotted data points (circular markers). Trends outside the circumscribed parameter space are not well constrained by the data so should not be considered to give an accurate account of the interaction between the two main predictor variables when considering extreme variations from the base case.

The spread of simulation results for simultaneously high K_d for Pu and Ac seems to be related to a changeover in whether the first Pu-239 peak, or the later arriving Ac-227 and Pa-231 peak is identified as that corresponding to the maximum radiotoxicity flux. When the later arriving breakthrough corresponds to the maximum, Pa-231 is found to be the dose dominant radionuclide. This is unusual since in all other cases (except for Rn-222 in the $4n + 2$ chain) the dose dominant radionuclide is always one of the top two ranked predictor variables. It is therefore interesting that the K_d for Pa is not identified as a predictor variable in the regression model since the changeover in peak dominance between Pu-239 and Pa-231 seems here to be related to a change in K_d for Pa. Further work will need to be done to fully understand the dynamics of this particular interaction, although it appears to be a localised edge case that is not captured by the regression model.

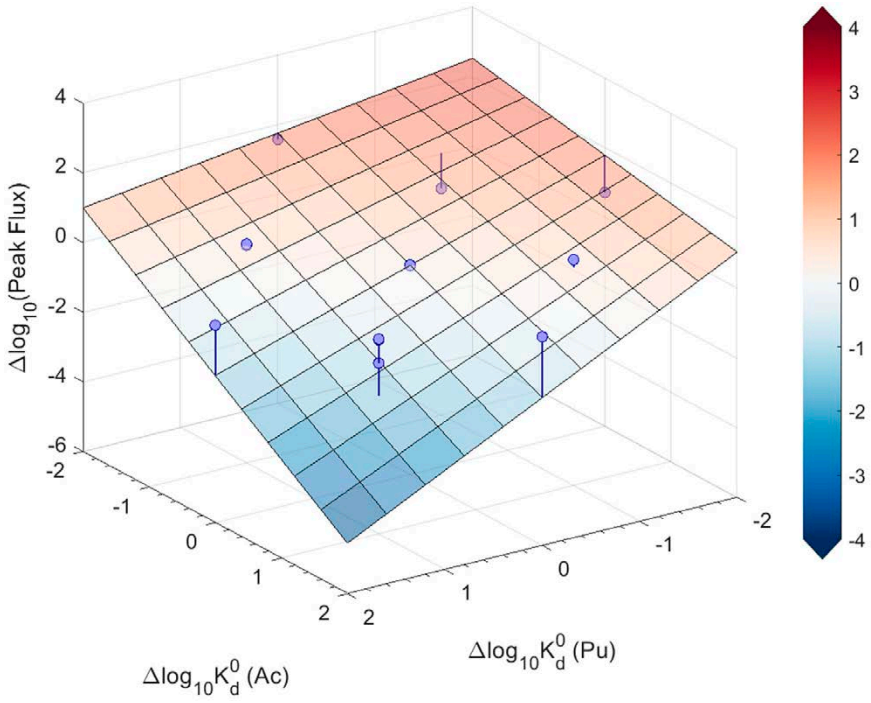

Figure 4-28. *Regression model response surface for peak far-field radiotoxicity flux (μSv/y) calculated for the 4n + 3 decay chain and a canister failure time of 100 ky (log_{10}-transformed data). Plotted circular markers with stems indicate deviations of the response surface from transport calculations. The activity flux to radiotoxicity conversion assumes the basic LDF factors taken from Table 2-4.*

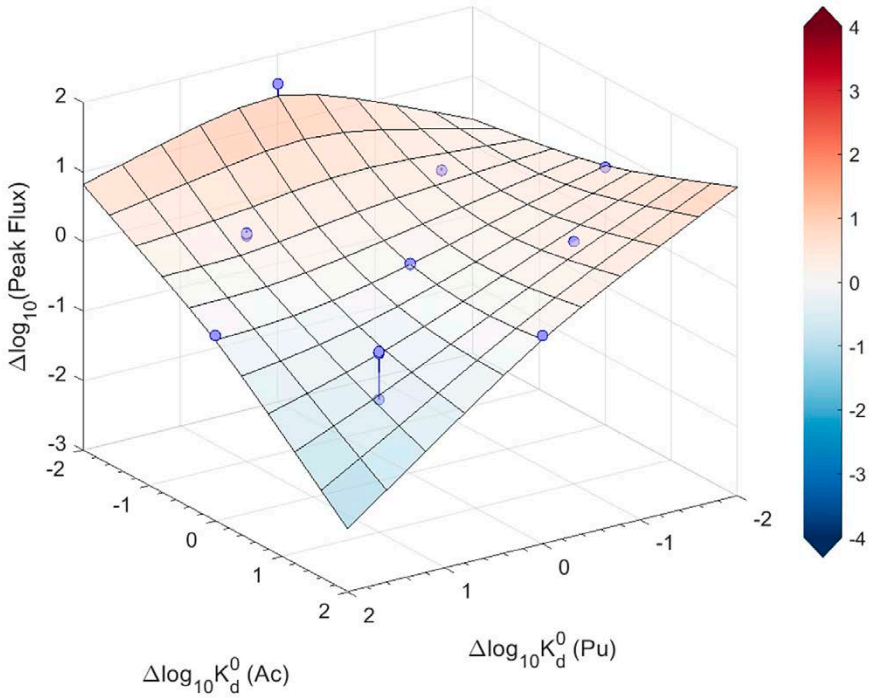

Figure 4-29. *Interpolated response surface for peak far-field radiotoxicity flux (μSv/y) calculated for the 4n + 3 decay chain and a canister failure time of 100 ky (log_{10}-transformed data). Plotted circular markers with stems indicate deviations of the response surface from transport calculations. The activity flux to radiotoxicity conversion assumes the basic LDF factors taken from Table 2-4.*

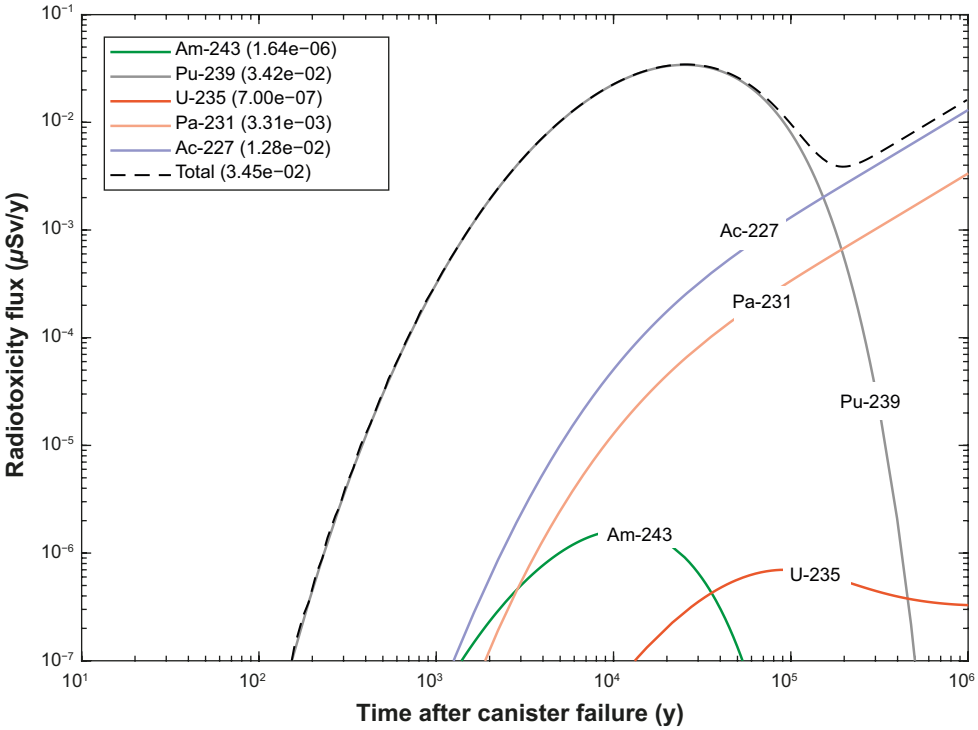

Figure 4-30. *Far-field radiotoxicity flux (μSv/y) calculated for the actinium series (4n + 3) decay chain assuming base case K_d values and a canister failure time of 100 ky. The legend is sorted sequentially in decay order with peak near-field radiotoxicity flux (μSv/y) noted for the time frame of the safety assessment. The activity flux to radiotoxicity conversion assumes the basic LDF factors taken from Table 2-4.*

Decreasing the K_d for Pu by a factor of 10 (Figure 4-31) increases the peak height of Pu-239 by about a factor of 3, while increasing the K_d by the same amount (Figure 4-32) results in a factor of 12 decrease in peak height relative to the base case. The half-life of the U-235 descendant is sufficiently long (0.704 Gy), however, that any change in the sorption status of Pu-239 doesn't have a significant impact on the flux of Pa-231 which seems to be largely source term dependent. Since the terminal chain member, Ac-227 has such a short half-life (21.8 y) one would expect its flux to be largely determined by ingrowth from Pa-231 decay along the migration path and thus sensitive to the sorption status of Pa-231.

Among the 27 different cases studies, the maximum peak radiotoxicity flux is obtained with base case K_d values for Am, Pu, U, Pa and reduced K_d for Ac. Otherwise, the first order effect of Pu K_d variation has the greatest impact on peak radiotoxicity breakthrough since Pu-239 is the dose dominant nuclide except in cases where its peak breakthrough is depressed below the late rising curve for Ac-227. A common feature of the top 6 ranked simulations (out of 27 case studies) regarding total peak radiotoxicity flux is a reduced K_d for Pu and Ac. The simulation featuring the lowest total peak radiotoxicity flux is associated with an increased K_d for Pu, Pa, and Ac.

Interestingly, altering the K_d for Pa by increasing or decreasing it by an order of magnitude seems to have only a small impact on the flux of Ac-227 (cf Figure 4-33 and Figure 4-34). Furthermore, both reduced and increased K_d for Pa results in a lower flux of Ac-227 relative to the base case which, at first glance, would appear to be a counterintuitive result. More detailed 2-parameter variation calculations confirm both that Ac-227 breakthrough is insensitive to Pu-239 sorption and indicate that the base case K_d settings approximately coincide with the Ac-227 flux maximum. Variation of K_d in either direction around the base case for Pa reduces the peak flux for Ac-227. The interpretation of this behaviour is, however, complicated by the observation window being truncated at 1 My at which point the breakthrough of both Pa-231 and Ac-227 are still increasing relatively rapidly in all case studies. Due to this, the peak breakthrough for both Pa-231 and Ac-227 are always found at the limit of 1 My. Since alteration of the K_d for Pa has an impact on both the delay and height of the breakthrough curve relative to the 1 My limit of the safety assessment time period, this may have some bearing on the interpretation of the result.

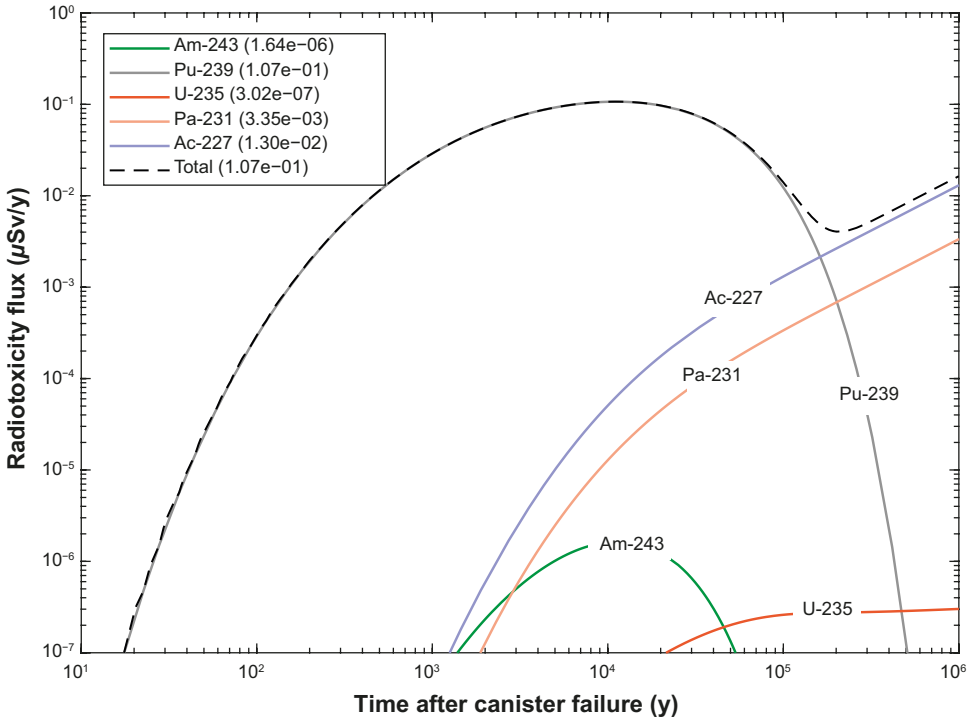

Figure 4-31. *Far-field radiotoxicity flux (μSv/y) calculated for the 4n + 3 decay chain where the K_d for Pu has been reduced by a factor of 10 (all other K_d values held constant at their base case values) and a canister failure time of 100 ky. The legend is sorted sequentially in decay order with peak near-field radiotoxicity flux (μSv/y) noted for the time frame of the safety assessment. The activity flux to radiotoxicity conversion assumes the basic LDF factors taken from Table 2-4.*

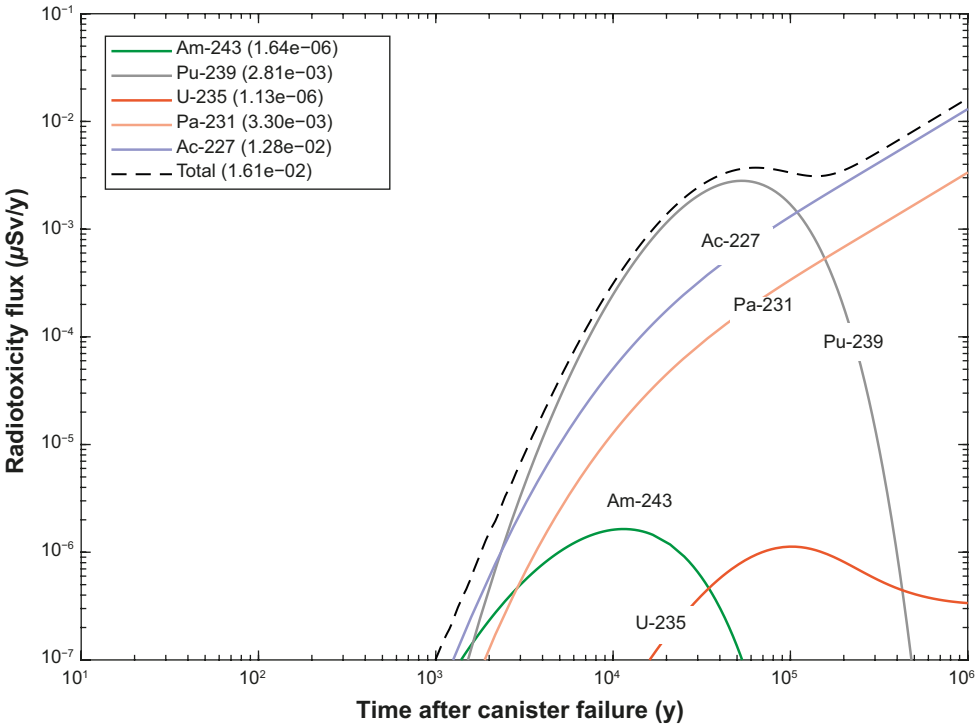

Figure 4-32. *Far-field radiotoxicity flux (μSv/y) calculated for the 4n + 3 decay chain where the K_d for Pu has been increased by a factor of 10 (all other K_d values held constant at their base case values)) and a canister failure time of 100 ky. The legend is sorted sequentially in decay order with peak near-field radiotoxicity flux (μSv/y) noted for the time frame of the safety assessment. The activity flux to radiotoxicity conversion assumes the basic LDF factors taken from Table 2-4.*

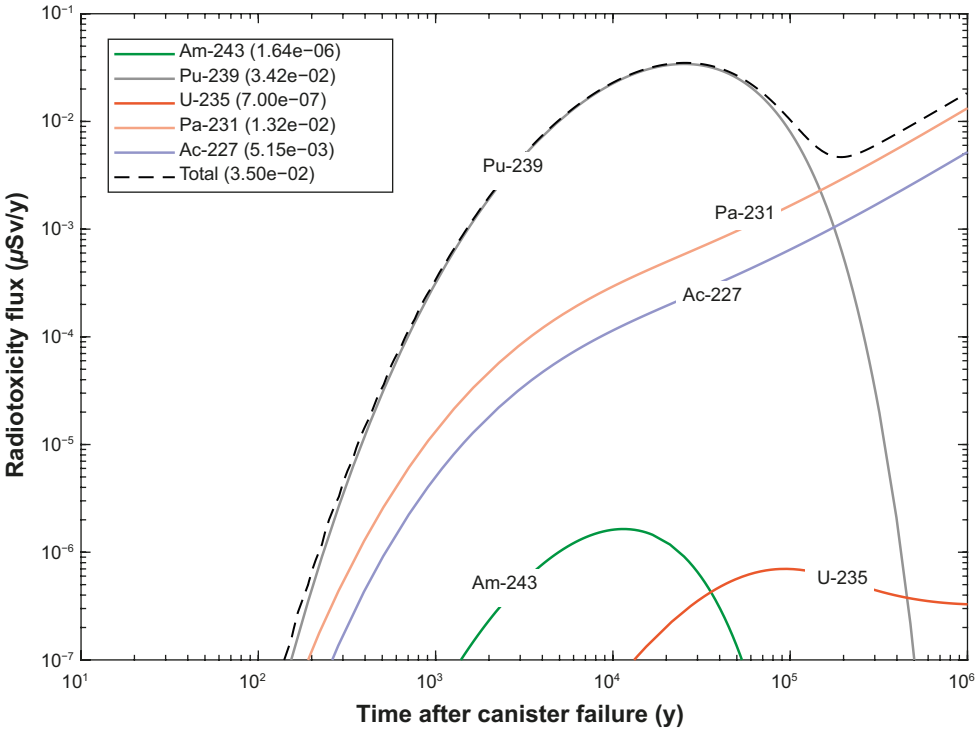

Figure 4-33. *Far-field radiotoxicity flux (μSv/y) calculated for the 4n + 3 decay chain where the K_d for Pa has been reduced by a factor of 10 (all other K_d values held constant at their base case values) and a canister failure time of 100 ky. The legend is sorted sequentially in decay order with peak near-field radiotoxicity flux (μSv/y) noted for the time frame of the safety assessment. The activity flux to radiotoxicity conversion assumes the basic LDF factors taken from Table 2-4.*

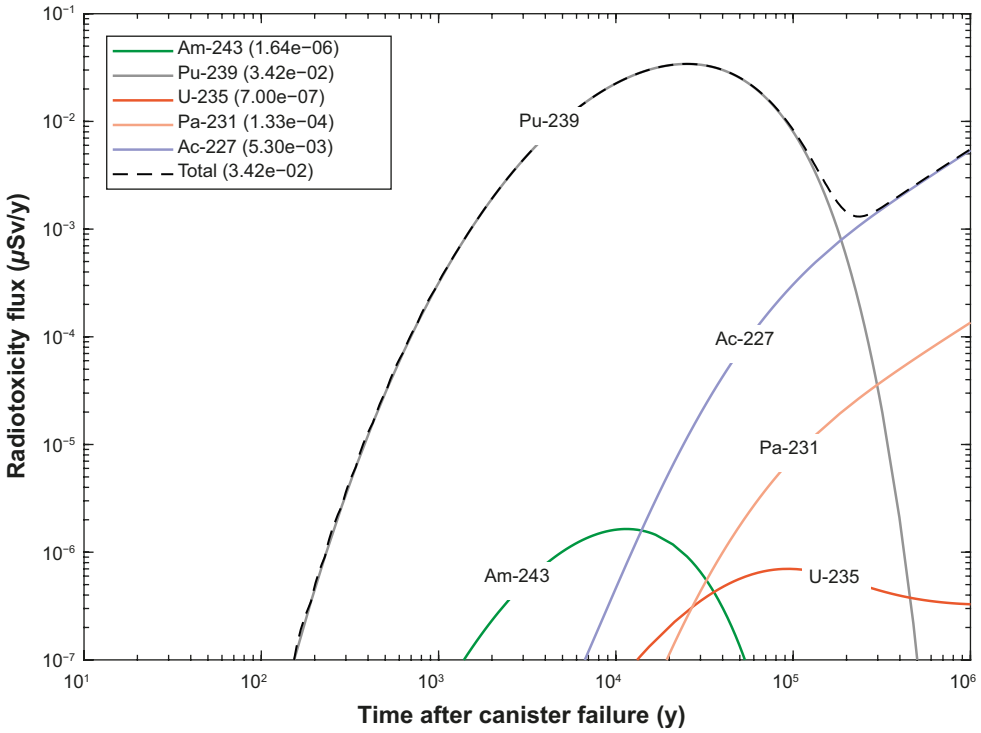

Figure 4-34. *Far-field radiotoxicity flux (μSv/y) calculated for the 4n + 3 decay chain where the K_d for Pa has been increased by a factor of 10 (all other K_d values held constant at their base case values)and a canister failure time of 100 ky. The legend is sorted sequentially in decay order with peak near-field radiotoxicity flux (μSv/y) noted for the time frame of the safety assessment. The activity flux to radiotoxicity conversion assumes the basic LDF factors taken from Table 2-4.*

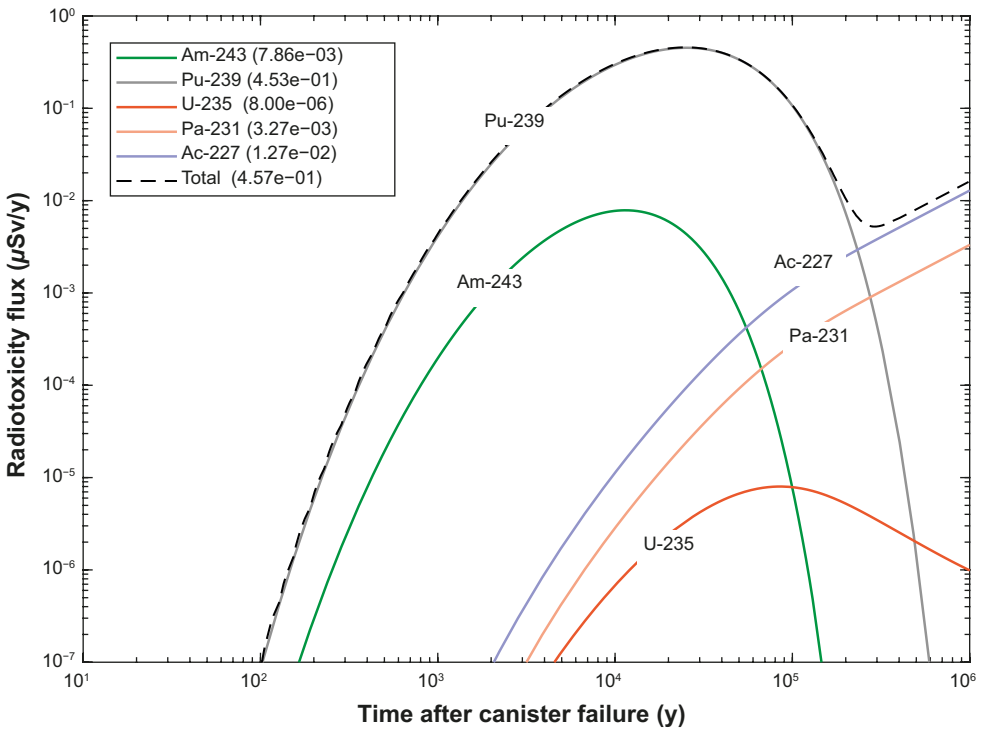

Figure 4-35. *Far-field radiotoxicity flux (μSv/y) calculated for the 4n + 3 decay chain assuming base case K_d values and a canister failure time of 10 ky. The legend is sorted sequentially in decay order with peak near-field radiotoxicity flux (μSv/y) noted for the time frame of the safety assessment. The activity flux to radiotoxicity conversion assumes the basic LDF factors taken from Table 2-4.*

For very short canister failure times, the total radiotoxicity flux is significantly higher than the 100 ky reference case, although Pu-239 still the dominant dose contributing radionuclide at short to intermediate times and Ac-227 at very long times. The main qualitative difference, however, is a much higher flux of the short-lived Am-243 (7.37 ky) which is strongly diminished in the 100 ky reference scenario.

4.3.5 Relative importance of actinides based on first-order impacts

The statistical analyses presented for each of the decay chains in the previous sections suggest that first-order effects involving individual radionuclides seem to be the most important determining factors for peak total radiotoxicity flux and interactions between radionuclides play only a subordinate role. This appears to be the case for radionuclides whose far-field flux is largely source-term determined and ingrowth along a migration path is less important. The only clear exception to this is associated with the radium ($4n + 2$) series where the short-lived Pb-210 (22.2 y) nuclide is predominantly formed by ingrowth and whose flux is therefore strongly coupled to the sorbing status of the parent nuclide Ra-226, which is both relatively short lived (1 600 y) and whose far-field flux is predominantly source determined. This is an interesting case since an increased K_d for Ra is clearly associated with both the lowest and highest total radiotoxicity fluxes modelled for this decay chain, although depending on its K_d variation relative to that for Pb. Based on the cases studied, however, it appears that a simultaneously high K_d for Ra and low K_d for Pb is probably conservative for dose calculations.

In principle, a similar coupling might be expected for Pa-231 (32.8 ky) and Ac-227 (21.8 y), although this is most likely obscured by the large predominance of Pu-239 in the total radiotoxicity flux for the actinium ($4n + 3$) chain. The biphasic breakthrough characteristic of the radiotoxicity breakthrough curve complicates the interpretation where the performance metric is taken to be the peak summed flux for the chain, since the peak radiotoxicity can be determined by either Pu-239, or Ac-227 depending on their relative transport retardation (cf Figure 4-31 and Figure 4-32). The impact of sorption upon which of these peaks is dominant appears to be why there is an apparent interaction between the sorption of Pu-239 and Ac-227 even though they are separated by the very long-lived nuclide U-235 (0.704 Gy) which otherwise might be expected to break the interaction via the ingrowth mechanism.

Since the interaction between Pu-239 and Ac-227 is apparently not ingrowth related, we might regard it as an indirect interaction (biphasic, relative peak height and timing) rather than a direct one (ingrowth). It has already been noted in Section 4.2 that there may be indirect interactions between various fission and activation product which depend on relative peak height and timing (e.g., I-129, Ni-59, Se-79), although these have been considered as less important artefacts of the analysis for the purpose of this work and therefore neglected. Despite these complicating factors, a simultaneously low K_d for Pu and Ac is probably conservative for dose calculations.

In the neptunium ($4n + 1$) series, the main first order effects are associated with the dose dominant Np-237 and to a lesser extent Th-229 radionuclides. Owing to the exceptionally low solubility assumed for Th in the source term, essentially all Th-isotopes presenting in the far-field breakthrough are ingrowth derived. There are secondary interactions between Np:Th, U:Th, and Cm:Th which reflect the ingrowth mechanism for Th-229, although these have only a minor impact on total peak radiotoxicity flux. A simultaneously low K_d for Np and Th appears to be conservative for dose calculations involving this decay chain. For the thorium ($4n$) series, Pu-240 is the most important radionuclide and its descendants U-236 and Th-232 are wholly unimportant for the contribution of this decay chain to total radiotoxicity flux. For this decay chain, a low K_d value for Pu is conservative.

If only first-order effects are considered, however, then it is possible to calculate both ϕ_k (Equation 4-2) and Ω_k (Equation 4-3) and plot the results of the sensitivity analysis in a similar fashion to that used previously for fission and activation products in Section 4.2. Although this cannot inform us of the importance of interactions, it still can be used to screen out many of the less important radionuclides from consideration in the importance ranking. The bubble plot for the performance measure Ω_k plotted versus ϕ_k is shown in Figure 4-36 for the first-order effects of K_d variation amongst the various actinide chain radionuclides. Ra-226 and Pb-210 are clearly the most important dose determining radionuclides, although Np-237 and Pu-239 also play a relatively significant role. Although Ac-227 contributes less than 0.01 % of the total radiotoxicity at the time of its peak breakthrough, its contribution to peak flux is relatively sensitive to altered K_d (presumably due to the indirect interaction between Pu-239 and Ac-227 peak height and timing). Rn-222 is also an important dose determining radionuclide and

contributes to the total radiotoxicity flux used to compute ϕ_k and Ω_k, although it is excluded in the bubble plots since, being a non-sorbing noble gas, it is not relevant for the analysis (i.e., its K_d is always zero). It is interesting to note that all of the radionuclides that dominate radiotoxicity breakthrough (i.e., top right-hand quadrant of Figure 4-36), also have non-negligible, direct or indirect second-order interactions.

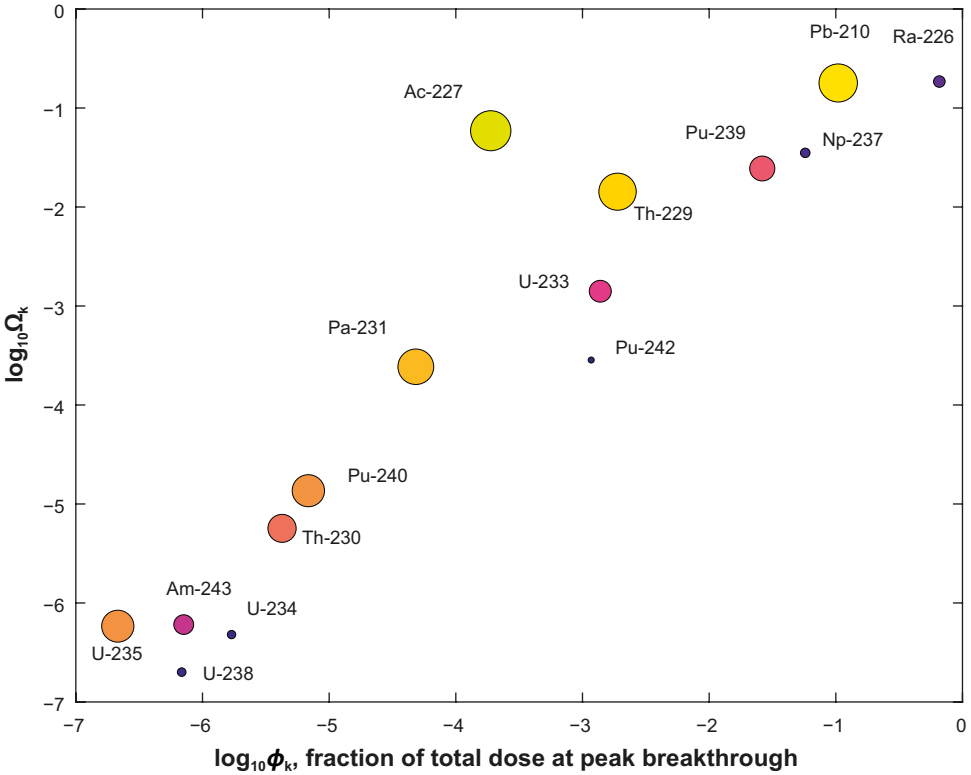

Figure 4-36. *Impact of K_d variation (first order effects) on actinide chain radionuclides as quantified by the performance variable, Ω_k plotted against base case ϕ_k (reference K_d values) in the 100 ky release scenario where K_d is varied up and down by a factor of 10. Only those radionuclides that contribute non-negligible amounts to the total transported radiotoxicity ($\phi_k > 10^{-7}$) are included in the analysis. The marker size and colour are scaled by the coefficient of variation of peak flux for each radionuclide to indicate the impact of altered K_d for each radionuclide individually.*

The corresponding bubble plots for the canister failure times of 1 ky and 10 ky are shown in Figure 4-37 and Figure 4-38, respectively. For the very early canister failure scenarios, there are only small differences relative to the 100 ky reference case. This is largely because the dose contributions from actinide chains tend to only become important over longer timescales (> 80 ky) and at earlier times the radiotoxicity flux attributable to fission and activation products are most important. The difference in the source term for the long-lived dose dominant actinides is only marginally different for early canister failure and those whose source flux increase over time due to ingrowth. The Pu-239 isotope, however, becomes increasingly important for earlier canister failure times owing to its moderately short half-life (24.1 ky) which depletes its inventory at later canister failure times. This also affects some of the minor dose determining radionuclides such as Pu-240 (6.56 ky) and Am-243 (7.37 ky).

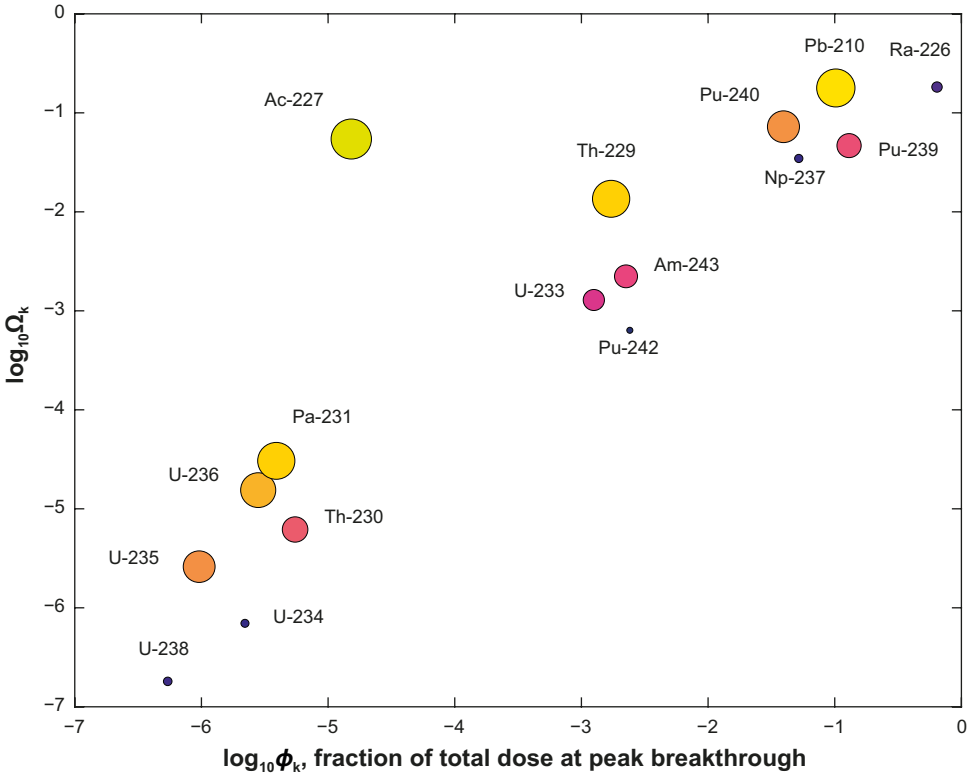

Figure 4-37. *Impact of K_d variation (first order effects) on actinide chain radionuclides as quantified by the performance variable, Ω_k plotted against base case ϕ_k (reference K_d values) in the 1 ky release scenario where K_d is varied up and down by a factor of 10. Only those radionuclides that contribute non-negligible amounts to the total transported radiotoxicity ($\phi_k > 10^{-7}$) are included in the analysis. The marker size and colour is scaled by the coefficient of variation of peak flux for each radionuclide to indicate the impact of altered K_d for each radionuclide individually.*

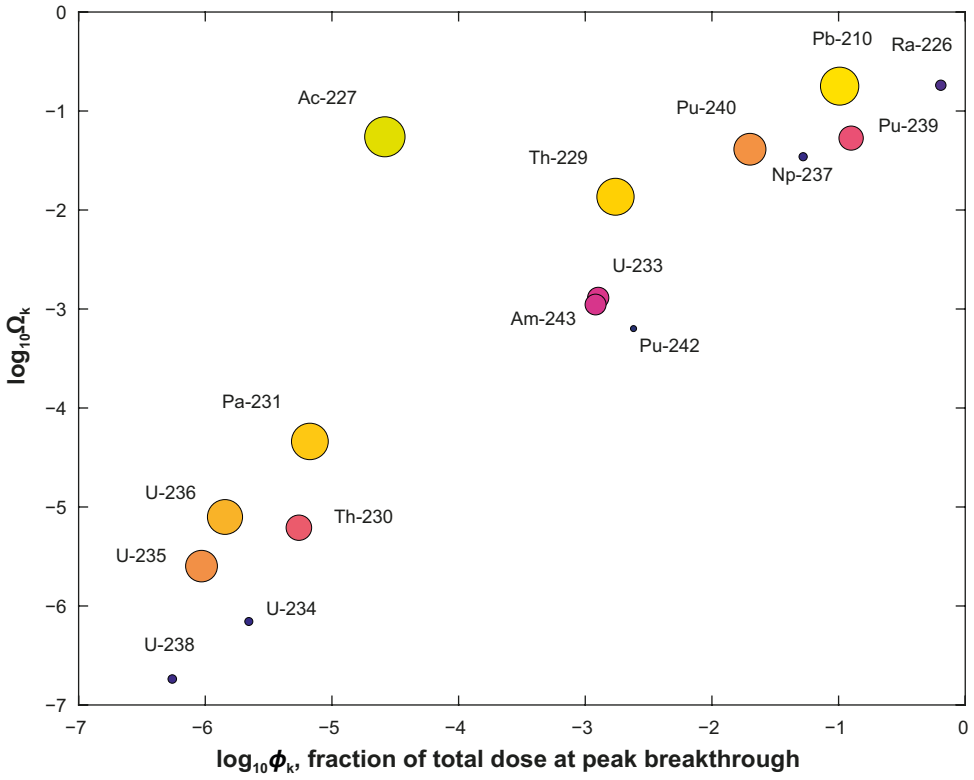

Figure 4-38. *Impact of K_d variation (first order effects) on actinide chain radionuclides as quantified by the performance variable, Ω_k plotted against base case ϕ_k (reference K_d values) in the 10 ky release scenario where K_d is varied up and down by a factor of 10. Only those radionuclides that contribute non-negligible amounts to the total transported radiotoxicity ($\phi_k > 10^{-7}$) are included in the analysis. The marker size and colour is scaled by the coefficient of variation of peak flux for each radionuclide to indicate the impact of altered K_d for each radionuclide individually.*

5 Conclusions

In this work we attempt to identify the most important radionuclides which have the potential to impact transport calculations in safety assessment of the KBS-3 repository in Forsmark. The intention is not necessarily to assess which radionuclides are dominant in dose calculations, but which elements have the greatest impact on results and consequently, whose sorption properties need to be determined with the greatest precision. To achieve this, transport calculations were made using the central corrosion case of SR-Site as a representative case study. As noted in Section 2, the central corrosion case is deemed the case study that has the most serious radiological consequences in both SR-Site and PSAR. The analysis is simplified by only considering the Q1 pathway for transport of radionuclides directly to the far field via a fracture directly intersecting the canister position. To account for a range of different release scenarios, hypothetical canister failure times of 1 ky, 10 ky, and 100 ky were considered. The hydrodynamic transport resistance (F-factor) for the representative flowpath was assumed to be the same as that for the SR-Site and PSAR central corrosion case which is a flowpath featuring relatively poor transport retardation ($F = 5.4 \times 10^4$ y/m). In general, flowpaths featuring low range F-factors of this magnitude are expected to dominate far-field release even if not statistically representative of potential transport paths in the geosphere.

Based on the sensitivity analyses for fission and activation products (Section 4.2) and actinide chains (Section 4.3.5), an overall ranking can be made where the ranking "score" is the maximised r_k value as defined in Equation 4-6. This score which gives equal weight to the performance measure ϕ_k (peak fractional contribution to total radiotoxicity flux), and Ω_k (altered fractional radiotoxicity contribution resulting from K_d variation) is used in this work to define which radionuclides should be prioritised in focused investigations of sorption. The r_k-score should be interpreted as the relative importance of a given radionuclide in terms of the influence it can exert on the total instantaneous radiotoxicity flux (i.e., overall shape of the breakthrough curve). It should not be confused with the order of relative importance of a radionuclide ranked in terms of peak radiotoxicity (i.e., dose-dominance) in safety assessment calculations.

The proposed priority list is shown in Table 5-1 for the reference scenario of canister failure at 100 ky and the two variant cases assuming much earlier canister failure times of 10 ky and 1 ky, respectively. Rankings are given for the case study assuming landscape dose factors (LDF) as well as a variant case assuming raw dose conversion factors for ingestion (DCF-I) as specified in Table 2-4. The rankings are based on simulations combining instant release (IRF) and corrosion-dissolution release (CDRF) fractions. For the IRF release, a continuously stirred tank reactor (CSTR) assumption is made to calculate the near field boundary condition (radionuclide fluxes in mol/y). The actual form of the assumed IRF release generally only affects the transport of I-129, Cl-36, and C-14. The corresponding boundary condition for the corrosion-dissolution release fraction is calculated by COMP23. Calculations of far-field transport are made separately for the IRF and CDRF fractions to permit the use of different landscape dose factors (LDF) for the different fractions.

It is noted that for the purposes of the present analysis an arbitrarily low, although non-zero K_d value has been assumed for the radionuclides I-129, Cl-36, and C-14 as a base case parametrisation. These radionuclides were assumed to have zero K_d in SR-Site and PSAR. The base case K_d for these is set to 10^{-6} m^3/kg which corresponds to a minimally relevant pore retardation factor of 2.5 for Forsmark site specific rock. In our variation analysis used to estimate the ranking performance measure, r_k this implies a K_d values ranging from effectively non-sorbing (10^{-7} m^3/kg) to very weakly sorbing (10^{-5} m^3/kg).

A strong caveat on the interpretation of the rankings indicated for the non-sorbing radionuclides discussed above is that the magnitude of the Ω_k variable may reflect subtle shifts in timing of peak breakthrough relative to other radionuclides and might overestimate the effect of K_d as it usually is associated with peak dilution and decay-related attenuation. We consider this to be an indirect effect of peak height and timing as it applies to a biphasic (i.e., double peak) breakthrough of a single nuclide. In the case of I-129 the instant release and dissolution release fraction are summed to give a breakthrough curve with biphasic properties. Assumptions concerning the form of the instant release function (i.e., a square pulse or a decaying elution function) can then have a very strong impact on the overall effect which is attributed to a change in K_d.

For I-129, the peak of the instant release fraction is only slightly higher than that of the dissolution release fraction when a decaying elution function (CSTR-model) is used to model the instant release. The instant release peak for I-129 is much more prominent when modelled as a square pulse. For the decaying elution function representation, a very modest increase in pore retardation can then decrease the instant release peak flux to just below that of the dissolution release flux. This results in the point of maximum peak breakthrough then becoming associated with the later peak breakthrough of the dissolution release fraction rather than the instant release fraction. Since, in the present example, the instant release peak for I-129 occurs at 20 y and the dissolution release associated peak occurs at 83 ky, a small decrease in peak height for the instant release pulse can suddenly cause a shift of many tens of thousands of years in the timing of maximum I-129 peak breakthrough at which point very different ϕ_k and Ω_k measures might be calculated (i.e., since we are comparing against the summed effect of radionuclides contributing to the total radiotoxicity flux at different times).

A similar effect is also seen for the actinium series ($4n + 3$) chain where changes in K_d can alter the relative heights and timing of Pu-230 and Ac-227 peak radiotoxicity fluxes, both associated with the dissolution release fraction. Since both Pu and Ac are considered to sorb relatively strongly, however, the effect is a real consequence of K_d parameterisation that complicates interpretations of which K_d values are considered conservative in the context of peak dose and not merely an effect of scenario definition.

Table 5-1. Overall priority ranking of radionuclides based on the r_k-score assuming the SR-Site/PSAR central corrosion case as a reference scenario and landscape dose factors (LDF), alternatively dose conversion factors for ingestion (DCF-I) as defined in Table 2-4. The ranking indicates the order in which updated or improved K_d data might be expected to have an impact on safety assessment outcomes for a typical flowpath featuring moderately poor transport retardation ($F = 5.366 \times 10^4$ y/m; $t_w = 6.401$ y). The given order is not necessarily the same as the order of dose dominance in the safety assessment. Rankings are given for the reference case canister failure time of 100 ky as well as the variant cases for early failure times of 10 ky and 1 ky. Radionuclides annotated with an asterisk have additional caveats that should be considered (see text for details).

Nuclide	100 ky		10 ky		1 ky	
	LDF	DCF-I	LDF	DCF-I	LDF	DCF-I
1	*I-129	*I-129	*C-14	Ra-226	*C-14	Ra-226
2	Ra-226	Ra-226	Nb-94	*I-129	Nb-94	Pu-239
3	Ni-59	Ni-59	Ra-226	Pu-239	Ra-226	*I-129
4	Se-79	Cs-135	Ni-59	Ni-59	Ni-59	Ni-59
5	Nb-94	Pu-239	Pb-210	Nb-94	Pb-210	Pu-240
6	Pb-210	Pb-210	Pu-239	Pu-240	Pu-239	*C-14
7	Np-237	Zr-93	Np-237	Pb-210	Pu-240	Nb-94
8	Ac-227	Nb-94	Ac-227	*C-14	Np-237	Am-241
9	Nb-93m	Ac-227	Pu-240	Zr-93	Ac-227	Pb-210
10	Pu-239	Th-229	*I-129	Cs-135	*I-129	Ac-227
11	Tc-99	Nb-93m	Se-79	Ac-227	Se-79	Zr-93
12	*Cl-36	Tc-99	Tc-99	Th-229	Th-229	Cs-135
13	Th-229	Se-79	Th-229	Am-243	Tc-99	Th-229
14	Zr-93	*Cl-36	Sn-126	Pu-242	Sn-126	Am-243
15	Sn-126	Np-237	Nb-93m	Se-79	Nb-93m	Ag-108m

The relative importance rankings shown in Table 5-1 are relatively stable across the different scenarios for canister failure with a couple of notable exceptions. It is interesting to note that the use of dose conversion factors for ingestion (DCF-I) gives a slightly different order of relative importance than landscape dose factors (LDF). Notably, C-14 has an elevated status when using an LDF-based conversion relative to other radionuclides. This is due to its preferential incorporation into dietary products when modelled in a compartmentalised biosphere representation (Avila et al. 2010). Many other radionuclides, however, are retained more strongly in landscape objects used in the biosphere modelling which downgrades their relative importance in the LDF case. When using the DCF-I conversion factor approach, dietary ingestion is a priori assumed for all radionuclides which tends to equalise the imbalance amongst the different dose contributing radionuclides.

Se-79 has a higher status when using the LDF approach, presumably for similar reasons to C-14 and also due to its relatively weak retention on geomaterials. Cs-135, on the other hand, is absent from the top 15 dose-contributing radionuclides when using LDF's although it does appear when using the DCF-I conversion. Pu-239 is also ranked as relatively more important when using the DCF-I factor rather than LDF. This is partly due to it being a strong alpha emitter and likely also due to it being strongly retained on sediments and soils in the LDF quantification. Zr-93 ranks at a relatively higher level in the DCF-I case also reflecting retention on sediments and soils in the LDF case.

For early failure times, C-14 becomes the most important dose determining nuclide by a considerable margin when using LDF values taken from SR-Site and PSAR. Due to its relatively short half-life, it has declined to insignificance for the reference scenario with canister failure at 100 ky. The high radiotoxicity flux of C-14 at canister failure times of 1 ky and 10 ky is largely due to the corrosion release fraction which is associated with a relatively high LDF. Although the instant release fraction comprises roughly 10 % of the total inventory of C-14, the estimated pulse LDF is at least three orders of magnitude less (cf Table 2-4) which reduces its importance relative to the corrosion release fraction.

Since the pulse LDF in the present work was approximated by the correlation described in Section 2.1.1, the treatment of the instant release fraction is a significant source of uncertainty in the present analysis and the radiological flux attributable to C-14 instant release could be as much as an order of magnitude higher than the peak flux indicated in Figure 3-3 or Figure 3-4. This uncertainty, however, does not affect the relative importance ranking since C-14 is unequivocally dose dominant in these cases regardless of assumptions concerning the proper LDF. Other radionuclides that have significantly increased relative status in the early canister failure scenarios are Nb-94 and Pu-239. These radionuclides are still relatively important in the 100 ky reference scenario, although subordinate to Ra-226, Ni-59, and Se-79.

The broken red curve in Figure 5-1 shows the summed flux for the abbreviated set of 11 radionuclides relative to the full breakthrough curve based on all 45 radionuclides represented by the broken black curve. The abbreviated set of radionuclides captures the variation of the full breakthrough curve with a fidelity of ~98 % for breakthrough times up to 1 My. With the addition of C-14, the same list of radionuclides can also reproduce the breakthrough curves for the 1 ky and 10 ky canister failure scenarios with roughly same level of fidelity.

Although the relative ranking in this work is based on a narrowly defined performance measure given by Equation 4-6, the breakthrough curve for the summed radiotoxicity flux is well approximated by including only the top 11 radionuclides in the first column of Table 5-1 (additionally including Rn-222), thereby indicating that the chosen performance measure is a competent metric of relative importance in the broader context of the breakthrough curve as a whole for the given near field boundary condition. Note also that the order of importance of the top 11 radionuclides is not the same as their dose dominance order (cf peak fluxes annotated in the legend of Figure 5-1). If ordered in terms of dose dominance, Ra-226, Se-79, Ni-59, Rn-222, Pb-210, and Np-237 would all be ranked higher than I-129.

In general, the top ranked fission and activation products are mostly of importance for early breakthrough and the actinide decay chains only become important at later times. This implies dominance of fission and activation products for the first few thousand years after canister failure in the 100 ky reference scenario. For the early canister failure scenarios, the dominance of fission and activation products persists for at least the first 10–20 ky after the onset of advective flow conditions in the deposition hole. Amongst the actinide decay chains, the radium series ($4n + 2$) is clearly most important due to the late time dominance of Ra-226 as well as the descendant radionuclides Rn-222 and Pb-210 produced by ingrowth along the transport flowpath. If the minor contributions of the fission product Tc-99, as well as Np-237 (neptunium series) and Pu-239 (actinium series) are neglected, then ~92 % of the variation of the total breakthrough can be captured by considering only contributions of C-14, I-129, Ni-59, Se-79, Nb-94 and the radium chain members (Ra-226, Pb-210, and Rn-222) for all scenarios based on LDF dose conversion factors.

It should be noted that this does not necessarily mean that radioelements outside the top 10 dose contributors as shown in Figure 5-1 can have K_d values set arbitrarily to zero since the minor radionuclides can still be influential if given trivial K_d values that conflict with chemical understanding. In principle, all radionuclides not included in the top 10, can have K_d values effectively set to zero except for lower-ranked trivalent and tetravalent radioelements (i.e., excluding Tc-99, Np-237, and

Pu-239) in the reference scenario of canister failure at 100 ky (see Appendix C). These, however, can have their K_d values varied by as much as five orders of magnitude from 10^{-4} m^3/kg to 10 m^3/kg with only very marginal impact on total radiotoxicity breakthrough. Increasing K_d values above the present base case parameterisation for trivalent and tetravalent radioelements has essentially no impact on total radiotoxicity breakthrough either directly, or indirectly by decay chain ingrowth. For the very low K_d setting of 10^{-4} m^3/kg, on the other hand, the peak total radiotoxicity is increased by about 10 % relative to the base case. This is entirely attributable to the influence of Zr-93 for the corrosion release breakthrough up to ~ 1 ky, and Sn-126 for positive deviations in the period from about 5 ky to 50 ky after canister failure. Increasing the K_d for Zr-93 and Sn-126 to more reasonable values reflecting their known strong sorptivity, however, closes the gap relative to the base case significantly.

Although I-129 is ranked among the most important dose contributors, the utility of a non-zero K_d value is deemed by the present author to be marginal. In the case of I-129, the impact of K_d on the weighted performance measure, r_k appears to be at least partly artefactual and related to peak dilution of the instant release fraction relative to the dissolution release fraction (as discussed previously). The result for I-129 is therefore strongly dependent on the assumed form that the instant release pulse takes which is subject to some uncertainty. The half-life of I-129 is sufficiently long (15.7 My) that attenuation by decay along flowpaths in the geosphere is insignificant, however strong the sorption might be.

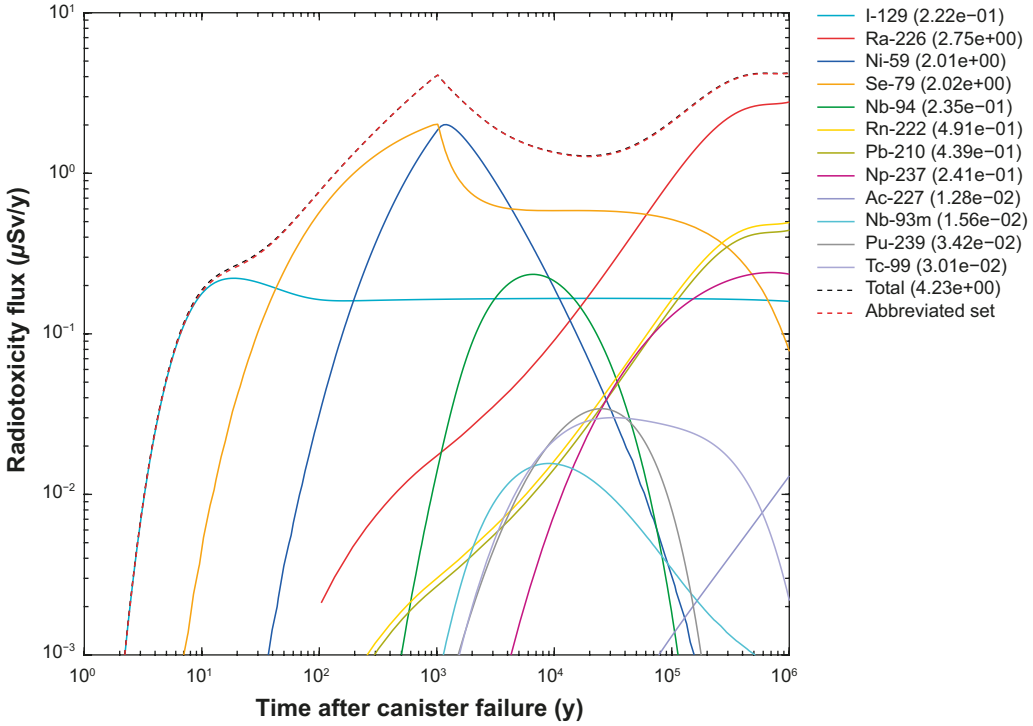

Figure 5-1. *Equivalent far-field radiotoxicity flux (μSv/y) for the base case K_d parameterisation and canister failure time of 100 ky, including both the instant release fraction (IRF) and corrosion/dissolution release fraction (CDRF) assuming the reference case LDF values. The red broken curve shows the summed contribution of the abbreviated set of top 11 radionuclides listed in Table 5-1 (additionally including Rn-222, which being non-sorbing is not included in Table 5-1) relative to the total radiotoxicity summed over all modelled radionuclides (black broken curve). The time on the x-axis is relative to canister failure at 100 ky post-closure.*

C-14, on the other hand, which has a short half-life (5.71 ky) experiences relatively strong decay-related transport attenuation. In the case of C-14, the additional attenuation that might be achieved with a non-zero K_d is likely to be modest, however, given that sorption is expected to be weak in the rock matrix. Given a relatively optimistic K_d of 2×10^{-3} m^3/kg, for example, the peak radiotoxicity might be reduced by about 50 % for the same modelled F-factor. Although a decrease in peak radiotoxicity of this magnitude is not large, it might still be worthwhile investigating within a laboratory program given the relative importance of C-14 for very early failure times. For flowpaths featuring higher F-factors, the potential decrease in peak radiotoxicity could be significantly greater and certainly worthwhile quantifying more accurately.

C-14 might sorb by way of surface complexation in the rock matrix or undergo isotope exchange with carbonate accessory minerals in the rock matrix. Although only minute quantities of calcite are expected to exist in the rock matrix, the ubiquitous presence of calcite in fracture coatings at Forsmark suggests that retardation by sorption on fracture coatings could be non-negligible and contribute meaningfully to C-14 attenuation in the far-field. Sorption of C-14 on fracture calcites should therefore be investigated further owing to its relevance for early canister failure scenarios.

The relative ranking of radionuclides for the two LDF variant cases (VC-LDF and SFR-LDF) is shown in Table 5-2 in terms of the maximised r_k value defined in Equation 4-6. Comparing the two LDF variant cases, we see that C-14, Nb-94, and Se-79 are significantly downgraded in importance when LDF's taken from SR-PSU (SKB 2015) are used in the sensitivity analysis. This is entirely attributable to the much lower LDF's assigned for these radionuclides in SR-PSU relative to SR-Site/PSAR. On the other hand, Zr-93, Cs-135, and the more short-lived Pu-isotopes (Pu-239 and Pu-240) attain upgraded status as relatively more important radionuclides. This is partly due to higher LDF's for these radionuclides in SR-PSU, although it also attributable to a decrease in relative importance of other radionuclides that otherwise overshadow the contributions of these radionuclides when using VC-LDF values taken from SR-Site/PSAR. This illustrates that the relative ranking of radionuclides is both directly sensitive to changes in LDF's assigned to individual radionuclides as well as indirectly by devaluation of competing radionuclides that exhibit contemporaneous peak breakthrough.

Table 5-2. Overall priority ranking of radionuclides based on the r_k-score assuming the SR-Site/PSAR central corrosion case as a reference scenario and variant case landscape dose factors (VC-LDF), alternatively landscape dose factors taken from SR-PSU (SFR-LDF) as defined in Table 2-4. The ranking indicates the order in which updated or improved K_d data might be expected to have an impact on safety assessment outcomes for a typical flowpath featuring moderately poor transport retardation (F = 5.366×10^4 y/m; t_w = 6.401 y). Rankings are given for the reference case canister failure time of 100 ky as well as the variant cases for early failure times of 10 ky and 1 ky. Radionuclides annotated with an asterisk have additional caveats that should be considered (see text for details).

Nuclide	100 ky		10 ky		1 ky	
	VC-LDF	SFR-LDF	VC-LDF	SFR-LDF	VC-LDF	SFR-LDF
1	*I-129	*I-129	*C-14	Ni-59	*C-14	Ni-59
2	Ra-226	Ni-59	Nb-94	*I-129	Nb-94	*I-129
3	Se-79	Ra-226	Ra-226	Ra-226	Ra-226	Ra-226
4	Ni-59	Cs-135	Ni-59	Pu-239	Ni-59	Pu-239
5	Pb-210	Zr-93	Pb-210	Cs-135	Pb-210	Pu-240
6	Nb-94	Pb-210	Pu-239	Pu-240	Pu-239	Pb-210
7	Np-237	Pu-239	Np-237	Pb-210	Pu-240	Am-241
8	Ac-227	Ac-227	Ac-227	Nb-94	Np-237	Cs-135
9	Nb-93m	*Cl-36	Pu-240	Zr-93	Ac-227	Nb-94
10	Pu-239	Th-229	*I-129	Ac-227	*I-129	*C-14
11	Th-229	Nb-94	Se-79	*C-14	Se-79	Zr-93
12	Tc-99	Tc-99	Tc-99	*Cl-36	Th-229	Ac-227
13	Sn-126	Se-79	Th-229	Th-229	Tc-99	Mo-93
14	Zr-93	U-233	Sn-126	Mo-93	Sn-126	*Cl-36
15	U-233	Nb-93m	Nb-93m	Tc-99	Nb-93m	Th-229

Based on the radionuclide importance ranking given in Table 5-1, a priority list of elements (and redox states) whose sorption should be more thoroughly investigated has been made. The list of prioritized elements is given in Table 5-3 and is split into three tiers reflecting their overall importance for safety assessment of the KBS-3 repository system. First tier elements and redox states are those which have been identified as being of central importance for transport calculations based on the present work. Second tier elements and redox states are moderately important, although whose sorption may not need to be as accurately quantified.

Third tier elements and redox states are not directly important although are deemed to be useful geochemical analogues for other elements. An exception is made for uranium, which although being identified as being of only minor importance in the present analysis, is included as a third-tier element to cover the possibility of alternative release scenarios that could give higher contributions to far-field radiotoxicity fluxes that have not been studied in the present work (e.g., differing solubility assumptions in the near-field). All other elements and redox states have been found to be relatively unimportant for far-field dose calculations based on the scenarios studied in the present work and existing data may be sufficient.

While the prioritization of elements in Table 5-3 largely reflects the relative ranking of radionuclides given previously in Table 5-1, it is important to acknowledge the uncertainty that the use of particular LDF values entails. For this reason, Cs and Zr are included as second tier elements owing to their elevated status when using the variant case LDF values taken from SR-PSU (cf Table 5-2) even though they play a much less important role in the reference case (LDF values from SR-Site/PSAR).

Table 5-3. List of elements (and redox states) for which K_d data are required for geosphere sorption. The list is divided into three tiers reflecting relative importance for safety assessment: (1) central importance (shaded red); 2) moderately important (shaded violet); 3) potentially useful as geological analogues or might be important in special variant cases (shaded green).

Element (redox State)	Tier	Proposal for handling in detailed site investigation phase/SAR
Ac(III)		Geochemical analogy with Am(III)/Eu(III).
Ag(I)		Relatively unimportant in studied scenarios (measurements on site specific materials, however, would be useful for demonstrating process understanding).
Am(III)*	3	Reinterpretation of existing SDM data (additional experiments required owing to uncertain pH and headspace pCO_2 in SDM-Site data).
C, HCO_3^-	1	Sorption on site specific materials required; additionally, possible retention on fracture calcite should be quantified (mostly important for early canister failure scenarios; limited impact for 100 ky canister failure).
C, CH_4		Can reasonably be presumed non-sorbing.
C, $-CO_2H$		Can reasonably be presumed non-sorbing.
Cd(II)		Unimportant in studied scenarios (an approximate geochemical analogy with Ni(II) can be invoked with appropriate thermodynamic correction).
Cl(-I)		Can be presumed non-sorbing (very limited utility of a non-zero K_d).
Cm(III)		Geochemical analogy with Am(III)/Eu(III).
Cs(I)	2	Reinterpretation of existing SDM data possible.
Eu(III)*	3	Reinterpretation of existing SDM data (additional experiments required owing to uncertain pH and headspace pCO_2 in SDM data).
H(I)		Unimportant in studied scenarios; can be presumed non-sorbing.
Ho(III)		Geochemical analogy with Am(III)/Eu(III).
I(-I)		Can be reasonably presumed non-sorbing (weak sorption reported for I is very likely due to sorption of IO_3^- which is not relevant for reducing conditions in the geosphere).
Mo(VI)		Relatively unimportant in studied scenarios (only weak sorption expected and can be reasonably presumed non-sorbing for purposes of KBS-3).
Nb(V)	1	Sorption measurements on site specific materials required.
Ni(II)	1	Reinterpretation of existing SDM data possible (additional measurements required owing to uncertain pH and headspace pCO_2 in SDM lab data).

Element (redox State)	Tier	Proposal for handling in detailed site investigation phase/SAR
Np(IV)	2	Sorption measurements on site specific materials required (or assumption of a suitable geochemical analogue).
Np(V)	2	Reinterpretation of existing SDM data possible (additional measurements required owing to uncertain Eh, pH and headspace pCO_2 in SDM lab data).
Pa(IV)		Unimportant in studied scenarios (existing recommendation likely to be inaccurate although probably sufficient).
Pa(V)		Unimportant in studied scenarios (existing recommendation likely to be inaccurate although probably sufficient).
Pb(II)	1	Sorption measurements on site specific materials required.
Pd(II)		Unimportant in studied scenarios (existing recommendation likely to be inaccurate although probably sufficient; measurements on site specific materials, however, would be useful for demonstrating process understanding).
Pu(III)	2	Geochemical analogy with Am(III)/Eu(III).
Pu(IV)	2	Sorption measurements on site specific materials required (or assumption of a suitable geochemical analogue such as Th(IV)).
Pu(V)		Deemed an unimportant redox state for geosphere transport in KBS-3.
Pu(VI)		Deemed an unimportant redox state for geosphere transport in KBS-3.
Ra(II)	1	Reinterpretation of existing SDM data possible (additional measurements required to improve statistical basis for K_d estimate).
S(-II)		Can be presumed non-sorbing.
Se(-II)		Can be presumed non-sorbing.
Se(IV)	1	Reinterpretation of LTDE-SD data. Additional measurements using site-specific materials recommended to increase statistical basis for K_d estimate.
Se(VI)	1	Presumed to be more weakly sorbing than Se(IV).
Sm(III)		geochemical analogy with Am(III)/Eu(III).
Sn(IV)		Sorption measurements on site specific materials required (not a good geochemical analogue for other tetravalent species).
Sr(II)		Reinterpretation of existing SDM data possible.
Tc(IV)	2	Sorption measurements on site specific materials required (not a good geochemical analogue for other tetravalent species).
Tc(VII)		Can be reasonably presumed non-sorbing.
Th(IV)*	3	Sorption measurements on site specific materials required (possible geochemical analogue for Np(IV), Pu(IV), and U(IV)).
U(IV)	3	Sorption measurements on site specific materials required (or assumption of a suitable geochemical analogue).
U(VI)	3	Reinterpretation of existing SDM Data (could be complemented with additional measurements owing to uncertain Eh, pH and headspace pCO_2 in SDM lab data).
Zr(IV)	2	Sorption measurements on site specific materials required (not a good geochemical analogue for other tetravalent species).

The sorption of Ra and Ni was investigated previously in the site investigations for Forsmark and Laxemar (Byegård et al. 2008, Selnert et al. 2009), while sorption of Se was studied on Forsmark site specific rock samples as part of the laboratory programme for the LTDE-SD project (Widestrand et al. 2010a,b, Nilsson et al. 2010). There is therefore reasonably qualified existing data support for these elements, although there are still issues of representativity and the data set could certainly be expanded and improved given the importance of these radioelements. The sorption of Nb-94, on the other hand, is very poorly quantified in the recommendation given for SR-Site and PSAR. It is based on data reported by Kulmala and Hakanen (1992) for Olkiluoto tonalite and Rapakivi granite which, although deemed a qualified source, may not be representative for Forsmark site-specific rock and groundwater types. The sorption of Pb-210 is also very poorly quantified in the existing K_d database and clearly needs to be improved.

While Pd-107 is not an important radionuclide for safety assessment, Pd(II) is nevertheless interesting since its hydrolysis constants differ considerably from other elements. It therefore might be useful for calibration of a linear free energy relation (LFER) for surface complexation reactions on biotite which is the mineral recognised as dominating sorption in granitic rocks. Similarly, while Ag-108m is deemed unimportant in most scenarios, Ag(I) has a first hydrolysis constant that differs significantly from other elements. Pd and Ag might therefore be considered as possible candidates for a laboratory program for demonstrating process understanding even if not directly relevant for repository safety.

Np, Pu, and Tc present challenges on account of their redox sensitivity and strong hydrolysis when in the tetravalent state. Pu is problematic due to regulatory issues which restricts the possibility of studying it in laboratory settings to a greater degree than other elements. Pu redox chemistry is also particularly complicated since multiple redox states can exist simultaneously in groundwater and redox disproportionation reactions can also occur. In the geosphere, however, the two dominant redox states are predicted to be Pu(III) and Pu(IV), both of which are strongly sorbing. Np can exist in either the weakly sorbing Np(V) redox form, or the more strongly sorbing tetravalent form, Np(IV) under reducing conditions at repository depth. Under reducing conditions, Tc is found in the strongly sorbing Tc(IV) state, although given sufficiently strong oxidising conditions changes to the Tc(VII) form which, being an oxyanion, sorbs only very weakly if at all.

The sorption of the relevant redox states of Pu might be best estimated by invoking geochemical analogies with other trivalent and tetravalent elements for which data is more easily accessible. For this, we have a relatively well qualified data set for Am(III) and Eu(III) from the Forsmark and Laxemar site investigations. Sorption data for Am(III) or Eu(III) can generally be used as a geochemical analogue for Pu(III), Ac(III), Ho(III), and Sm(III) based on the very close correspondence between their hydrolysis constants. As noted previously for Ra(II) and Ni(II), however, there are representativity issues concerning the existing data set and there is room for improvement.

For tetravalent elements, Th(IV) can be reasonably invoked as an approximate geochemical analogy for Np(IV), U(IV), and Pu(IV), although the analogy is expected to be less accurate than that for the trivalent elements due to a larger spread of hydrolysis constants for these elements. Th(IV) is not redox sensitive under ambient conditions and sorption experiments can therefore be carried out more easily than for Np(IV), U(IV), and Pu(IV). The sorption of Np and U was studied experimentally in the Forsmark and Laxemar site investigations, although the laboratory glovebox environment was probably not sufficiently reducing to ensure tetravalent speciation. For Np it is likely that the sorption measured was more likely representative of Np(V), or perhaps a mixed redox state. For U it is likely that the measurement data were more representative of U(VI) sorption.

Laboratory experiments designed specifically for studying the sorption of Np(IV), U(IV), and Tc(IV) on site specific materials would be best if sufficiently reducing conditions can be achieved in the glovebox and contact solutions. Tc(IV), Zr(IV), and Sn(IV) are sufficiently strongly hydrolysed that it is not possible to invoke a reasonable geochemical analogy with other tetravalent solutes. The tetravalent state is also generally difficult to work with owing to strong hydrolysis and propensity to form colloids. This was a problem that precluded the use of measurement data acquired for Th(IV) in the Forsmark and Laxemar site investigations for the reference groundwater compositions used in the laboratory studies. Future laboratory investigations of sorption for Th(IV) and other tetravalent species may necessitate the use of simplified electrolyte compositions and the use of surface complexation and speciation modelling to transfer K_d data to in situ conditions.

References

SKB's (Svensk Kärnbränslehantering AB) publications can be found at www.skb.com/publications.

Avila R, Ekström P-A, Åstrand P-G, 2010. Landscape dose conversion factors used in the safety assessment SR-Site. SKB TR-10-06, Svensk Kärnbränslehantering AB.

Bertetti F P, 2014. Detailed assessment of radionuclide K_d-values for the geosphere. SSM Technical Note 2014:38, Swedish Radiation Safety Authority.

Byegård J, Selnert E, Tullborg E-L, 2008. Bedrock transport properties. Data evaluation and retardation model. Site descriptive modelling. SDM-Site Forsmark. SKB R-08-98, Svensk Kärnbränslehantering AB.

Crawford J, 2010. Bedrock K_d data and uncertainty assessment for application in SR-Site geosphere transport calculations. SKB R-10-48, Svensk Kärnbränslehantering AB.

Crawford J, Löfgren M, 2019. Modelling of radionuclide retention by matrix diffusion in a layered rock model. SKB R-17-22, Svensk Kärnbränslehantering AB.

D'Errico J, 2006. Surface Fitting using gridfit. MATLAB Central File Exchange. Available at: https://www.mathworks.com/matlabcentral/fileexchange/8998-surface-fitting-using-gridfit [7 March 2022].

Elert M, Gylling B, Lindgren M, 2004. Assessment model validity document FARF31. SKB R-04-51, Svensk Kärnbränslehantering AB.

Fogler H S, 2019. Elements of chemical reaction engineering. 6th ed. Prentice Hall.

Fuhrmann M, Bajt S, Shoonen M A A, 1998. Sorption of iodine on minerals investigated by X-ray absorption near edge structure (XANES) and ^{125}I tracer sorption experiments. Applied Geochemistry 13, 127–141.

Hakanen M, Ervanne H, Puukko E, 2014. Safety case for the disposal of spent nuclear fuel at Olkiluoto: Radionuclide migration parameters for the geosphere. Posiva 2012-41, Posiva Oy, Finland.

Hanrahan G, Lu K, 2006. Application of factorial and response surface methodology in modern experimental design and optimization. Critical Reviews in Analytical Chemistry 36, 141–151.

Hedström M, Ekvy Hansen E, Nilsson U, 2016. Montmorillonite phase behaviour. Relevance for buffer erosion in dilute groundwater. SKB TR-15-07, Svensk Kärnbränslehantering AB.

ICRP, 2012. Compendium of dose coefficients based on ICRP Publication 60. Amsterdam: Elsevier. (ICRP Publication 119; Annals of the ICRP 41 (Suppl.))

Joyce S, Simpson T, Hartley L, Applegate D, Hoek J, Jackson P, Swan D, Marsic N, Follin S, 2010. Groundwater flow modelling of periods with temperate climate conditions – Forsmark. SKB R-09-20, Svensk Kärnbränslehantering AB.

Kulmala S, Hakanen M, 1993. The solubility of Zr, Nb and Ni in groundwater and concrete water, and sorption on crushed rock and cement. Report YJT-93-21, Nuclear Waste Commission of Finnish Power Companies.

Kulmala S, Hakanen M, Lindberg A, 1998. Sorption of iodine on rocks from Posiva investigation sites. Posiva 98-05, Posiva Oy, Finland.

Lindgren M, Gylling B, Elert M, 2002. FARF31 Version 1-2. User's guide. SKB TS-02-03, Svensk Kärnbränslehantering AB.

Neretnieks I, 1980. Diffusion in the rock matrix: An important factor in radionuclide retardation? Journal of Geophysical Research: Solid Earth 85, 4379–4397.

Nilsson K, Byegård J, Selnert E, Widestrand H, Höglund S, Gustafsson E, 2010. Äspö Hard Rock Laboratory. Long Term Sorption Diffusion Experiment (LTDE-SD) Results from rock sample analyses and modelling. SKB R-10-68, Svensk Kärnbränslehantering AB.

Norman S, Kjellbert N, 1990. FARF31 – A far field radionuclide migration code for use with the PROPER package. SKB TR 90-01, Svensk Kärnbränslehantering AB.

Painter S, Mancillas J, 2013. MARFA user's manual: migration analysis of radionuclides in the far field. Posiva Working Report 2013-01, Posiva Oy, Finland.

Randall M, 2012. Review of radionuclide sorption on bentonite and Forsmark bedrock material. SSM Technical Note 2012:63, Swedish Radiation Safety Authority.

Rearden B T, Jessee M A (eds), 2016. SCALE Code System. ORNL/TM-2005/39, Version 6.2.1, Oak Ridge National Laboratory, TN.

Sandström B, Stephens M, 2009. Mineralogy, geochemistry, porosity and redox properties of rocks from Forsmark. Compilation of data from the regional model volume for SR-Site. SKB R-09-51, Svensk Kärnbränslehantering AB.

Selnert E, Byegård J, Widestrand H, Carlsten S, Döse C, Tullborg E-L, 2009. Bedrock transport properties. Data evaluation and retardation model. Site descriptive modelling, SDM-Site Laxemar. SKB R-08-100, Svensk Kärnbränslehantering AB.

Singh B, 2016. Nuclear Data Sheets for A = 79. Nuclear Data Sheets 135, 193–382.

Singh S, Jain A K, Tuli J K, 2011. Nuclear Data Sheets for A = 222. Nuclear Data Sheets 112, 2851–2886.

SKB, 2010a. Spent nuclear fuel for disposal in the KBS-3 repository. SKB TR-10-13, Svensk Kärnbränslehantering AB.

SKB, 2010b. Radionuclide transport report for the safety assessment SR-Site. SKB TR-10-50, Svensk Kärnbränslehantering AB.

SKB, 2010c. Data report for the safety assessment SR-Site. SKB TR-10-52, Svensk Kärnbränslehantering AB.

SKB, 2010d. Corrosion calculations report for the safety assessment SR-Site. SKB TR-10-66, Svensk Kärnbränslehantering AB.

SKB, 2010e. Design, production and initial state of the canister. SKB TR-10-14, Svensk Kärnbränslehantering AB.

SKB, 2011. Long-term safety for the final repository for spent nuclear fuel at Forsmark. Main report of the SR-Site project. SKB TR-11-01, Svensk Kärnbränslehantering AB.

SKB, 2014. Biosphere synthesis report for the safety assessment SR-PSU. SKB TR-14-06, Svensk Kärnbränslehantering AB.

SKB, 2015. Radionuclide transport and dose calculations for the safety assessment SR-PSU. Revised edition. SKB TR-14-09, Svensk Kärnbränslehantering AB.

SKB, 2022a. Post-closure safety for the final repository for spent nuclear fuel at Forsmark – Main report, PSAR version. SKB TR-21-01, Svensk Kärnbränslehantering AB.

SKB, 2022b. Radionuclide transport report – PSAR version. SKB TR-21-07, Svensk Kärnbränslehantering AB.

Tang D, Frind E, Sudicky E, 1981. Contaminant transport in fractured porous media: Analytical solution for a single fracture. Water Resources Research 17, 555–564.

Vahlund F, Hermansson H, 2006. Compulink. Implementing the COMP23 model in Simulink. SKB R-06-86, Svensk Kärnbränslehantering AB.

Vilks P, Miller N, Stanchell F, 2005. Laboratory program supporting SKB's long term diffusion experiment. Report 06819-REP-01300-10111-R00, Ontario Power Generation, Nuclear Waste Management Division, Canada.

Werme L O, Johnson L H, Oversby V M, King F, Spahiu K, Grambow B, Shoesmith D W, 2004. Spent fuel performance under repository conditions: A model for use in SR-Can. SKB TR-04-19, Svensk Kärnbränslehantering AB.

Widestrand H, Byegård J, Selnert E, Skålberg M, Höglund S, Gustafsson E, 2010a. Long Term Sorption Diffusion Experiment (LTDE-SD). Supporting laboratory program – Sorption diffusion experiments and rock material characterisation. With supplement of adsorption studies on intact rock samples from the Forsmark and Laxemar site investigations. SKB R-10-66, Svensk Kärnbränslehantering AB.

Widestrand H, Byegård J, Nilsson K, Höglund S, Gustafsson E, Kronberg M, 2010b. Long Term Sorption Diffusion Experiment (LTDE-SD). Performance of main in situ experiment and results from water phase measurements. SKB R-10-67, Svensk Kärnbränslehantering AB.

Zhao P, Zavarin M, Dai Z, Kersting A B, 2020. Stability of plutonium oxide nanoparticles in the presence of montmorillonite and implications for colloid facilitated transport. Applied Geochemistry 122, 104725. doi:10.1016/j.apgeochem.2020.104725

Appendix A

Handling of instant release fraction

Overview of radionuclide release processes

In SR-Site and PSAR, radionuclide release from a damaged canister was apportioned into three separate source terms. These were the initial release fraction (IRF), the corrosion release fraction (CRF), and the spent fuel dissolution release fraction (DRF). Radionuclide release associated with these source terms occurs on different time scales. The instant release fraction consists of radionuclides that have segregated to the gap between the fuel and cladding as well as grain boundary porosity of fuel elements. The instant release fraction is also conceptualised to include the inventory of so-called "crud" deposits on the outer surface of the cladding (i.e., mineral precipitates formed during reactor operation). For C-14, part of the inventory in the fuel cladding is included as well as the Ag-108m and Cd-113m inventories in the Ag-In-Cd alloy of the control rods.

In SR-Site and PSAR, the instant release fraction was assumed to be mobilised immediately on contact with water without any solubility limitation. This is a relatively pessimistic assumption that is likely to overestimate the peak fluxes associated with the instant release. In the SR-Site and PSAR calculations, the entire IRF inventory, apart from Tc-99, was assumed to reach the biosphere within a year after canister failure. For the CRF, radionuclides were assumed to be released at a constant rate due to corrosion over a defined time interval. In the deterministic modelling scenario, the uniform release rate (mol/y) was calculated for each radionuclide by taking the product of the CRF and the total inventory and dividing it by the corrosion time (1 000 y). The corrosion time was pessimistically estimated based on the time required to fully corrode the thinnest Inconel spacers (~0.3 mm) assuming an average anoxic corrosion rate for stainless steel and nickel-based alloys of 0.15 μm/year. For the corrosion release fraction, solubility limits need to be taken into account.

The processes governing the dissolution of the spent fuel matrix is more complex than can be covered here, although a very good overview can be found in Werme et al. (2004) and the Data Report to SR-Site (SKB 2010c). Although the UO_2 ceramic comprising the fuel elements is stable under anoxic conditions, it will dissolve slowly at a rate determined by the chemical environment in the canister/deposition hole and the rate at which dissolving solutes are transported away from the deposition hole by flowing water. Even in the absence of flowing water, the fuel is conceptualised to undergo "conversion" due to oxidative dissolution related to oxidising species associated with water radiolysis. Based on data from experimental studies, a pessimistic linear dissolution rate with a best estimate of 10^{-7} y^{-1} was assumed for the rate of spent fuel conversion in the SR-Site and PSAR deterministic cases (i.e., implying a spent fuel lifetime of 10 My).

For the dissolution release, a similar calculation procedure was adopted as for the modelling of corrosion release. Here, the uniform release rate (mol/y) was calculated for each radionuclide by taking the product of the DRF and the total inventory and dividing it by the spent fuel conversion time (10 My). Since the inventory changes in the fuel matrix over time as result of decay, the release rates of individual radionuclides are not constant. Similarly to the handling of corrosion release, solubility limitations must be considered for elements mobilised during the spent fuel dissolution/conversion.

In SR-Site and PSAR, the instant release fraction was not modelled explicitly in transport calculations but handled in a separate screening calculation where peak annual doses were quantified. In 2013, the Swedish Radiation Safety Authority (SSM) requested supplementary information concerning, among other things, the inclusion of the instant release fraction in calculations of the far-field release. In a previous report (Crawford and Löfgren 2019), the instant release fraction was modelled in an integrated fashion together with the corrosion and dissolution fractions. In the previous work, the same assumption was made as in SR-Site and PSAR that the instant release occurs as a constant concentration pulse of exactly 1 y duration, although with regard to the near field boundary condition rather than far-field arrival time.

In this report, we have attempted to expand on the previous work and include a more realistic account of the instant release by modelling the canister deposition hole as a continuous stirred tank reactor (CSTR) as is frequently encountered in the Chemical Engineering literature (e.g., Fogler 2019). The following sections contain an account of the simplified approach adopted in the work for modelling the release of specific radionuclides of interest.

Derivation of CSTR reactor model for the near-field boundary condition

Assuming buffer erosion has occurred to the extent that the canister holding the spent fuel is completely corroded, direct release of radionuclides to groundwater will occur. In this case, water flows by free advection through the canister hole and there is effectively no transport resistance for mass transfer. Radionuclides leached from the spent fuel will reach a concentration level that depends on the relative rate of dissolution and flow through the canister hole. If the flow is very low, solubility limits of some radionuclides might be exceeded leading to secondary mineral precipitation. In principle, this sets an upper limit to the concentration levels that can be achieved in the outflowing groundwater. For some radioelements such as U and Th, limitations on mobility prescribed by solubility limits can be a conservative assumption. In the case of the $4n + 2$ chain, for example, low solubility of U-238 and Th-230 gives rise to higher fluxes of Ra-226 which is the dose dominant radionuclide at long times in the scenarios studied in this work. Radioelements that form trivalent and tetravalent species are sufficiently strongly hydrolysed that they can form intrinsic colloidal precipitates (also known as "eigencolloids"). This is particularly the case for Pu(IV), although the formation and persistence of such colloids under repository conditions in the absence of strong geochemical gradients is unclear.

In cases where buffer integrity is retained, the bentonite acts as a colloid filter preventing any intrinsic colloidal precipitates from escaping the canister hole. Since the buffer is assumed to be completely eroded in the corrosion case, migration of intrinsic colloids potentially formed by precipitating radionuclides will not be hindered. In the case of Pu(IV), recent work by Zhao et al. (2020) suggests that dilution below the saturation limit of amorphous hydrous PuO_2 when undergoing transport in the geosphere will permit intrinsic colloids to dissolve at a sufficiently fast rate that they will not be significant for long distance transport. Sorption of radionuclides on bentonite and other natural carrier colloids ("pseudocolloids"), however, might be more important for long range transport, particularly if desorption is kinetically hindered (irreversible) on the timescale of transport. In SR-Site and PSAR, the effect of colloid mediated transport was modelled as part of the "hypothetical residual scenarios" as separate case studies to bound the potential impact on dose rates (see SKB 2010b). In the present work, we neglect colloid mediated transport and focus on the central corrosion case from SR-Site and PSAR as being most relevant for identifying a prioritised list of elements for in-depth study of sorption properties. This might be revisited in later work if deemed important.

If flow rates are sufficiently high, concentration levels will be too low for precipitation of most solid phases to occur, although there are exceptions. In this section, we derive the mass balance equations for a canister hole where buffer erosion has occurred to the extent that free flow and direct contact of spent fuel with the groundwater can occur. Firstly, we derive the mass balance equations for the more general case where instant-, corrosion-, and dissolution-release fractions are modelled concomitantly. Then we present the simplified case where only the instant release fraction is considered. Although we can use the general formulation to calculate a complete near-field boundary condition (which is useful for quickly exploring the parameter space of release and transport for arbitrary hydrodynamic conditions), the simplified formulation considering only the instant release fraction is that which has been used to supplement the SKB supplied near-field boundary condition[4] (SKB 2022b) which doesn't include the instant release fluxes.

CSTR model for a single decaying solute (IRF, CRF and DRF fractions)

Assuming a continuously stirred tank reactor (CSTR) analogue of a canister deposition hole, the mass balance for a single nuclide undergoing decay can be written as:

$$\left(1+K_d m_b\right)\frac{dc}{dt} = \left(r_{d(t)} + r_{c(t)}\right)\varphi_{n(t)} - \frac{q}{V}c - \lambda_r\left(1+K_d m_b\right)c + k_m\left(1-\frac{c}{c_{eq}}\right)n_s \qquad \text{(A-1)}$$

[4] Additional information may be found in SKBdoc 1929341 ver 1.0 – Radionuclide transport calculations for the PSAR.

If there is an immobile secondary mineral present, its mass balance is given by:

$$\frac{dn_s}{dt} = -\left(k_m \left(1 - \frac{c}{c_{eq}} \right) + \lambda_r \right) \left(n_s + \xi \right) \tag{A-2}$$

Where,

$$\xi = \begin{cases} 0 & \text{if} \quad c/c_{eq} < 1 \\ 10^{-6} \cdot c_{sol} & \text{if} \quad c/c_{eq} > 1 \,,\, n_s < 10^{-6} \cdot c_{sol} \end{cases} \tag{A-3}$$

The variables in Equations A-1 and A-2 are:

V	(m^3)	water-filled volume of (buffer-eroded) canister deposition hole
m_b	(kg/m^3)	specific mass of equilibrated solids in canister deposition hole
n_s	(mol/m^3)	molar concentration of secondary solid phase formed by precipitation of radionuclide
ξ	(mol/m^3)	nucleation constant (intended to force a nucleation event if solution is oversaturated, although no secondary mineral is initially present)
q	(m^3/y)	flow rate through deposition hole
c	(mol/m^3)	aqueous molar concentration of solute in deposition hole (assumed well mixed)
c_{eq}	(mol/m^3)	aqueous saturation concentration (solubility) of solute
$r_{c(t)}$	($1/m^3y$)	specific rate of corrosion (assumed zero-order process)
$r_{d(t)}$	($1/m^3y$)	specific rate of spent fuel dissolution (assumed zero-order process)
$\varphi_{n(t)}$	(mol)	molar inventory of radionuclide at time, t
λ_r	(1/y)	radioactive decay constant ($\lambda_r = \ln(2)/t_{½}$)
K_d	(m^3/kg)	sorption coefficient for adsorption to residual solids in canister deposition hole
k_m	(1/y)	secondary mineral, far-from-equilibrium kinetic rate of dissolution-precipitation.

For calculating near-field boundary condition fluxes, it is adequate to assume an arbitrarily high value for the kinetic constant, k_m so that the precipitation-dissolution process is maintained approximately in local equilibrium (say, $k_m \sim 10^6\ y^{-1}$). Given that the solubility is only approximately specified, this is sufficiently accurate for purpose. The nucleation constant, ξ is a simplified means of forcing an initial nucleation event in situations where the solubility of the radionuclide is exceeded although no secondary mineral is initially present. It can be set to an arbitrarily low numerical fraction of the solubility without having a significant impact on the results.

Equation A-1 can be rearranged to give:

$$\frac{dc}{dt} = \alpha \left(\left(r_{d(t)} + r_{c(t)} \right) \varphi_{n(t)} + k_m n_s \right) - \left(\alpha \left(q/V + \left(k_m / c_{eq} \right) n_s \right) + \lambda_r \right) c \tag{A-4}$$

Where, the storage capacity parameter, α for the canister deposition hole is given by:

$$\alpha = \frac{1}{1 + K_d m_b} \tag{A-5}$$

The equations describing the specific rate of release for the corrosion and dissolution release fractions are:

$$r_{c(t)} = \frac{f_c}{V} \cdot \frac{1}{t_c} \cdot \left(1 - H\left[t - t_c\right]\right) \tag{A-6}$$

$$r_{d(t)} = \frac{f_d}{V} \cdot \frac{1}{t_d} \cdot \left(1 - H\left[t - t_d\right]\right) \tag{A-7}$$

Where, t_c (y) is the time required for complete mobilisation of the corrosion release fraction (10^3 y) and f_c is the corrosion release fraction. Similarly, for the dissolution release fraction, t_d (y) is the characteristic time for dissolution of the spent fuel (10^7 y), and f_d is the dissolution release fraction. In both equations, $H[t-\tau]$ is the boxcar function which is equal to zero at times less than τ, and unity thereafter. The boxcar function defines the time schedule of the release where τ is the time at which the corrosion (t_c) or spent fuel dissolution (t_d) reaches its conclusion.

If the radionuclide is not a member of a decay chain, $\varphi_{n(t)}$ is defined simply as:

$$\varphi_{n(t)} = \varphi_{n(0)} \exp\left(-\lambda_r t\right) \tag{A-8}$$

Where, $\varphi_{n(0)}$ is the initial inventory (mol) of the radioelement in the spent fuel at the time of canister failure ($t = 0$). The instant release fraction is assumed to be immediately dissolved in the water filling the deposition hole at the moment of canister failure and therefore defines the initial condition for the integration of Equation A-4. If there is initially no secondary mineral phase present for the dissolving radionuclide, we would have:

$$\begin{aligned} c_0 &= \alpha \frac{f_i}{V} \cdot \varphi_{n(0)} \qquad \left(c_0 < c_{eq}\right) \\ n_{s0} &= 0 \end{aligned} \tag{A-9}$$

Where f_i is the instant release fraction. If the solubility, c_{eq} is exceeded already due to the instant release, we would have instead:

$$\begin{aligned} c_0 &= c_{eq} \qquad \left(c_0 \geq c_{eq}\right) \\ n_{s0} &= \frac{f_i}{V} \cdot \varphi_{n(0)} - c_{eq} \end{aligned} \tag{A-10}$$

In the general case, the solution of Equation A-4 (including corrosion and dissolution release and where the solubility limit is exceeded) requires a numerical integration. If the solubility limit is not exceeded, however, then a simplified approach is possible whereby the contributions of instant, corrosion, and dissolution release can be solved separately using an analytical approach and then added in post processing. This is useful as it also allows one to plot the separate contributions of the different fractions in a transparent fashion that is not possible to do if Equation A-4 is solved numerically.

Simplified analytical solution for undersaturated solute and no secondary mineral

For the limiting case, where $n_s = 0$ and the aqueous concentration never reaches the solubility limit, the mass balance is wholly linear which implies that the contribution of each fraction (i.e. IRF, CRF, and DRF) can be calculated separately and added in post-processing. The overall mass balance is:

$$\frac{dc}{dt} = \alpha\left(r_{d(t)} + r_{c(t)}\right)\varphi_{n(t)} - \left(\alpha\left(q/V\right) + \lambda_r\right)c \tag{A-11}$$

Since the system is linear in concentration, Equation A-11 can be written as the summed contribution of the three spent fuel fractions:

$$\frac{dc_{irf}}{dt} = -\left(\alpha\left(q/V\right) + \lambda_r\right)c_{irf} \tag{A-12}$$

$$\frac{dc_{crf}}{dt} = \alpha r_{c(t)} \varphi_{n(0)} \exp\left(-\lambda_r t\right) - \left(\alpha\left(q/V\right) + \lambda_r\right) c_{crf} \tag{A-13}$$

$$\frac{dc_{drf}}{dt} = \alpha r_{d(t)} \varphi_{n(0)} \exp\left(-\lambda_r t\right) - \left(\alpha\left(q/V\right) + \lambda_r\right) c_{drf} \tag{A-14}$$

Where, the total concentration is given by the sum of individual contributions:

$$c\left(t\right) = c_{irf}\left(t\right) + c_{crf}\left(t\right) + c_{drf}\left(t\right) \tag{A-15}$$

For the instant release fraction, there is no ongoing dissolution and the initial condition is defined directly by the IRF:

$$c_{irf(0)} = \alpha \frac{f_i}{V} \cdot \varphi_{n(0)} \qquad \left(c_0 < c_{eq}\right) \tag{A-16}$$

For the CRF and DRF, however, we have the initial conditions:

$$c_{crf(0)} = 0 \tag{A-17}$$

$$c_{drf(0)} = 0 \tag{A-18}$$

The falling concentration period ($t > 0$) during elution of the IRF pulse is described by:

$$c_{irf} = c_{irf(0)} \exp\left(-\kappa t\right) \tag{A-19}$$

Where,

$$\kappa = \alpha\left(q/V\right) + \lambda_r \tag{A-20}$$

For the corrosion release fraction, we have for the initial phase of active dissolution:

$$c_{crf} = b_{crf}\left(\frac{\exp\left(-\lambda_r t\right) - \exp\left(-\kappa t\right)}{\kappa - \lambda}\right) \tag{A-21}$$

Where,

$$b_{crf} = \alpha\left(\frac{f_c}{V} \cdot \frac{1}{t_c}\right)\varphi_{n(0)} \tag{A-22}$$

For the falling concentration period after the CRF is exhausted ($t > t_c$), we have instead:

$$c_{crf} = b_{crf}\left(\frac{\exp\left(-\lambda_r t_c\right) - \exp\left(-\kappa t_c\right)}{\kappa - \lambda_r}\right) \cdot \exp\left(-\kappa\left(t - t_c\right)\right) \qquad \left(t > t_c\right) \tag{A-23}$$

For the dissolution release fraction, we have for the initial phase of active dissolution:

$$c_{drf} = b_{drf}\left(\frac{\exp\left(-\lambda_r t\right) - \exp\left(-\kappa t\right)}{\kappa - \lambda_r}\right) \qquad \left(t \le t_d\right) \tag{A-24}$$

Where,

$$b_{drf} = \alpha\left(\frac{f_d}{V} \cdot \frac{1}{t_d}\right)\varphi_{n(0)} \tag{A-25}$$

For the falling concentration period after the DRF is exhausted ($t > t_d$), we have:

$$c_{drf} = b_{drf}\left(\frac{\exp\left(-\lambda_r t_d\right) - \exp\left(-\kappa t_d\right)}{\kappa - \lambda_r}\right) \cdot \exp\left(-\kappa\left(t - t_d\right)\right) \qquad \left(t > t_d\right) \tag{A-26}$$

Considerations related to the storage capacity parameter, α

While the storage capacity parameter given in Equation A-5 is nominally intended to consider the possibility of incompletely eroded buffer which might provide additional transport retardation, the concept has been extended in this work to additionally consider diffusive-sorptive retention in the rock matrix on the outer surfaces of the deposition borehole as illustrated in Figure A-1.

For the calculations of deposition hole elution with the CSTR model, the geometric data shown in Table A-1 are assumed. These are taken from the canister design report (SKB 2010e) and are presumed to be internally consistent with the COMP23 model used to calculate the near-field boundary condition of the corrosion and dissolution release fraction in this work.

Table A-1. Geometric parameters for the CSTR model of deposition hole radionuclide elution taken mostly from the canister design report (SKB 2010e). In this work, the fraction of residual buffer f_B is assumed to be zero, although the possibility of residual buffer is considered in the model derivation.

Parameter	Value	Comment
d_o	1.75 m	Outer diameter of deposition hole.
d_c	1.05 m	Outer diameter of canister.
h	7.935 m	Deposition hole length.
h_c	4.835 m	Canister length.
V_0	19.09 m^3	Volume of deposition hole.
V_c	4.19 m^3	Volume of canister.
V_b	14.90 m^3	Original volume of buffer ($V_b = V_0 - V_c$).
V_f	0.22 m^3	Volume of spent fuel ($V_f = m_{snf}/\rho_{snf} - 2.3823/10.97$).
V_e	18.87 m^3	Effective volume of deposition hole ($V_e \approx V_0 - V_f$) after canister corrosion.
f_B	~0	Fraction of non-eroded buffer remaining in deposition hole (neglected in the present work).
V	18.87 m^3	Water filled volume of deposition hole excluding buffer ($V \approx V_e - f_B \times V_b$).
A_0	46.03 m^2	Rock matrix adjacent surface area of deposition hole (including floor of deposition hole but not top which is open to backfill tunnel).
q	0.733 m^3/y	Equivalent flowrate through the canister deposition hole used to calculate flux and elution rate.
t_{wc}	25.74 y	Equivalent water residence time of deposition hole ($t_{wc} = V/q$).

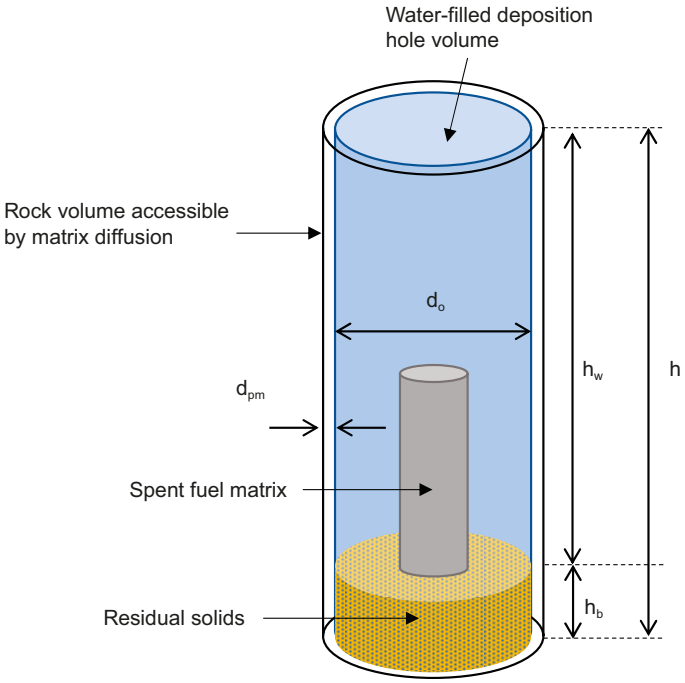

Figure A-1. *Conceptual illustration of a canister deposition hole showing residual solids (buffer and corrosion products), undissolved spent fuel, and water-filled volume (post buffer-erosion).*

Estimation of equivalent sorptive mass in deposition hole

For the matrix diffusion-sorption on deposition hole outer surfaces, we calculate an approximate effective penetration depth based on the approach documented in Crawford and Löfgren (2019). The effective penetration depth is approximately given by the relation:

$$\delta_m \approx \frac{D_e F_c}{4 \cdot \mathrm{erfc}^{-1}\left(0.5\right)^2} = 1.0991 \cdot D_e F_c \tag{A-27}$$

Where, F_c (m/y) is the equivalent F-factor for the deposition hole. The F-factor is given by the mass-transfer surface area of rock bordering the deposition hole divided by the advective flowrate through the hole. For the central corrosion case considered in this work, we have:

$$F_c \approx \frac{A_c}{q_c} = \frac{46.03}{0.733} = 62.8 \text{ y/m} \tag{A-28}$$

The effective penetration depth, δ_m is the equivalent depth of rock matrix which if instantaneously equilibrated would give approximately the same retardation effect as would be calculated using a proper description of matrix diffusive-sorptive mass transfer. It is only an approximate measure since it only considers the median retarded residence time of a solute in the deposition hole and does not consider the long tailing effects of matrix diffusion. For a solute that undergoes decay, however, the value given by Equation A-27 may overestimate the accessible rock matrix. For a decaying radionuclide, the "maximum" penetration depth is given by the alternative expression (Crawford and Löfgren 2019):

$$\delta_{\max} = \sqrt{\frac{D_p}{R_p \lambda_r}} \tag{A-29}$$

In practice, for the estimation of accessible rock matrix in this work we calculate the penetration depth using Equation A-27 as well as A-29 and then take whichever is the minimum value so as to not to overestimate the retardation effect. To additionally simplify calculations in the present work, the residual solid materials in the deposition hole are assumed to have the same K_d values as the recommended values assigned to the rock matrix. Obviously, this is not correct for residual clay buffer (and oxide products of corrosion if there are any), so the mass of residual buffer is rescaled to an "effective" value such that the sorptive storage capacity is correctly accounted for. If a fraction, f_B of initially installed buffer remains in the deposition hole, the actual mass of residual buffer is given by:

$$m_{\mathrm{MX80}} = f_B \cdot V_b \cdot \rho_{bw} \tag{A-30}$$

Here, ρ_{bw} is the wet density of the (MX-80 bentonite) water-saturated clay buffer at installation which is taken to be ~1 800 kg/m^3 (Hedström et al. 2016). The mass of rock surrounding the deposition hole that is equilibrated can be calculated from the estimated effective penetration depth using the expression:

$$m_{\mathrm{rock}} = \rho_{\mathrm{s}} \left(1 - \varepsilon_p\right) \frac{\pi}{4} \left(h \left(\left(d_o + 2\delta_m \right)^2 - d_o^2 \right) + \delta_m d_o^2 \right) \tag{A-31}$$

For a relative long-lived radionuclide that is not subject to anion exclusion, the effective penetration depth calculated using Equation A-27 could be as much as 0.046 mm implying a diffusively accessible rock mass on the order of 3.96 kg using Equation A-31. Assuming that cation exchange capacity (CEC) is a reasonable proxy for relative sorptivity, the mass of diffusion-accessible rock and residual buffer can be combined to give an equivalent mass of solids using the expression:

$$m_b = m_{\mathrm{rock}} + m_{\mathrm{MX80}} \cdot \left(\frac{\mathrm{CEC}_{\mathrm{MX80}}}{\mathrm{CEC}_{\mathrm{rock}}} \right) \approx m_{\mathrm{rock}} + m_{\mathrm{MX80}} \cdot \left(\frac{75}{1} \right) \tag{A-32}$$

In this work, we assume the CEC of 75 meq/100 g (MX-80 bentonite clay) to be approximately representative of residual buffer materials, while the CEC of Forsmark metagranite has been estimated to be on the order of 1 meq/100 g (Crawford 2010) for the purposes of K_d extrapolation. It should be noted that the above calculation of equivalent mass of buffer assumes that the residual, non-eroded buffer

is well-mixed slurry with the water in the deposition hole which might not always be a very good assumption. While the fact that the buffer has been eroded in the central corrosion case implies the loss of swelling pressure and sol formation, it is not clear in what state any residual clay should be expected to be. If the clay forms a gel layer or more compact plug-like residue at the bottom of the canister hole, then this can be considered in the model derivation.

"What-if" case for a plug of buffer solids residing at the bottom of the deposition hole

In this case, we simplify the problem by assuming that the rock wall occluded by the presence of the residual buffer "plug" is inaccessible and consider diffusive-sorptive transport into the plug in an analogous fashion as for the rock. If one neglects the additional presence of ~0.22 m^3 of spent fuel (which might also be expected to reside at the bottom of the deposition hole), the height, h_b of the buffer plug is obtained from a mass balance:

$$h_b = \frac{4 f_B V_b \left(\rho_{bw} / \rho_{bw}^* \right)}{\pi d_o^2} \tag{A-33}$$

Where, ρ_{bw}^* (kg/m^3) is the density of the residual clay in the canister hole as a gel plug, or otherwise less compact state than its initial saturated density at deposition, ρ_{bw} (kg/m^3). The mass of rock that is equilibrated then becomes:

$$m_{\text{rock}} = \rho_s \left(1 - \varepsilon_p\right) \frac{\pi}{4} \left(h - h_b\right) \left(\left(d_o + 2\delta_m\right)^2 - d_o^2 \right) \tag{A-34}$$

The effective penetration depth for diffusion-sorption in the clay is given by Equation A-27 or A-29, although using material properties specific for the clay instead. If the calculated penetration depth is greater than the physical depth of the clay, however, then the physical depth is the value that should be used as the effective depth for the purpose of the transport retardation calculation:

$$\delta_{\text{mb}} = \min\left[h_b, \delta_{\text{mb}}, \delta_{\max}\right] \quad \begin{cases} \delta_{\text{mb}} = 1.0991 \cdot D_{e(\text{clay})} F_{c(\text{clay})} \\ \delta_{\max} = \sqrt{\left(D_{p(\text{clay})} / R_{p(\text{clay})}\right) / \lambda_r} \end{cases} \tag{A-35}$$

Provided there is enough residual clay to cover the bottom of the deposition hole, the equivalent flow-wetted surface to flow ratio (F-factor) for the clay plug, $F_{c(\text{clay})}$ is given by:

$$F_{c(\text{clay})} \approx \frac{\pi d_o^2 / 4}{q} = \frac{2.4053}{0.733} = 3.28 \text{ y/m} \tag{A-36}$$

For the rock wall exposed to the water filled cavity of the deposition hole, we now have:

$$F_{c(rock)} \approx \frac{\pi\left(h - h_b\right) d_o}{q} \tag{A-37}$$

Since the height of buffer depends on the volume and density of the residual material (which are both unknown), an assumption needs to be made about the state of the clay before Equation A-37 can be evaluated. If one makes the very rough assumption that the density ratio ρ_{bw}/ρ_{bw}^* is approximately unity and only 1 % of the original buffer remains in the deposition hole, we would have a plug height, h_b equal to about 6.2 cm. The F-factor for the rock now becomes:

$$F_{c(rock)} \approx \frac{\pi\left(h - h_b\right) d_o}{q} = \frac{43.284}{0.733} = 59.1 \text{ y/m} \tag{A-38}$$

The void porosity of the water-saturated clay can be estimated from a volume balance (if its density is known) using the expression:

$$\varepsilon_p \approx \frac{\rho_w\left(\rho_{bc}-\rho_{bw}^*\right)}{\rho_{bw}^*\left(\rho_{bc}-\rho_w\right)} \tag{A-39}$$

Where, ρ_w is the density of water at the in situ temperature (~ 10^3 kg/m^3), ρ_{bc} is the crystallographic density of montmorillonite clay (2 765 m^3/kg), and ρ_{bw}^* is the saturated density of the residual buffer material. Since we have assumed a density ratio of unity for the residual buffer (i.e., $\rho_{bw}/\rho_{bw}^* \approx 1$), this implies a saturated porosity of about 0.3 in the present example. Based on Figure 5-9 in Crawford and Löfgren (2019), the effective diffusivity of the residual buffer plug would be on the order of 7×10^{-11} m^2/s. The effective penetration depth calculated using Equation A-35 for this effective diffusivity and F-factor would be roughly 0.8 cm (assuming a relatively long-lived nuclide). For the rock itself, we would have an effective penetration depth of 0.043 mm which is only slightly less than that calculated for the previous case without residual buffer. In the present example (f_B = 0.01), the effective mass of remaining buffer that can be diffusively equilibrated with water in the deposition hole is given by:

$$m_{\mathrm{MX80}} = \frac{\pi}{4}\delta_{mb} d_o^2 \rho_{bw}^* \approx 0.19 \text{ kg} \tag{A-40}$$

The corresponding effective mass of rock that can be diffusively equilibrated with water in the deposition hole is: $m_{\mathrm{rock}} = \rho_{\mathrm{s}}\left(1-\varepsilon_p\right)\frac{\pi}{4}\left(h-h_b\right)\left(\left(d_o+2\delta_m\right)^2 - d_o^2\right) \approx 3.72 \text{ kg}$ (A-41)

The total effective mass of residual buffer and diffusion accessible rock is given by Equation A-32:

$$m_b = m_{\mathrm{rock}} + m_{\mathrm{MX80}} \cdot \left(\frac{\mathrm{CEC}_{\mathrm{MX80}}}{\mathrm{CEC}_{\mathrm{rock}}}\right) \approx 3.72 + 0.19 \cdot \left(\frac{75}{1}\right) = 17.97 \text{ kg} \tag{A-42}$$

If we were to neglect the diffusive transport in the clay (1 % remaining of initial buffer mass), we would have instead:

$$m_b = m_{\mathrm{rock}} + m_{\mathrm{MX80}} \cdot \left(\frac{\mathrm{CEC}_{\mathrm{MX80}}}{\mathrm{CEC}_{\mathrm{rock}}}\right) \approx 3.96 + 268 \cdot \left(\frac{75}{1}\right) \approx 20 \cdot 10^3 \text{ kg} \tag{A-43}$$

Clearly, the neglection of diffusion in the residual buffer would lead to a significant overestimation of the sorptive capacity of the geological material in the deposition hole which might be non-conservative. In both cases, however, it is interesting to note that the clay component is overwhelmingly dominant, and the diffusion accessible rock can be neglected if there is any appreciable quantity of clay remaining in the deposition hole.

It should be noted that the mathematical treatment developed above only gives an approximate account of retardation processes associated with the rock and residual clay in the deposition hole. A more accurate calculation can be made using a frequency domain solution of the coupled transport problem and inverting the solution to the time plane using a numerical inverse Laplace transform, however, this is beyond the scope of the present work and only mentioned as a possibility if the need arises to calculate deposition hole retardation more accurately.

Calculations of near-field release using the CSTR-analogue model

In the COMP23 calculations of the near field boundary condition supplied by SKB, the volume of the deposition hole is assumed to be 1 m^3 based on the void space in the spent fuel canister at deposition. Furthermore, there is assumed to be no sorption in the deposition hole, which implies $\alpha = 1$ for all radionuclides. The COMP23 calculations assume a free volume which is easily 13–14 times less than that estimated in the previous section for a buffer-free deposition hole where the containment structure has completely corroded.

Although the assumed volume of 1 m^3 is substantially less than what would be expected in the case of catastrophic buffer loss, it is a relatively conservative assumption and has very limited impact on the results of far-field transport for the corrosion and dissolution fraction since the differences only affect the rapidity of the concentration "ramp-up" at the onset of advective flow conditions. This occurs on a timescale that is not relevant for the far-field transport as it relates to the breakthrough curves for the corrosion and dissolution release. For the instant release fraction, on the other hand, such assumptions can have a larger impact on the far-field breakthrough for the modelled radionuclide release. The assumption of a small mixing volume (and thus low water residence time) in the deposition hole may, or may not be a conservative assumption for the instant release fraction depending on the handling of radionuclide solubilities and the use of pulse – rather than basic-LDF factors for the subsequent calculation of far-field dose rates.

To check that our simplified model of near-field release gives similar results to COMP23, the model was run with the water-filled volume of the deposition hole, V set to 1 m^3. The results of this validation calculation (plotted in terms of activity flux) are shown in Figure A-2 for Cl-36 and show a good agreement with the analytical calculation for the sum of corrosion and dissolution release fractions. There is a slight difference in the total release after 10 ky although this because the COMP23 calculations neglect the instant release fraction. Since the dissolution release fraction, f_d is defined in the COMP23 calculations as $f_d = 1 - f_c$, the inclusion of an instant release pulse gives a slightly lower dissolution release flux in the analytical model. This also implies that the inclusion of an instant release pulse in calculations using the COMP23 calculated near-field boundary condition double counts the activity of the instant release fraction, although the effects of this are relatively insignificant for far-field calculations.

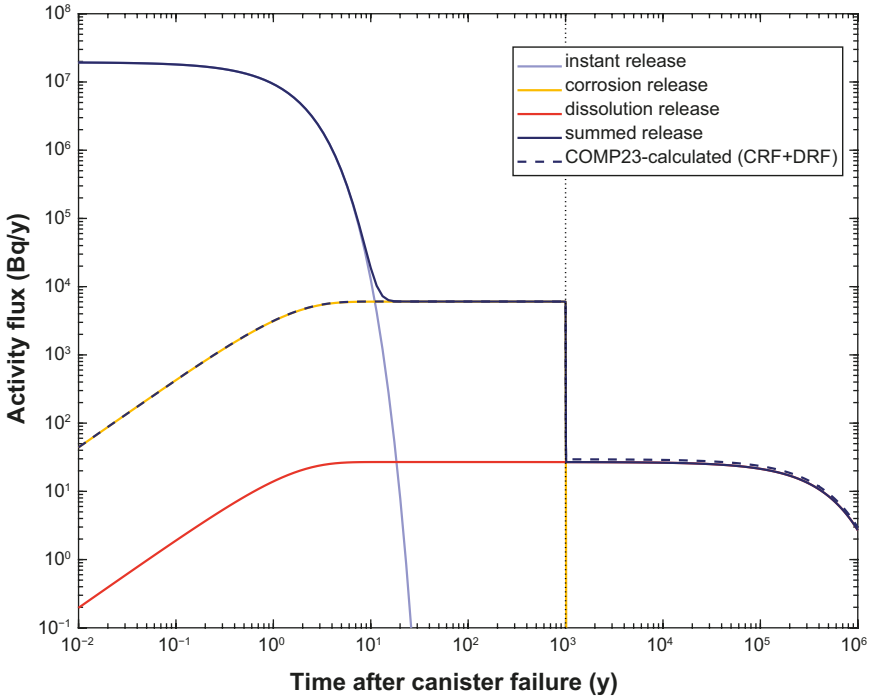

Figure A-2. *Validation case showing agreement between the simplified analytical model for the near-field boundary condition calculated using COMP23 (corrosion and dissolution release fraction only) for Cl-36 and assuming an effective deposition hole volume of 1 m^3. The slight discrepancy at later times is due to the dissolution release fraction being slightly higher in the COMP23 calculations since the instant release fraction is neglected. The vertical broken line indicates the conclusion of the corrosion release pulse at 1 ky.*

Although only the instant release fraction calculated using the analytical model is actually used in the present work (the corrosion and dissolution release fluxes are taken directly from the COMP23 simulations), the figures in this section include all contributions calculated by the analytical model to illustrate their relative importance. If the near-field release is calculated using the higher effective free volume estimate of 18.87 m^3 (see Table A-1) as well as matrix diffusive-sorptive retardation on rock wall surfaces, a much slower ramp-up of corrosion and dissolution release related fluxes occurs and the instant release pulse has both a longer persistence in time due to the slower elution and an order of magnitude decreased peak flux due to the greater dilution achieved in the larger deposition hole volume for the same flowrate (for non-sorbing solutes, the matrix diffusive effect is insignificant with $\alpha \approx 1$). This effect can be seen for Cl-36 in Figure A-3.

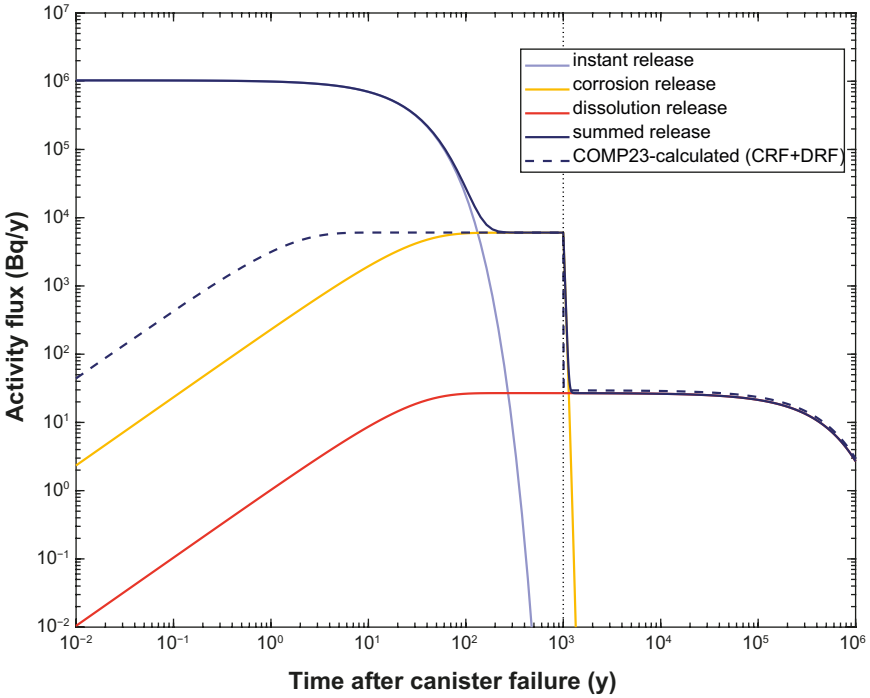

Figure A-3. *Comparison of near-field boundary condition for Cl-36 calculated using the simplified analytical model with the effective deposition hole volume, V set to 18.87 m^3 and retention by matrix diffusion-sorption on rock wall surfaces. For comparison, the COMP23 (corrosion and dissolution release fraction only) results are shown where V = 1 m^3. The slight discrepancy at later times is due to the dissolution release fraction being slightly higher in the COMP23 calculations since the instant release fraction is neglected. The vertical broken line indicates the conclusion of the corrosion release pulse at 1 ky.*

The near-field boundary condition calculated for Ni-59 is shown in Figure A-4 for the free volume case, V = 18.87 m^3 where matrix diffusion-sorption on rock wall faces is permitted. Here, also the free volume effect on water residence time has the greatest impact and rock matrix interaction plays only a minor role (α = 0.994). The corresponding calculation case for Se-79 is shown in Figure A-5 and shows the additional impact of the solubility limitation for Se-79. In this case the peak flux is truncated at the solubility limit (red broken line) and the near-field boundary condition must be calculated by numerical integration of Equations A-2 and A-4 (broken green curve).

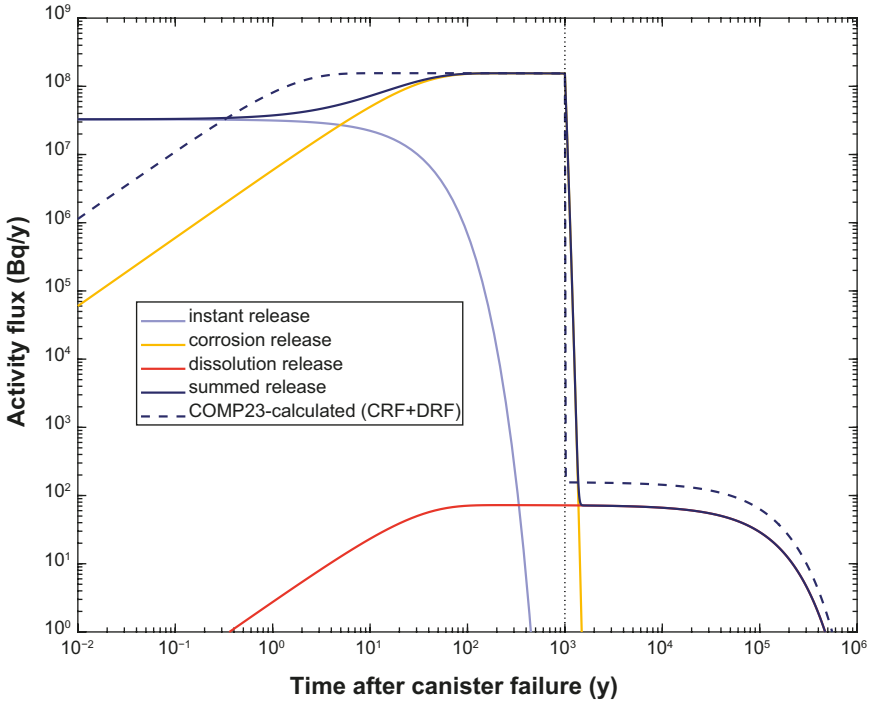

Figure A-4. *Comparison of near-field boundary condition for Ni-59 calculated using the simplified analytical model with the effective deposition hole volume, V set to 18.87 m^3 and retention by matrix diffusion-sorption on rock wall surfaces. For comparison, the COMP23 (corrosion and dissolution release fraction only) results are shown where V = 1 m^3 (no sorptive retention). The discrepancy at later times is due to the dissolution release fraction being slightly higher in the COMP23 calculations since the instant release fraction is neglected. The vertical broken line indicates the conclusion of the corrosion release pulse at 1 ky.*

As the flux of Se-79 is capped at a lower level by the solubility limit than what would otherwise be implied by the instant release fraction, the flux associated with the instant release persists over a longer time than if solubility is neglected. Since the COMP23 calculated near-field boundary condition does not consider solubility limitation of Se, this has also been neglected in the formulating the combined source term for the calculations made in this report and must therefore be considered as part of the overall description of uncertainty considering the analyses presented in this work.

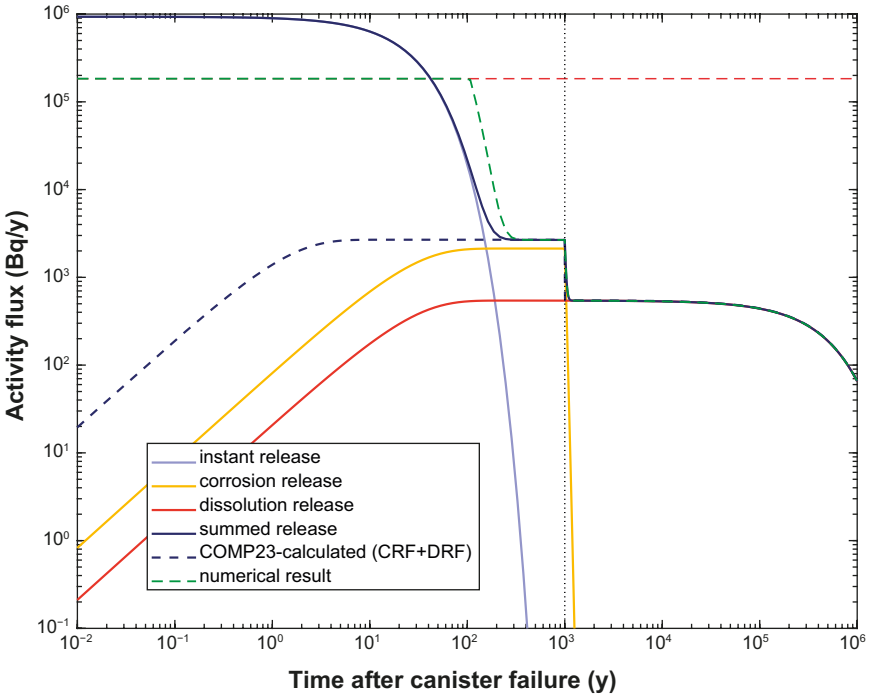

Figure A-5. *Comparison of near-field boundary condition for Se-79 calculated using the simplified analytical model with the effective deposition hole volume, V set to 18.87 m^3 and retention by matrix diffusion-sorption on rock wall surfaces. For comparison, the COMP23 (corrosion and dissolution release fraction only) results are shown where V = 1 m^3 (no sorptive retention). The solubility of Se is exceeded by the instantaneous release giving a different flux curve (broken green curve – numerically calculated) relative to the analytical solution. The broken red line indicates the solubility limit for Se. The vertical broken line indicates the conclusion of the corrosion release pulse at 1 ky.*

A similar result can be shown for Tc-99 in Figure A-6 and for Zr-93 in Figure A-7. While the solubility limit for Se and Tc is exceeded immediately due to the relatively large instant release fraction, the solubility limit for Zr is exceeded only after the corrosion release fraction starts to ramp up. In this situation the nucleation constant, ξ is required in Equation A-2 since the instant release does not quite reach the solubility limit instantaneously.

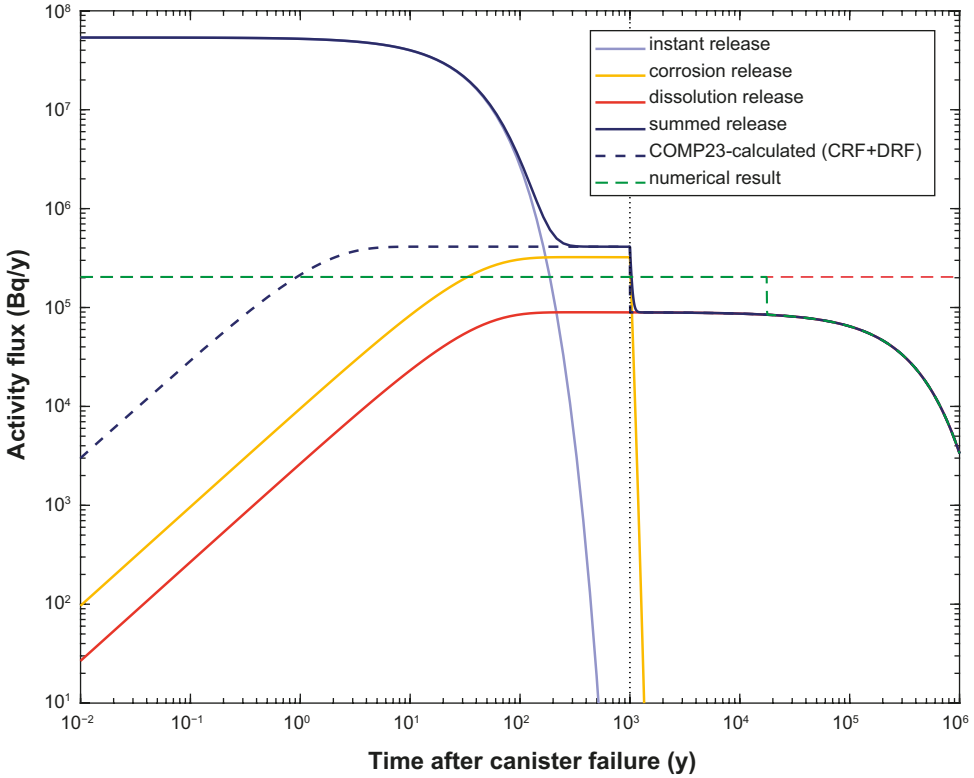

Figure A-6. *Comparison of near-field boundary condition for Tc-99 calculated using the simplified analytical model with the effective deposition hole volume, V set to 18.87 m^3 and retention by matrix diffusion-sorption on rock wall surfaces. For comparison, the COMP23 (corrosion and dissolution release fraction only) results are shown where V = 1 m^3 (no sorptive retention). The solubility of Tc is exceeded by the instantaneous release giving a different flux curve (broken green curve – numerically calculated) relative to the analytical solution. The broken red line indicates the solubility limit for Tc. The vertical broken line indicates the conclusion of the corrosion release pulse at 1 ky.*

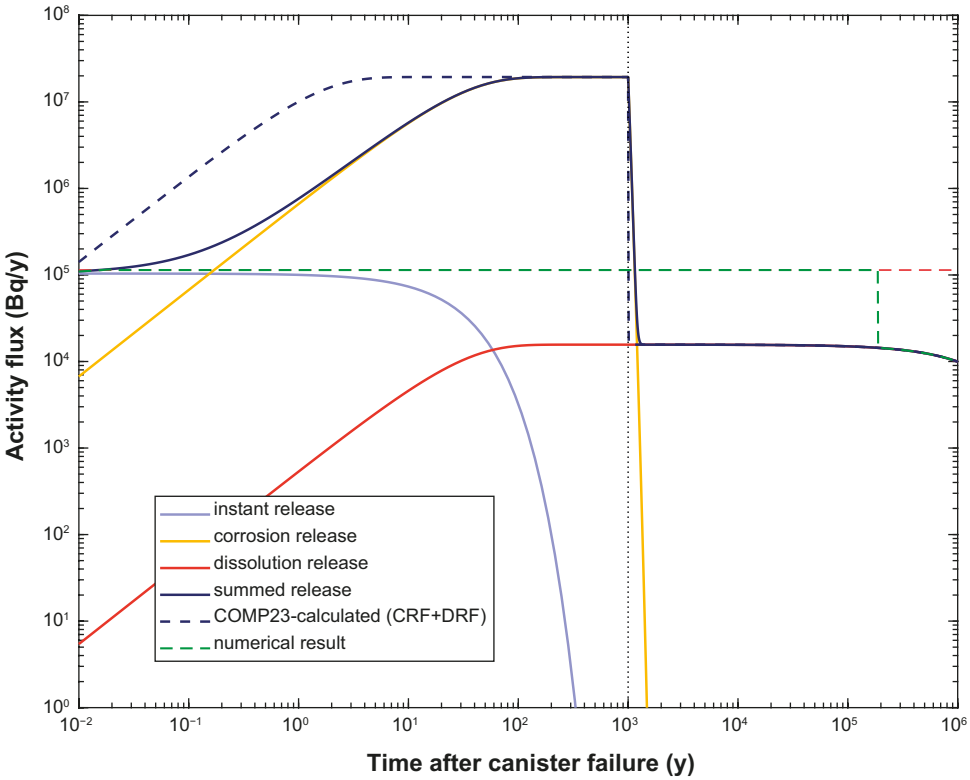

Figure A-7. *Comparison of near-field boundary condition for Zr-93 calculated using the simplified analytical model with the effective deposition hole volume, V set to 18.87 m^3 and retention by matrix diffusion-sorption on rock wall surfaces. For comparison, the COMP23 (corrosion and dissolution release fraction only) results are shown where V = 1 m^3 (no sorptive retention). The solubility of Zr is exceeded by the instantaneous release giving a different flux curve (broken green curve – numerically calculated) relative to the analytical solution. The broken red line indicates the solubility limit for Zr. The vertical broken line indicates the conclusion of the corrosion release pulse at 1 ky.*

Calculations of instant release in the present work

Given that the COMP23-calculated near field flux boundary condition is supplied by SKB for this work, only the boundary condition associated with the instant release fraction needs to be calculated. Since solubility limitations are neglected in the SR-Site/PSAR central corrosion case except for uranium and thorium, the flux-time curves for instant release are calculated using the simplified analytical expression:

$$N_{mol,irf} = \frac{\alpha}{t_{wc}} \cdot f_i \, \varphi_{n(0)} \cdot \exp\left(-\left(\frac{\alpha}{t_{wc}} + \lambda_r \right) t \right) \qquad \text{(mol/y)} \qquad \text{(A-44)}$$

As sorption in the near-field is also neglected in the COMP23-calculated near-field boundary condition, this has also been neglected in the calculations made in this work implying $\alpha = 1$. For non-sorbing or weakly sorbing radionuclides the effect is very small if the equivalent mass of sorbing solids in the deposition hole is modest, although for strongly sorbing radionuclides the flux may be decreased by a larger amount. The molar flux calculated using Equation A-44 can be converted to activity flux using the customary conversion:

$$N_{Bq,irf} = \left(N_{av} \cdot \frac{\ln(2)}{t_{½} \cdot \tau_{y2s}} \right) \cdot N_{mol,irf} \qquad \text{(Bq/y)} \qquad \text{(A-45)}$$

where, N_{av} is Avogadro's number (6.022×10^{23}) and τ_{y2s} is the number of seconds in a year (3.156×107 s/y), and $t_{½}$ (y) is the half-life of the migrating radionuclide. Since the radiotoxicity fluxes for instant release and corrosion-dissolution release fractions use different landscape dose factors, the total radiotoxicity flux is calculated using:

$$N_{Sv,tot} = LDF_{\text{pulse}} \cdot N_{Bq,irf} + LDF_{\text{basic}} \cdot \left(N_{Bq,crf} + N_{Bq,drf} \right) \qquad \text{(Sv/y)} \qquad \text{(A-46)}$$

Reference scenario for canister failure at 100 ky

The total boundary condition where near-field radiotoxicity flux is summed with the COMP23-calculated corrosion-dissolution radiotoxicity flux is plotted in Figure A-8 for the refence scenario of canister failure at 100 ky. Since the pulse LDF is typically much smaller than the basic LDF, the contribution of the instant release fraction to the total boundary condition is relatively minor with the exception of Tc-99, I-129, and Cs-135. In the case of Tc-99, however, the transport retardation in the far-field is sufficiently high that the same basic LDF is used for the pulse release. The different timescales of the pulse release (t_{wc} = 25.74 y) and corrosion-dissolution release (t_{wc} = 1.36 y) can be clearly seen from the inflexion point for the instant release dominated radionuclides relative to the timescale of corrosion and dissolution release "ramp-up". This is because the COMP23 calculation for the corrosion and dissolution release fractions assumes a much smaller free volume in the deposition hole (1 m^3) than our simplified CSTR model (18.87 m^3) for instant release. As discussed previously, this discrepancy has very little impact on the far-field calculation results for the corrosion-dissolution release fraction.

We use the deposition hole volume of 18.87 m^3 in this work, however, since it is more consistent with the reference scenario as it is defined (i.e., complete erosion of buffer, no transport resistance) than the lower value of 1 m^3 used in the COMP23 calculations. Furthermore, given that the aim of this work is to identify the most important dose determining radionuclides regarding sensitivity to altered K_d, it would be counterproductive to use overconservative parameter values for the instantaneous release since it may give a less credible result relative to the corrosion and dissolution release fractions which are only trivially impacted by the water residence time in the deposition hole.

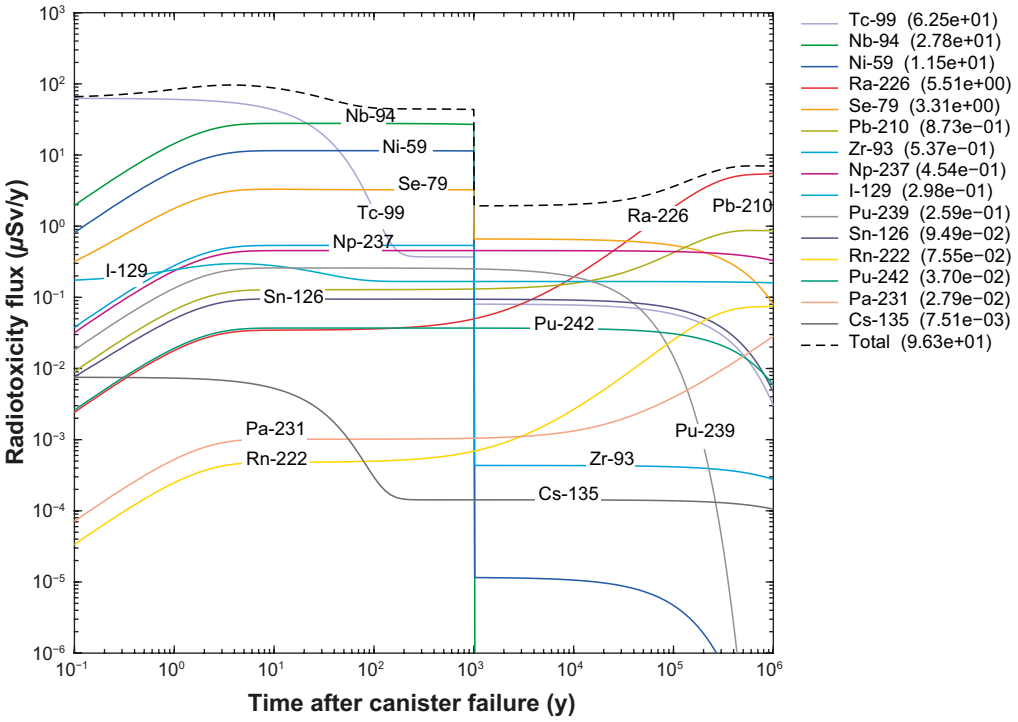

Figure A-8. *Combined near-field boundary condition for the instant release fraction (IRF) modelled as a CSTR system as well as corrosion and dissolution release fractions (CDRF) calculated by COMP23 for canister failure at 10^5 y. Data are presented as equivalent radiotoxicity fluxes (μSv/y) based on the LDF factors defined separately for IRF and CDRF release fractions. The time on the x-axis is in relation to canister failure. Only the top 15 radiotoxicity contributing radionuclides are plotted.*

For comparison with the CSTR-analogue model, a simplified boundary condition assuming a square pulse of 1 y duration was also modelled in this work. The molar flux leaving the deposition hole is defined using the following expression:

$$N_{mol,irf} = \left(\frac{f_{irf}}{t_{irf}}\right)\varphi_{n(0)}\exp\left(-\lambda_r t\right)\cdot\left(1-H\left[t-t_{irf}\right]\right) \qquad \text{(mol/y)} \qquad \text{(A-47)}$$

The results of this calculation are shown in Figure A-9. As can be seen from the peak flux annotated for the different radionuclides in the legend, the flux of Tc-99 in the square pulse case is roughly 25.8 times higher than that calculated by the CSTR-analogue model which roughly corresponds to the ratio of dilution volumes implicit in the two calculation methods. It should be noted that, in both cases, the solubility of Tc-99 is exceed by a considerable margin (at least 2–3 orders of magnitude) and even with the larger dilution volume of 18.87 m^3, the near-field flux attributed to instant release of Tc-99 is probably over-conservatively estimated. The fluxes of most radionuclides with an instant release fraction are higher in the square-pulse release calculation case relative to the corresponding fluxes calculated using the CSTR-analogue model. The sudden discontinuity in near-field radiotoxicity flux at 1 y in the square pulse case is due to the sudden disappearance of the instant release while the corrosion release fraction is still ramping up.

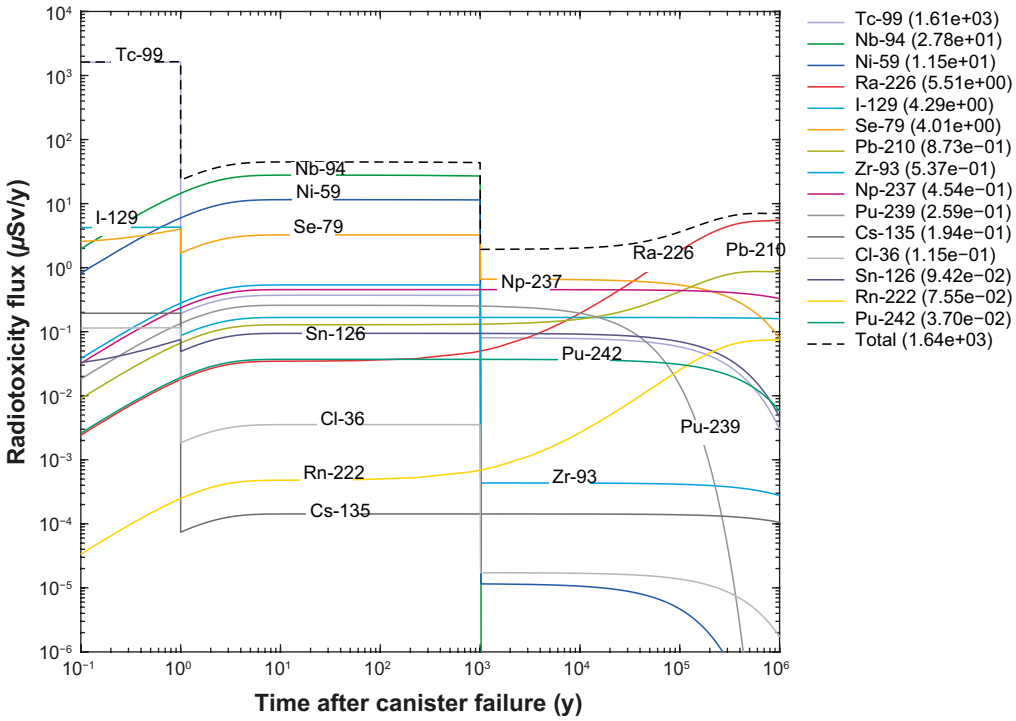

Figure A-9. *Combined near-field boundary condition for the instant release fraction (IRF) modelled as a square pulse of 1 y duration as well as corrosion and dissolution release fractions (CDRF) calculated by COMP23 for canister failure at 10^5 y. Data are presented as equivalent radiotoxicity fluxes (μSv/y) based on the LDF factors defined separately for IRF and CDRF release fractions. The time on the x-axis is in relation to canister failure. Only the top 15 radiotoxicity contributing radionuclides are plotted.*

Alternative scenario for canister failure at 10 ky

The total boundary condition where near-field radiotoxicity flux is summed with the COMP23-calculated corrosion-dissolution radiotoxicity flux is plotted in Figure A-10 for the variant case scenario with canister failure at 10 ky and instant release pulse calculated using the CSTR-analogue model (Equation A-44). The corresponding result for the square pulse instant release (Equation A-47) is shown in Figure A-11. As for the previous calculation case, the near-field flux of Tc-99 calculated using the square pulse assumption is much higher than that calculated using the CSTR-analogue model. The difference is particularly great for Cs-135 which is not even ranked in the top 15 radionuclides when using the CSTR-analogue model although is ranked as number 13 when using the square pulse assumption. The flux of I-129 is also higher by a factor of about 14 in the square pulse case relative to the CSTR-approximation. The instant release flux associated with Se-79 is relatively high for the square pulse case, although is almost absent from the CSTR-analogue model case, presumably due to the dominance of the corrosion release in the latter. The fluxes of Nb-94, C-14, and Ni-59 are barely affected by the instant release in both cases. This is also due to the dominant influence of the corrosion release fraction.

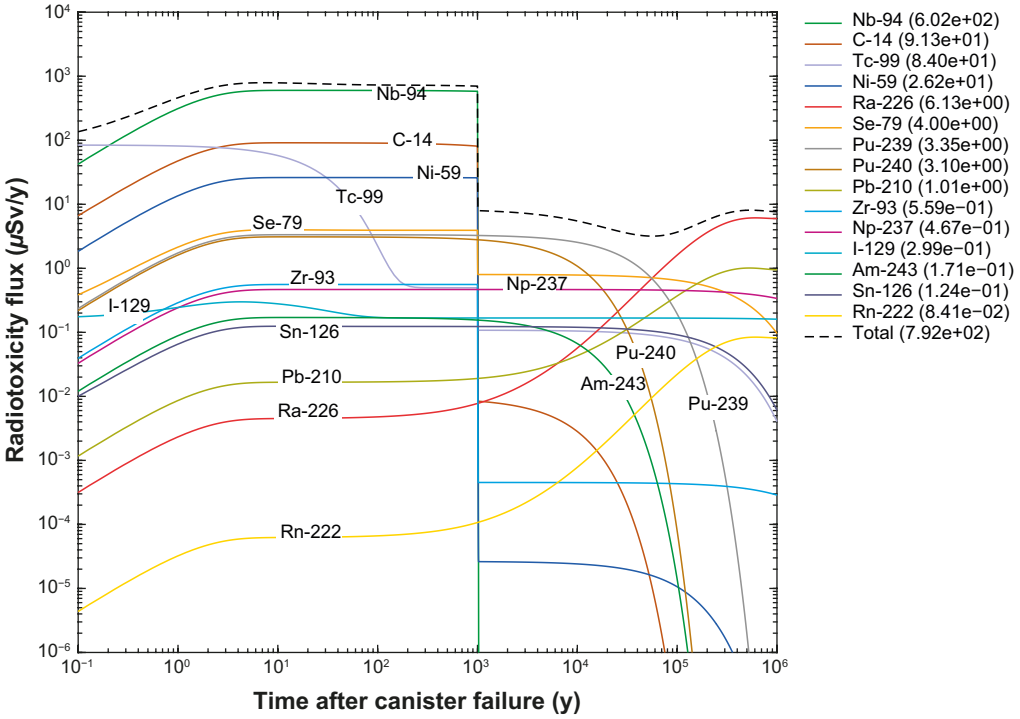

Figure A-10. *Combined near-field boundary condition for the instant release fraction (IRF) modelled as a CSTR system as well as corrosion and dissolution release fractions (CDRF) calculated by COMP23 for canister failure at 10^4 y. Data are presented as equivalent radiotoxicity fluxes (μSv/y) based on the LDF factors defined separately for IRF and CDRF release fractions. The time on the x-axis is in relation to canister failure. Only the top 15 radiotoxicity contributing radionuclides are plotted.*

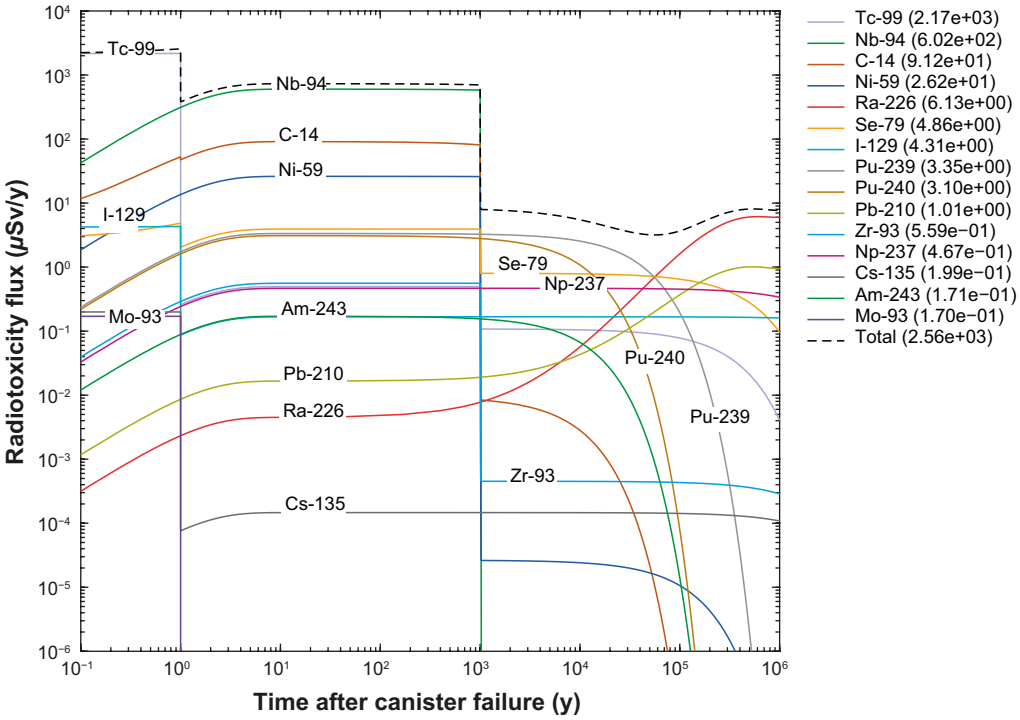

Figure A-11. *Combined near-field boundary condition for the instant release fraction (IRF) modelled as a square pulse of 1 y duration as well as corrosion and dissolution release fractions (CDRF) calculated by COMP23 for canister failure at 10^4 y. Data are presented as equivalent radiotoxicity fluxes (μSv/y) based on the LDF factors defined separately for IRF and CDRF release fractions. The time on the x-axis is in relation to canister failure. Only the top 15 radiotoxicity contributing radionuclides are plotted.*

Alternative scenario for canister failure at 1 ky

The total boundary condition where near-field radiotoxicity flux is summed with the COMP23-calculated corrosion-dissolution radiotoxicity flux is plotted in Figure A-12 for the variant case scenario with canister failure at 1 ky and instant release pulse calculated using the CSTR-analogue model (Equation A-44). The corresponding result for the square pulse instant release (Equation A-47) is shown in Figure A-13. This variant case follows a similar pattern as for the 10 ky canister failure case and there are no significant differences with the exception of Mo-93 which appears in the top 15 dose determining radionuclides in the 1 y square pulse calculation case, although not in the results for the CSTR-analogue model.

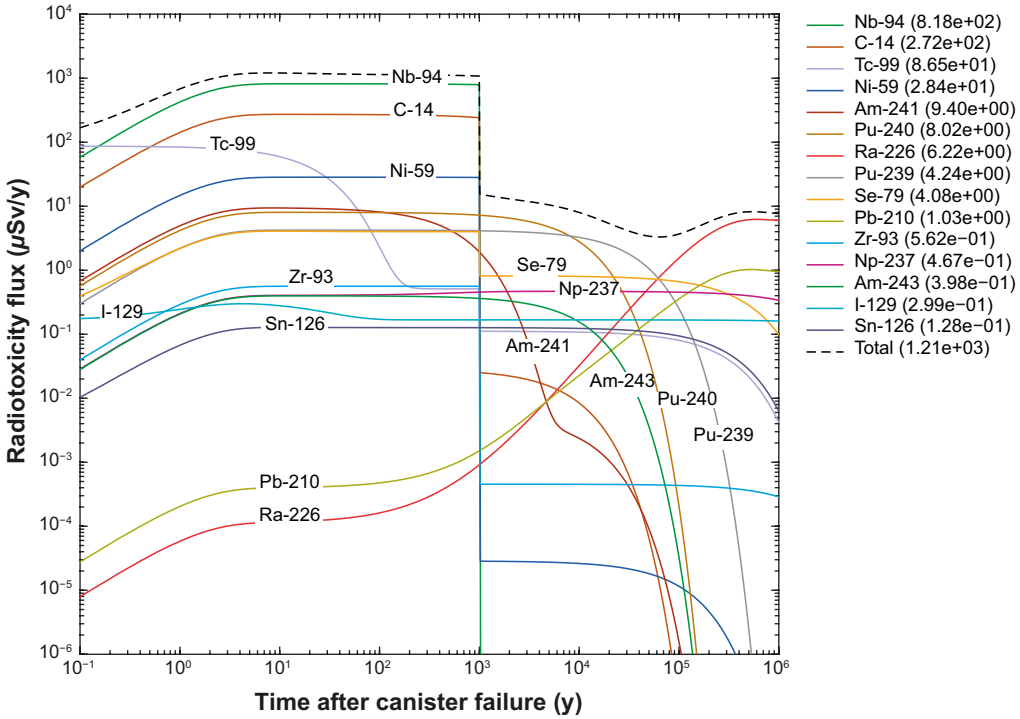

Figure A-12. *Combined near-field boundary condition for the instant release fraction (IRF) modelled as a CSTR system as well as corrosion and dissolution release fractions (CDRF) calculated by COMP23 for canister failure at 10^3 y. Data are presented as equivalent radiotoxicity fluxes (μSv/y) based on the LDF factors defined separately for IRF and CDRF release fractions. The time on the x-axis is in relation to canister failure. Only the top 15 radiotoxicity contributing radionuclides are plotted.*

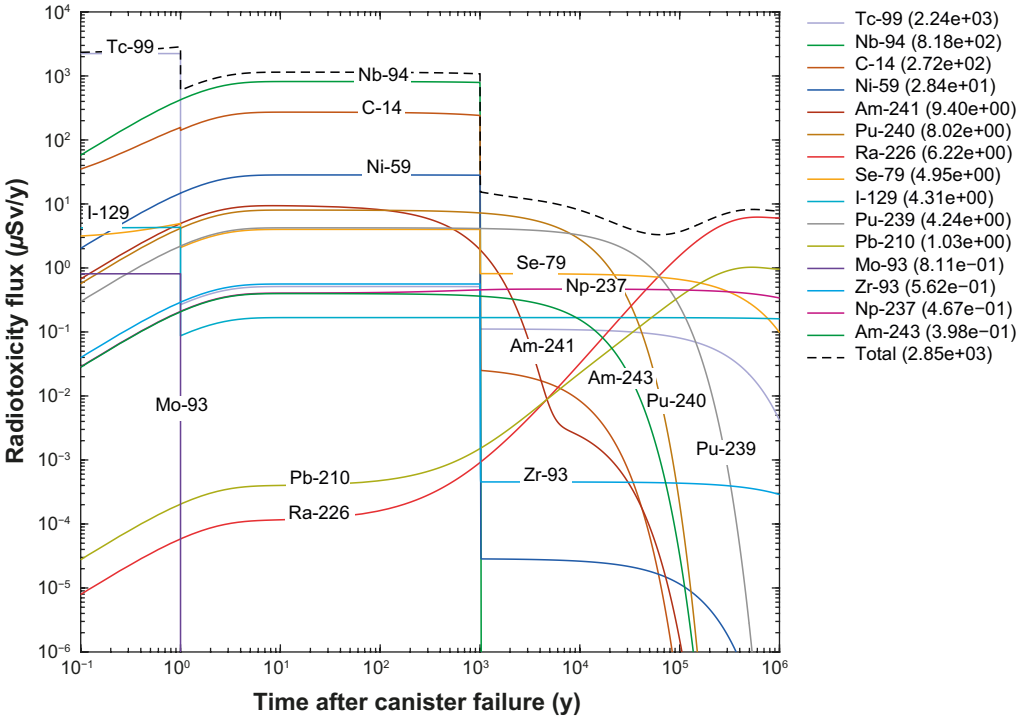

Figure A-13. *Combined near-field boundary condition for the instant release fraction (IRF) modelled as a square pulse of 1 y duration as well as corrosion and dissolution release fractions (CDRF) calculated by COMP23 for canister failure at 10^3 y. Data are presented as equivalent radiotoxicity fluxes (μSv/y) based on the LDF factors defined separately for IRF and CDRF release fractions. The time on the x-axis is in relation to canister failure. Only the top 15 radiotoxicity contributing radionuclides are plotted.*

Alternative scenario for immediate canister failure at 0 y

Although the case for immediate canister failure at 0 y (time of deposition) is not considered relevant to the present work, the near-field radiotoxicity fluxes have been calculated, nevertheless. The total boundary condition where near-field radiotoxicity flux is summed with the COMP23-calculated corrosion-dissolution radiotoxicity flux is plotted in Figure A-14 where the instant release pulse is calculated using the CSTR-analogue model (Equation A-44). The corresponding result for the square pulse instant release (Equation A-47) is shown in Figure A-15. The radiotoxicity fluxes for this case are clearly very different to those shown previously and indicate a strong influence of the short-lived radionuclides H-3, Sn-121m, Mo-93, Nb-93m, and to a much lesser extent Cs-137.

An interesting feature is that the initial flux of Nb-93m rises to a peak and then subsides rapidly, effectively vanishing from the results after a few hundred years. This may not be an accurate reflection of reality, however, since the COMP23-calculated fluxes for the corrosion release fraction (the instant release fraction is relatively insignificant) do not consider ingrowth and replenishment of the Nb-93m inventory by decay of Mo-93 and Zr-93. If the ingrowth mechanism for replenishment of Nb-93m were to be considered, it may become more relevant for the near-field boundary condition calculated for later canister failure times (at least the fraction generated by Zr-93 decay).

The far-field transport calculations made in support of nuclide prioritisation, however, are probably not strongly influenced by the extra flux of Nb-93m since it has sufficiently short half-life that most should be produced by ingrowth along a migration path and only very little originating in the source term should survive to make a contribution to the far-field flux. In any case, the relative importance of Nb as a radioelement is already strengthened by the presence of Nb-94, so minor inaccuracies in the representation of the Nb-93m near field boundary condition arguably has very little relevance for the present work.

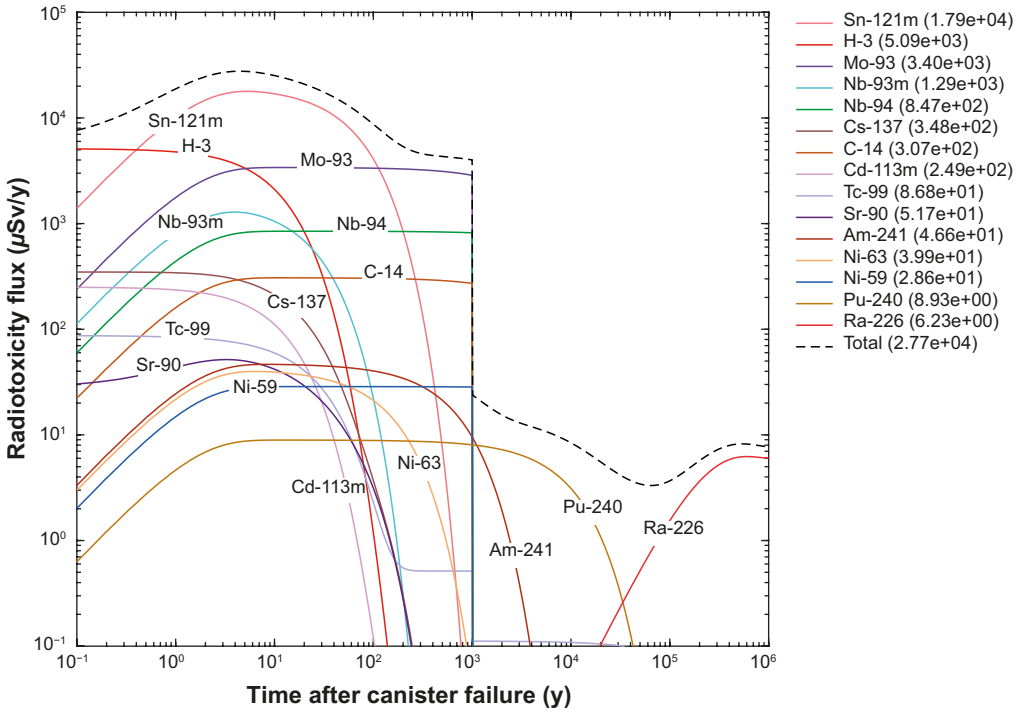

Figure A-14. *Combined near-field boundary condition for the instant release fraction (IRF) modelled as a CSTR system as well as corrosion and dissolution release fractions (CDRF) calculated by COMP23 for canister failure at 0 y (i.e. immediate canister failure at time of deposition). Data are presented as equivalent radiotoxicity fluxes (μSv/y) based on the LDF factors defined separately for IRF and CDRF release fractions. The time on the x-axis is in relation to canister failure. Only the top 15 radiotoxicity contributing radionuclides are plotted.*

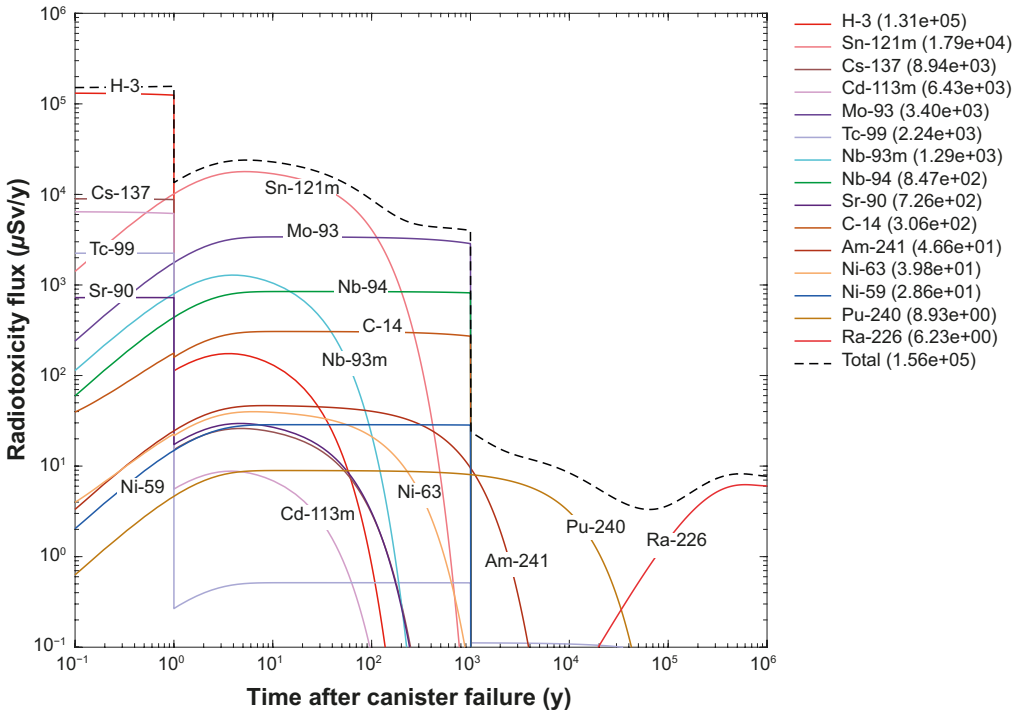

Figure A-15. *Combined near-field boundary condition for the instant release fraction (IRF) modelled as a square pulse of 1 y duration as well as corrosion and dissolution release fractions (CDRF) calculated by COMP23 for canister failure at 0 y (i.e. immediate canister failure at time of deposition). Data are presented as equivalent radiotoxicity fluxes (μSv/y) based on the LDF factors defined separately for IRF and CDRF release fractions. The time on the x-axis is in relation to canister failure. Only the top 15 radiotoxicity contributing radionuclides are plotted.*

Appendix B

Impact of different dose conversion assumptions

In this appendix, breakthrough curves obtained using the different dose conversion assumptions discussed in Section 2.1.3 are presented.

1) SR-Site/PSAR modelling approach. Use of separate Pulse LDF and Basic LDF values for the instant release (IRF) and corrosion/dissolution release fractions (CDRF), respectively. Pulse LDF values for radionuclides that were not explicitly modelled in SR-Site/PSAR are taken from the correlation in Figure 2-3;
2) Use of raw dose conversion factors for direct ingestion (labelled here as DCF-I);
3) Use of Basic LDF values taken from SR-Site/PSAR without differentiating between IRF and CDRF fractions (labelled here as VC-LDF);
4) Use of LDF values taken from SR-PSU (SKB 2014, Table 10-1, p 161) without differentiating between IRF and CDRF fractions (labelled here as SFR-LDF).

All results presented in the appendix use the CSTR-analogue model (see Appendix A) to calculate the near-field boundary condition.

Reference scenario for canister failure at 100 ky

The results for the base case parameterisation (original SR-Site/PSAR-recommended K_d values) of the reference scenario with canister failure at 100 ky are shown in Figure B-1 (LDF calculation case), Figure B-2 (DCF-I calculation case), Figure B-3 (VC-LDF calculation case), and Figure B-4 (SFR-LDF calculation case). As can be seen from the plotted data, the results of the DCF-I case are very dense with a much larger number of radionuclides contributing towards the total radiotoxicity flux (i.e., over the plot cut-off limit of 0.1 %). Also, the total radiotoxicity flux and that of all radionuclides is several orders of magnitude higher in the DCF-I calculation case which is largely because there is no dilution or attenuation of the far-field flux in biosphere objects. Although the absolute value of the radiotoxicity fluxes calculated in the DCF-I case may not be particularly relevant for human dose rates, the relative impact of altered K_d values on the individual radionuclide fluxes in relation to the total flux is still a relevant performance measure in the present context.

As has already been pointed out in Section 5, the same top dose contributing radionuclides are present although with a slightly different order depending on the relative weighting given to them by the dose conversion calculation. The DCF-I case therefore functions as a limiting case to illustrate the impact of the assumed landscape dose factors on the outcome of the transport modelling evaluation. Since pulse LDF values are generally several orders of magnitude lower than the basic LDF values, the VC-LDF calculation case exaggerates the impact of the instant release fraction. In the SFR-LDF case there is also a significant downgrading of the relative importance of Se-79 and Nb-94 while Cs-135, Zr-93, and Pu-239 increase in importance reflecting the relative changes in LDF's assigned to these radionuclides in SR-PSU (SKB 2014).

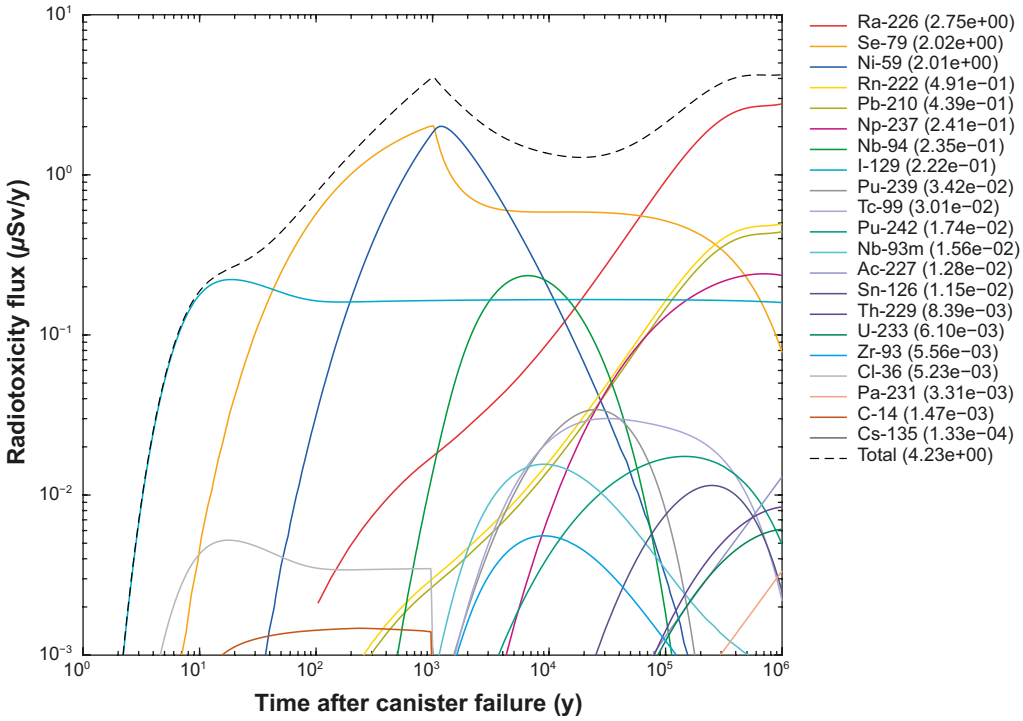

Figure B-1. *Equivalent radiotoxicity flux (μSv/y) calculated using NuDec-Farf31 (LDF calculation case), for the base case parameterisation, including both the instant release fraction (IRF) and corrosion/dissolution release fraction (CDRF). The legend is sorted by peak flux within the time frame of the safety assessment. The time on the x-axis is relative to the assumed canister failure at 100 ky post-closure. Only radionuclides contributing more than 0.1 % of the total radiotoxicity are plotted.*

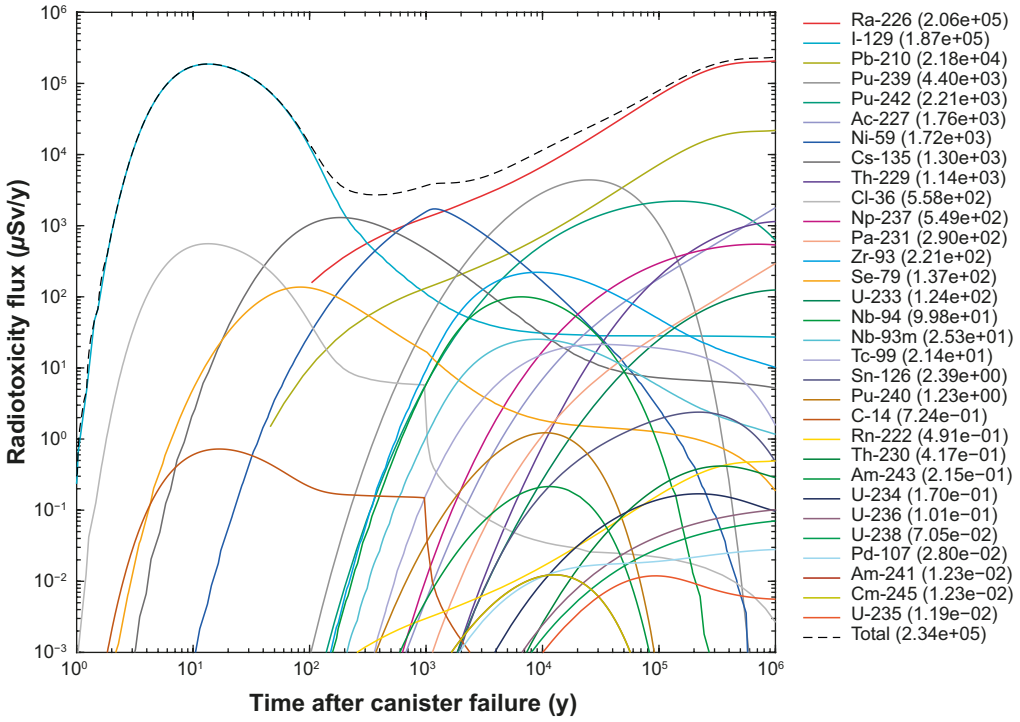

Figure B-2. *Equivalent radiotoxicity flux (μSv/y) calculated using NuDec-Farf31 (DCF-I calculation case), for the base case parameterisation, including both the instant release fraction (IRF) and corrosion/dissolution release fraction (CDRF). The legend is sorted by peak flux within the time frame of the safety assessment. The time on the x-axis is relative to the assumed canister failure at 100 ky post-closure. Only radionuclides contributing more than 0.1 % of the total radiotoxicity are plotted.*

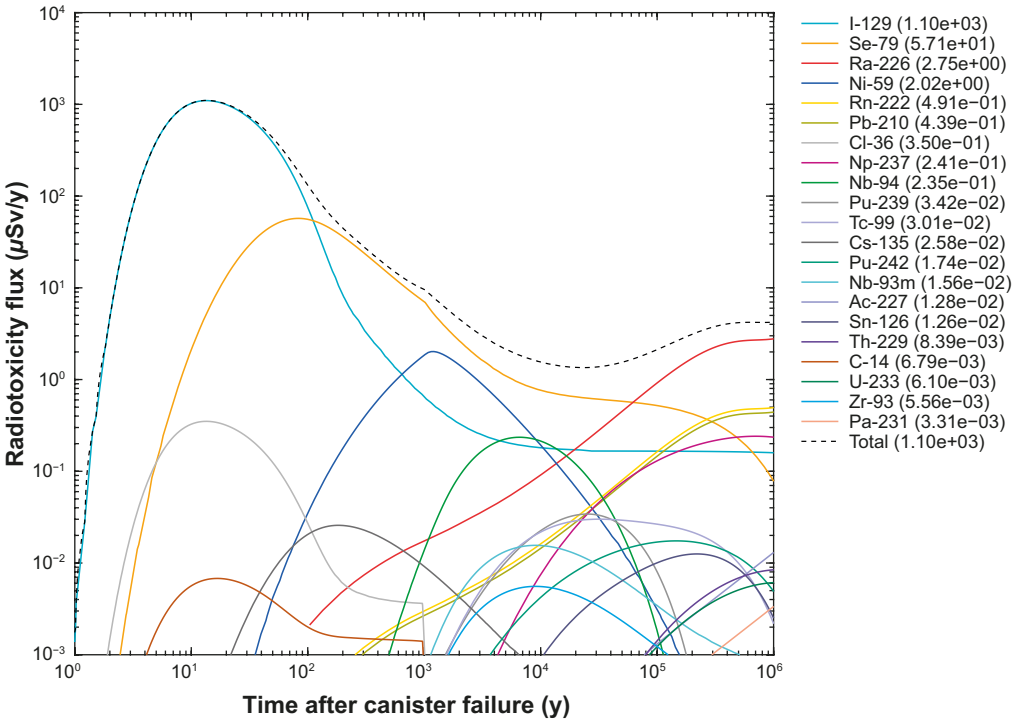

Figure B-3. *Equivalent radiotoxicity flux (µSv/y) calculated using NuDec-Farf31 (VC-LDF calculation case), for the base case parameterisation, including both the instant release fraction (IRF) and corrosion/dissolution release fraction (CDRF). The legend is sorted by peak flux within the time frame of the safety assessment. The time on the x-axis is relative to the assumed canister failure at 100 ky post-closure. Only radionuclides contributing more than 0.1 % of the total radiotoxicity are plotted.*

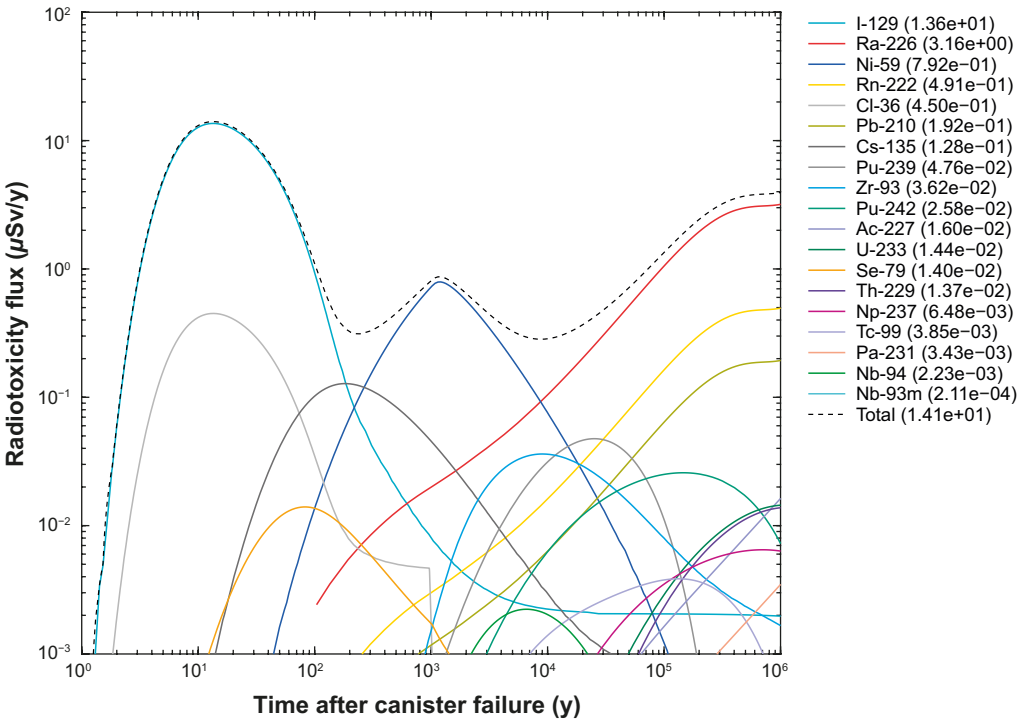

Figure B-4. *Equivalent radiotoxicity flux (µSv/y) calculated using NuDec-Farf31 (SFR-LDF calculation case), for the base case parameterisation, including both the instant release fraction (IRF) and corrosion/dissolution release fraction (CDRF). The legend is sorted by peak flux within the time frame of the safety assessment. The time on the x-axis is relative to the assumed canister failure at 100 ky post-closure. Only radionuclides contributing more than 0.1 % of the total radiotoxicity are plotted.*

Alternative scenario for canister failure at 10 ky

For the release scenario with early canister failure at 10 ky, the results are similar to the reference scenario although with more prominent role for short-lived C-14. The actinides Pu-239 and Pu-240 are also more strongly represented in the DCF-I calculation case relative to the LDF calculation case. This is presumably due to the greater attenuation of these radionuclides in the biosphere as reflected in the LDF weightings relative to DCF-I. The far-field radiotoxicity fluxes for the LDF calculation case are shown in Figure B-5, for the DCF-I calculation case in Figure B-6, VC-LDF calculation case in Figure B-7, and the SFR-LDF calculation case in Figure B-8.

As in the reference scenario, the main effect of using the DCF-I approach rather than LDF is the different weighting given to individual radionuclides and the much higher absolute radiotoxicity fluxes when using DFC-I values for the dose conversion. As in the previous canister failure scenario, the VC-LDF case exaggerates the impact of the pulse release particularly for I-129, Se-79, and Mo-93. Comparing the VC-LDF case with the SFR-LDF case shows a downgrading of the role played by C-14, Mo-93, Se-79, and Nb-94 and an increase in the relative importance of Pu-239, Pu-240, Zr-93, and Cs-135. The changes for Pu are particularly noticeable relative to the scenario for canister failure at 100 ky and reflect the greater inventory of the short-lived Pu isotopes at the early canister failure time of 10 ky.

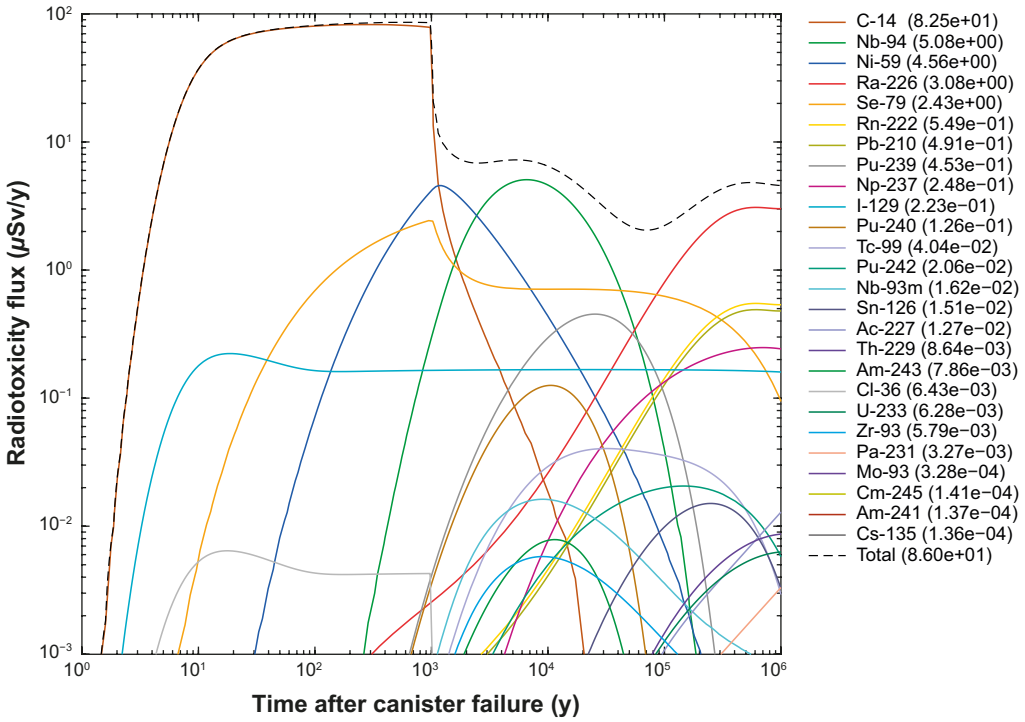

Figure B-5. *Equivalent radiotoxicity flux (μSv/y) calculated using NuDec-Farf31 (LDF calculation case), for the base case parameterisation, including both the instant release fraction (IRF) and corrosion/dissolution release fraction (CDRF). The legend is sorted by peak flux within the time frame of the safety assessment. The time on the x-axis is relative to the assumed canister failure at 10 ky post-closure. Only radionuclides contributing more than 0.1 % of the total radiotoxicity are plotted.*

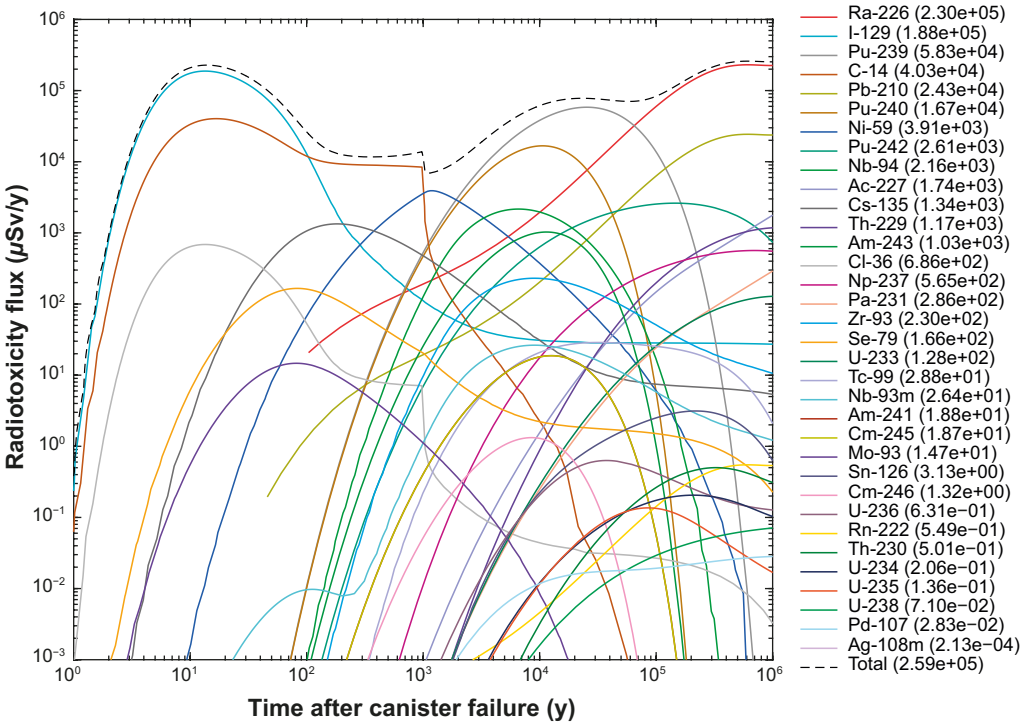

Figure B-6. *Equivalent radiotoxicity flux (µSv/y) calculated using NuDec-Farf31 (DCF-I calculation case), for the base case parameterisation, including both the instant release fraction (IRF) and corrosion/dissolution release fraction (CDRF). The legend is sorted by peak flux within the time frame of the safety assessment. The time on the x-axis is relative to the assumed canister failure at 10 ky post-closure. Only radionuclides contributing more than 0.1 % of the total radiotoxicity are plotted.*

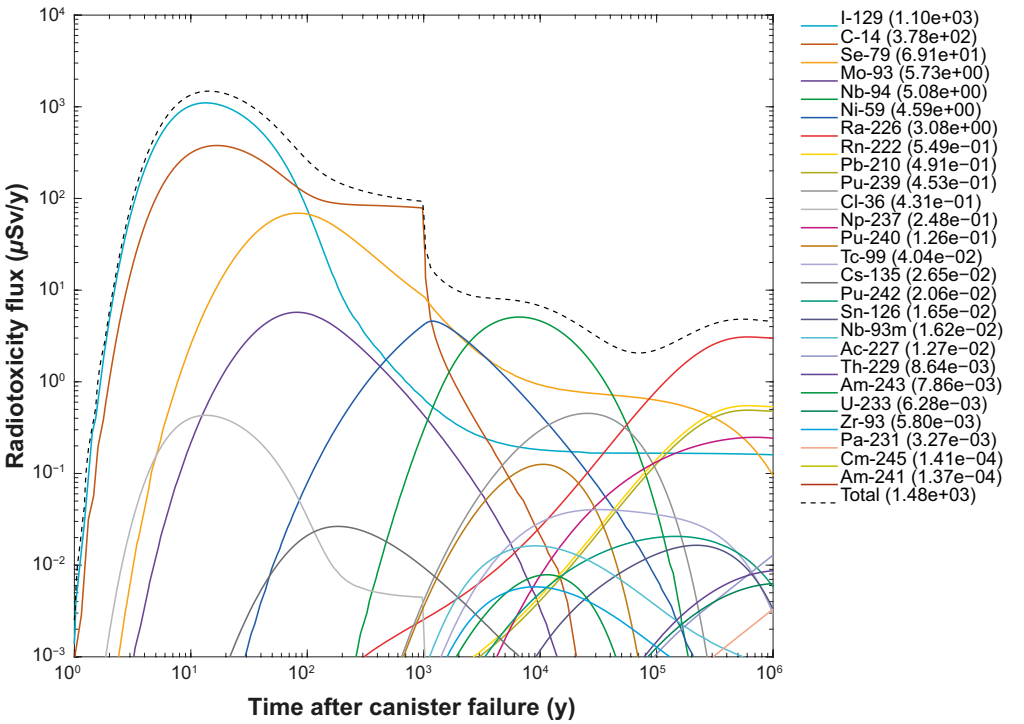

Figure B-7. *Equivalent radiotoxicity flux (µSv/y) calculated using NuDec-Farf31 (VC-LDF case), for the base case parameterisation, including both the instant release fraction (IRF) and corrosion/dissolution release fraction (CDRF). The legend is sorted by peak flux within the time frame of the safety assessment. The time on the x-axis is relative to the assumed canister failure at 10 ky post-closure. Only radionuclides contributing more than 0.1 % of the total radiotoxicity are plotted.*

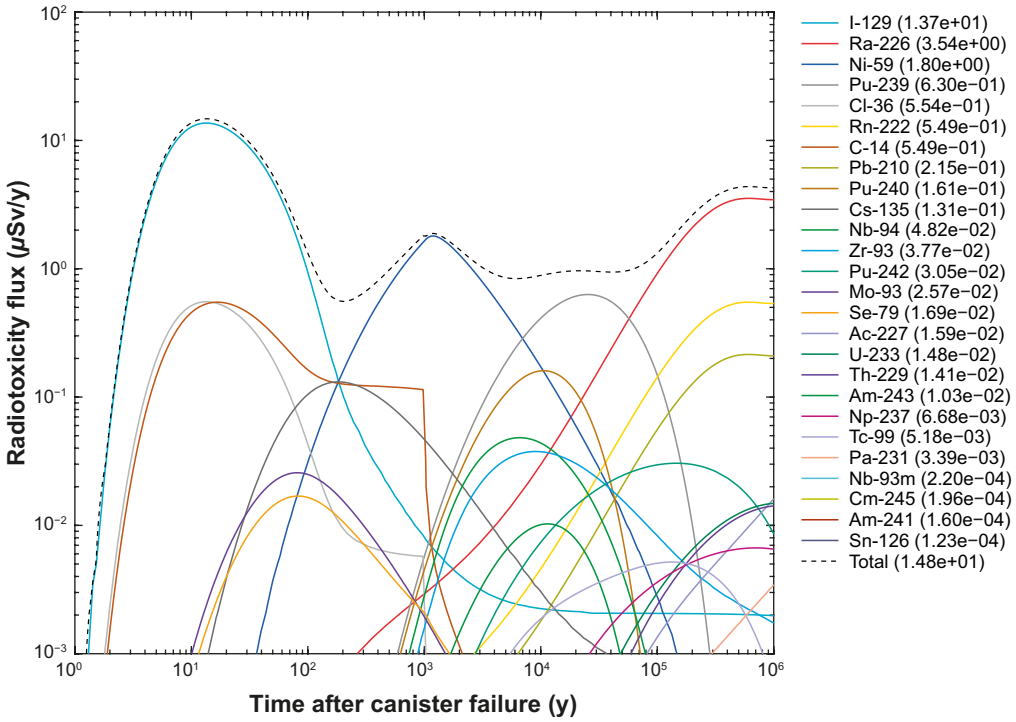

Figure B-8. *Equivalent radiotoxicity flux (μSv/y) calculated using NuDec-Farf31 (SFR-LDF case), for the base case parameterisation, including both the instant release fraction (IRF) and corrosion/dissolution release fraction (CDRF). The legend is sorted by peak flux within the time frame of the safety assessment. The time on the x-axis is relative to the assumed canister failure at 10 ky post-closure. Only radionuclides contributing more than 0.1 % of the total radiotoxicity are plotted.*

Alternative scenario for canister failure at 1 ky

The results for the far-field transport in the scenario for very early canister failure at 1 ky are shown in Figure B-9 for the LDF calculation case, Figure B-10 for the DCF-I calculation case, Figure B-11 for the VC-LDF case, and Figure B-12 for the SFR-LDF case. The main difference in this scenario is an increasingly dominant role for C-14 at early times in all calculation cases, although slightly less so in the SFR-LDF case. For the DCF-I case, the actinides Pu-239 and Pu-240 are also much more significant than in previous cases. For the VC-LDF case, the radiotoxicity flux of I-129, Se-79, and Mo-93 are significantly elevated relative to the reference LDF calculation case. Comparing the VC-LDF case with the SFR-LDF case shows a similar pattern as previously with a relative downgrading of the role played by C-14, Mo-93, Se-79, and Nb-94 and an increase in the relative importance of Pu-239, Pu-240, Zr-93, and Cs-135. As noted previously, the changes for Pu are particularly noticeable and reflect the greater inventory of the short-lived Pu isotopes at the early canister failure time of 1 ky.

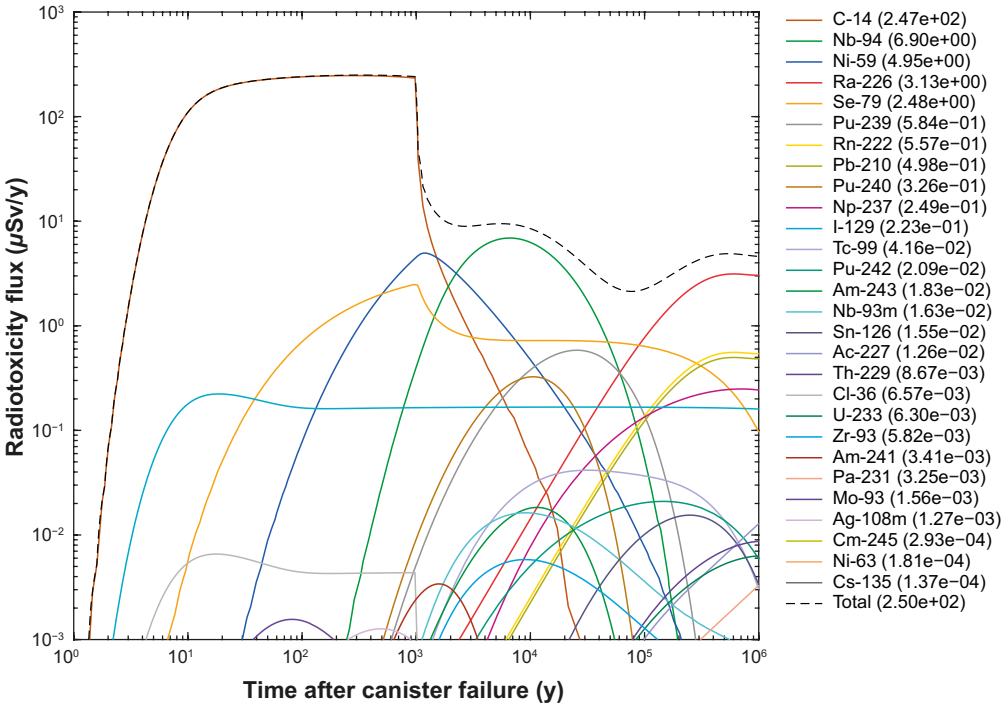

Figure B-9. *Equivalent radiotoxicity flux (µSv/y) calculated using NuDec-Farf31 (LDF calculation case), for the base case parameterisation, including both the instant release fraction (IRF) and corrosion/dissolution release fraction (CDRF). The legend is sorted by peak flux within the time frame of the safety assessment. The time on the x-axis is relative to the assumed canister failure at 1 ky post-closure. Only radionuclides contributing more than 0.1 % of the total radiotoxicity are plotted.*

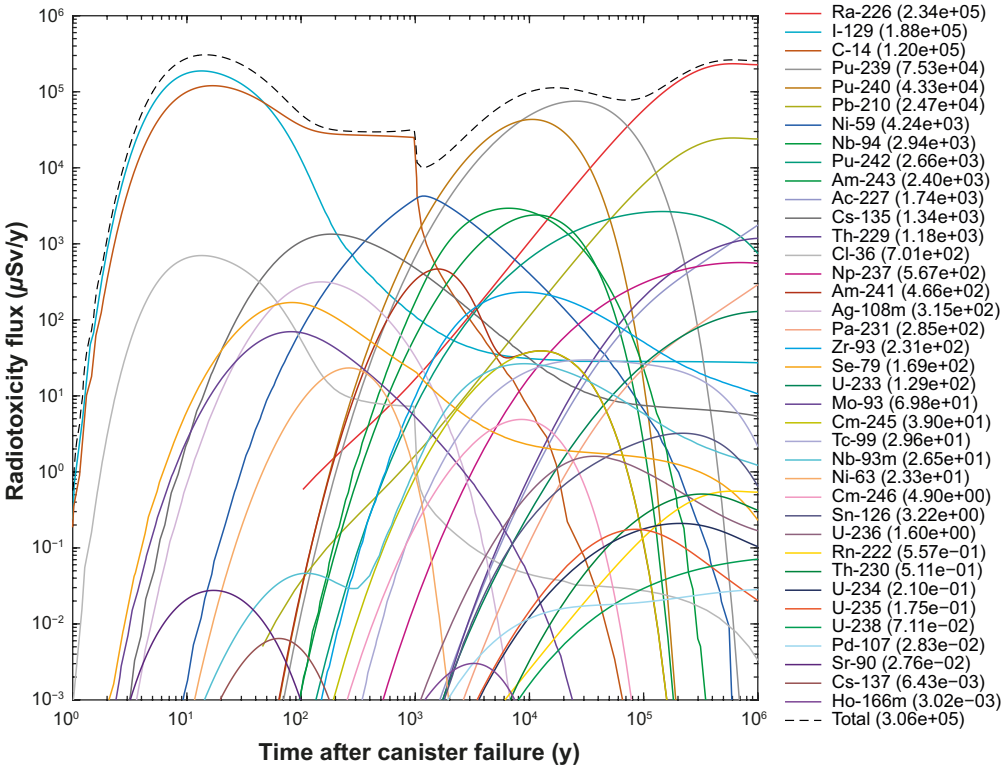

Figure B-10. *Equivalent radiotoxicity flux (µSv/y) calculated using NuDec-Farf31 (DCF-I calculation case), for the base case parameterisation, including both the instant release fraction (IRF) and corrosion/dissolution release fraction (CDRF). The legend is sorted by peak flux within the time frame of the safety assessment. The time on the x-axis is relative to the assumed canister failure at 1 ky post-closure. Only radionuclides contributing more than 0.1 % of the total radiotoxicity are plotted.*

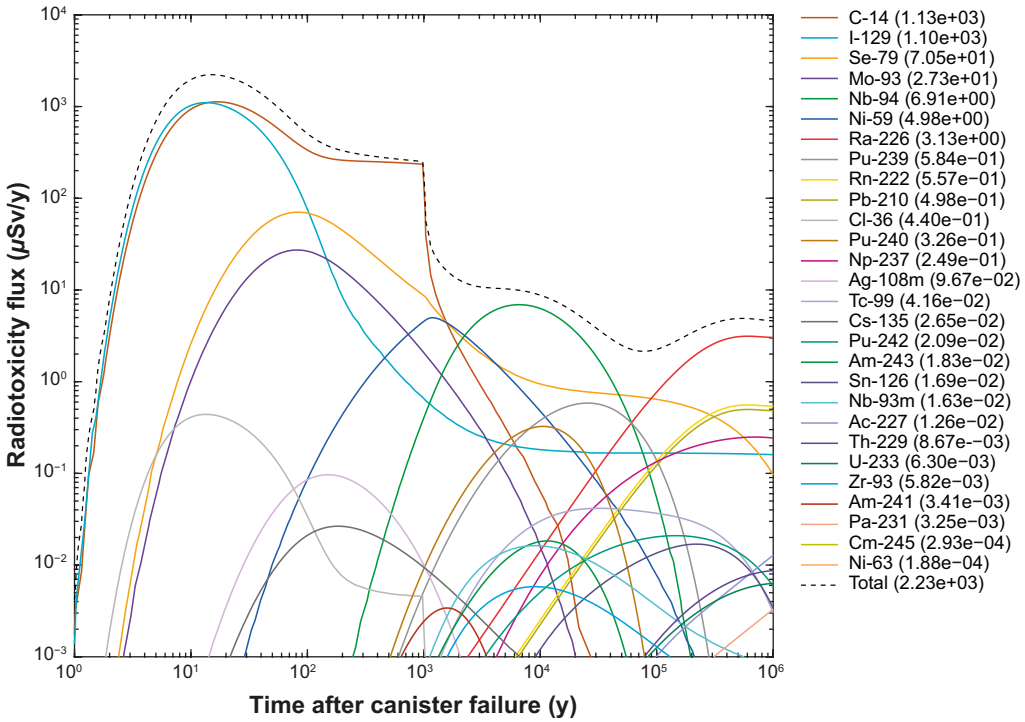

Figure B-11. *Equivalent radiotoxicity flux (µSv/y) calculated using NuDec-Farf31 (VC-LDF case), for the base case parameterisation, including both the instant release fraction (IRF) and corrosion/dissolution release fraction (CDRF). The legend is sorted by peak flux within the time frame of the safety assessment. The time on the x-axis is relative to the assumed canister failure at 1 ky post-closure. Only radionuclides contributing more than 0.1 % of the total radiotoxicity are plotted.*

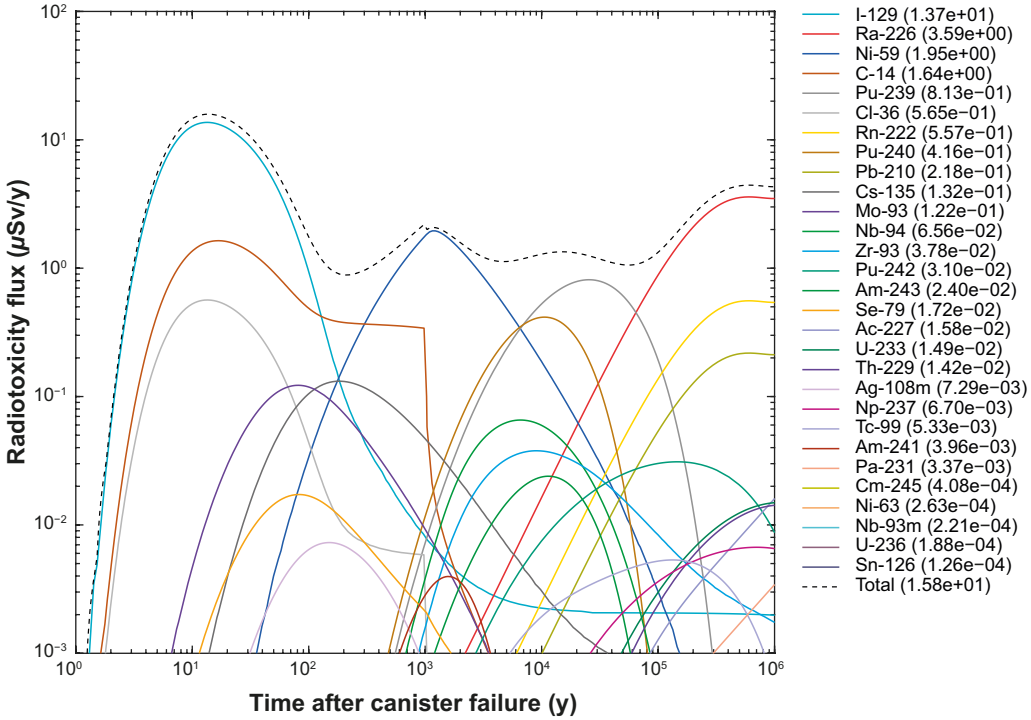

Figure B-12. *Equivalent radiotoxicity flux (µSv/y) calculated using NuDec-Farf31 (SFR-LDF case), for the base case parameterisation, including both the instant release fraction (IRF) and corrosion/dissolution release fraction (CDRF). The legend is sorted by peak flux within the time frame of the safety assessment. The time on the x-axis is relative to the assumed canister failure at 1 ky post-closure. Only radionuclides contributing more than 0.1 % of the total radiotoxicity are plotted.*

Appendix C

Additional calculations for screening of insignificant dose contributors

In this appendix, additional far-field transport calculations are detailed which are used to support the selection of prioritised radionuclides discussed previously in Section 5. Here, we consider the reference scenario of canister failure at 100 ky and LDF values for pulse and corrosion/dissolution release as used in SR-Site/PSAR. It is noted that different assumptions such as the use of LDF factors taken from SR-PSU (see Appendix B, SFR-LDF calculation case) might lead to different outcomes in the case of Zr (and possibly also Cs). Other elements identified as being less important in the analysis discussed in this appendix are likely to also remain so when using LDF values corresponding to the SFR-LDF calculation, although this has not been confirmed in numerical calculations.

Based on the overall rankings given in Table 5-1, simulations were made where the K_d values for radioelements associated with lesser-ranked sorbing radionuclides were systematically altered over a large range to ascertain the impact that this might have on the far-field breakthrough of total radiotoxicity flux. In total, five simulations were made of far-field transport using the reference scenario with canister failure at 100 ky as a calculation basis. The K_d values used in the calculations are summarised in Table C-1 where the different variation cases are labelled VC1 to VC5, respectively.

To begin with, all radioelements not represented amongst the top 15 radionuclides were given K_d values of 10^{-6} kg/m^3 which, as discussed in Section 4.1.1, may be considered effectively non-sorbing (grey-shaded rows in Table C-1). All of these are either monovalent, or divalent cations with the exception of Pa which is expected to be speciated in a pentavalent form under prevailing groundwater conditions at repository depth (and Mo which has decayed to insignificance in the reference scenario). Sorbing radioelements corresponding to radionuclides ranked in the top 11 in the reference scenario (LDF-basis, 100 ky canister failure), on the other hand, were maintained at their base case values without change as these were already identified as important dose contributors in Section 4.

Other trivalent and tetravalent radioelements (e.g., Ac, Am, Cm, Eu, Ho, Sm, Th, and U) are known to sorb strongly even if they are relatively unimportant for total radiotoxicity flux. Since the assignment of very low, or effectively zero K_d values to these radioelements is not physically meaningful (i.e., they are known to sorb strongly in spite of uncertainties), their K_d values were varied over a range from 10^{-4} m^3/kg (weakly sorbing) to 10 m^3/kg (strongly sorbing) to assess the sensitivity of the total radiotoxicity flux to uncertainty in the sorptive strength of these radioelements (green-shaded rows in Table C-1). The two remaining tetravalent elements were identified as having a slightly larger impact on total radiotoxicity flux and therefore had their K_d values varied over a narrower range (red-shaded rows in Table C-1).

Table C-1. Material properties of the undisturbed rock used in the corrosion scenario screening calculations. The K_d values (kg/m^3) corresponding to the base case parameterisation are given in the second column while variant cases (VC1–VC5) are in adjacent columns to the right. Rows with grey shading indicate radioelements assigned arbitrarily low K_d values. K_d values for radioelements in rows with green shading were varied over seven orders of magnitude in matching sequence as part of the screening calculation. Radioelements in red shaded rows (Sn and Zr) were also varied in a matching sequence, although over a narrower range than the green shaded rows.

Radio-element	Base Case	VC1	VC2	VC3	VC4	VC5
Ac	1.5×10^{-2}	1.0×10^{-4}	1.0	1.0×10^{-4}	1.0×10^{-4}	10.0
Ag	3.5×10^{-4}	1.0×10^{-6}	1.0×10^{-6}	1.0×10^{-6}	1.0×10^{-6}	1.0×10^{-6}
Am	1.5×10^{-2}	1.0×10^{-4}	1.0	1.0×10^{-4}	1.0×10^{-4}	
C	0	0	0	0	0	0
Cd	1.1×10^{-3}	1.0×10^{-6}	1.0×10^{-6}	1.0×10^{-6}	1.0×10^{-6}	1.0×10^{-6}
Cl	0	0	0	0	0	0
Cm	1.5×10^{-2}	1.0×10^{-4}	1.0	1.0×10^{-4}	1.0×10^{-4}	10.0
Cs	3.5×10^{-4}	1.0×10^{-6}	1.0×10^{-6}	1.0×10^{-6}	1.0×10^{-6}	1.0×10^{-6}
Eu	1.5×10^{-2}	1.0×10^{-4}	1.0	1.0×10^{-4}	1.0×10^{-4}	10.0
H	0	0	0	0	0	0
Ho	1.5×10^{-2}	1.0×10^{-4}	1.0	1.0×10^{-4}	1.0×10^{-4}	10.0
I	0	0	0	0	0	0
Mo	3.0×10^{-4}	1.0×10^{-6}	1.0×10^{-6}	1.0×10^{-6}	1.0×10^{-6}	1.0×10^{-6}
Nb	2.0×10^{-2}	2.0×10^{-2}	2.0×10^{-2}	2.0×10^{-2}	2.0×10^{-2}	2.0×10^{-2}
Ni	1.1×10^{-3}	1.1×10^{-3}	1.1×10^{-3}	1.1×10^{-3}	1.1×10^{-3}	1.1×10^{-3}
Np	5.3×10^{-2}	5.3×10^{-2}	5.3×10^{-2}	5.3×10^{-2}	5.3×10^{-2}	5.3×10^{-2}
Pa	5.9×10^{-2}	1.0×10^{-6}	1.0×10^{-6}	1.0×10^{-6}	1.0×10^{-6}	1.0×10^{-6}
Pb	2.5×10^{-2}	2.5×10^{-2}	2.5×10^{-2}	2.5×10^{-2}	2.5×10^{-2}	2.5×10^{-2}
Pd	5.2×10^{-2}	1.0×10^{-6}	1.0×10^{-6}	1.0×10^{-6}	1.0×10^{-6}	1.0×10^{-6}
Pu	1.5×10^{-2}	1.5×10^{-2}	1.5×10^{-2}	1.5×10^{-2}	1.5×10^{-2}	1.5×10^{-2}
Ra	2.4×10^{-4}	2.4×10^{-4}	2.4×10^{-4}	2.4×10^{-4}	2.4×10^{-4}	2.4×10^{-4}
Rn	0	0	0	0	0	0
Se	3×10^{-4}	3×10^{-4}	3×10^{-4}	3×10^{-4}	3×10^{-4}	3×10^{-4}
Sm	1.5×10^{-2}	1.0×10^{-4}	1.0	1.0×10^{-4}	1.0×10^{-4}	10.0
Sn	1.6×10^{-1}	1.0×10^{-4}	1.0	1.0×10^{-3}	0.01	0.1
Sr	3.4×10^{-6}	1.0×10^{-6}	1.0×10^{-6}	1.0×10^{-6}	1.0×10^{-6}	1.0×10^{-6}
Tc	5.3×10^{-2}	5.3×10^{-2}	5.3×10^{-2}	5.3×10^{-2}	5.3×10^{-2}	5.3×10^{-2}
Th	5.3×10^{-2}	1.0×10^{-4}	1.0	1.0×10^{-4}	1.0×10^{-4}	10.0
U	5.3×10^{-2}	1.0×10^{-4}	1.0	1.0×10^{-4}	1.0×10^{-4}	10.0
Zr	2.1×10^{-2}	1.0×10^{-4}	1.0	1.0×10^{-3}	0.01	0.1

Based on the parameterisation specified in Table C-1, simulations were made of far-field transport for each of the variation cases. The results of these calculations are plotted in Figure C-1 in terms of total radiotoxicity flux summed over all radionuclides. In the plot shown in Figure C-1, the axes are zoomed in to highlight the locations of maximum deviation. The radiotoxicity flux for the base case (blue curve) is otherwise identical to that previously shown in Figure 3-1. Based on the simulation results, two time points of maximum deviation from the base case K_d parameterisation were identified at approximately 1 ky and 20 ky, respectively. In the following discussion, deviations of the total radiotoxicity flux from the base case are considered at these two time points.

Variation case 1 is clearly associated with the lowest transport retardation for the lesser-ranked radionuclides with the total flux exceeding the base case by roughly 9.7 % at 1 ky and 6.3 % at 20 ky. This is closely followed by variation case 3 where the deviation is 3.1 % and 5.2 %, respectively. Variation cases 2 and 5, with high K_d values (very strong sorption) assigned to the trivalent and tetravalent radioelements exhibit the smallest deviations from the base case. For variation case 2, the radiotoxicity flux has insignificant deviation at 1 ky, although a negative deviation of roughly −2.1 % (i.e., lower flux) at 20 ky relative to the base case. For variation case 5, the deviation at 1 ky is also insignificant although −2.5 % at 20 ky.

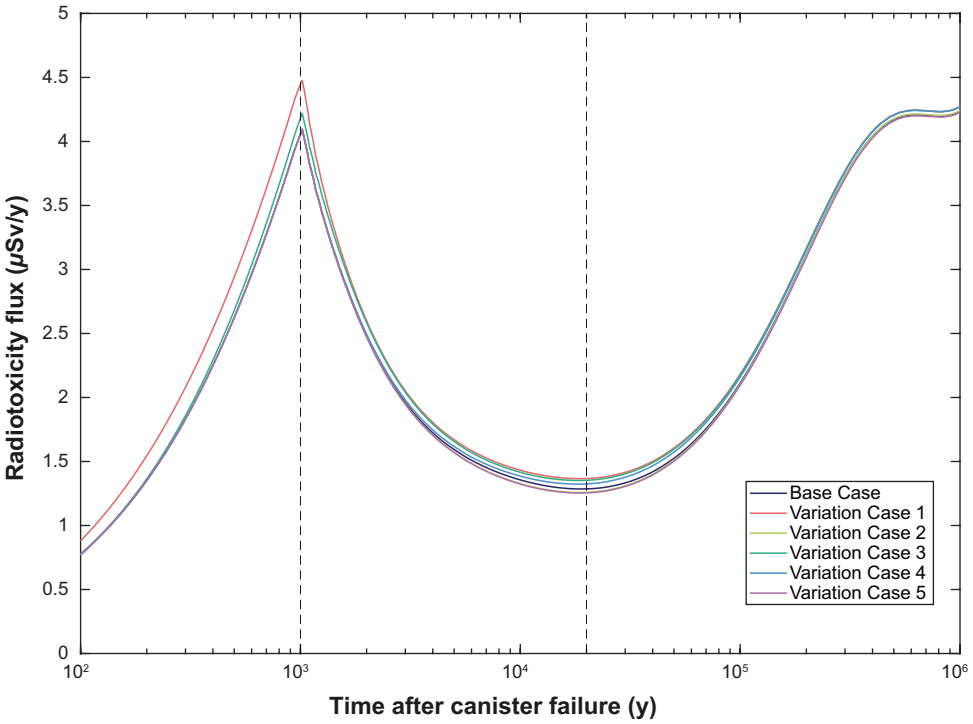

Figure C-1. *Total far-field radiotoxicity flux (μSv/y) for the base case K_d parameterisation and variation cases with K_d values as specified in Table C-1 for canister failure at 100 ky. Two points of comparison relevant for the variation cases are identified at roughly 1 ky and 20 ky, respectively (see text for explanation).*

Based on the differences between variant cases 1 and 4 it is postulated that much of the modelled variation can be related to the sorption status of Sn and Zr. Although Sn-126 and Zr-93 only contribute to total radiotoxicity flux in a minor way, there appears to be some sensitivity to K_d values in the modelled range 10^{-4} m^3/kg – 1 m^3/kg with decreasing K_d values giving larger positive deviations of the total radiotoxicity flux (i.e., too low sorptivity will give dose overestimates for the far-field). For the trivalent and tetravalent radioelements not already included in the top ranked list (i.e., Np, Pu, and Tc), the total radiotoxicity flux is remarkably insensitive to the choice of K_d value even when varied over seven orders of magnitude as in these screening calculations.

Based on this simple complementary analysis, it therefore appears that Safety Assessment performance measures can tolerate relatively large uncertainty in the K_d specified for Ac, Am, Cm, Eu, Ho, Sm, Th, and U for the reference scenario. Given that some of these are important geochemical analogues for the important ranked radionuclides (Np, Pu, and Tc), however, they still play an important role in data assimilation and cannot be completely neglected. Even the minor uncertainty in total breakthrough that can be attributed to the sorption status of Sn and Zr is very minor and unlikely to be a controlling factor in the overall uncertainty assessment for the scenarios considered. The radioelements with K_d values set to very low values (10^{-6} m^3/kg), on the other hand, have essentially no impact on total radiotoxicity breakthrough regardless of K_d value and could reasonably be deprecated from the Safety Assessment calculations, at least for the reference scenario with canister failure at 100 ky and LDF values corresponding to those used in SR-Site/PSAR.

Arkitektkopia AB, Bromma, 2022

SKB is responsible for managing spent nuclear fuel and radioactive waste produced by the Swedish nuclear power plants such that man and the environment are protected in the near and distant future.

skb.se